Computational investigation into jet impingement boiling on pin-fin surfaces

by

Luwan Ludick

Submitted in partial fulfilment of the requirement for the degree
MASTER OF ENGINEERING (MECHANICAL ENGINEERING)

in the

Department of Mechanical and Aeronautical Engineering

Faculty of Engineering, Built Environment and Information Technology

University of Pretoria

March 2023

Abstract

Computational investigation into jet impingement boiling on pin-fin surfaces

by

Luwan Ludick

Supervisor:	Prof KJ Craig
Co-Supervisors:	Prof P Valluri (The University of Edinburgh), Prof JP Meyer
Department:	Mechanical and Aeronautical Engineering
University:	University of Pretoria
Degree:	Master of Engineering (Mechanical Engineering)
Keywords:	Jet Impingement, Boiling, pin-fin surface, dry-out region, Computational Fluid Dynamics (CFD), RPI boiling model, Pin-fin parametric study

Thermal management of densely packed chips is critical for developing prevailing chips. For years, conventional air-cooling techniques have been utilised for numerous microsystems where fans and heat sinks were used in high-power computing systems due to their low cost and high reliability. Unfortunately, recent developments have exceeded the heat dissipation capability of these conventional techniques, leading to a shift towards liquid-to-vapour phase-change cooling techniques. Various multiphase cooling techniques have been reported in the literature. Over the last few decades, jet impingement has been shown to be an effective and attractive way to transfer energy from high heat flux components by the substantial amount of thermal energy transferred between the solid and the liquid. Surface enhancement techniques have also gained traction due to the increased average surface heat transfer coefficient and surface area by disrupting boundary layer growth and improving turbulent transport. This research combined jet impingement with phase change or boiling and surface area enhancement to improve heat transfer from a surface.

Different boiling types arise in boiling jet impingement on pin-fin surfaces due to the various flow patterns caused by the pin-fin layout, thereby increasing the numerical complexity. All relevant numerical studies documented in the literature focused on boiling jet impingement on flat surfaces, whereas no studies were found on pin-fin surfaces. Therefore, conducting a well-documented numerical study of pin-fin surfaces formed an essential part of the current work. The complex flow patterns and boiling types between the pin fins had to be better understood before they could be widely implemented in electronic cooling applications.

In this study, the heat transfer effect of pin-fin surfaces in boiling jet impingement was investigated using the RPI boiling model embedded in the Eulerian multiphase framework, which is an option in ANSYS Fluent. The numerical results of wall surface temperature in the stagnation area of the jet correlated well with experimental data reported in the literature. Not measured in the reference experiment, the pool-boiling areas caused by flow obstruction led to the cyclic behaviour of vapour formation and condensation. Furthermore, the cyclic behaviour was linked to the dry-out behaviour in the pool-boiling regions. An automatic mesh adaption tool allowed cell refinement at cells experiencing unrealistically high vapour velocities and increased numerical stability. The temperature distribution over the pin-fins formed cool regions corresponding to the flow-boiling regions; and warmer pockets corresponding to the pool-boiling regions. The turbulent kinetic energy followed the formation and condensation of the vapour column in the pool-boiling regions. The highest turbulent kinetic energy

was produced as the liquid was forced into the staggered-facing pin-fins. These results highlighted the advantage of a validated numerical study to understand the detailed jet impingement boiling behaviour.

Finally, a parametric study was conducted on a single jet impinging on a pin-fin surface to comprehend the effect of the inlet Reynolds number, pin-fin height, spacing and distribution on the heat transfer characteristics. The study of the inlet Reynolds number considered a lower and higher inlet velocity than for the validation case. An increase in jet velocity increased heat transfer at the stagnation region but had a limited effect on eliminating the dry-out areas at the outer regions of the domain. The study of pin-fin height and spacing suggested that heat transfer was mainly linked to surface augmentation. However, the decrease in pin-fin height allowed the liquid to spread to the outer regions of the domain and eliminated dry-out. The height and spacing study also suggested that the pressure drop over the domain was mainly linked to the stagnation pressure drop of the jet, while the pin-fin height and spacing had a negligible influence on the pressure drop for the parameter variation considered. The change in pin-fin configuration allowed the liquid to reach the outer regions of the domain while keeping the surface augmentation factor at a maximum. A star arrangement eliminated dry-out at 23.2 W/cm^2 and increased the average surface heat transfer.

Therefore, the RPI boiling model, along with the use of a y^+ insensitive near-wall treatment model could accurately predict the heat transfer of a single jet boiling on pin-fin surfaces. The findings of the parametric study aligned well with expectations to eliminate dry-out at the outer regions of the domain while increasing the overall surface heat transfer. The CFD model suggested that researchers would have to measure local dry-out if pin-fins were used in boiling jet impingement. Furthermore, the influence of pin-fin shape, distributions and the working fluid needs further investigation to allow for heat transfer at higher heat fluxes, which align with modern-day electronic applications.

Declaration of Originality

The **Department of Mechanical and Aeronautical Engineering** places great emphasis upon integrity and ethical conduct in the preparation of all written work submitted for academic evaluation.

The following declaration is required by the **Department of Mechanical and Aeronautical Engineering**:

Full names of student: Luwan Ludick

Student number: u17057419

Topic of work: Computational investigation into jet impingement boiling on pin-fin surfaces

Declaration

1. I understand what plagiarism is and am aware of the University's policy in this regard.

2. I declare that this dissertation is my own original work. Where other people's work has been used (either from a printed source, Internet, or any other source), this has been properly acknowledged and referenced in accordance with departmental requirements.

3. I have not used work previously produced by another student or any other person to hand in as my own.

4. I have not allowed and will not allow anyone to copy my work with the intention of passing it off as his or her own work.

SIGNATURE ....

iii

Acknowledgements

I would like to acknowledge the following people and organisations:

Publications

Conference presentations

- Ludick, L, Craig, K, Valluri, P, Meyer, JP. Boiling jet impingement on pin-fin surfaces. in *American Physical Society's Division of Fluid Dynamics,* 20/21/22 November 2022. Indianapolis, IN, USA

Workshop presentations

- Ludick, L, Craig, K, Valluri, P, Meyer, JP. Boiling jet impingement on pin-fin surfaces. in *3rd ThermaSMART workshop,* 24/25 November 2022. York University, Toronto, Canada

Journal Article (Submitted, waiting upon approval)

- Ludick, L, Craig, K, Valluri, P, Meyer, JP. Influence of pin-fin patterns and geometry on the effectiveness of jet impingement boiling – a computational study. *Applied thermal engineering*, 2023.

Table of Contents

List of Figures

List of Tables

Nomenclature

A	Area	m^2
C	Correlation constant	-
Cp	Constant pressure specific heat capacity	$J/(kg \cdot K)$
D	Nozzle diameter	m
d	Bubble diameter	m
d_h	Long axis of the deformable bubble	
E	Near-wall treatment constant	-
F	Force	N
f	Drag force function	-
G	Production of turbulent kinetic energy	$kg/m \cdot s^3$
h	Convective heat transfer coefficient	$W/m^2 \cdot K$
h_{fg}	Latent heat of vaporisation	J/kg
J	Diffusive heat flux	W/m^2
Ja	Jacob number	-
k	Turbulent kinetic energy	m^2/s^2
K,m	Empirical constants	-
L	Length	m
$\dot{m}$	Mass flow rate	kg/s
Nu	Nusselt number	-
N	Number of jets	-
Pr	Prandtl number	-
P	Pressure	Pa
q''	Heat flux	W/m^2
Q	Heat exchange intensity	W/m^3
Ra	Surface roughness	μm
Re	Reynolds number	-
R_ε	RNG additional term	-
r/D	Radial distribution	-
R	Interaction force	N
S	Source term in turbulence and energy Equations	-
t	Time	s
T	Period	s^{-1}
T	Temperature	K
V	Volume	m^3
v	Velocity	m/s
y	Perpendicular distance from wall	m
y_v	Physical viscous sublayer	-
y_v^*	Viscous sublayer constant	-

Greek Symbols

α	Volume fraction	
δ	Boundary layer region	
ε	Turbulent dissipation rate	
η	Surface efficiency	
λ	Phase diffusivity	m^2/s
μ	Dynamic viscosity	$Pa \cdot s$
v	Kinematic viscosity	m^2/s
ρ	Density	kg/m^3

$\sigma_{\varepsilon,m}$	Inverse of the effective Prandtl number	-
τ	Shear stress	Pa
κ	Thermal conductivity	$W/(m \cdot K)$

Subscripts

aw	Adiabatic wall
b	Bulk
b	Buoyancy
c	Convection
c	Corrected
cp	Contact pressure
$crit$	Critical bubble diameter
d	Drag
D	Drag coefficient
du	Asymmetric growth
E	Evaporative heat flux
eff	Effective
f	Fins
fl	Fluid
h	Hydrostatic pressure
i	Inertia
$Lift$	Lift coefficient
ls	Liquid saturated
m	Mixture
o	Overall
p	Phase p
p	Pressure
$part$	Particle
q	Phase q
Q	Quench
ref	Reference
s	Solid
s	Surface tension
sat	Saturated
sub	Subcooled
TD	Turbulent dispersion
vm	Virtual mass coefficeint
w,W	Wall
wl	Wall lubrication
wt	Waiting time
Eo'	Modified Eötvös number
i	Interfacial area concentration
x_e	Thermodynamic equilibrium

Superscripts

n	Lemmert and Chawla empirical coefficient

Acronyms and abbreviations

AMG	Algebraic multigrid
CFD	Computational fluid dynamics
CFL	Courant Friedrichs Lewy
CHF	Critical heat flux
HFE	Hydrofluorether
HTC	Heat transfer coefficient

IC	Integrated circuit
OND	Onset of nucleate boiling
PCB	Printed circuit boards
PEEK	Polyether ether ketone
PRESTO!	PREssure Staggering Option
RNG	Renormalisation group methods
RPI	Rensselaer Polytechnic Institute
SIMPLE	Semi-Implicit Method for Pressure-Linked Equations
UDF	User-defined function

1 Introduction

1.1 Background and Motivation

Computing power has become a predominant component in society, connecting our world's real and virtual dimensions. Electronic manufacturers strive to outperform their rivals by reducing the size of their electronic components to allow for higher populated printed circuit boards (PCB), resulting in performance enhancement with associated high-power densities [25]. Currently, surface heat fluxes range between 100 and 1 000 W/cm^2 and are continuously increasing [26]. A trend known as Moore's law predicts that integrated circuits' performance and component density keep increasing. Therefore, the law is used to guide developers and researchers [7]. Integrated circuits (IC) are integrated into various electronic devices, as shown in Figure 1, which significantly improves life, work and production [7].
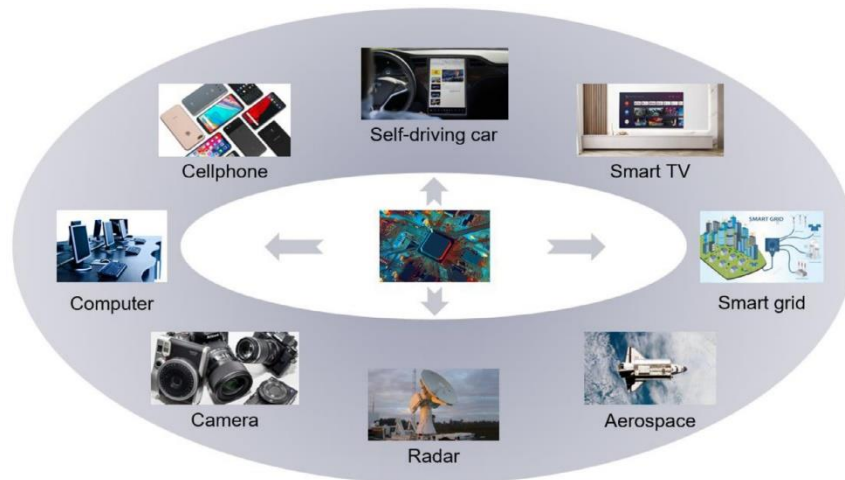
Figure 1: Applications for ICs [7]

Thermal management of densely packed chips is critical for developing prevailing chips. A paradigm shift has occurred in the design process, with heat transfer being conducted in parallel with electronic component performance [27]. Significant temperature rises occur due to the reduction in surface area and promotion in power, which brings forth the need to remove more heat to maintain the chip within the specified operating temperatures. The need to remove heat falls in line with Black's equation, namely that an increase in temperature accelerates the failure of electronic devices [28]. Figure 2 depicts the basic thermal architecture of a microchip, with the dominant heat transfer path being shown as a red arrow.
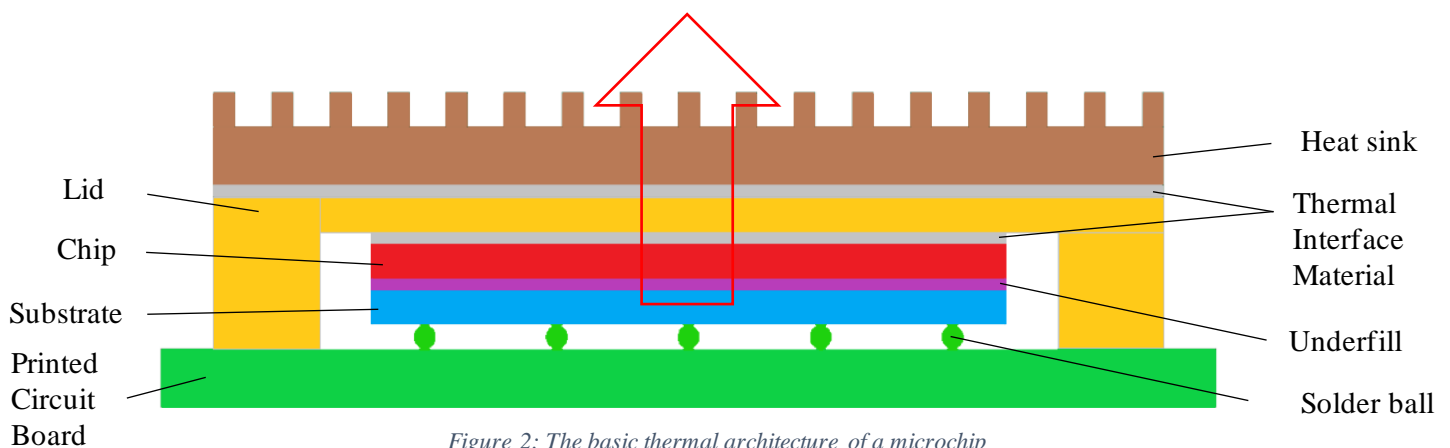
Figure 2: The basic thermal architecture of a microchip

Thermal management is divided into passive and active cooling schemes [7]. Passive schemes rely on natural occurrences and do not use any external energy sources, whereas active cooling schemes require a source of external energy. Generally, active cooling schemes produce higher heat transfer coefficients (HTCs); consequently, they are the primary choice for high heat flux applications despite power consumption [7]. For years, conventional air-cooling techniques have been used for numerous microsystems where fans and heat sinks have prevailed in high-power computing systems due to their low cost and high reliability. Unfortunately, recent developments have exceeded the heat dissipation capability of these conventional techniques, and a shift has been made towards liquid-to-vapour phase-change cooling techniques [16]. Figure 3 compares the range of heat transfer coefficients achievable through natural convection, single-phase forced convection and boiling (or phase change). A few orders of magnitude improvement in heat transfer coefficient can be seen from natural convection to boiling cooling schemes. Phase-change cooling schemes take advantage of the fluid's sensible and latent heat, yielding a much higher heat transfer coefficient with respect to single-phase cooling schemes that rely only on sensible heat transfer [16].
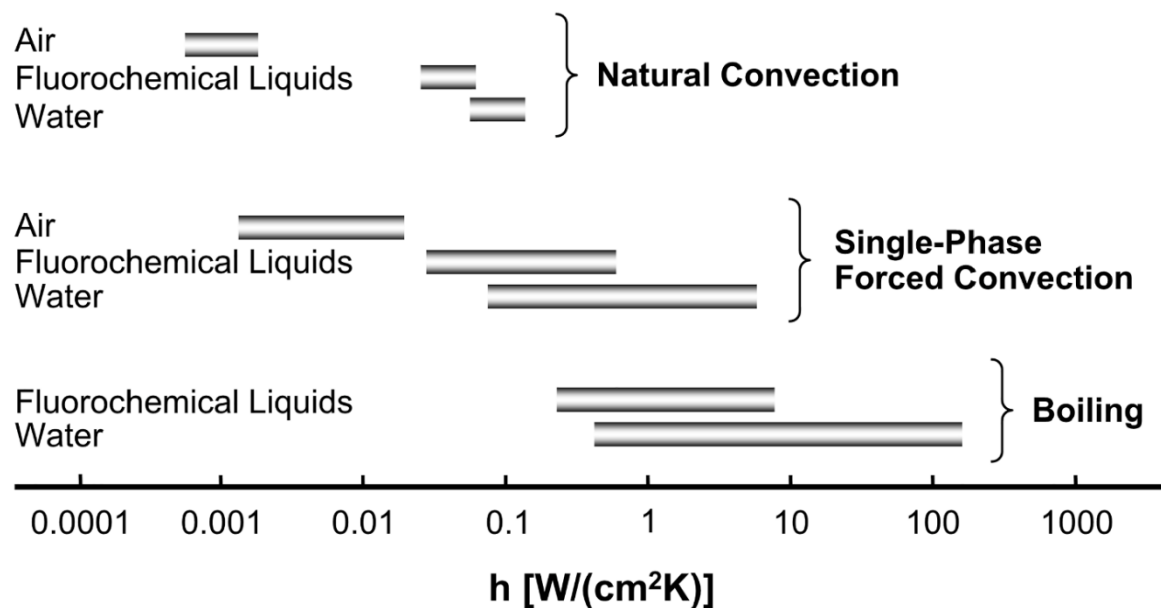
Figure 3: Heat transfer coefficient range comparison, adapted from [16]

As the surface heat flux increases, the fluid reaches the onset of nucleate boiling (ONB), where the fluid changes from single-phase to multiphase, known as the boiling phenomenon with studies dating back to 1930, when boiling was considered a natural and self-evident process [29]. Engineering challenges posed by the design of devices such as spacecraft, rocket engines and nuclear reactors became more complex, so that the need for energy transfer and conservation became more relevant. Therefore, an abrupt change in boiling heat transfer studies occurred [29]. As early as 1756, Leidenfrost [30] documented scientific studies on the interaction between a liquid and an extremely hot surface. Metallurgists have noticed that a two-step process follows when hot metals are submerged in water, known now as the quenching process, where at first, a slow rate of cooling is observed and as the process moves on, the rate of cooling increases even though the temperature of the metal decreases [29]. However, it was not until 1931 that Jakob [31] conducted the first systematic study of the nucleation boiling regime. Following this, several researchers have made significant ground by obtaining the boiling characteristic curve and other phenomena discussed later.

Various multiphase cooling techniques have been reported in the literature. These techniques include pool boiling, channel flow boiling, boiling jet impingement, spray cooling, and hybrid cooling systems based on a combination of flow boiling and jet impingement [16]. Flow boiling outperforms pool boiling in electronic cooling applications due to its capability of spent fluid recirculation and CHF

enhancement [32]. Oscillations in pressure drop have been reported in microchannel flow boiling and have yet to be fully resolved [7]. Spray cooling is considered one of the most effective thermal management techniques for high heat flux components, considering its sizeable cooling area and high heat flux dissipation capability [7].

Nevertheless, spray cooling has drawbacks, such as nozzle clogging, high operating pressures and fluid recirculation in closed-loop applications [7]. Over the last few decades, it has been proved that jet impingement is an effective and attractive way to transfer energy from high heat flux components [8] by the substantial amount of thermal energy transferred between the solid and the liquid [4]. Multiphase jet impingement demonstrates numerous advantages over pool- and flow-boiling techniques because impinging flow actively removes developing vapour, increasing the critical heat flux (CHF) significantly [33]. Similar to spray cooling, the heat transfer coefficient of jet impingement is significantly affected by liquid properties, nozzle configurations and surface structures [7].

Heat and mass transfer rates are highly enhanced by turbulence [34], which is a phenomenon initially encountered by H. Martin [35], where turbulent jets increased the Nusselt number by a factor of 11, thus making turbulent jets an attractive option with respect to laminar jets. Heat transfer enhancement techniques have gained traction in recent literature, focusing on surface enhancements, spent fluid removal and fluid investigations. Surface enhancements increase the product of average surface heat transfer coefficient and surface area by disrupting boundary layer growth and improving turbulent transport [36]. Rau and Garimella [17] and Ndao *et al.* [36] performed boiling jet impingement experiments on microstructured surfaces, concluding that microstructured surfaces produced a higher heat transfer coefficient than flat surfaces do. Apart from using grooved surfaces, Jenkins *et al.* [37] gained the same increase in heat transfer coefficient. Dielectric fluids have received ample attention in recent studies due to their surface wettability and low global warming potential [7]. Spent fluid removal methods yielded promising results in jet impingement due to the elimination of cross-flow created by jet arrays [19].

Figure 4 (a) depicts the high liquid velocity regions of a single jet impinging on a confined surface populated with a uniform distribution of pin-fins (figure taken from the results section of this study, described in Chapter 4.3). The liquid flow distribution in the pin-fin vicinity formed a cross through the centre of the heated block as the uniform pattern of the fins allowed liquid to flow along the channels perpendicular to the impingement periphery. Conversely, a compact staggered arrangement obstructed flow from advancing towards the edges of the heated block, creating stagnant flow regions at the edge of the heated block. Figure 4 (b) depicts the spatial distribution of the local boiling type, consisting of pool boiling at the outer regions of the domain and in the wake of each pin-fin, flow boiling and impingement boiling.

Numerical simulations of two-phase flow remain challenging and complex, and few numerical investigations into boiling jet impingement exist in the literature all of which predict heat transfer using the Eulerian multiphase framework incorporating the Rensselaer Polytechnic Institute (RPI) boiling model. These are led by Narumanchi, Troshko, Bharathan and Hassani [38], who explored the nucleate boiling regime numerically through a 2D axisymmetric domain. Abishek, Narayanaswamy and Narayanan [39] and Esmailpour, Azizi and Hosseinalipour [40] investigated the effect of controlling parameters such as the jet Reynolds number, degree of subcooling and jet-to-target spacing. Subsequent work was done by Qiu, Dubey, Choo and Duan [41], who incorporated thermal mass or conjugation in their study of a single axisymmetric jet. Wright, Craig, Valluri and Meyer [42] extended numerical investigations to 3D jet arrays. All numerical investigations of perpendicular jet impingement boiling have been limited to flat surfaces, and surface augmentation has not yet been explored numerically.

Jet pipe

Liquid flow distribution

Uniform pin-fin layout

Insulation

Outlet boundary

(a)

Pool boiling in fin wakes

Pool boiling

Impingement boiling

Flow boiling

Velocity Magnitude (liquid) [m/s]

0.3   0.7   1.1   1.5   1.9   2.3   2.7

(b)
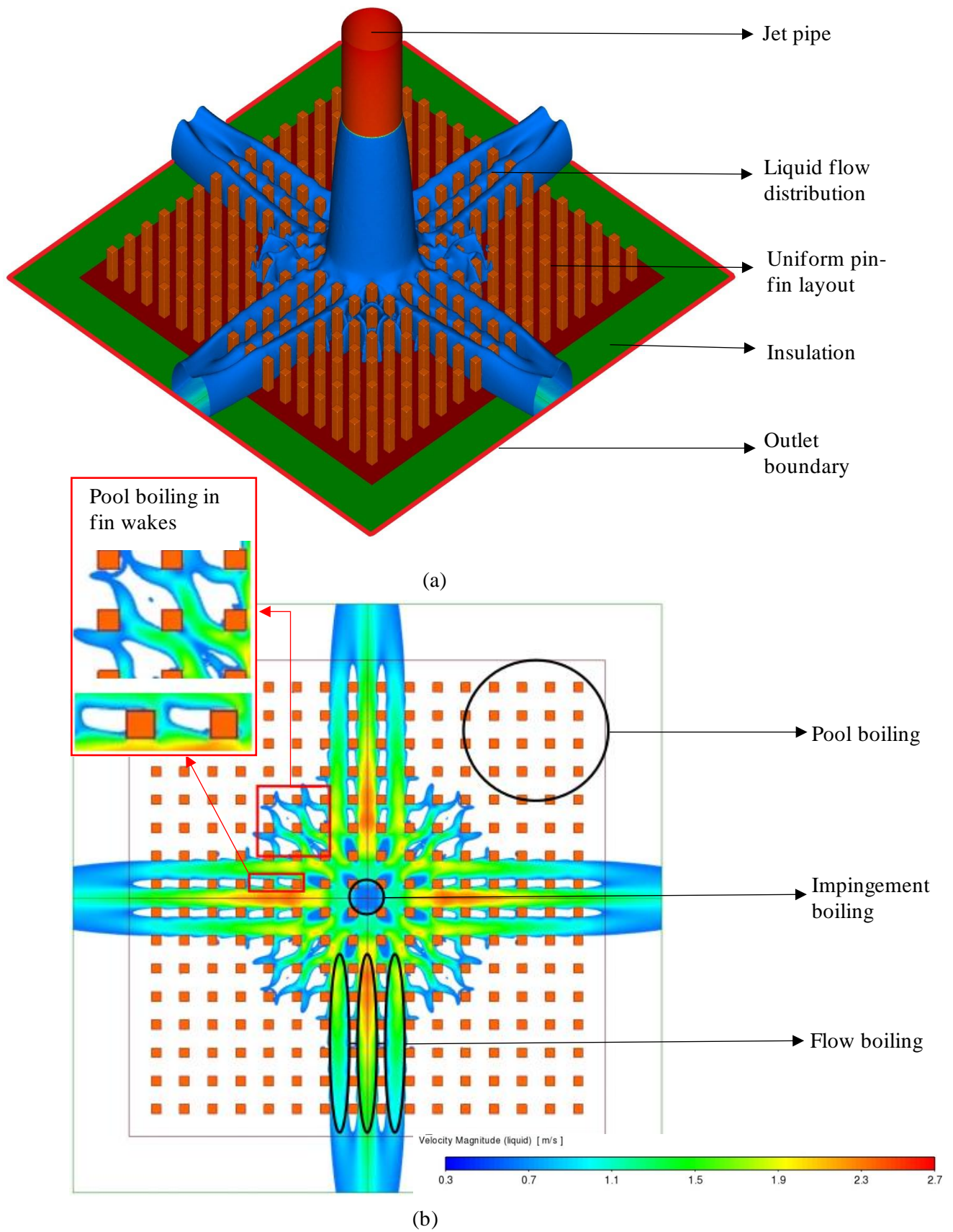
Figure 4: (a) Liquid velocity distribution of a single jet impinging on a pin-fin surface (defined as an iso-surface with a liquid velocity > 0.3 m/s) and (b) spatial distribution of local boiling type along a uniformed pin-fin distribution

1.2 Problem statement

Heat dissipation has become a critical and essential aspect in the design process of high heat flux electronic components. Recent literature popularised boiling jet impingement as a promising thermal management technique due to its effective heat transfer performance, where numerous experimental studies demonstrated its high heat transfer capabilities on both flat and enhanced surfaces. However, experimental studies have mainly focused on the heat transfer effect in the jet stagnation region, lacking the ability to capture heat transfer distribution over the entire surface. Local dry-out is a consequence of stagnating flow initiated by flow obstruction. However, the influence of stagnating flow on the CHF due to surface augmentation has not been resolved.

Numerical simulations can capture the heat transfer distribution over the entire surface, including identifying local dry-out spots. For design purposes, numerical simulations provide the ability to investigate a range of complex geometries, capturing essential data in a cheaper and less time-consuming fashion. However, to the best of the author's knowledge, no numerical work on surface enhancements in boiling jet impingement has been described in the literature. Thus, a numerical validation of experimental results is a prerequisite. Pin-fins are well-known surface enhancement methods in electronics cooling, but the detailed effect of fin dimensions, distribution and quantity remains unexplored.

1.3 Objectives and scopes

To resolve the above problem statement, the objectives of the study were as follows:

- to conduct a literature study of single-phase jet impingement hydrodynamics, pool- and flow-boiling processes, boiling jet impingement on both flat and enhanced surfaces, and the numerical modelling of turbulent multiphase jets;
- to validate a three-dimensional (3D) single boiling jet on pin-fin surfaces;
- to conduct a fin height, fin spacing and fin distribution parametric study of overall surface heat transfer and local dry-out.

1.4 Layout of dissertation

Chapter 1 presents the necessity of thermal management of densely packed microchips, introducing different developments and cooling schemes. This chapter further provides the context for the current study by discussing the history of boiling heat transfer and the influence of multiphase flow on modern cooling techniques. The effect of surface enhancements in boiling jet impingement is discussed by comparing experimental investigations, including a flow distribution plot, highlighting the flow obstruction caused by pin-fins. Finally, the advantages of numerical studies are presented, including past numerical work on boiling jet impingement.

Chapter 2 provides a literature review of the fundamentals of jet impingement, boiling heat transfer, flow past immersed bodies and a combination thereof. The chapter explores single-phase liquid jet impingement and provides potential jet configurations, jet impingement hydrodynamics and heat transfer characteristics. The chapter further provides an investigation into boiling heat transfer on flat surfaces, describing the boiling process and bubble dynamics of pool, flow and impingement boiling. The heat transfer and jet reach characteristics of a single and an array of jets are compared, followed by spent fluid removal techniques. An analysis is provided of flow over and boiling on enhanced and structured surfaces, flow past immersed bodies and driven cavity flow, including pool, flow and jet impingement boiling on structured surfaces. The last section of the chapter concludes the literature study.

Chapter 3 provides the numerical framework of the study, consisting of the eulerian framework, conservation equations, turbulence modelling, interphase transfer models, wall-boiling model and the solution method, demonstrating the technique implemented in ANSYS Fluent 2022 R2.

Chapter 4 presents the computational fluid dynamics model and validation case of boiling jet impingement on pin-fin surfaces. A problem description and experimental procedure give a deeper understanding of the validation case, followed by a description of the computational domain and boundary conditions. Further, a mesh independence study investigates the effect of mesh density and type on the stagnation wall superheat, including the resulting cyclic behaviour of the evaporation contribution area. The results of the boiling curve and evaporation contribution area are presented, followed by various contour plots highlighting the solid pin-fin temperature distribution and liquid and vapour formation at the outer regions in the domain.

Chapter 5 provides a numerical parametric study of the effect of the jet inlet Reynolds number, determining the outcome of jet velocity on the stagnation wall superheat and evaporation area contributions, and monitoring parameters such as turbulent kinetic energy and pressure drop across the domain. The chapter further provides a pin-fin height and spacing study of the impact of pin-fin height and spacing on the above parameters. The chapter concludes with a pin-fin distribution study aiming to attain heat transfer capabilities and eliminate dry-out regions formed by flow obstruction.

Chapter 6 summarises the study, providing gaps in the literature, crucial design considerations and limitations of structured surfaces. Finally, suggestions for future work are given.

2 Literature study

2.1 Introduction

Jet impingement cooling techniques are incorporated into various engineering applications, including turbine blades, aerospace technology, plastic sheets, solar systems, hot metals and electronic systems [43]. Flow characteristics significantly impact the heat transfer phenomena. Therefore, the investigation thereof has received increasing attention in the literature. Section 2.2 describes the hydrodynamics of liquid jet impingement on flat surfaces, breaking down the liquid jet classification, jet hydrodynamics, and liquid jet impingement heat transfer. Furthermore, Section 2.3 discusses the pool-, flow- and impingement boiling phenomena on flat surfaces while introducing the boiling curve and different boiling regimes. Section 2.3.4 extends the previous two sections to understand the boiling patterns associated with boiling jet impingement on structured surfaces (see Figure 4), through investigating driven cavity flow and flow around blunt bodies, and pool and flow boiling on structured surfaces. The chapter concludes with a literature review of single and multi-jet array jet impingement boiling on structured surfaces to provide an understanding of the hydrodynamics and phase change associated with jet impinging boiling on structured surfaces.

2.2 Liquid jet impingement

2.2.1 Liquid jet configurations

Liquid jet impingement falls into four main categories (see Figure 5). Figure 5 (a) shows a free-surface jet where a liquid jet is exposed to a gaseous environment before impinging on an unconstrained surface where the liquid is free to flow without constraint [5]. Figure 5 (b) depicts a single jet impinging into a liquid layer and acts as a plunging jet [5]. Submerged jets can be subdivided into confined or submerged cases [44] (see Figure 5 (c-d)). For the submerged case, the jet interacts with ambient and quiescent surroundings [44]. The confined case is defined by a surface surrounding the submerged
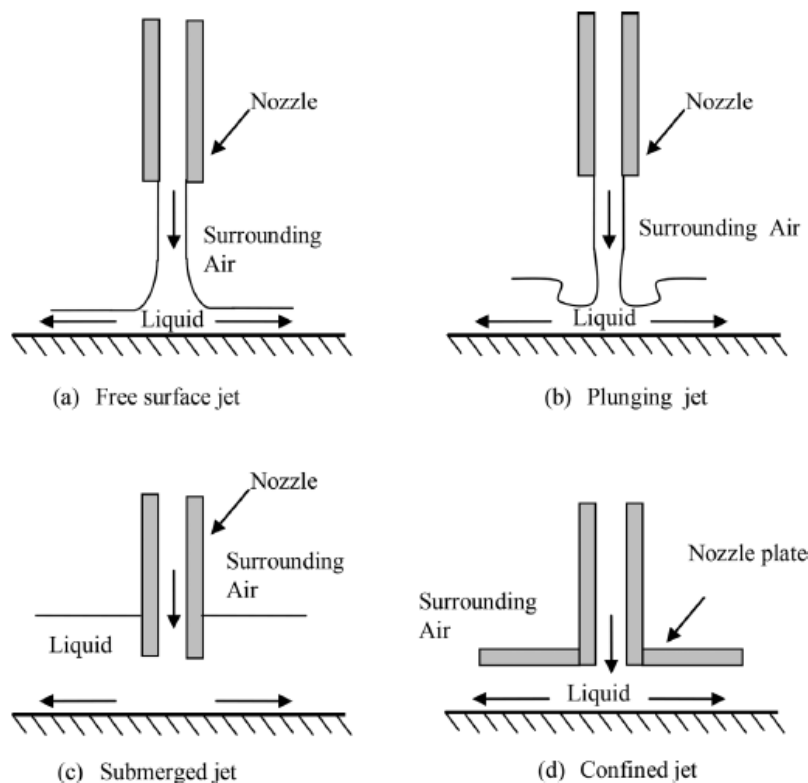
Figure 5: Liquid impinging jet configurations [5]

liquid, and in some cases, the impinged liquid is recirculated from the outflow zone [44]. Confined impinging jets have the advantage of small-space design [45], making them favourable for cooling electronic devices.

2.2.2 Liquid jet impingement hydrodynamics

Figure 6 (a) shows that the jet flow structure can be subdivided into free, stagnation and wall-jet regions. The free-jet region initiates at the nozzle exit emerging from an upstream-determined velocity profile. The upstream velocity profile can be categorised as laminar or turbulent. A turbulent mean velocity profile is fuller with a sharp drop to zero at the wall with an associated higher wall shear stress than for laminar flow [2].

Figure 6 (a) shows the jet exit region as fully developed turbulent flow. Figure 6 (b) illustrates the three distinct zones in the free-jet region. As the jet enters the free-jet region, a potential core is formed in a conical shape for a round jet. The length of the potential core is measured from the jet inlet to the point where the average jet velocity drops below 95% of the nozzle exit velocity. Jambunathan *et al.* [46] reported that the average jet velocity decreased abruptly after the potential core as the flow entered the developing zone, thus signifying that jet-to-target spacing was an important parameter affecting the rate of heat transfer [43]. Significant shear stresses at the jet periphery cause a decay in axial velocity as the shear stresses start to pierce into the core of the jet. The fully developed zone is reached after the shear stresses reach the centre of the potential core, resulting in a maximum axial velocity component and minimum radial velocity component at the centre line of the jet. Reichardt [47] found that a Gaussian velocity distribution fitted his experimental results in the fully developed zone. Figure 7 (a) depicts the core region as the initial high lateral velocity gradient of the shearing layer decreases due to the impinging liquid spreading away from the nozzle exit. Momentum is transformed laterally outwards due to the shearing layer, while increasing the mass flow as the momentum pulls additional fluid along with the initial jet [4]. This process leads to widening of the velocity profile, while decreasing the magnitude of the velocity at the jet's edge [4]. The core region remains unaffected by the transferred momentum and experiences a higher total pressure dependent on the velocity gradient present in the
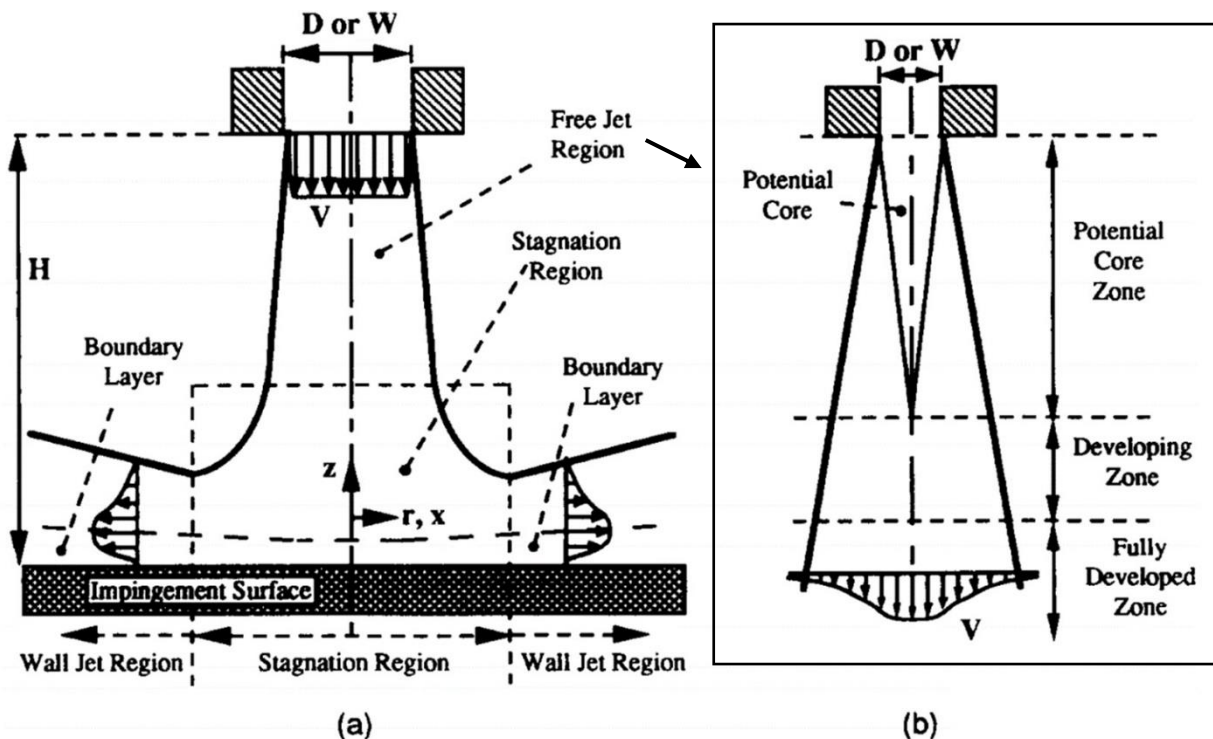
Figure 6: (a) Jet impingement flow regions and (b) main flow zones in the free-jet region, adapted from [7]

8

nozzle exit [4]. Jet-to-target spacing in jet impingement applications usually does not exceed the second frame in Figure 7 (a).

The stagnation region is classified as the region where the jet impinges on the surface, resulting in a sharp increase in static pressure due to the conversion from kinetic energy to pressure energy. The stagnation region spans about 1.25 times the nozzle diameter for laminar flow and varies in size for turbulent flow [48], while commonly extending 1.2 nozzle diameters above the wall for round jets [35]. A jet acceleration region is categorised between the stagnation and wall-jet region, formed as the flow accelerates through the stagnation region due to a difference in static pressure between the stagnation and outer region [48]. To maintain continuity of the flow, the flow velocity in the acceleration region becomes higher than the flow velocity at the nozzle exit [48].

(a)   (b)
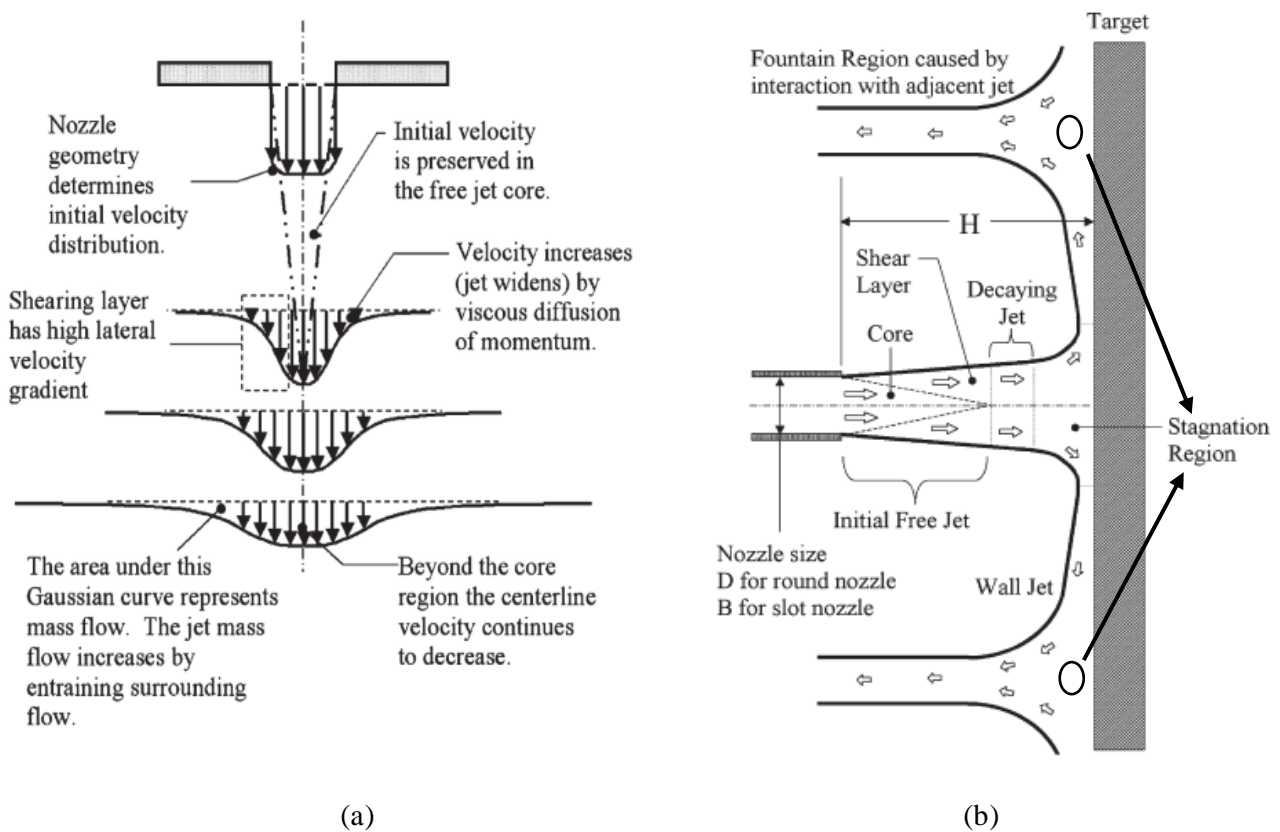
Figure 7: (a) Development of jet profile [4] and (b) jet array interaction, adapted from [4]

The flow enters the wall-jet region as the flow is directed radially outwards, forming a velocity boundary layer between the impinged wall and the submerged liquid. As the fluid flows parallel to the wall surface, the velocity decreases due to viscous effects, and loses momentum due to an increasing flow area and surface friction [48]. Figure 6 (a) shows that the wall jet has a minimum thickness at the edge of the stagnation region within 0.75-3 diameters from the jet axis and continues to grow as the jet moves further away from the nozzle centre axis [4]. The growth of the wall jet is due to the retardation of flow following mass and momentum conservation [48].

Multiple jets cover larger surface areas but display different flow patterns from single-jet impingement. Figure 7 (b) depicts the fountain region caused by the interaction of adjacent jets, illustrating that an additional stagnation region is formed underneath the produced fountain region [48]. Jet interaction produces additional turbulence in the domain and further enhances heat transfer. Turbulence is governed through the Reynolds number, typically classified at the nozzle inlet and defined as

$$Re = \frac{U_o D}{v} \qquad (1)$$

where U_o is the initial average flow velocity at the nozzle entrance, the characteristic length D is the nozzle exit diameter or double the slot width (2B), and v is the fluid kinematic viscosity [4]. Reynolds numbers for jet impingement are usually classified at the jet inlet. Heat and mass transfer rates are highly enhanced by turbulence [4], thus making turbulent jets an attractive option compared with laminar jets. Martin [35] obtained average Nusselt numbers of about 19 for an isolated round jet at Re = 2 000 calculated at the jet inlet, six diameters in length away from the impingement point. When using the same set-up and increasing the Reynolds number to approximately Re = 100 000, Nusselt numbers on the same surface reached 212 for a working fluid of air. These findings confirm that turbulent flow results in enhanced heat transfer.

The intensity of the turbulent flow can be measured through the specific turbulent kinetic energy. The nature and extent of turbulence present are required to describe the problem entirely. Turbulence is influenced by various conditions, mainly the inlet velocity profile, jet interaction and surface configuration. The turbulent flow starts in the free-jet region as the jet pierces into the surrounding fluid due to the shear flow at the jet periphery [4]. Figure 8 (a) depicts the growth of the shear layer for a free submerged jet: it starts as a thin vortex ring and develops primary vortices as the jet-shearing layer becomes unstable [4]. These vortex rings are classified as eddies [4]. Eddies have a length in the same order of magnitude as the jet diameter and are preserved until they interact with features downstream of the jet or independently break up into tiny eddies [4]. When the jet impinges on a surface, the situation changes. As the eddies reach the stagnation region, they are laterally displaced and stretched further due to the high-pressure field present in the stagnation region. Figure 7 (b) shows that in the decaying jet region, turbulence is affected through shearing as the shear layer extends through the centre of the jet, forming turbulent pockets and small eddies on the jet axis and finally causing the flow to develop into unstructured turbulent flow in the jet core [4]. Eddies formed in the free-jet-shearing layer can brush away the velocity boundary layer as they moves across the wall, increasing local heat and mass transfer [4]. Turbulence is also enhanced in the wall-jet region through normal strains and stresses, allowing pressure gradients in the flow to influence and turn the shear layer, forming secondary vortices due to the turbulent fluctuations in the radial velocity and the pressure gradient, causing reversed flow along the wall, leading to separation (see Figure 8 (b)) [4]. Large-scale eddies in the wall-jet region are the leading cause of adequate heat and mass transfer [49]. The ability to disrupt the thermal boundary layer at the stagnation region establishes jet impingement as an effective heat transfer method [43]. Due to surface roughness, eddies lose their intensity and diminish in the radial direction [50], resulting in an overall loss in flow kinetic energy [4].

Velocity and thermal boundary layers are formed in the wall-jet region (see Figure 6 (a)). The velocity boundary layer is defined as the region δ above the wall where viscous shearing forces occur due to fluid viscosity [50]. For turbulent flow, the boundary layer thickness experiences a viscous sublayer just above the wall, followed by a buffer layer before reaching the turbulent region [50]. The friction force per unit area experienced at the wall is defined as the wall shear stress:

$$\tau_w = \mu \left.\frac{\partial u}{\partial y}\right|_{y=0} \qquad (2)$$

where μ is the dynamic viscosity of the fluid and $\frac{\partial u}{\partial y}$ the velocity gradient at the wall [50].

(a)   (b)
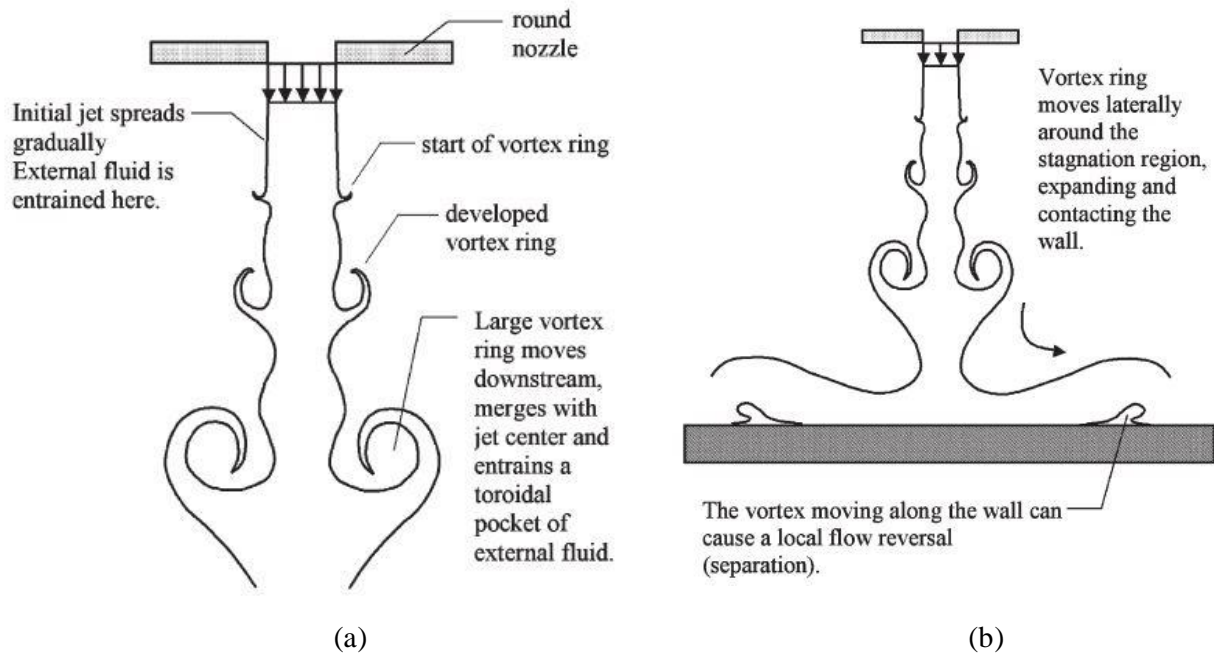
Figure 8: (a) Impinging jet turbulent vortex ring development and (b) near-wall turbulent vortex ring development, adapted from [4]

2.2.3 Liquid jet impingement heat transfer characteristics

A thermal boundary layer develops due to the difference in temperature between the fluid and the wall. A dimensionless number called the Prandtl number was developed to relate the thickness of the velocity and thermal boundary layer and is defined as

$$Pr = \frac{Molecular\ diffusivity\ of\ momentum}{Molecular\ diffusivity\ of\ heat} = \frac{\upsilon}{\alpha} = \frac{\mu C_p}{k} \qquad (3)$$

Pr ranges between 1.7 and 13.7 for water and 0.7 and 1.0 for gases [50].

The Nusselt number represents heat transfer enhancement through a fluid layer due to convection relative to conduction across the fluid [50] and contains the convective heat transfer coefficient h and is defined as

$$Nu = \frac{hL_c}{\kappa} \qquad (4)$$

where L_c is the characteristic length and κ is the thermal conductivity. The characteristic length for impinging jets is D, which is the nozzle diameter [10].

Equation (4) indicates that an increase in convection heat transfer increases the Nusselt number. Heat transfer through pure conduction across the fluid layer is represented by a Nusselt number of 1 [50]. The heat transfer coefficient h can be represented through

$$h = \frac{q_w}{T_w - T_{ref}} \tag{5}$$

where q_w is the wall heat flux, T_w is the wall temperature and T_{ref} is a reference temperature. The reference temperature is chosen to be either the wall adiabatic temperature (T_{aw}), the total temperature of the jet flow (T_f), or the fluid saturation temperature (T_{sat}) in the case of multiphase heat transfer. In an impinging jet correlation, convective heat transfer coefficients can reach the proximity of tens of kW/m^2K [51]. The heat transfer distribution from an impinging jet is non-uniform due to the complex flow patterns [10]. The spacing between the jet nozzle and the impinged surface has a significant influence on the radial distribution of the Nusselt numbers [10]. Figure 9 depicts the local Nusselt number distribution for different jet-to-wall spacings of a single jet on a flat plate [10]. Figure 9 shows that an increase in spacing between the nozzle and the wall decreases the local Nusselt number throughout the radial extent. The decrease in heat transfer can be attributed to the retreat of the potential core in Figure 6 (b). A second peak is formed if the dimensionless spacing between the nozzle and the wall is lower than six and the peak is smoothed out as the spacing increases. This second peak is due to a transition from laminar to turbulent flow, creating secondary vortices that disturb the boundary layer flow and enhance the mixing process with surrounding fluids, as shown in Figure 8 (b) [10]. The location of the secondary peak in the local Nusselt number is affected by the location of the peak turbulent kinetic energy near the wall surface [4]. Various correlations of Nusselt numbers for different jet impingement set-ups and conditions have been developed over the years.
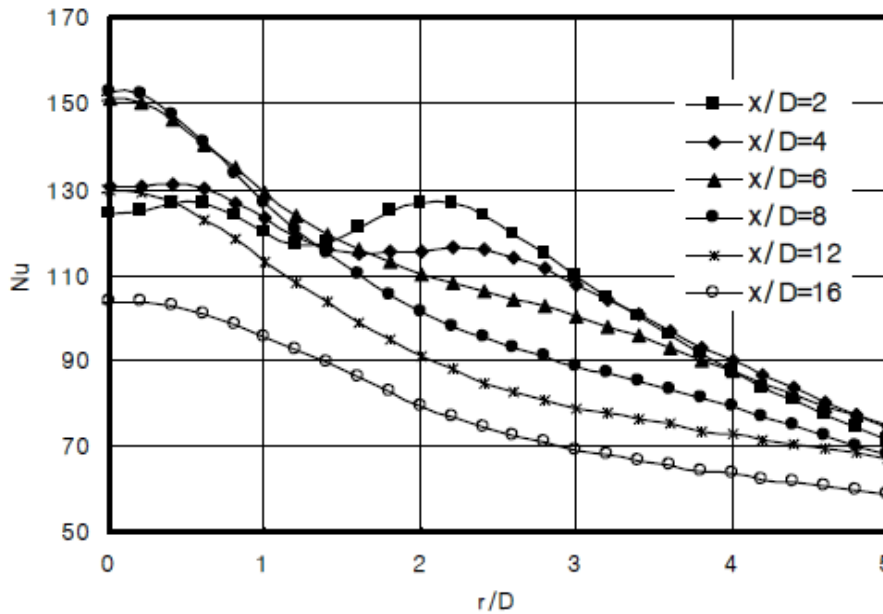
Figure 9: Local Nusselt number radial distribution on a flat surface with a single jet [10]

2.3 Boiling on flat surfaces

2.3.1 Boiling description

The boiling phenomenon is considered a type of two-phase flow composed of a mixture between liquid and vapour; the transition from liquid to vapour is defined as boiling heat transfer [52], causing evaporation [1]. The irreproducibility and complexity of the boiling phenomenon sparked interest in researchers to study the different boiling regimes, leading to the hydrodynamics of both pool and flow boiling with the prediction of the boiling regimes. The spatial distribution of the local boiling type in

Figure 4 (b) indicates that boiling jet impingement on pin-fins consists of a combination of impingement boiling, flow-boiling and pool-boiling regimes. Pool boiling describes the boiling process of a fluid submerged in an initially quiescent liquid where the natural convective phenomenon is the only driver of fluid flow [1], while flow boiling is driven through a stream of fluid forced by an external source [52]. The main difference between pool and flow boiling is the influence of the flow effect [52]. Buoyancy is essential in pool boiling, whereas forced flow convection dominates in flow boiling [52]. Impingement boiling is defined at the stagnation region due to the local accumulation of pressure created by the impinging flow perpendicular to the wall.

2.3.2 Pool boiling on flat surfaces

2.3.2.1 Pool-boiling curve and boiling regimes

Pool boiling was first explained by Nukiyama [53], who measured the temperature of an electrically heated wire submerged in a latent saturated liquid pool and compared this temperature with the heat flux calculated from the power of the supplied electricity. Nukiyama found that the heat transfer increased with an increase in surface temperature but reached a turning point as the wall superheat reached a specific limit. Figure 10 depicts the boiling curve with its three main near-wall regimes: nucleate boiling, transition boiling and film boiling [1].

The left- and right-pointing blue arrows in Figure 10 indicate the path followed if the heat flux (electric power) is decreased or increased respectively, bypassing the curved path between CDE. Nukiyama accurately suggested that the curved paths would be followed for both cases if the change in wall superheat

$$\Delta T_{sat} = T_w - T_{sat} \qquad (6)$$

was controlled rather than the heat flux, represented in equation (6), where T_w is the wall temperature and T_{sat} is the saturation temperature of the working fluid. Region I in Figure 10 is categorised as convection heat transfer without any boiling present. The transition point from Region I to Region II is defined as the ONB point. Wall superheat excursion at the ONB results from the ability of highly wetting fluids to flood nucleation sites [17] and bubbles that form on wall crevices for the first time, causing a delay in bubble departure [1]. Both boiling and natural convection account for heat transfer in the partial nucleate boiling region. As the contribution of boiling increases, indicated in the images above Region II and transition at B, the slope of the boiling curve increases along with an increase in temperature. Before the curve reaches a maximum heat flux at C, defined as the critical heat flux (CHF), the curve transitions into the fully developed nucleate boiling region where natural convection heat transfer is insignificant [1].

The nucleate boiling regime can be divided into local and bulk boiling [52]. Local boiling is classified as the point where bubbles form on the heated surface and are condensed locally, whereas, in bulk boiling, the bubbles tend not to collapse [52]. As the bubbles grow and intensify, they block the incoming liquid from reaching the surface and increase the surface temperature, known as the boiling crisis. The critical heat flux occurs just before reaching the boiling crisis [52]. Several parameters affect the pool-boiling crisis concerning ordinary liquids, including surface tension, wettability, bubble density at elevated saturation pressures, surface conditions, surface orientation, surface diameter and size, the addition of agitation, and subcooling [52].
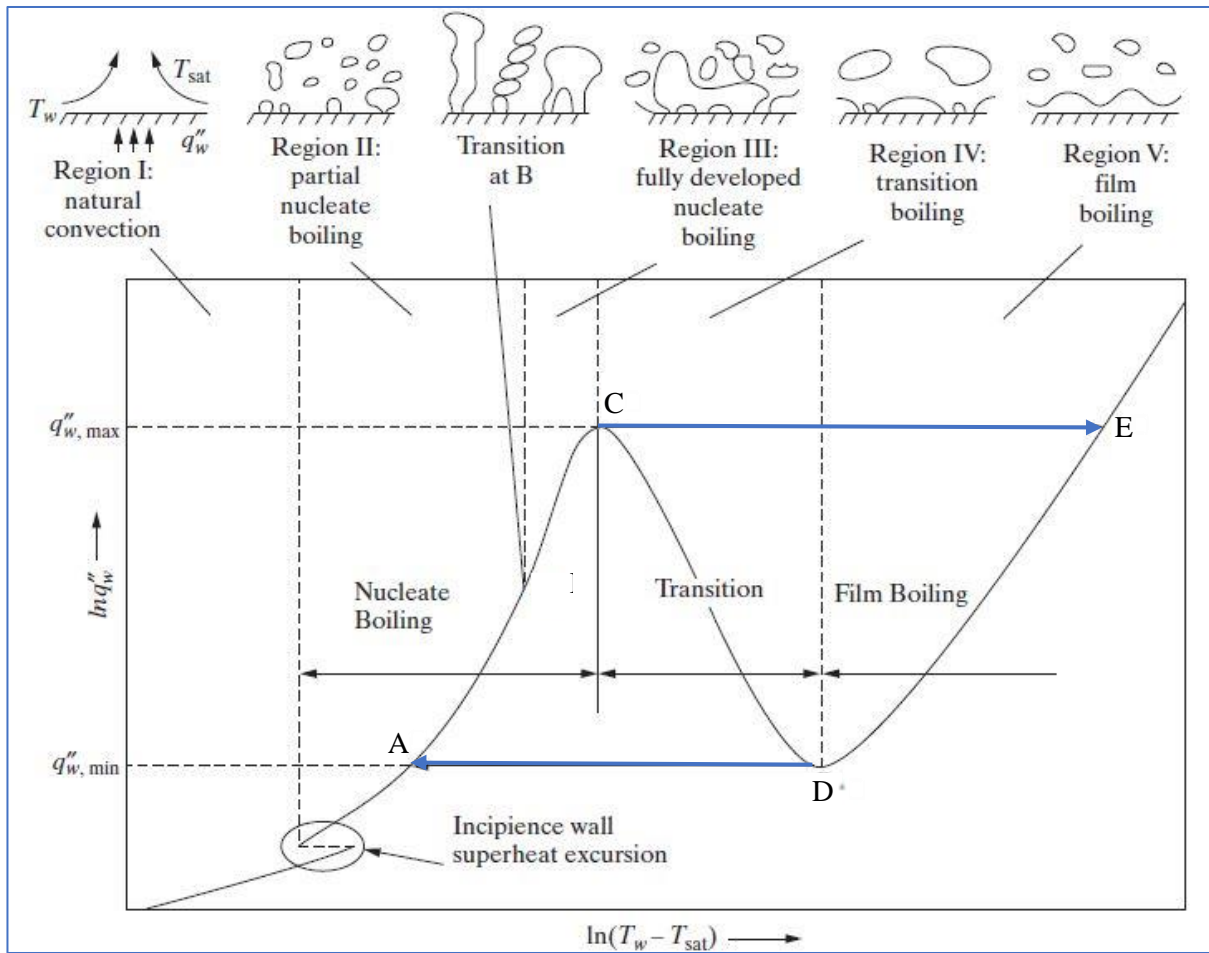
Figure 10: Pooling and boiling regions, adapted from [1]

Tipping over Point C, the curve enters the transitional boiling regime. In this region, boiling becomes unstable [52] and is periodically dry or in microscopic contact with liquid [1]. As the temperature increases, the dry fraction of the surface increases [1], leading to an oscillation and surge in the measured surface temperatures with a drop in heat flux [52]. While maintaining the power input, the heat flux decreases steadily, while the temperature increases rapidly until the minimum film-boiling point (MFB) has been reached [1]. Microscopic contact between liquid and the surface no longer occurs past Point D; and the fluid covers the surface in a vapour film [1]. Thermal radiation increases heat transfer as the wall temperature increases [52]. The wall temperature needs to be limited for practical purposes because the wall may be damaged if the temperature is too high, depending on the material properties of the wall.

Various changes in parametric design can affect the above boiling curve. An increase in surface wettability will shift the boiling curve to the right and increase the CHF, interrupting the evaporation process by increasing the ability of the liquid to quench evaporating fluid [1]. Surface roughening increases potential nucleation sites, intensifying evaporation heat transfer, but reducing the CHF [1]. Figure 11 depicts a slight improvement in heat transfer in the nucleation boiling regime by increasing the degree of subcooling, with a noticeable elongation of the nucleate boiling regime and extended CHF [1]. Jun *et al.* [54] suggested that bubble size reduced with an increase in the degree of subcooling due to the ability of the subcooled liquid to condense evaporating bubbles.
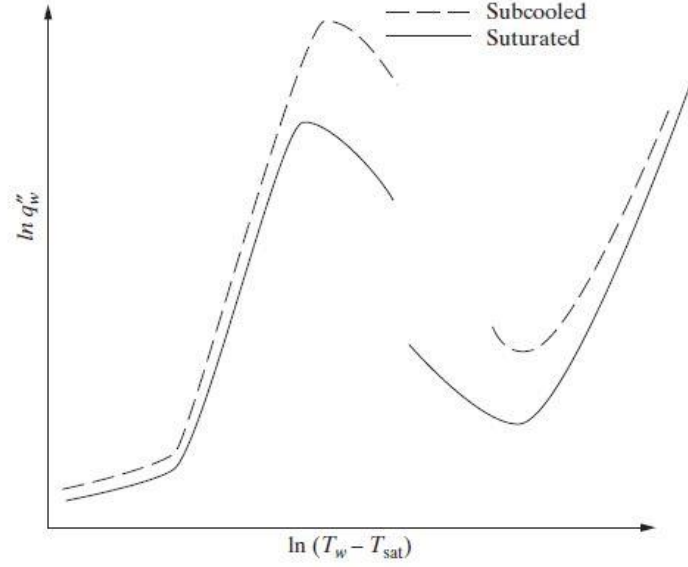
Figure 11: Effect of liquid subcooling on the boiling curve [1]

2.3.2.2 Pool-boiling bubble dynamics

The growth period of a bubble on a smooth plate can be divided into an initial rapid growth period followed by a later slow growth period [14]. Some general assumptions about the pool-boiling process were made to analyse the different forces acting on the bubble during the growth period. Figure 12 illustrates the different forces acting on a bubble during its growth period, where the force balance is expressed as

$$\overrightarrow{F_d} + \overrightarrow{F_s} = \overrightarrow{F_b} + \overrightarrow{F_i} + \overrightarrow{F_p} \tag{6}$$

where the drag force $\overrightarrow{F_d}$ and the surface tension force $\overrightarrow{F_s}$ restrict bubble growth with the buoyancy force $\overrightarrow{F_b}$, inertia force $\overrightarrow{F_i}$, and the pressure force $\overrightarrow{F_p}$ driving bubble growth [14]. The vapour inertia force is negligible compared with the liquid inertia force due to the significant difference between the density of the liquid and the vapour. Nucleation site density refers to the number of bubble nucleation sites per unit area [14]. If the applied heat flux increases, the nucleation site density will increase, leading to a high bubble departure frequency, creating additional drag force due to the previously departed bubble pulling the growing bubble upwards [55].

15
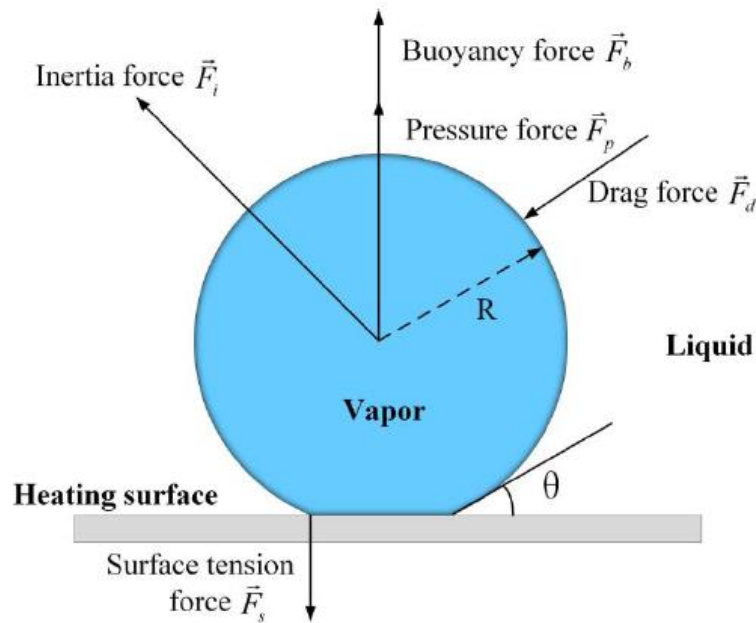
Figure 12: Pool-boiling bubble dynamics [14]

2.3.3 Flow boiling on flat surfaces

2.3.3.1 Flow-boiling regimes

Flow boiling is viewed as a slightly more complicated phenomenon than pool boiling because of the coupling between hydrodynamics and the boiling heat transfer process. The bulk of flow-boiling studies has been conducted on vertical tubes. Figure 13 (a) depicts the boiling regimes for vertical pipe flow subject to a moderate and uniform heat flux operating under a constant mass flow rate [1]. The influence of four separate degrees of subcooling is depicted in Figure 13 (a), with a highly subcooling inlet at the left pipe and a saturated inlet at the fourth pipe. If a highly subcooled liquid is applied to the inlet of the pipe, the entire flow in the pipe remains subcooled due to inadequate energy transfer between the supplied heat flux and the liquid throughout the length of the pipe. As the degree of subcooling decreases, the energy transfer required to reach the ONB decreases. Nucleation sites form on the sides of the pipe and transition to bubbly flow, where bubbles coalescence causes a further transition to slug flow. This is followed by annular flow, which has a vapour core flowing inside a thin liquid film at the near-wall region [1]. As in the case of pool boiling, flow boiling reaches the CHF when there is no more contact between the liquid and the walls. Figure 13 (b) translates the flow and heat transfer regimes described in Figure 13 (a) to a horizontal tube subject to a moderate and uniform heat flux [1]. Note the effect of the rotation of the gravity vector.

The flow and heat transfer regimes are similar to those of a vertical tube. At the same time, the main difference lies in the buoyancy effects which promote stratification between the two phases that become dominant in the force convective evaporation regimes, leading to partial dry-out as the liquid film evaporates. Stratification is why the CHF is usually reached at a lower vapour quality than in vertical tubes [1]. Figure 14 illustrates the factors contributing to heat transfer from the surface to the liquid in the nucleate boiling regime. Bubble formation agitates the velocity boundary layer and causes a liquid-vapour exchange [52]. While bubbles are attached to the wall, heat is transported through evaporation at the root of the bubble and condensation at the top [52]. Heat is emitted and absorbed at the circumference of the bubble through latent heat transfer, while single-phase convection exists between nucleation sites.

16
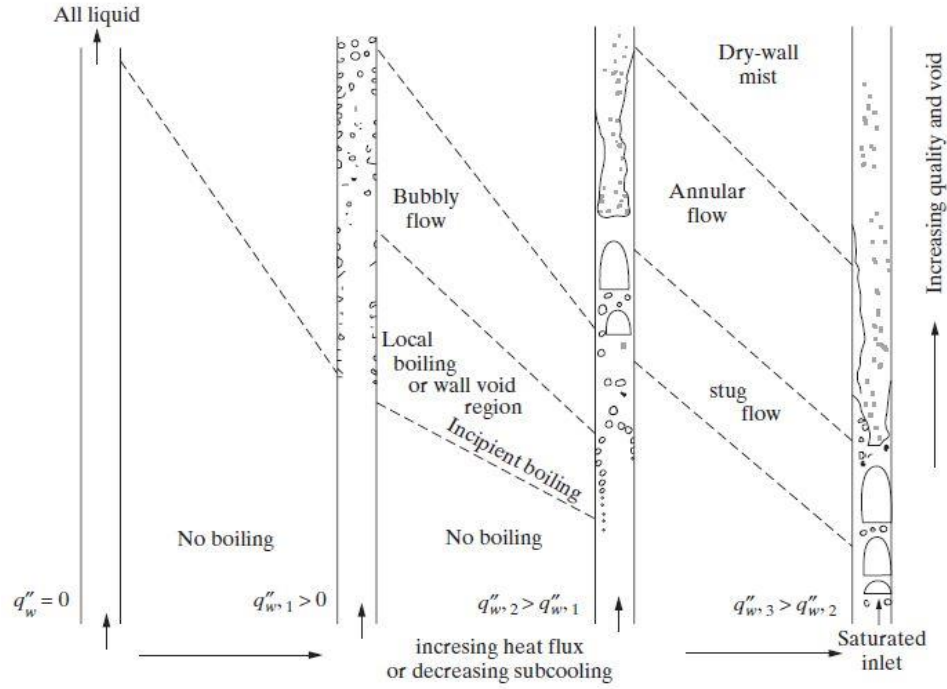
(a)
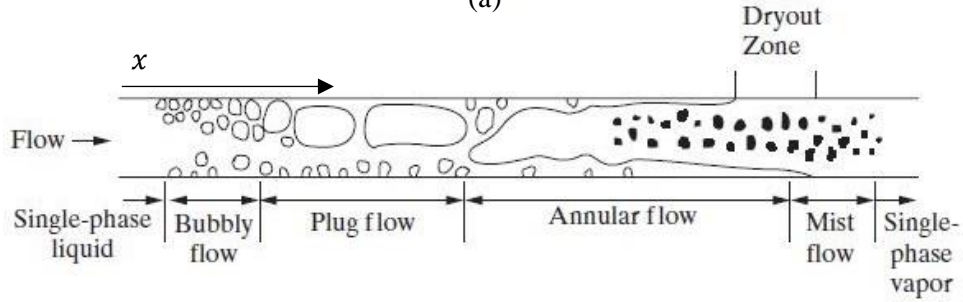
(b)

Figure 13: (a) Boiling regimes for vertical pipe flow [1] and (b) horizontal flow-boiling regimes, adapted from [1]

The thermodynamic equilibrium quality x_e is used to describe the flow-boiling condition with respect to the axial position in the pipe, depicted in Figure 13 (b) [56]. Thermodynamic equilibrium quality in pipe flow boiling is expressed as

$$x_e = \frac{h_{in} + \left(\frac{\pi D q'' z}{\dot{m}}\right) - h_{ls}}{h_{fg}} \tag{7}$$

where h_{in} is the liquid enthalpy, h_{ls} the saturated enthalpy of the fluid, h_{fg} the latent heat of the fluid, D the pipe diameter, z the axial position from the inlet, q'' the applied heat flux, and $\dot{m}$ the mass flow rate. The bulk fluid is classified as subcooled if $x_e < 0$, saturated if $0 \leq x_e \leq 1$, and superheated if $x_e > 1$.
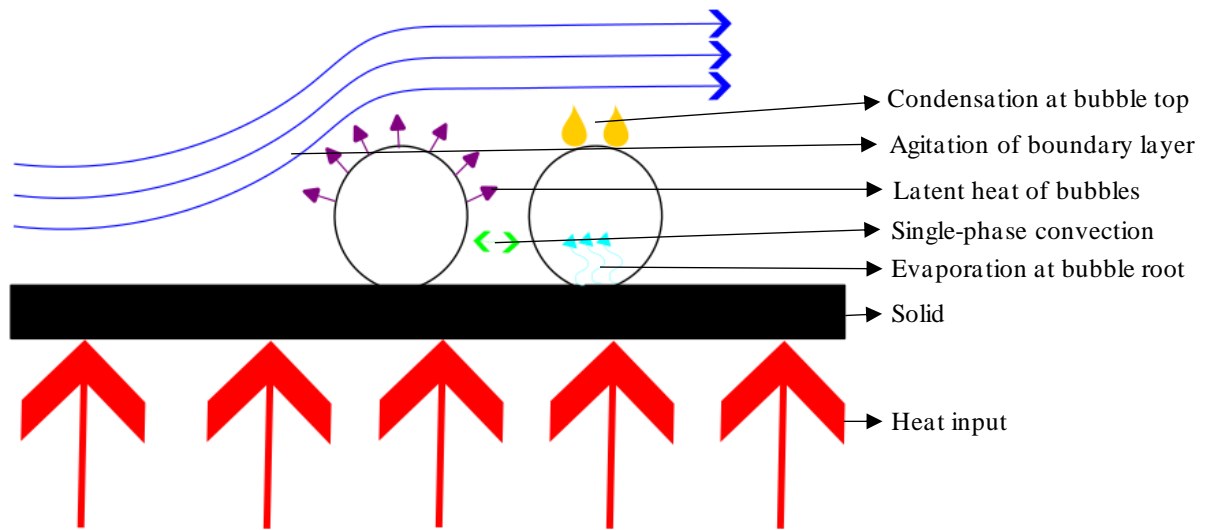
Figure 14: Heat transfer from the surface to the liquid in the nucleate boiling region

2.3.3.2 *Flow-boiling bubble dynamics*

Flow-boiling bubble dynamics follow the same principles outlined in Figure 12, with the only difference induced by the shear cross-flow. Figure 15 depicts the flow-boiling bubble dynamics [15] with the buoyancy force F_b, shear lift force F_{sl}, and contact pressure force F_{cp}, acting vertically upwards. The shear surface tension force, F_{sx}, F_{sy}, act in the horizontal and vertical direction alongside the bubble inertia force F_{du}, and the hydrodynamic pressure force F_h, due to the shearing nature of the bubble departure caused by the cross-flow.
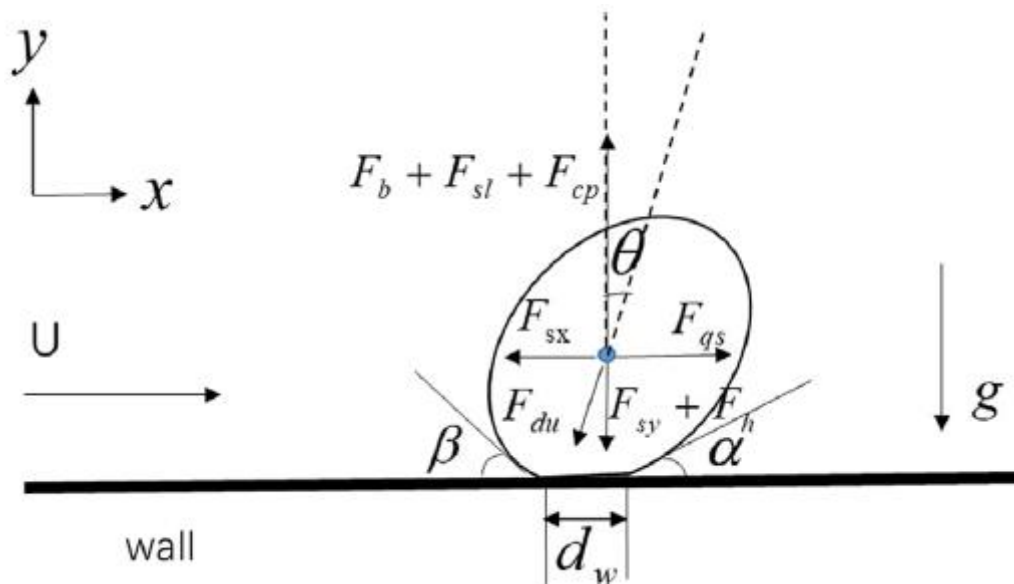
Figure 15: Flow-boiling bubble dynamics [15]

2.3.4 Boiling jet impingement on flat surfaces

2.3.4.1 Boiling jet impingement definitions

Two-phase jet impingement combines the heat transfer advantages of liquid jet impingement, discussed in Section 2.2.3, with boiling heat transfer, discussed in Section 2.3.2 and Section 2.3.3. Boiling jet impingement shows several advantages over other multiphase cooling schemes with low-pressure drops, including the ability to cool down a large surface area with multiple jets, cooling complex systems, and improving temperature uniformity on flat surfaces [22]. In addition, confined boiling jets produce superior heat transfer performance due to the confinement wall forcing the liquid to stay in contact with the heated surface [22]. Figure 16 shows that bubble generation at the wall, along with the momentum of the liquid and the bubbles, leads to liquid splashing in a free-surface jet and can lead to dry-out at the edges of the surface. In addition, an increase in the surface heat flux leads to increased liquid splashing [11]. The boiling curve for submerged impinging jets follows the same trend as described in Section 2.3.2.1. Submerged and confined jets increase surface wettability, thus improving the CHF [57].

For small applications such as electronic cooling, the nucleate boiling region is preferred because a slight increase in wall superheat leads to a significant increase in the dissipated wall heat flux [8]. The heat transfer characteristics depend on the configuration of the impinged jet, and for a free-surface jet, heat transfer is affected by droplet breakup, which does not occur in the submerged configuration [57]. The submerged configuration shares the same qualities as pool boiling and is considered an enhancement method of pool boiling [57]. As electronic devices become smaller, confined submerged jet impingement becomes inevitable as space tends to be limited. Most nucleate boiling investigations have focused on the limit between the ONB and the CHF [57].
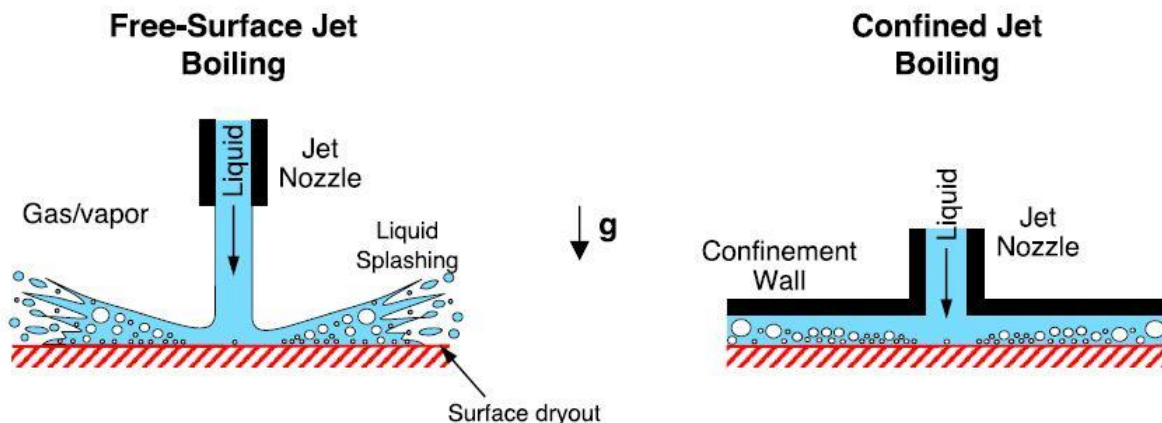
Figure 16: Fluid behaviour in free-surface and confined boiling jets [11]

Throughout the years, most of the wall heat flux correlations have been given in the following form:

$$q''_{sat} = C\Delta T_{sat}^m \tag{8}$$

where C and m are experimentally determined through curve fitting [8]. ΔT_{sat} is defined as the wall superheat and is expressed as

$$\Delta T_{sat} = T_{wall} - T_{sat} \tag{9}$$

where T_{wall} is the temperature of the impinged wall and T_{sat} is the saturated temperature of the impinging liquid [8]. Equation (8) can be rewritten to gain the heat transfer coefficient as

$$h = \frac{q''}{\Delta T_{sub} + \left(\frac{q''}{C}\right)^{\frac{1}{m}}} \tag{10}$$

where ΔT_{sub} is the amount of subcooling in the liquid and is expressed as

$$\Delta T_{sub} = T_{sat} - T_f \tag{11}$$

and T_f is defined as the impinging liquid temperature [8]. Section 2.3.1 described the nucleate boiling regime consisting of bubbly and mixing flow, as depicted in Figure 16, for confined jet boiling. Most investigations include water and dielectric fluids such as R113 and FC72, which have a low boiling point [57]. A notable difference between water and dielectric fluids occurs at the ONB. The ONB is delayed in the case of dielectric fluids because these fluids are highly wetted and can deeply penetrate the surface cavities [57]. This penetration obstructs residual vapour being fostered in the cavities [57]. The heat flux at which ONB boiling occurs increases as the jet velocity increases or the jet-to-target spacing decreases for both water and dielectric fluids [57]. Heat transfer in the fully nucleate boiling regime only depends on a few jet parameters compared with single-phase jets. Jet parameters such as jet configuration, diameter, orientation and velocity have a negligible impact on heat transfer in the nucleate boiling regime [8]. Cardenas and Narayanan [58] found that in the velocity range associated with a Reynolds number between 0 for pool boiling and 14 000 under a submerged water jet, the fully developed nucleate boiling heat transfer coefficient remained unaffected. This phenomenon was found by several researchers while using water and dielectric fluids in both submerged and confined configurations [57]. However, it was found that the impinged surface substantially impacted the heat transfer result, including surface conditions and ageing [8]. Differences in surface conditions made obtaining non-dimensional correlations for nucleate boiling challenging.

The CHF in the liquid sublayer has also been given much attention over the years. Figure 17 depicts the CHF being reached under an impinging jet [8]. Figure 17 also shows that a vapour column formed just alongside the stagnation region and created bubbles that flowed alongside the liquid in the wall-jet region. Bubbles in the wall-jet region can coalesce and form larger vapour bubbles, as depicted in Figure 17. Reaching the CHF on a microchip will be detrimental to the chip surface due to the high rate of temperature increase. Thus, boiling jet impingement cooling on microchips must operate in the nucleate boiling regime to prevent causing any damage to the chip surface.
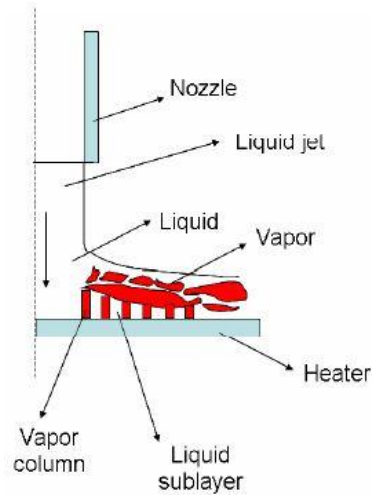
Figure 17: Schematic of CHF under an impinging jet [8]

2.3.4.2 Bubble dynamics under an impinging jet

Momentum interaction between the surrounding liquid and the growing bubble, and heat diffusion, are critical aspects of bubble growth. Bubble growth is predominantly controlled through inertia forces at low pressures, but heat diffusion dominates the growth process at high pressures. Two extra forces can be added to the dynamic effect of a growing bubble directly under an impinging jet when compared with flow boiling [3]. Figure 18 illustrates the forces acting on a bubble growing under an impinging jet [3]. A hydrostatic pressure force (F_h) compresses the bubble from the top due to the jet stagnation, while a buoyancy (F_b) and contact pressure force (F_{cp}) drive the bubble upwards. An asymmetric growth force (F_{du}) further acts on the bubble surface due to moving liquid.
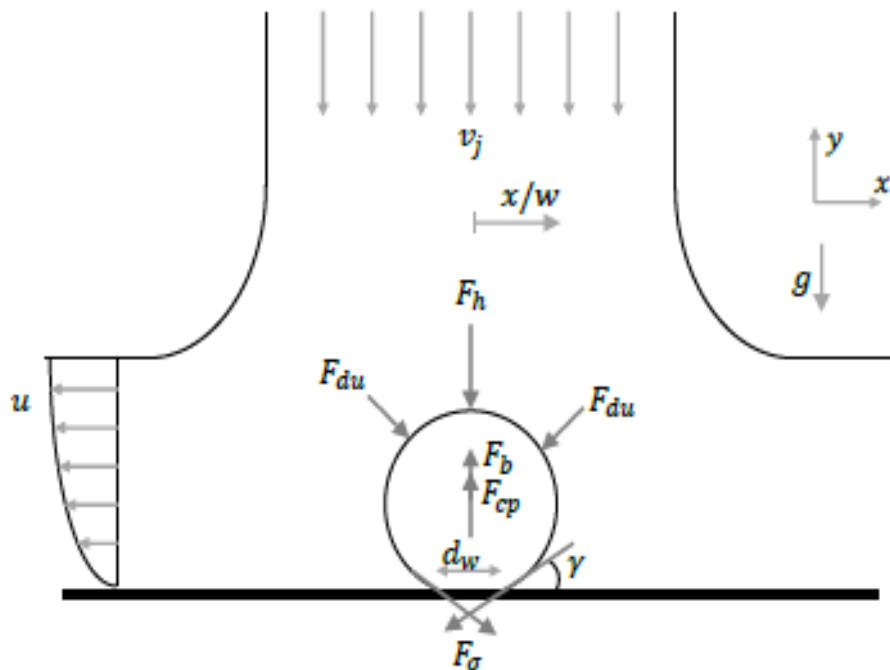
Figure 18: Bubble dynamics growing under an impinging jet [3]

21

2.3.4.3 Single jet

Boiling jet impingement on flat surfaces was first attempted by Katto and Kunihiro [59] by impinging a water jet at atmospheric pressure on a 10 mm heated copper surface. However, burnout was reached due to the inability of the liquid jet to replace generated vapour on the heated surface. Katto and Kunihiro found that increased liquid jet velocity increased the ability of the liquid to remove generated vapour, thus prolonging burnout under the impinging jet. In addition, a large heated surface area per liquid jet and jet flow rate led to burnout at the heated surface circumference due to generated vapour blocking the liquid from reaching the surface circumference, as shown in Figure 16. Qui and Liu[12] also found that jet velocity and nozzle diameter affected the CHF in both saturated and subcooled boiling jet impingement on a flat heated surface. Figure 19 shows that an increase in inlet subcooling increases heat transfer and the CHF [12], as described in Section 2.3.2. Cardenas and Narayanan [60] experienced boiling incipience while using a highly wetting dielectric fluid (FC-72), confirming the incipience phenomenon discussed in Section 2.3.2. The incipience of wall superheat disappears if the boiling curve is determined from a decreasing heat flux rather than an increasing heat flux [60]. Cardenas and Narayanan [58] found that an increase in saturation pressure led to an increase in CHF for circular submerged jets, but Katto and Shimizu [61] found the opposite to be true.
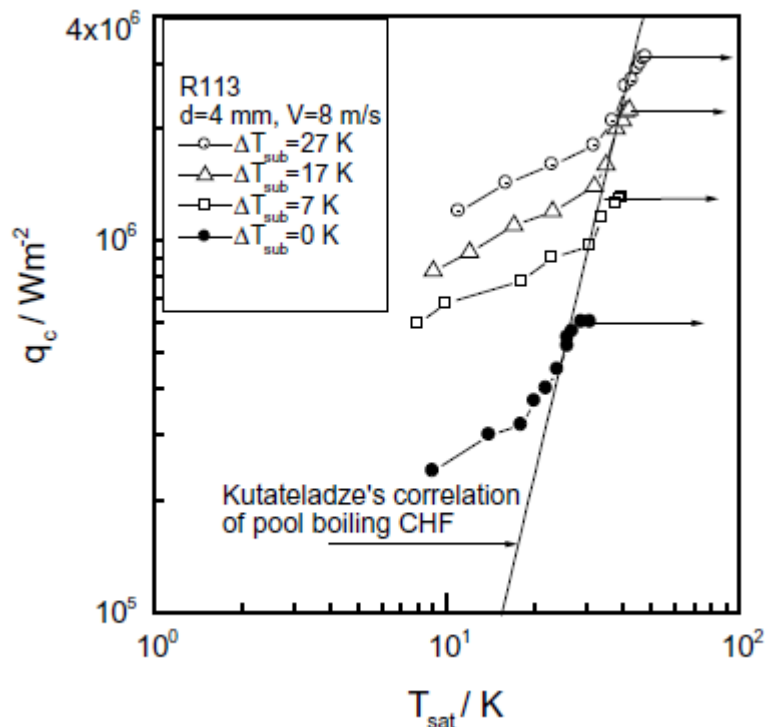
Figure 19: Boiling curve for a single submerged jet on a flat surface using R-113 [12]

2.3.4.4 Jet array

An array of jets can cool down a larger surface area, eliminating surface circumference dry-out [22]. However, maintaining a high coolant flow rate is a crucial drawback of jet impingement, which is necessary when multiple jets are used to keep a uniform surface temperature [22]. The most common arrangement of array jets is in the symmetric form of

$$(\sqrt{N}, \sqrt{N}) \qquad\qquad (12)$$

where N is the total number of jets. Narumanchi *et al.* [8] compared wall heat fluxes with respect to the wall superheat between different liquids and configurations for circular single and array jets in the nucleate boiling regime. All fluids experienced a higher wall heat flux when multiple jets were used.

Devahdhanush and Mudawar [22] studied the CHF of boiling jet impingement on a flat surface with a single and array jet configuration (see Figure 20). Figure 20 (a) shows an apparent increase in the CHF from single to array jet configurations over a wide range of velocities. These results were also found by Monde, Masanori, Kusuda, Hisao, Uehara, and Haruo [62]. However, a configuration change from a 3x3 jet array to a 6x6 jet array only gained a slight increase in CHF. Figure 20 (b) also shows a noticeable decrease in thermodynamic equilibrium exit quality ($x_{e,out}$) with an increase in the number of jets. A negative value of $x_{e,out}$ indicates a state of "subcooled CHF", whereas a value between 0 and 1 indicates a state of "saturated CHF". In addition, the decrease in jet diameter leads to a decrease in the CHF and an increase in $x_{e,out}$. Skema and Slanciauskas [63] studied the influence of jet array layout on the CHF from changing the symmetric in-line array expressed in equation (12) to a staggered jet array. They found that the staggered jet array produced a higher CHF than an in-line array.
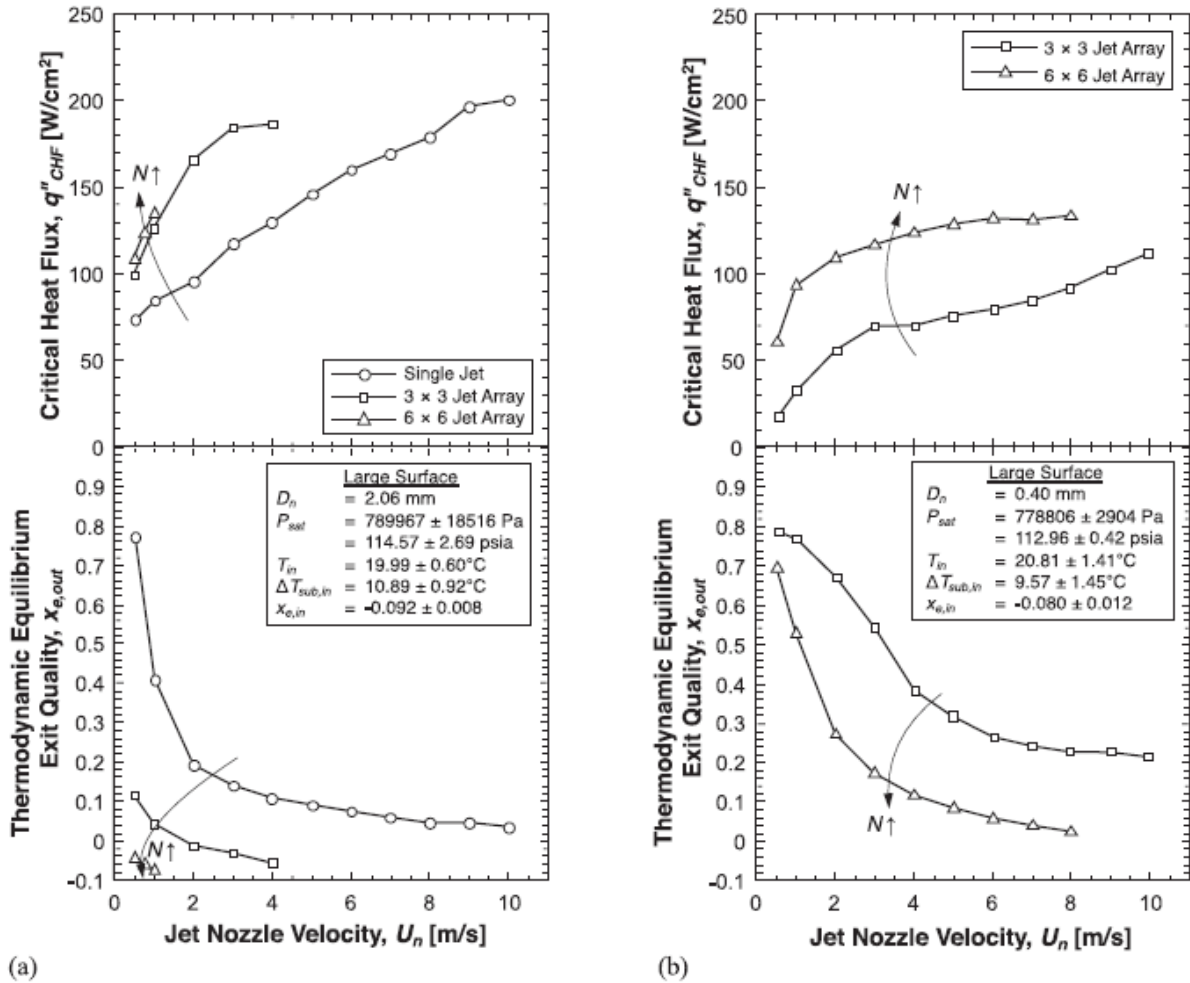
Figure 20: CHF and thermodynamic equilibrium exit quality comparison for a single, 3x3 and 6x6 jet configuration with nozzle diameters of (a) D_n = 2.06 mm and (b) D_n = 0.4 mm [22]

2.3.4.5 Spent fluid removal

Spent fluid is commonly removed from the sides of the heated surface for single-jet impingement but becomes a reasonably complex process when an array of jets is used. Therefore, in pursuit of a higher CHF, a more specialised spent fluid removal scheme is needed. Cui, Hong, and Cheng. [19] investigated the effect of using two different spent fluid removal techniques for both smooth and pin-finned surfaces.

Figure 21 depicts the two different removal techniques where (a) uses a normal jet array with the spent fluid removed at the edge of the chamber and (b) uses a distributed jet array with the spent fluid removed through effusion holes between the jet holes [19]. Cross-flow is a disadvantage in the normal jet array technique as it hinders downstream jets from adequately impinging onto the heated surface by disrupting the potential core of the jet. The strategic placement of effusion holes between the distributed array of jets eliminates the drawback of cross-flow by sucking the spent fluid upwards between the array of jets. Removing spent fluid through effusion holes also increases the CHF compared with a normal jet array [19].
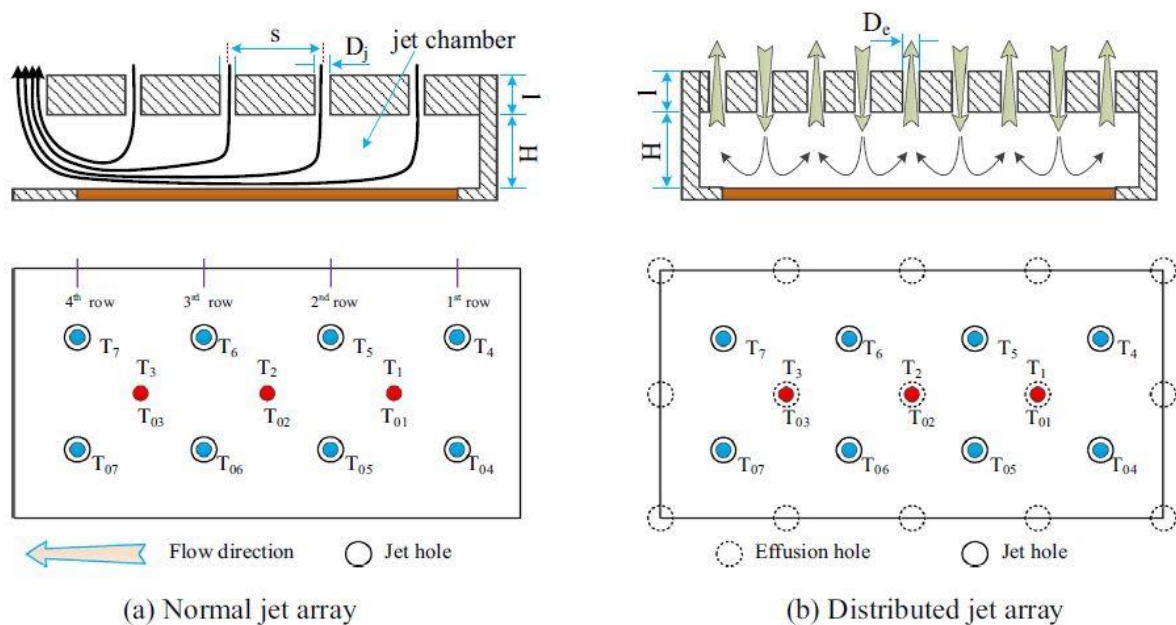
Figure 21: Spent fluid removal techniques: (a) normal jet array and (b) distributed jet array [19]

2.4 Flow over and boiling on enhanced and structured surfaces
2.4.1 Flow past immersed bodies and driven cavity flow

External flow around bodies, such as pin-fins or rods submerged in a fluid stream in the wall-jet region, is subject to viscous effects due to the no-slip and shear effects near the body surface [2]. Figure 22 indicates that a thin boundary layer is formed on the windward side of the body due to the favourable pressure gradient. A sharp rise in pressure ahead of the separation point leads to the creation of an adverse pressure gradient, significantly slowing down fluid particles at the near-wall region and ultimately breaking off from the wall, leading to the appearance of reversed flow downstream of the separation point [64]. A wake is formed at the rear end of the body as flow separation broadens.
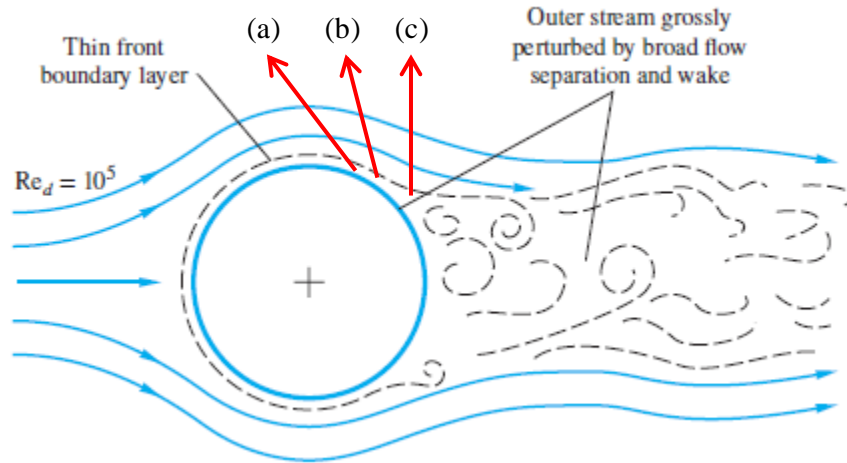
Figure 22: Flow separation around a blunt body, adapted from [2]

Figure 23 shows the effect of an adverse pressure gradient on the velocity boundary profile. Figure 23 (a) depicts a weak adverse gradient where the flow does not separate. A critical pressure gradient is reached as the adverse pressure gradient increases where the wall shear stress equals zero (see Figure 23 (b)). At this point, separation occurs, and a further increase in gradient will thicken the boundary layer and cause backflow at the wall after separation [2]. Figure 23 (a-c) illustrates a sequence of events as depicted schematically by a) to c) in Figure 22 over the blunt body.
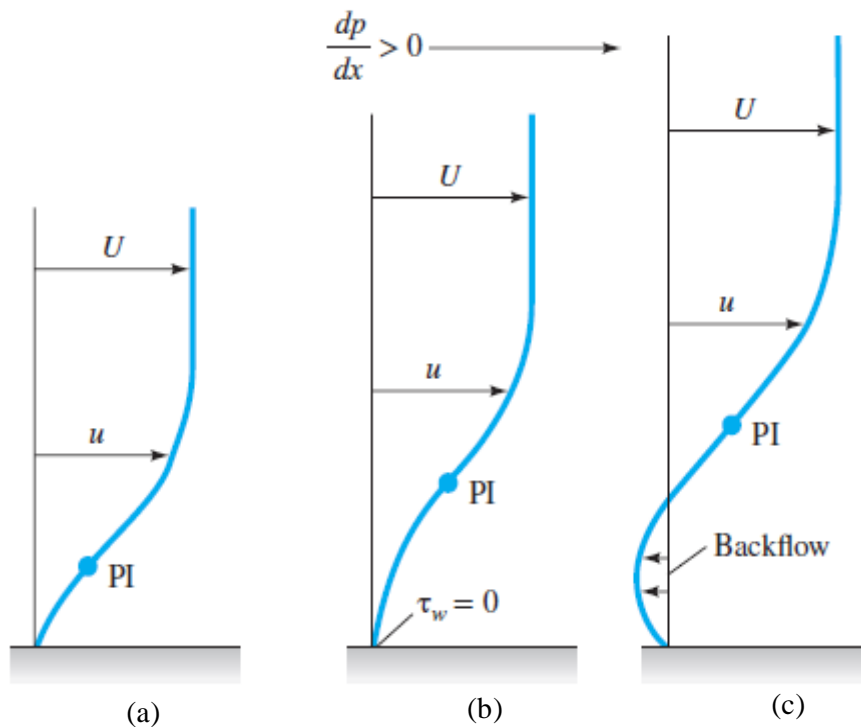
Figure 23: Effect of pressure gradient on the velocity boundary profile, adapted from [2]

Figure 24 illustrates the streamlined distribution for cavitation flow [18], also known as "driven cavity flow". A primary vortex is created at the centre of the cavity, with secondary vortices developed at the corners of the cavity. Figure 24 shows that the primary vortex will rotate in a clockwise direction agreeing with the upstream flow direction. In contrast, the secondary vortices will both rotate in an anti-clockwise direction.
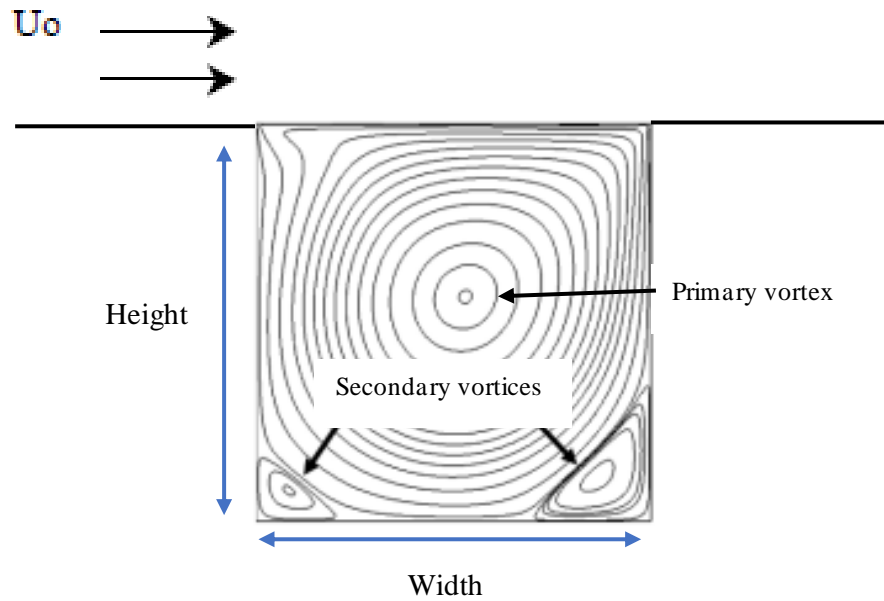
Figure 24: Cavity vortex, adapted from [18]

Cavity dimensions and upstream velocity are primary drivers of cavity vortex configurations [65]. Figure 25 shows that the increase in cavity height also creates a secondary vortex [6]. A second primary vortex is formed due to the merging of the two secondary corner vortices. Flow patterns over and between consecutive pin-fins change due to the aspect ratio defined as the ratio of the height (H) of each fin and the distance between fins (W) [24]. The different flow patterns can be classified under three types of flow patterns: isolated roughness flow, wake interference flow and skimming flow (see Figure 26).
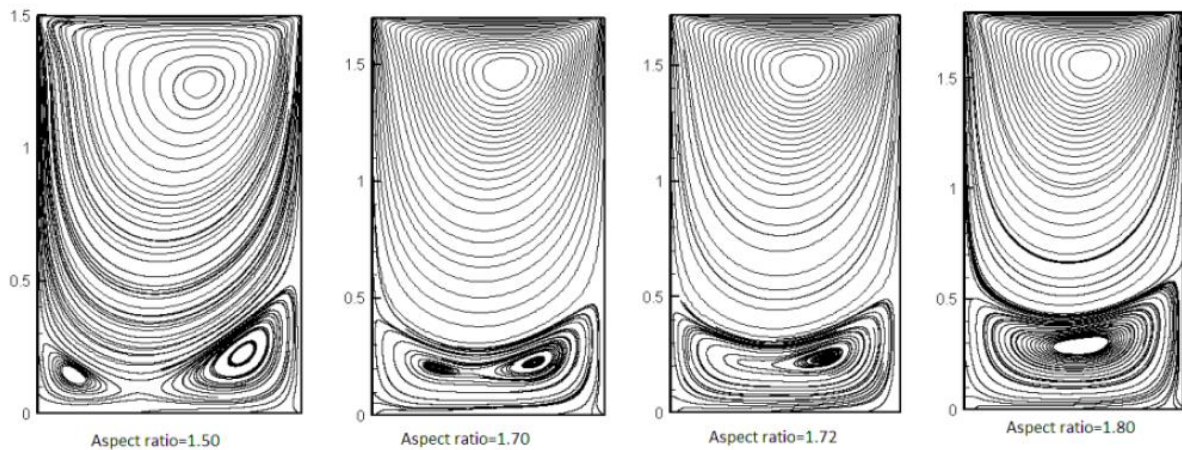
Figure 25: Deep cavity configuration [6]

Figure 26 (a) shows that isolated roughness flow occurs if fin spacing is large enough so that the generated turbulence of successive fins do not interfere with each other. Reducing fin spacing leads to wake interference flow (see Figure 26 (b)), where the windward recirculation zone interferes with the wake of the previous fin. A further reduction in fin spacing leads to skimming flow between successive fins (see Figure 26 (c)). The skimming flow is identical to the driven cavity flow depicted in Figure 24. 3D flow patterns over blunt bodies and inside cavities lead to significantly more complex flow patterns due to turbulent mixing.
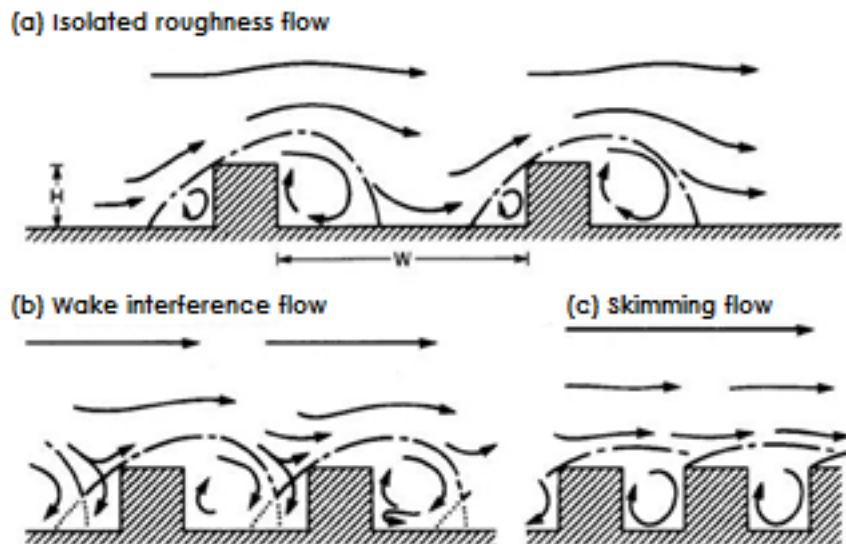
Figure 26: Flow patterns based on fin/groove aspect ratio [24]

2.4.2 Pool Boiling on structured surfaces

Surface augmentation in pool boiling has shown effective cooling enhancements [66]. Figure 27 (a) depicts the pool-boiling curve on a uniform rectangular pin-fin array [66]. The surface cooling performance was evaluated using equation (5) where $\Delta T_{sat} = \Delta T_e$ and the surface boiling phenomenon was captured through a microlens camera. Each fin had a height of 1.36 mm and a width of 1 mm with a variable fin cap c. HFE-7100 was used as a working fluid due to its high surface wettability [17], low boiling point and high dielectric strength. Figure 27 (a) shows two main flow regimes: natural convection and nucleation boiling. Nucleation boiling can be subdivided into two sub-regimes: isolated bubbles and merged bubbles. An apparent increase in the slope of the boiling curve can be observed between the transition from isolated bubbles to merged bubbles. The rise in the contribution of evaporative heat transfer in the merged bubble sub-regime can be attributed to an increase in overall heat transfer. The heat transfer increased when the gap (c) between the fins was increased. The heat transfer degradation in the isolated bubble sub-regime could primarily be attributed to an increase in bubble departure resistance [67], but the enhancement effect by increasing the gap was limited [66]. All three fin spacing configurations joined in the merged bubble subdivision as the fluid entered the fully developed nucleate boiling region shown in Figure 10.

Figure 27 (b) depicts the pool-boiling curve on a uniform circular pin-fin array [66]. Similar trends were observed with respect to the uniform rectangular pin-fin array, with a noticeable difference in the merged bubble subdivision, indicating that an increase in fin gap was more significant for the circular fin array, thus suggesting that the rectangular fin spacing had already breached its minimum fin gap limit that restricted the effect of flow resistance [66]. An apparent increase in heat transfer is observed at 25 W/cm^2 with a uniform rectangular array with respect to a uniform circular array at a spacing of 1 mm.
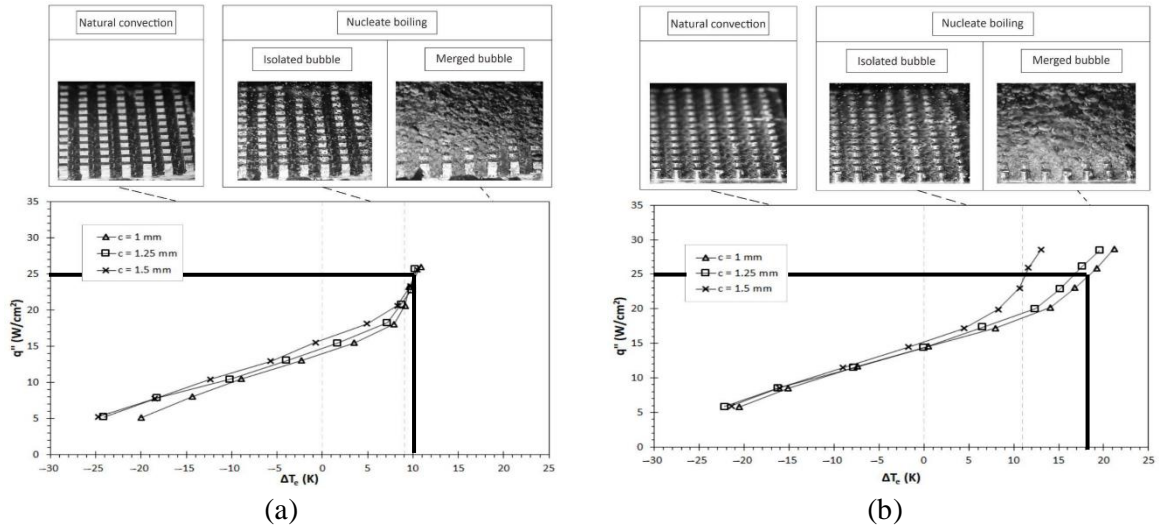
Figure 27: Pool-boiling curve on (a) in-line uniform square pin-fin array [66] and (b) in-line uniform circle pin-fin array [66]

2.4.3 Flow boiling in microstructures

Flow-boiling heat transfer can be improved through microstructures. However, premature critical heat flux triggered by bubble backflow and local dry-out induced by microstructures are detrimental to flow-boiling heat transfer [21]. Feng, Yan, and Lai [21] studied the flow-boiling characteristics of
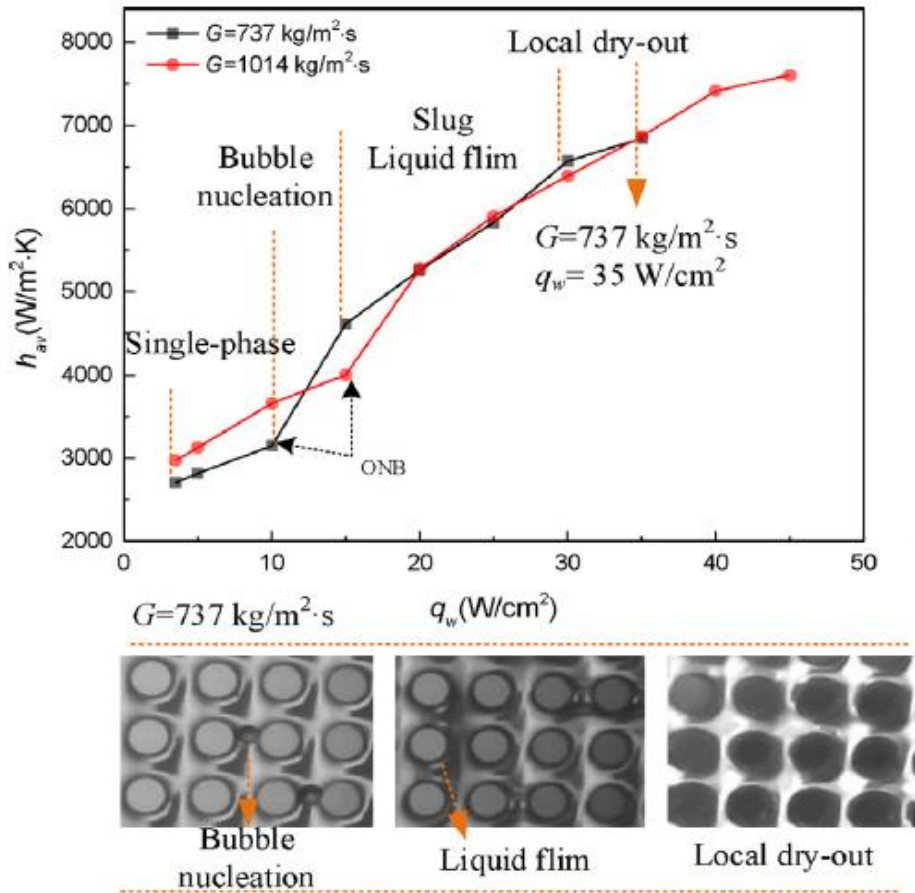
Figure 28: Flow-boiling heat transfer coefficient characteristics for a uniform pin-fin array [21]

28

microchannels with various pillar distributions. Figure 28 depicts the microchannel flow-boiling heat transfer characteristics over a uniform distributed circular pin-fin array with a highly dielectric fluid HFE 7000. Three boiling stages are marked in Figure 28: bubble nucleation, liquid film and local dry-out. A slight increase in the heat transfer coefficient with an increase in heat flux is found in the single-phase regime. After the ONB, the gradient of both mass velocities increased rapidly throughout the bubble nucleation region. A phenomenon also depicted in Figure 13 (a-b) is bubbly flow. The rapid increase in gradient can also be attributed to the fast bubble growth and departure of HFE 7000, causing latent heat release. With an increase in heat flux, a thin liquid film formed around the fins, and heat transferred from the base to the liquid and was transported through forced convection. Liquid film evaporation is critical in heat transfer enhancements [21]. Wana *et al.* [20] found that the liquid film formation was consistent with various fin shapes and distributions. A further increase in heat flux led to local dry-out, completely evaporating the liquid film and deteriorating heat transfer. An increase in mass velocity led to negligible differences in heat transfer after the bubble nucleation regime, with the postponement of the CHF as the only heat transfer enhancement factor. Wana *et al.* [20] studied the effect of pin-fin shapes in flow boiling.

Figure 29 (a) depicts the different shapes consisting of circular, square, streamlined and diamond micro pin-fins. Pin-fin shape had a negligible effect on the initiation of the ONB, as the ONB was triggered for all shapes at a wall superheat of $1°C - 3°C$. After the ONB, all curves had slightly different gradients, with the square micro pin-fins maintaining the lowest wall temperatures throughout the boiling curve up until a heat flux of approximately $650 \ W/cm^2$. Circular and streamlined pin-fins yielded approximately similar results with a slight shift to the right from the square pin-fins. A sharp deterioration in heat transfer resulted in the diamond pin-fins after a heat flux of $300 \ W/cm^2$.
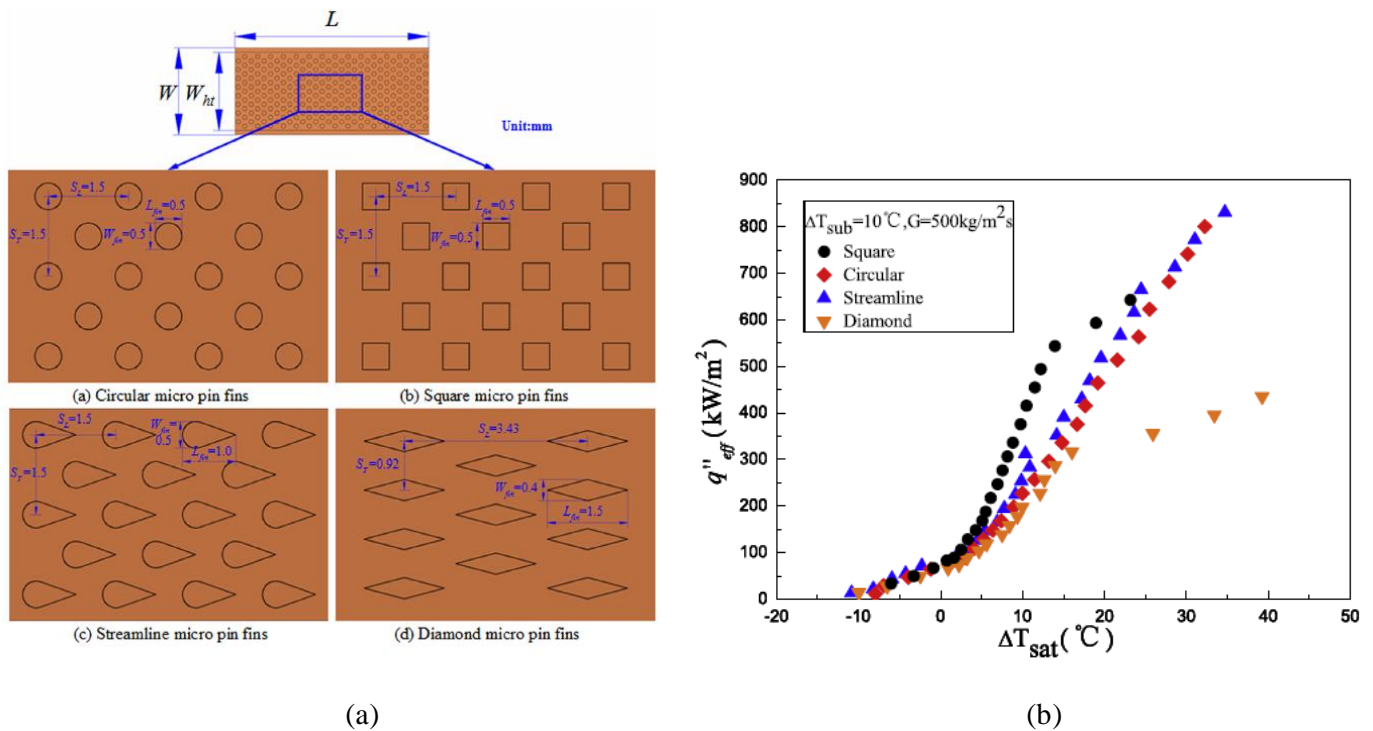
Figure 29: (a) Geometry of different pin-fin shapes and (b) flow-boiling curve of different pin-fin shapes [20]

2.4.4 Boiling jet impingement on structured surfaces

Most boiling jet studies were conducted on flat surfaces, while others changed the impinged surface to enhance the CHF. These attempts include changing the surface curvature, extending the surface, adding extra coatings to the heated surface and combinations of the above [11].

2.4.4.1 Surface efficiency

Overall surface efficiency is used to evaluate the design of an augmented surface [17], and a pin-fin augmented surface is expressed as

$$\eta_o = 1 - \frac{NA_f}{A_t}\left(1 - \eta_f\right) = \frac{q''A_b}{h_{eff}A_t\Delta T_b} \tag{13}$$

where N represents the total number of pin-fins, A_f is the surface area of a single pin-fin with the assumption of an active tip, A_t is the total wetted surface area, A_b is the top planform surface area, ΔT_b is the temperature difference between the base of the fin and the liquid inlet and h_{eff} is the assumed constant effective heat transfer coefficient. The effective fin efficiency η_f is calculated through

$$\eta_f = \frac{\tanh\left(mL_c\right)}{mL_c} \tag{14}$$

where L_c is the corrected fin length expressed as

$$L_c = L + w/4 \tag{15}$$

with L the height of each fin and w the width of a square fin. m in equation (14) is expressed as

$$m = \sqrt{\frac{4h_{eff}}{\kappa_f w}} \tag{16}$$

where κ_f is the thermal conductivity of the fin [68]. Equations (13) and (14) are solved iteratively to calculate the overall surface efficiency (η_o). This calculation is based on the assumption that the fin experiences a constant effective heat transfer coefficient but the calculation is still a valuable tool to evaluate a chosen fin design. Figure 30 compares the above overall surface efficiency of coated and uncoated pin-fins [17]. Smooth pin-fins resulted in higher surface efficiency throughout the range of heat fluxes due to a lower boiling heat transfer coefficient than for coated pin-fins. At first, the overall surface efficiency decreased due to an increase in the boiling heat transfer coefficient. However, as a vapour blanket formed on the base surface, the upper regions of each fin participated more in the overall heat transfer and the overall fin efficiency increased.
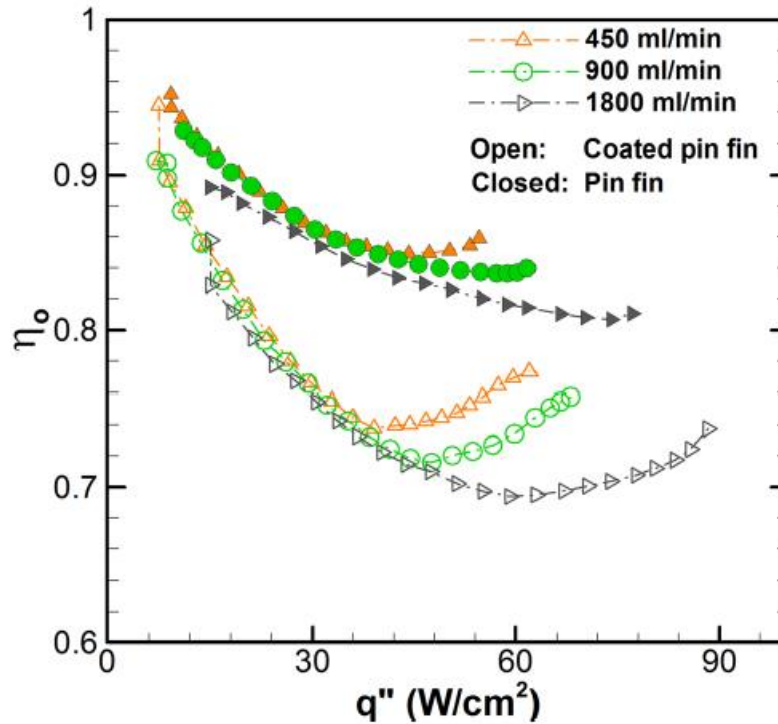
Figure 30: Pin-fin overall surface efficiency comparison [17]

2.4.4.2 Single jet

Wadsworth and Mudawar [69] were among the first researchers to investigate the effect of extended surfaces on the CHF. Their investigation included an experiment that used the same single-slot jet on a smooth flat surface, a surface with pin-fines (also called studs) and a surface with grooves. All these investigations were done on a microscale. Figure 31 (a) depicts the surface enhancement dimensions used in these experiments. Figure 31 (b) shows the CHF based on the planform area with respect to the nozzle outlet velocity. Both stud and grooved surfaces enhanced the CHF throughout the range of velocities, with the grooved surfaces showing superior results. The calculation of the CHF based on the planform area neglected the surface augmentation and solely focused on the electrical input at which the CHF occurred. Figure 31 (c) plots the CHF based on the total wetted area. The total wetted area considers surface augmentation and illustrates that a bare flat surface has the highest critical heat flux based on the total wetted area. Figure 31 (c) thus does not directly represent the total electrical power at which each surface type reaches the CHF.
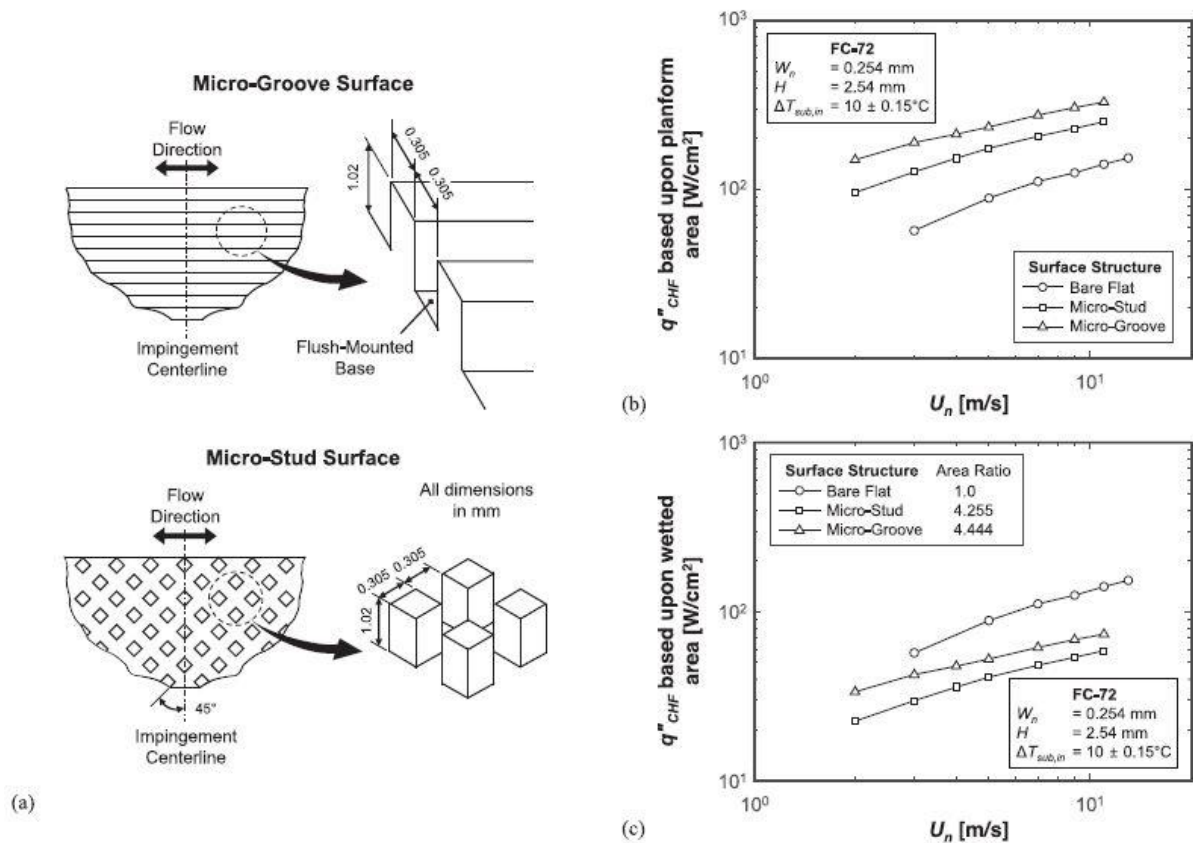
Figure 31: (a) Stud and grooved surfaces layout, (b) CHF based on planform area and (c) CHF based on the wetted area [11]

Rau and Garimella [17] investigated confined boiling jet impingement on flat and pin-fin surfaces with and without a microporous coating. An increase in the jet inlet velocity led to an increase in the CHF for all surface types. In addition, the smooth, uniform distribution of pin-fins produced higher heat transfer coefficients throughout the range of velocities and heat fluxes than for the smooth flat surfaces. The heat transfer enhancement of the smooth pin-fins was due to the additional turbulence generated by the pin-fins and an increase in the area where nucleation sites could occur. A microporous coating on flat and pin-fin surfaces produced dramatically higher heat transfer coefficients than for smooth surfaces in the nucleate boiling regime. Microporous coatings allowed for numerous additional nucleation sites, increasing the heat transfer and resulting in an almost vertical slope in the boiling curve. A significant temperature incipience resulted when a surface was coated with a microporous coating (see Figure 32) and this incipience could damage the surface if the temperature incipience exceeded the maximum operating temperature. Rau and Garimella also found that the pressure drop remained constant with an increase in heat flux and only changed with a change in inlet velocity.

Figure 32 depicts a series of high-speed images on the boiling curve of a single jet impinging on a microporous-coated uniform distributed pin-fin surface [17]. At the ONB, discrete bubble nucleation formed at the corners of the square surface, nucleating at the base of the pin-fins and growing towards the centre of the surface with an increase in heat flux. Local dry-out occurred at the base surface and decreased the slope of the boiling curve as a vapour film started to cover the base surface.
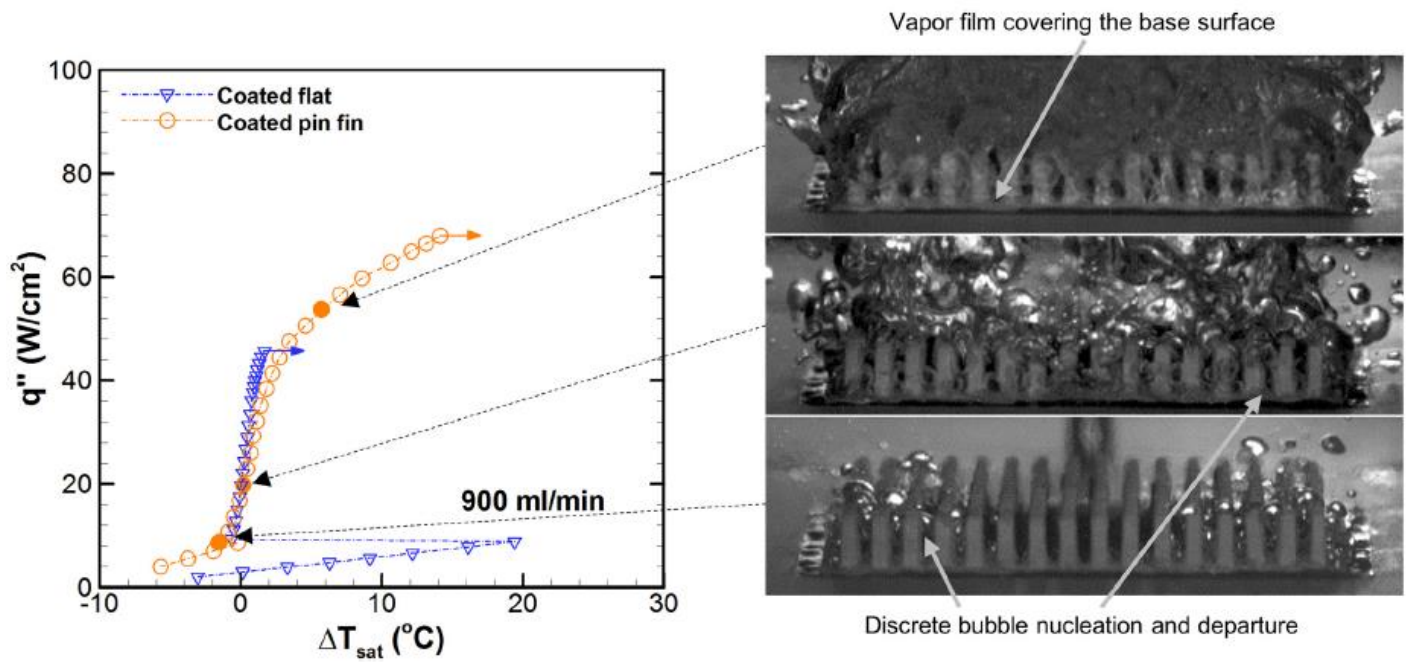
Figure 32: High-speed images extracted at different locations on the boiling curve of a single jet impinging on a coated pin-fin surface [17].

2.4.4.3 Jet array

As described in Section 2.3.4.4, a jet array can cool down a larger surface area. However, it can also accelerate the flow by strategically placing jets over stagnant pool-boiling regimes, as described in Section 1.1. Figure 33 illustrates the vapour formation on pin-fins while using a normal and distributed array of jets, as discussed in Section 2.3.4.5. The tiny bubbles are generated at the centres of the four jet arrays, which agrees with the study by Ariz *et al.* [70]. A normal jet array leads to vapour bubbles coalescing in the bulk flow due to the formed cross-flow. In contrast, the vapour is sucked out through the effusion holes in the distributed jet array, leading to a higher CHF.

Rau *et al.* [23] investigated the effect of a jet array on the same uniform pin-fin distribution, as depicted in Figure 32. Figure 34 (a) shows the flow paths on a pin-fin surface impinged due to flow following the path of least resistance, which is also shown in Section 1.1 (Figure 4). Figure 34 (b-c) shows the fluid flow paths of a single jet and an array of jet configurations. The jet array led to an increase in flow-boiling regimes, which led to an increase in heat transfer and CHF [23]. However, even though the pool-boiling area decreased, local dry-out was still a concern at the corners of the surface.

Jenkins *et al.* [37] investigated the heat transfer performance of a boiling jet array impinging on micro-grooved surfaces. The micro-grooved surfaces gained higher stagnation region heat transfer coefficients than for the flat surface. However, local dry-out due to recirculating flow inside the grooves (see Section 2.4.1) was a concern and has yet to be fully explored.
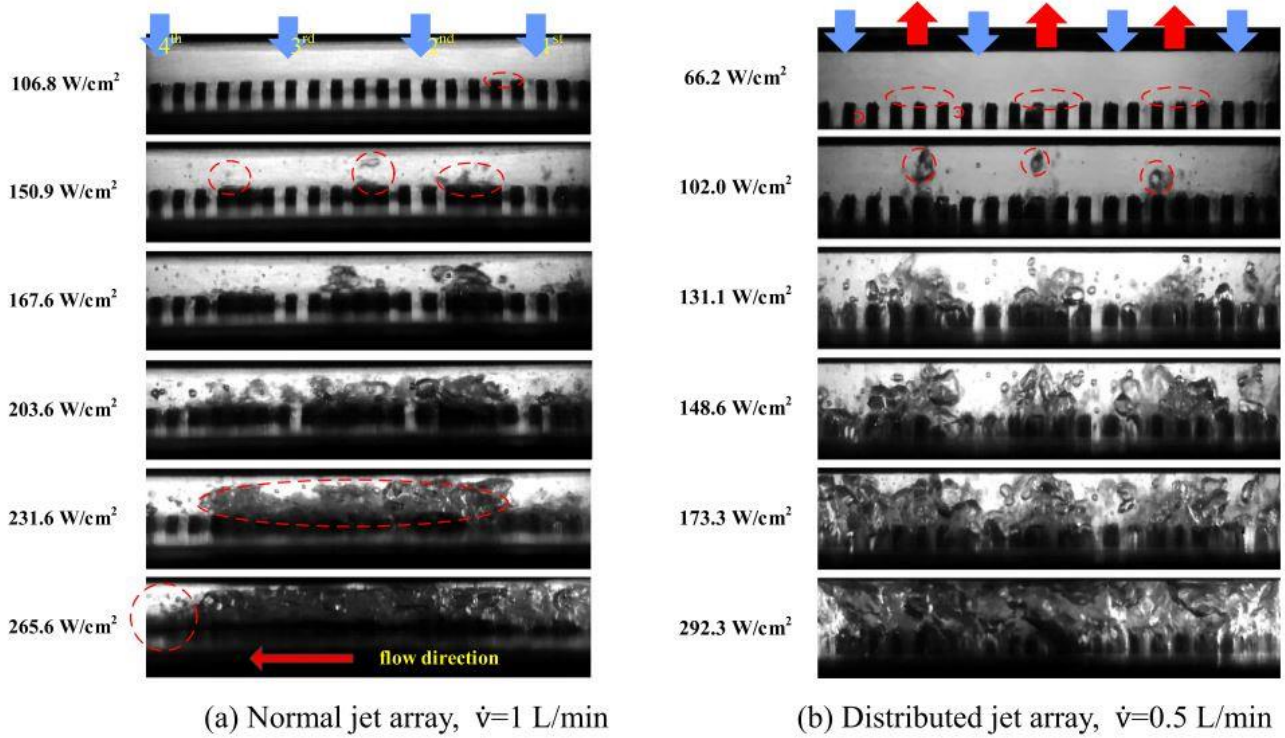
Figure 33: Pin-fin vapour formation on (a) normal jet array and (b) distributed jet array [19]
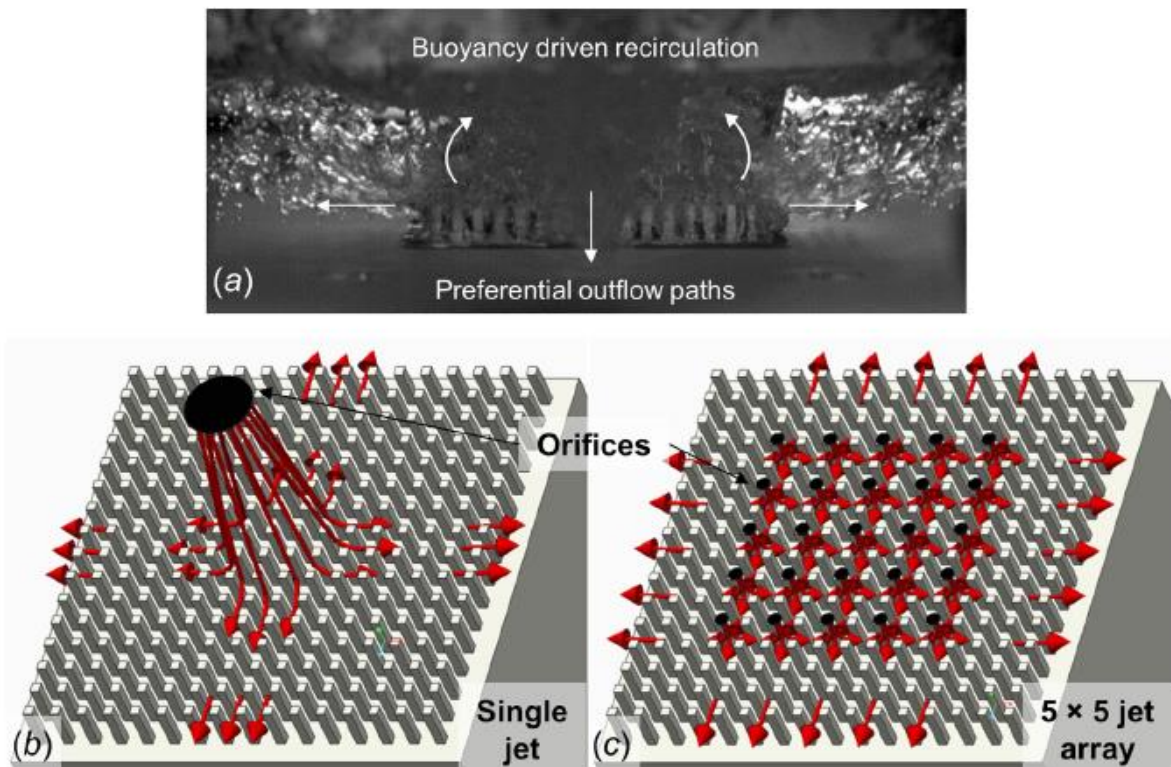
Figure 34: (a) High-speed image of flow visualisation of a single jet and flow pattern visualisation between (b) single jet and (b) array of jets on a pin-fin surface [23]

2.5 Conclusion

Implementing microstructured surfaces in boiling jet impingement enhanced multiphase heat transfer by increasing the product of the average surface heat transfer coefficient and the surface area. The enhancement was driven by disrupting boundary layer growth and improving turbulent transport. Liquid jet impingement generated a high-pressure stagnation region resulting from the conversion of kinetic energy into pressure energy. The difference in pressure between the stagnation and outer regions accelerated the flow outwards from the stagnation region. Submerged and confined jets increased surface wettability, thus improving the CHF. The nucleate boiling regime yielded the highest heat transfer coefficients due to the ability of the liquid to rewet evaporating vapour on the surface. Discrete bubble nucleation formed at the outer regions of the heated microstructured surface, nucleating at the base of the pin-fins and growing towards the centre of the surface with an increase in heat flux. However, stagnating flow caused by microstructures could harm the local heat transfer due to the local transition from flow boiling to pool boiling, leading to premature dry-out in pool-boiling regions. Jet arrays could cool down a larger surface area, eliminating surface circumference dry-out and accelerating the flow by strategically placing jets over stagnant pool-boiling regimes. Cross-flow was a disadvantage in the jet array technique because it hindered downstream jets from adequately impinging onto the heated surface by disrupting the potential core of the jet. The strategic placement of effusion holes between the distributed array of jets eliminated the drawback of cross-flow by sucking the spent fluid upwards between the array of jets.

Boiling jet impingement heat transfer can be enhanced through microstructures if special attention is given to eliminating local dry-out, preventing any damage to the heated surface.

3 Numerical Framework

A commercial CFD software, Ansys Fluent 2022 R2, was used to model subcooled boiling jet impingement on enhanced surfaces. A transient, Euler-Euler approach was used as the foundation of the numerical model, with liquid as the primary phase and vapour as the dispersed phase. Conjugate heat transfer was predicted through the Rensselaer Polytechnic Institute (RPI) wall-boiling model, embedded in the Eulerian multiphase model [71] as a wall boundary condition.

3.1 Eulerian framework

The Eulerian approach is a method to develop equations for a collection of fluid elements at a fixed region in space [72]. For example, it is possible to develop equations for fluid flow by tracking each particle through space, termed the Lagrangian approach. However, it is far more common in CFD approaches to use the Eulerian approach because the Eulerian multiphase model allows for a separate treatment of the liquid and gas phases and their interaction at fixed locations in space. A study conducted by Guerrero, Munoz, and Ratkovich [73] and Shademan [74] found that the Eulerian model produced the most accurate results when validating two-phase flow in confined boiling experimental work. The Eulerian model is also suggested by the Ansys Fluent Theory guide [71] for confined two-phase flow where phases mix or dispersed phase volume fractions exceed 10%. Multiphase flows are treated as interpenetrating continua where volume fractions represent the space of each phase occupied in a control volume [71] and expressed as

$$V_q = \int \alpha_q \, dV \qquad (17)$$

where the sum of the volume fractions (α_q) of each phase is equal to 1 inside a control volume. The effective density of each phase is expressed as

$$\hat{\rho}_q = \alpha_q \rho_q \qquad (18)$$

and ρ_q is the physical density of the phase q. Equation (18) can be implicitly solved [71] through

$$\frac{\alpha_q^{n+1} \rho_q^{n+1} - \alpha_q^n \rho_q^n}{\Delta t} V + \sum_f (\rho_q^{n+1} v_f^{n+1} \alpha_{q,f}^{n+1}) = [S_{\alpha_q} + \sum_{p=1}^{N} (\dot{m}_{pq} - \dot{m}_{qp})] V \qquad (19)$$

where n denotes the current time step, $n+1$ is the next time step and N the number of phases; α_q denotes the volume fraction cell value, $\alpha_{q,f}$ the face value of the qth volume fraction and V the cell volume; $\dot{m}_{pq}$ represents the mass transfer from phase p to phase q and $\dot{m}_{qp}$ the mass transfer from phase q to phase p. The mass source term S_{α_q} is set to zero as there is no chemical or nuclear reaction that has to be considered. The mass, momentum and energy conservation laws of each phase are met individually. The derivation is done by ensembling the average local instantaneous balance for each phase, where each phase is coupled through pressure and interphase interaction coefficients [9].

3.2 Conservation equations

The continuity equation [71] for phase q is expressed as

$$\frac{\partial}{\partial t}(\alpha_q \rho_q) + \nabla \cdot (\alpha_q \rho_q \vec{v}_q) = \sum_{p=1}^{N}(\dot{m}_{pq}) + S_q \tag{20}$$

where $\vec{v}_q$ is the velocity of phase q, and again the source term S_q is set to zero. If there is no phase change present, $\dot{m}_{pq}$ drops out of equation (20). The momentum equation [71] is expressed as

$$\frac{\partial}{\partial t}(\alpha_q \rho_q \vec{v}_q) + \nabla \cdot (\alpha_q \rho_q \vec{v}_q \vec{v}_q)$$
$$= -\alpha_q \nabla p + \nabla \cdot \bar{\bar{\tau}}_p + \alpha_q \rho_q \vec{g} + \sum_{p=1}^{N}(\vec{R}_{pq} + \dot{m}_{pq} \vec{v}_{pq}) + F \tag{21}$$

where ∇p is the shared pressure across all phases, $\bar{\bar{\tau}}_p$ is the stress tensor, $\vec{R}_{pq}$ an interaction force between phases p and q, n the number of phases, $\vec{v}_{pq}$ the interphase velocity and

$$F = (\vec{F}_q + \vec{F}_{lift,q} + \vec{F}_{wl,q} + \vec{F}_{vm,q} + \vec{F}_{td,q}) \tag{22}$$

where $\vec{F}_q$ is the external body force, $\vec{F}_{lift,q}$ the lift force, $\vec{F}_{wl,q}$ the wall lubrication force, $\vec{F}_{vm,q}$ the virtual mass force and $\vec{F}_{td,q}$ is the turbulent dispersion force in the case of turbulent flow; $\bar{\tau}$ defines the q phase stress-strain tensor expressed as

$$\bar{\bar{\tau}}_q = \alpha_q \mu_q \left(\nabla \vec{v}_q + \nabla \vec{v}_q^T \right) + \alpha_q \left(\lambda_q - \frac{2}{3}\mu_q \right) \nabla \vec{v}_q \bar{I} \tag{23}$$

The interaction force [71] between phases is expressed as

$$\sum_{p=1}^{N} \vec{R}_{pq} = \sum_{p=1}^{N} K_{pq}(\vec{v}_p - \vec{v}_q) \tag{24}$$

where K_{pq} in the interphase momentum exchange coefficient. The conservation of energy is described as a separate enthalpy equation of each phase per unit volume [71] and is expressed as

$$\frac{\partial}{\partial t}(\alpha_q \rho_q h_q) + \nabla \cdot (\alpha_q \rho_q \vec{v}_q h_q)$$
$$= \bar{\bar{\tau}}_q : \nabla \cdot \vec{v}_q - \nabla \cdot \vec{q}_q + \sum_{p=1}^{N}(Q_{pq} + \dot{m}_{pq}h_{pq}) + p\frac{\partial \alpha_q}{\partial t} + S_q \tag{25}$$

where h_q is the specific enthalpy of phase q, $\vec{q}_q$ is the heat flux, S_q the energy source term (set to zero in the current study as there is no chemical reaction or radiation), $\vec{J_q}$ the diffusive heat flux in phase q, Q_{pq} the heat exchange intensity between phases p and q, and h_{pq} is the interphase enthalpy.

3.3 Turbulence modelling

Multiphase turbulence is modelled on the renormalisation (RNG) k-ε mixture turbulence model, where an additional source term is added to the turbulence dissipation equation to account for the dispersed phase-induced turbulence and the differences between the production and destruction thereof. The turbulent kinetic equation [71] is expressed as

$$\frac{\partial}{\partial t}(\rho_m k) + \nabla \cdot (\rho_m \vec{v}_m k) = -\nabla \cdot (\sigma_{k,m} \mu_{t,m} \nabla k) + G_{k,m} - \rho_m \varepsilon + S_{k_m} \tag{26}$$

where ρ_m is the mixture density, $\vec{v}_m$ is the mixture velocity, μ_m is the mixture of dynamic viscosity, k the turbulent kinetic energy, ε the turbulent dissipation rate, $\mu_{t,m}$ the mixture turbulent viscosity, $\sigma_{k,m}$ the inverse of the effective Prandtl number for k, $G_{k,m}$ the production of turbulent kinetic energy and S_{k_m} the source term to include the dispersed phase-induced turbulence for k. The turbulent dissipation rate [71] is expressed as

$$\frac{\partial}{\partial t}(\rho_m \varepsilon) + \nabla \cdot (\rho_m \vec{v}_m \varepsilon)$$
$$= -\nabla \cdot (\sigma_{\varepsilon,m} \mu_{t,m} \nabla \varepsilon) + \frac{\varepsilon}{k}(C_{1\varepsilon} G_{k,m} - C_{2\varepsilon} \rho_m \varepsilon) + S_{\varepsilon_m} - R_\varepsilon \tag{27}$$

where $\sigma_{\varepsilon,m}$ is the inverse of the effective Prandtl number for ε, $C_{1\varepsilon}$ and $C_{2\varepsilon}$ are model constants, S_{ε_m} the source term to include the dispersed phase-induced turbulence for ε and R_ε is the RNG additional term. The factor $\frac{\varepsilon}{k}$ in equation (27) ensures that the production and destruction of turbulent kinetic energy are always closely related and avoids non-physical negative values of the turbulent kinetic energy if k decreases [72]. The mixture properties discussed above are expressed as

$$\rho_m = \sum_{i=1}^{N} \alpha_i \rho_i \tag{28}$$

$$\mu_m = \sum_{i=1}^{N} \alpha_i \mu_i \tag{29}$$

$$\vec{v}_m = \frac{\sum_{i=1}^{N} \alpha_i \rho_i \vec{v}_i}{\sum_{i=1}^{N} \alpha_i \rho_i} \tag{30}$$

where α_i is the phase volume fraction, ρ_i the phase density, μ_i the phase dynamic viscosity, and $\vec{v}_i$ the phase velocity. The mixture of turbulent viscosity is expressed as

$$\mu_{t,m} = \rho_m C_\mu \frac{k^2}{\varepsilon} \tag{31}$$

where C_μ is a model constant. The production of turbulent kinetic energy is expressed as

$$G_{k,m} = \mu_{t,m}(\nabla\vec{v}_m + (\nabla\vec{v}_m)^T):\nabla\vec{v}_m \tag{32}$$

The accuracy of numerical solutions is significantly impacted through near-wall modelling because walls act as the primary source of turbulence and vorticity. In the case of complex flows involving separation, reattachment and impingement where the turbulence and the mean flow are subject to pressure gradients and rapid changes, a two-layer-based, non-equilibrium wall function [75] is used rather than standard wall functions because the assumption of local equilibrium is no longer valid as the production of turbulent kinetic energy is no longer equal to the destruction thereof. The non-equilibrium wall functions remain partly the same as the standard wall functions, but the log law for mean velocity is sensitised to pressure gradients by formulating a y^+ insensitive near-wall function expressed as

$$\frac{\tilde{U} C_\mu^{1/4} k^{1/2}}{\tau_w/\rho_p} = \frac{1}{\kappa_p} \ln\left(E\frac{\rho_p C_\mu^{1/4} k^{1/2} y}{\mu_p}\right) \tag{33}$$

where κ_p is the thermal conductivity of the p_{th} phase and

$$\tilde{U} = U - \frac{1}{2}\frac{dp}{dx}\left[\frac{y_v}{\rho\kappa_p\sqrt{k}}\ln\left(\frac{y}{y_v}\right) + \frac{y - y_v}{\rho_p\kappa_p\sqrt{k}} + \frac{y_v^2}{\mu_p}\right] \tag{34}$$

where y_v is the physical viscous sublayer thickness, which is computed as

$$y_v \equiv \frac{\mu_m y_v^*}{\rho_p C_\mu^{1/4} k_p^{1/2}} \tag{35}$$

where $y_v^* = 11.225$. Wall neighbouring cells are assumed to consist of a viscous sublayer and a fully turbulent layer. The following assumptions are made to calculate the turbulent quantities:

$$\tau_t = \begin{cases} 0, y < y_v \\ \tau_w, y > y_v \end{cases} \tag{36}$$

$$k = \begin{cases} \left(\dfrac{y}{y_v}\right)^2 k_p, & y < y_v \\ k_p, & y < y_v \end{cases} \tag{37}$$

$$\varepsilon = \begin{cases} \dfrac{2v_m k}{y^2}, & y < y_v \\ \dfrac{k^{3/2}}{c_l^* y}, & y > y_v \end{cases} \tag{38}$$

where $C_l^* = \kappa C_u^{-\frac{3}{4}}$. Through the use of the above quantities, the cell-averaged production of k, G_k and dissipation rate ε can be computed from the volume average of G_k and ε at wall-adjacent cells and for hexahedral cells expressed as

$$G_k \equiv \frac{1}{y_n} \int_0^{y_n} \tau_t \frac{\partial v}{\partial y} dy \tag{39}$$

and

$$\varepsilon = \frac{1}{y_n} \int_0^{y_n} \varepsilon dy \tag{40}$$

where y_n is the height of the cell. The appropriate cell volume averages are used for different cells.

3.4 Interphase transfer models

The interfacial area concentration is an important parameter because a strong relationship exists between the transport terms of interfacial area concentration and mass, momentum and energy [9]. The interfacial area concentration can be defined through the Ishii model [71], which results in a piecewise linear function of α_p, which approaches 0 if α_p approaches 1, which then switches the model if there is no boiling present in the domain. The interfacial area concentration is expressed as

$$A_i = \frac{6(1 - \alpha_p)\min(\alpha_p, \alpha_{p,crit})}{d_p(1 - \min(\alpha_p, \alpha_{p,crit}))} \tag{41}$$

where α_p is the volume fraction of the liquid phase, d_p is the bubble diameter and $\alpha_{p,crit} = 0.25$. The evaporation-condensation model [71] determines the liquid-vapour mass transfer rates included in equation (20). The summation of mass transfer from the wall to the vapour and interfacial mass transfer is expressed as [41]

$$\sum_{p=1}^{N} (\dot{m}_{pq}) = m_{lv} = \frac{[h_{ls}(T_l - T_{sat}) + h_{vs}(T_v - T_{sat})]A_i}{h_{fg}} + \frac{q_E'' A_{i,W}}{h_{fg} + C_{p,l}(T_s - T_l)} \tag{42}$$

where h_{ls} and h_{vs} are the liquid- and vapour-side interfacial heat transfer coefficients respectively; h_{fg} is the latent heat of vaporisation, T_l and T_v the liquid and vapour temperature, q_E'' the evaporative heat flux component of the RPI boiling model (discussed later), T_s the interfacial temperature, determined through considering thermodynamic equilibrium, $A_{i,W}$ the interfacial area density of the wall, and $C_{p,l}$ the liquid heat capacity. The computation of the phase enthalpies takes into account the discontinuity in static enthalpy due to latent heat between the two phases as well as the heat transfer from either phase to the phase interface. If $m_{lv} \geq 0$ the liquid phase is the outgoing phase, classified as evaporation, and if $m_{lv} < 0$ the liquid phase is the incoming phase, classified as condensation. Linking the interfacial mass transfer to the components of the RPI wall-boiling model (discussed later). h_{ls} and h_{vs} are related to the phase Nusselt number by

$$h_{pq} = \frac{\kappa_q Nu_p}{d_p} \tag{43}$$

The Tomiyama correlation [76] is used to express the Nusselt number as

$$Nu_p = 2.0 + 0.15 Re_p^{0.8} Pr^{0.5}. \tag{44}$$

The Tomiyama correlation is frequently used for bubbly flows with a relatively low Reynolds number [71]. The interphase momentum exchange expressed in equation (24) is defined as

$$K_{pq} = \frac{\rho_p f}{6 t_{part}} d_p A_i \tag{45}$$

where t_{part} is the particulate relaxation time and is expressed as

$$t_p = \frac{\rho_p d_p^2}{18 \mu_q} \tag{46}$$

while f is the drag function and is expressed as

$$f = \frac{C_D Re}{24} \tag{47}$$

The drag coefficient can be modelled on the Ishii model [9] in bubbly flow and is expressed as

$$C_D = \min\left(\frac{24}{Re}\left(1 + 0.15Re^{0.75}\right), \frac{2}{3}\frac{d_p}{\left(\frac{\sigma}{g|\rho_p - \rho_g|}\right)^{\frac{1}{2}}}\right) \tag{48}$$

where the drag is calculated based on the minimum between the viscous and distorted region, Re is the relative Reynolds number, g is gravity, and σ is the surface tension. The lift force in equation (22) is expressed as

$$\vec{F}_{lift} = -C_{lift}\rho_q\alpha_p(\vec{v}_q - \vec{v}_p) \times (\nabla \times \vec{v}_q) \tag{49}$$

where C_{lift} is the lift coefficient, which can be modelled on the Tomiyama lift force model [76], which is expressed as

$$C_{lift} = \begin{cases} \min\left[0.228\,tanh(0.121Re_p), f(Eo')\right] & if \ Eo' \leq 4 \\ f(Eo') & if \ 4 < Eo' \leq 10 \\ -0.27 & if \ Eo' \geq 10 \end{cases} \tag{50}$$

where

$$f(Eo') = 0.00105Eo'^3 - 0.0159Eo'^2 - 0.0204Eo' + 0.474 \tag{51}$$

where Eo' is defined as the modified Eötvös number and expressed as

$$Eo' = \frac{g(\rho_q - \rho_p)d_h^2}{\sigma} \tag{52}$$

where σ is the surface tension coefficient and its surface-dependent d_h is the long axis of the deformable bubble and is expressed as

$$d_h = d_b(1 + 0.163Eo^{0.757})^{1/3} \tag{53}$$

and

$$Eo = \frac{g(\rho_q - \rho_p)d_b^2}{\sigma}. \tag{54}$$

The wall lubrication force is expressed as

$$\vec{F}_{wl} = C_{wl}\rho_q\,\alpha_p \left|(\vec{v}_q - \vec{v}_p)\right|^2 \vec{n}_w \tag{55}$$

where C_{wl} is the wall lubrication coefficient, $\left|\vec{v}_q - \vec{v}_p\right|$ is the phase-relative velocity component tangential to the wall surface and $\vec{n}_w$ is the unit normal, pointing away from the wall. The Antal *et al.* model [77] can be used to model the wall lubrication coefficient and is expressed as

$$C_{wl} = \max\left(0, \frac{C_{w1}}{d_b} + \frac{C_{w2}}{y_w}\right) \tag{56}$$

where $C_{w1} = -0.01\ and\ C_{w2} = 0.05$, y_w is the distance to the nearest wall. The turbulent dispersion force can be modelled on the Lopez de Bertodano model [78] and is expressed as

$$\vec{F}_{td,q} = -\vec{F}_{td,p} = -C_{TD}\rho_q k_q \nabla\alpha_p \tag{57}$$

where k_q is the turbulent kinetic energy, $\nabla\alpha_p$ is the gradient of the dispersed phase volume fraction and C_{TD} is a constant, which is usually 1. The virtual mass force occurs when the vapour phase accelerates relative to the liquid phase due to the significant difference in density between the liquid and vapour phase, and the inertia of the liquid phase mass is encountered by the accelerating particles, exerting a force on the particles. This phenomenon is expressed as

$$\vec{F}_{vm} = C_{vm}\rho_q\,\alpha_p \left(\frac{d_q\vec{v}_q}{dt} - \frac{d_p\vec{v}_p}{dt}\right) \tag{58}$$

where C_{vm} is the virtual mass coefficient and is chosen to be the theoretical value of 0.5 for a spherical bubble in an infinite medium [42]. Turbulence interaction can be modelled on the Troshko-Hassam turbulence models [79], which accounts for the turbulence of the dispersed phase in the $k - \epsilon$ equations in equations (26) and (27). The interaction terms when using mixture turbulence models are

$$S_{k_m} = C_{ke}K_{pq}\left|\vec{v}_p - \vec{v}_q\right|^2 \tag{59}$$

and

$$S_{\varepsilon_m} = C_{td}\frac{1}{\tau_p}S_{k_m} \tag{60}$$

and the constants $C_{ke} = 0.75$ and $C_{td} = 0.45$. The characteristic time of the induced turbulence is expressed as

$$\tau_p = \frac{2C_{vm}d_p}{3C_D\left|\vec{v}_p - \vec{v}_q\right|} \tag{61}$$

3.5 Wall-boiling model

Subcooling boiling occurs when the wall temperature is high enough to cause the fluid to boil even though the bulk fluid has an average temperature lower than the saturated temperature. In cases like this, the wall transfers energy directly to the fluid, which causes the average fluid temperature to

increase and generate vapour. Interphase heat transfer also increases the average fluid temperature, but saturated vapour will condense. Energy may also be transferred directly from the wall to the vapour. The RPI boiling model is formulated on this premise. To the best of the author's knowledge, all numerical work done on boiling jet impingement used the RPI wall-boiling model (as stated in section 1.1). However, many researchers used the RPI wall-boiling model to model boiling flows such as pool boiling [80, 81], flow boiling [82-84], boiling in low pressure [85, 86], medium pressure [87-89], and high pressure [82] conditions.

Kurul and Podowski [90] established the RPI wall-boiling model, explaining that the total wall heat flux consists of three components and this model is expressed as

$$\dot{q}_W = \dot{q}_C + \dot{q}_Q + \dot{q}_E \tag{62}$$

Figure 35: RPI boiling model heat flux contributions [9]

where $\dot{q}_C$ relates to the convective heat flux, $\dot{q}_Q$ to the quenching heat flux and $\dot{q}_E$ to the evaporative heat flux, as depicted in Figure 35 [9]. Figure 35 shows that the convective heat flux component approximates the heat transfer due to single-phase forced convection, the evaporative heat flux component approximates heat transfer due to the formation of vapour in the microlayer where the wall temperature is higher than the saturation temperature of the fluids, the quenching heat flux component approximates the heat transfer according to the ability of the liquid to rewet the evaporating vapour. The convective heat flux is expressed as

$$\dot{q}_C = h_c(T_w - T_l)(1 - A_b) \tag{63}$$

where h_c is the single-phase convective heat transfer coefficient, T_w the wall temperature, T_l the liquid temperature and A_b the effective area of influence, which refers to the area occupied by bubbles across the nucleation site [9], whereas the portion of the wall covered by liquid is represented by $(1 - A_b)$. Quenching heat flux is expressed as

$$\dot{q}_Q = C_{wt}\frac{2\kappa_l(T_w - T_l)}{\sqrt{\pi\lambda_l T}} \tag{64}$$

where κ_l is the liquid thermal conductivity, λ_l the liquid diffusivity and T the periodic time, which is cyclic averaged, T_l the near-wall liquid temperature, and C_{wt} a Fluent-introduced correcting time between consecutive bubbles, which is chosen as 1. This process refers to the average heat transfer due to the instant periodic displacement of cold liquid after removing bubbles from the impinged surface [9]. The evaporative heat flux is expressed as

$$\dot{q}_E = V_d N_w \rho_v f h_{fv} \tag{65}$$

where V_d is the volume of the bubble at its departure diameter, N_w is the nucleation site density, which is greatly influenced by microscale surface roughness, ρ_v the vapour density, f the bubble departure frequency and h_{fv} the latent heat for vaporisation [9]. The effective area is expressed as

$$A_b = \min\left(1, K\frac{N_w \pi D_w^2}{4}\right) \tag{66}$$

where the effective area is restricted to an upper bound of 1 to avoid numerical instabilities due to unbound empirical correlations. D_w is the bubble departure diameter, and the empirical constant K is usually set to 4, however is has been found that this value may vary between 1.8 and 5. Thus the empirical constant is modified by Del valle and Kenning [91] and expressed as

$$K = 4.8 e^{(-0.0125 Ja_{sub})} \tag{67}$$

where the subcooled Jakob number, representing the ratio of sensible heat to latent heat absorbed during the phase change process, is expressed as

$$Ja_{sub} = \frac{\rho_l C_{pl} \Delta T_{sub}}{\rho_v h_{fg}} \tag{68}$$

The bubble departure frequency was calculated by Cole [92] through a photographic study for pool boiling of distilled water in the region just before the CHF. The Cole correlation is based on the inertia growth of the vapour bubble that does not occur in subcooled boiling. Yet, studies [38, 41] have shown that the Cole correlation produces accurate results for low degrees of subcooling. The Cole correlation is expressed as

$$f = \frac{1}{T} = \sqrt{\frac{4g(\rho_l - \rho_v)}{3\rho_l D_w}} \tag{69}$$

Nucleation site density, representing the number of nucleation sites per unit area of the heated wall and has a negligible effect on both the liquid temperature and the gas volume fraction but has a large impact on the wall superheat [93] and is expressed as a semi-empirical correlation that depends on wall superheat

$$N_w = C^n (T_w - T_{sat})^n \tag{70}$$

where Lemmert and Chawla [94] suggested empirical coefficients of

$$n = 1.805 \,\&\, C = 210 \tag{71}$$

The evaporation heat flux is highly dependent on the prediction of the bubble departure diameters. Unal [13] calculated the bubble departure diameter as

$$D_w = 2.42 \times 10^{-5} p^{0.709} \left(\frac{a}{b\sqrt{\varphi}} \right) \tag{72}$$

where

$$a = \frac{T_w - T_{sat}}{2\rho_v h_{fg}} \sqrt{\frac{\rho_s C_{ps} k_s}{\pi}} \tag{73}$$

$$b = \begin{cases} \dfrac{\Delta T_{sub}}{2\left(1 - \dfrac{\rho_v}{\rho_l}\right)} e^{\left(\frac{\Delta T_{sub}}{3} - 1\right)} & for \ \Delta T_{sub} \leq 3 \\[2em] \dfrac{\Delta T_{sub}}{2\left(1 - \dfrac{\rho_v}{\rho_l}\right)} & for \ \Delta T_{sub} \geq 3 \end{cases} \tag{74}$$

$$\varphi = max\left(\left(\frac{U_b}{U_o}\right)^{0.47}, 1.0 \right) \tag{75}$$

where U_b is the near-wall bulk velocity, $U_o = 0.61 m/s$, and subscripts $s, l, and \ v$ denote the solid material, liquid and vapour phase respectively. The key wall-boiling parameters, including bubble departure frequency (f), nucleation site density (N_w), and bubble departure diameter (D_w) have a significant impact on the boiling physics and local flow patterns and should be carefully identified [84]. The implementation of the Unal correlation considers local pressure, the amount of subcooling and wall superheat through considering a spherical or an ellipsoidal bubble growth on a very thin partially dried liquid film which is formed between the bubble and the heated surface as shown in Figure 36 [13]. Snyder [95] first postulated the formation of a thin liquid film between the bubble and the heating surface and has been later verified experimentally by Cooper and Lloyd [96], Cooper [97], and Torikai *et al.* [98]. The volume of a sphere of diameter D is equal to the instantaneous bubble volume and the dry area under the bubble is in the form of a circular shape which is verified experimentally by Torikai *et al.* [98].
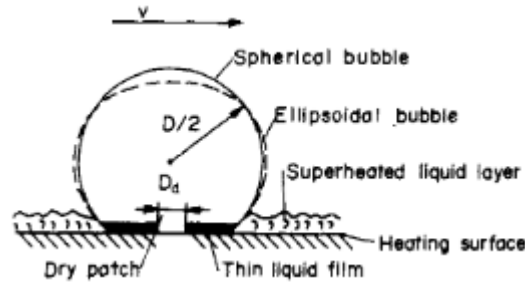
Figure 36: Bubble growth description [13]

As described in Section 2.3.3.1, the bubble takes up heat during the evaporation process of the very thin liquid film and dissipates heat to the surrounding liquid by condensation at the upper half of the bubble, as reported by Abdelmessih *et al.* [99]. All equations and models in this section had already

been implemented in Ansys Fluent, and the researcher assumed that all models were implemented correctly due to the quality assurance program of Ansys.

3.6 Solution method

A pressure-based solver was implemented with the phased-coupled SIMPLE scheme for pressure-velocity coupling. The Semi-Implicit Method for Pressure-Linked Equations (SIMPLE) algorithm is an iterative method that obtains an initial guess for the pressure field and solves the discretised momentum equations using the guessed pressure field. First, a correction term is added to the resulting face flux if it does not satisfy the continuity equation. Then, the corrected face flux is used to solve a pressure correction which, in turn, is used to correct the pressure field and face flux. Finally, all other discretised transport equations are solved from the resulting pressure and face flux: all variables are checked for convergence through comparison with the initial values. If one variable does not satisfy the convergence criteria, all final values are used as initial values to repeat the above iteration. An algebraic multigrid (AMG) solver enhances convergence and cuts computational costs. An AMG solver is particularly attractive for unstructured meshes as coarser-level equations are not generated through a change in geometry or rediscretisation.

Spatial discretisation was achieved through the first-order upwind method. However, the numerical discretisation error was increased in the case of complex flows where the flow crossed the mesh lines obliquely. More accurate results could be obtained through second-order discretisation, but first-order discretisation improved convergence and computational costs. The PREssure Staggering Option (PRESTO!) was used to determine the "staggered" pressures through the use of the discrete continuity balance for a "staggered" control volume. The least squares cell-based gradient evaluation was used for constructing values of a scalar at cell faces and computing secondary diffusion terms and velocity derivatives. The least squares cell-based averaging scheme is known to be as accurate as the node-based gradient method for unstructured meshes. However, it was less expensive to compute than with the node-based method. Warped-face gradient correction was implemented to improve gradient accuracy, especially in meshes with a significant difference in the volume of neighbouring cells. Finally, the first-order implicit formulation was used to achieve time discretisation. The implicit formulation was unconditionally stable and allowed for a much larger time step size than for the explicit formulation. Implicit formulations were used to solve the body forces and the volume fractions.

Due to a coarse mesh and a few poor cells in the pin-fin vicinity, a truncated virtual mass force value was used to enhance convergence. On the other hand, cells that experienced a high vapour velocity were prone to cause divergence. Therefore, an automatic mesh adaption scheme was formulated to refine cells with an abnormally high vapour velocity leading to better convergence in the targeted cells. In addition, a numerical noise filter was applied to the energy equation due to the fluctuations caused in heat transfer by the drastic change in fluid density and thermal properties at the wall in the phase-change process.

An additional detailed implementation of the poor mesh numerics, noise filters, stability enhancements, multigrid implementation and suggested under-relaxation factors are provided in Appendix C. All data presented in the following chapters are time-averaged values after a case reached a steady state and the total heat transfer rate into the fluid equalled the total heat transfer rate into the solid.

3.7 Numerical model conclusion

The above numerical model was implemented in Ansys Fluent without using additional UDFs. The Eulerian approach provided a high-quality framework to model multiphase flows at fixed points in space. The momentum equation included force source terms to account for bubble growth and phase interaction, while the energy conservation equations were calculated separately for each phase. The RNG k-ε mixture turbulence model accounted for dispersed phase-induced turbulence and the

difference between the production and dissipation thereof. Non-equilibrium near-wall treatment sensitised the log law for mean velocity to pressure gradients, increasing the accuracy of the numerical solution in complex flow separation and reattachment. Including interphase transfer models to approximate the interaction between the liquid and vapour phases was essential. The RPI boiling model computed the total heat flux as the summation of the evaporation, quenching and convection heat flux and predicted the heat transfer at the wall.

The robustness of the numerical model highly depended on the solution methods used. Using first-order methods increased numerical stability as well as automatic mesh adaption. Gradients were improved using the least squares cell-based averaging scheme and the warped-face gradient correction and energy noise filter dampened the fluctuations caused by heat transfer.

4 Computational Fluid Dynamics Model and Validation

4.1 Problem description

Extensive literature highlights the potential benefits of enhanced surfaces for two-phase cooling systems. Rau and Garimella [17] experimentally investigated the effect of structured surfaces in the form of pin-fins in boiling jet impingement using the dielectric working fluid HFE-7100. The heat transfer performance of a confined, single 3.75 mm diameter jet was compared on various surfaces, including a smooth flat surface, a smooth pin-fin surface and a hybrid combination of a flat surface with a microporous coating and a pin-fin surface with a microporous coating. Only the smooth flat and smooth pin-fin surface results were considered as validation cases in the current computational study. This chapter first explains the experimental set-up and the results of Rau and Garimella and details how their conditions were replicated in the CFD model. All the data handling code of this section is included in Appendix E: Data handling code. The current numerical model is tested for robustness, included in Appendix A, through the validation of the experimental work of Devahdhanush and Mudawar [22] on jet impingement boiling of a multi-jet array on a flat surface. The current model is also compared to the numerical work of Wright *et al.* [42] in Appendix A.

4.2 Experimental background [17] and test module

A closed-loop experimental facility was utilised to recirculate flow through the jet impingement test section [33]. The test section (shown in Figure 37) for confined and submerged jet impingement was assembled with polyether ether ketone (PEEK) and polycarbonate to mitigate heat loss and allow visual observation [33]. The heater assembly (shown in Figure 38) consists of a copper block and provides a 25.4 mm x 25.4 mm wetted surface area [17]. A 4 mm-thick PEEK capping plate is sealed around the copper block with four spring-loaded screws to finely adjust the level between the copper block and the capping plate. Twelve 25.4 mm long, 36 Ω cartridge heaters are embedded in the copper block to act as a uniformly distributed heat source. Four T-type sheathed thermocouples are placed inline at the centreline of the block, spaced 2.54 mm apart to measure the centreline temperature, allowing for the surface temperature's extrapolation. The measurement of the centreline temperature only allows the experiments to measure the temperature at the stagnation region, neglecting the surface temperature at
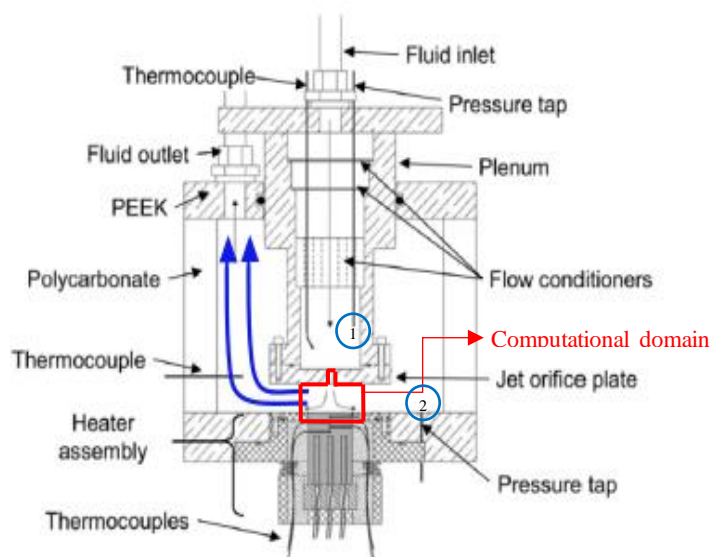
Figure 37: Rau and Garimella [17] cross-sectional view of the jet impingement test section

the outer regions of the domain. Thus, it is recommended that the average surface temperature is measured as in Devahdhanush and Mudawar [11].
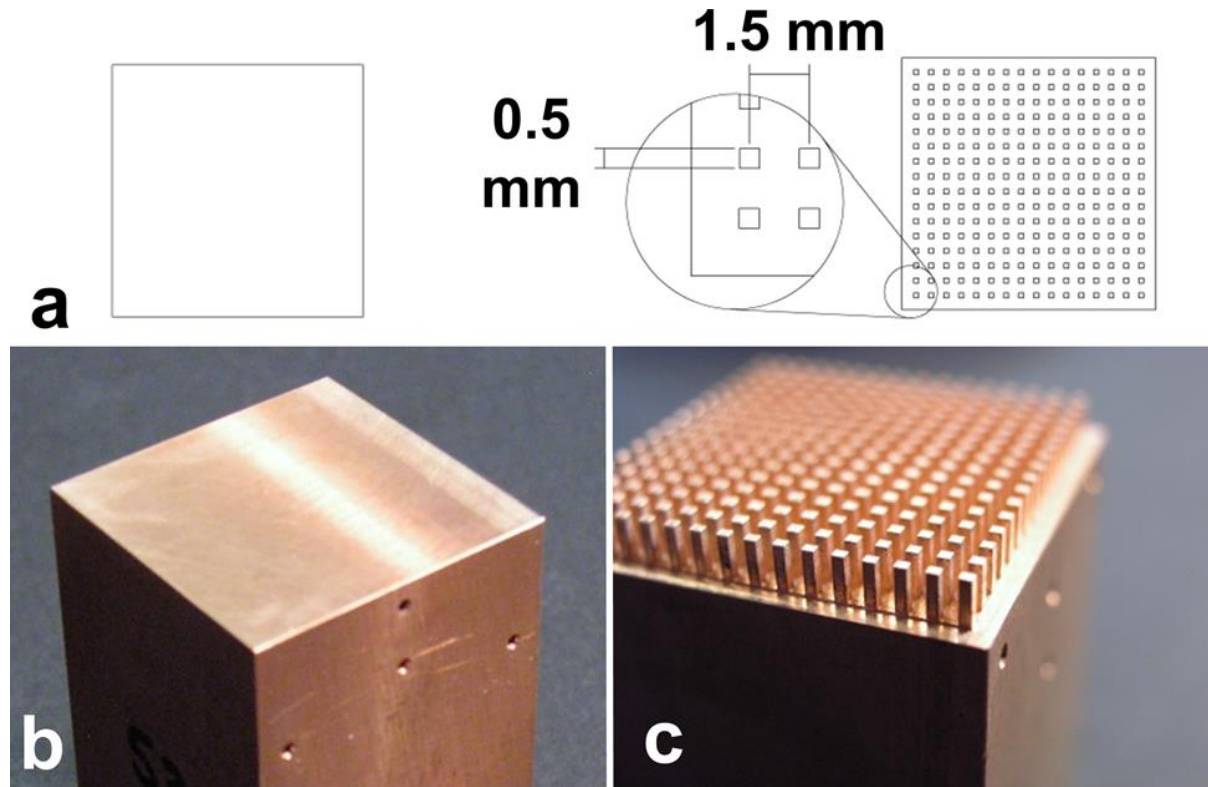
Figure 38: Rau and Garimella [17] (a) illustration of surface design parameters for (b) smooth flat surface and (c) smooth pin-fin surface

The blue arrows in Figure 37 indicate the flow path of the fluid from the computational domain towards the outlet. It was found that extending the domain radially had a negligible influence (1%) on the reported wall superheat at the stagnation point, and a no influence on the single-phase flow patterns in the region of interest and caused a limited modification of the vapour formation during heating. This results of this extended domain (shown in Appendix B) motivated the use of the chosen computational domain.

Table 1 shows all operating conditions for the flat and pin-fin surface test at a single flow rate. Three different flow rates (400, 900 and 1 800 ml/min) were used in the experimental investigation. However, the highest flow rate was chosen to ensure a fully turbulent flow and served as a validation case for the present study.

Table 1: Operating conditions of confined jet impingement with boiling on flat and pin-fin surfaces [17]

Parameter	Value
Jet diameter [mm]	3.75
Orifice thickness [mm]	7.5
Jet-to-target spacing [mm]	15
Jet flow rate [ml/min]	1800
Jet Reynolds number	38 900
Jet velocity [m/s]	2.716
Inlet temperature [℃]	51
Test section pressure [Pa]	101 345

The maximum uncertainty for all pressure transducers and thermocouples resulted in $\pm 0.13\,kPa$ and $\pm 0.3\,°C$ respectively [17]. Rau and Garimella [17] conducted a numerical heat loss analysis in Ansys Fluent to estimate the heat flux to the fluid using a 3D conduction model. With the known heat flux, the area-averaged heat flux was estimated through

$$q'' = \frac{P - q_{loss}}{A_b} \tag{76}$$

where P is the total electrical power dissipated by the cartridge heaters, q_{loss} is the estimated total heat loss, and A_b the surface area of the smooth flat copper block. A temperature gradient was calculated from the four in-line thermocouples embedded inside the copper block, which was used to extrapolate the surface temperature assuming one-dimensional conduction in the copper block. The one-dimensional Fourier conduction equation was used to extrapolate the surface temperature and expressed as

$$T_s = T_{tc} - \frac{q'' H_{tc}}{k_c} \tag{77}$$

where T_{tc} is the temperature of the thermocouple below the surface, H_{tc} the distance between the surface and the thermocouple, and κ_c the thermal conductivity of the copper block. The experimental surface temperature extrapolation resulted in an uncertainty of $\pm 0.4\,°C$ at low heat fluxes and $\pm 0.8\,°C$ at a heat flux of $88\,W/cm^2$ [17]. The jet inlet temperature was used to calculate the average heat transfer coefficient expressed as

$$HTC = \frac{q''}{(T_s - T_{in})} \tag{78}$$

where T_{in} is the jet inlet temperature. The determination of local heat fluxes was not possible due to the copper block heat source used.

Through a standard uncertainty analysis, including uncertainty contributions from the power dissipated from the cartridge heaters, extrapolated surface temperature and heat loss calculated in Ansys Fluent, Rau and Garimella [17] estimated experimental uncertainty in heat flux to be less than 2%.

4.3 Computational domain and boundary conditions

The present study aimed to estimate the boiling curve obtained by Rau and Garimella [17], along with the heat transfer characteristics and local boiling heat flux contributions. In addition, Wright *et al.* [42] and Qiu *et al.* [41] suggest that the numerical model set-up should include the effect of conjugation, because neglecting it may lead to inaccurate surface temperature predictions as the heat source would then be incorrectly assumed to be constant at the solid-fluid interface. Furthermore, the effect of conjugation also increased the contribution of the evaporative heat flux compared with the case without conjugation.
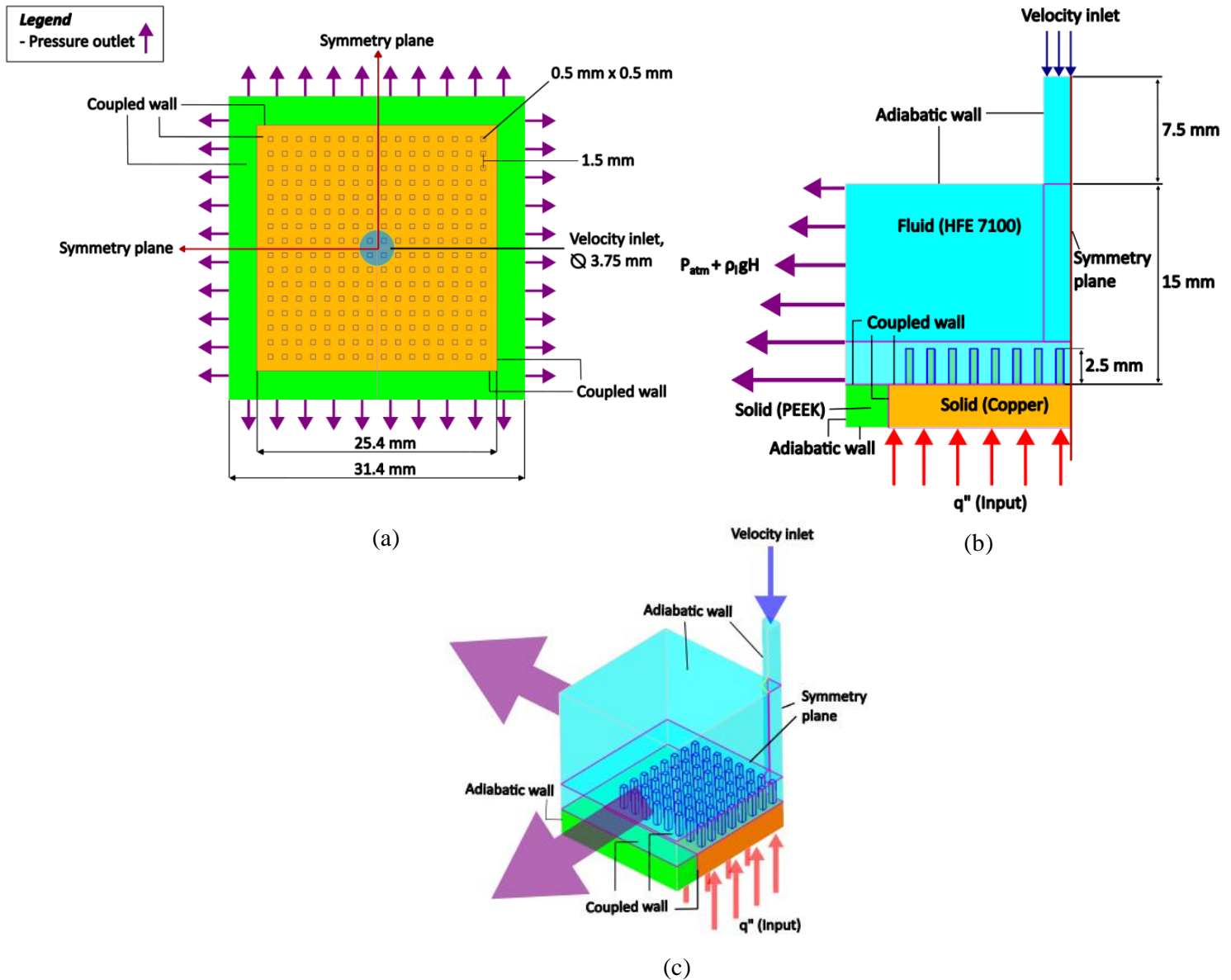
Figure 39: Computational domain of a single jet on pin-fins: (a) top view, (b) side view, and (c) isometric view, including the effects of conjugation

The Cole bubble departure frequency used in the present study was susceptible to the degree of subcooling. Wright *et al.* [42] found that an increase in the degree of subcooling from 5 °C *to* 9 °C led to an increase in wall superheat of approximately 5 °C when tested in the fully developed nucleate boiling regime for an R134a fluid. The current application used 10 °C of subcooling for HFE-7100, which could be at the limit of the applicability of the Cole model.

The experimental set-up presented in Figure 37 was used to construct a 3D computational domain. The sketching of the geometry was automated and can be found in Appendix D: Ansys SpaceClaim Script. Figure 39 shows the top view of the computational domain (Figure 39 (a)), neglecting the confined fluid from the sketch and the side view (Figure 39 (b)), including all boundary conditions and dimensions. Only a quarter of the domain was modelled (isometric view included in Figure 39) because a symmetry plane could be drawn to divide the domain into four symmetrical quarters. As a result, a quarter model obtained the same level of accuracy while decreasing the computational costs under the assumption that the vapour formation and flow patterns were also symmetric. A velocity inlet was defined at the top of the orifice plate, normal to the longitudinal axis of the opening in the orifice plate. In the present study, liquid entered the domain at 2.716 m/s at a pressure of 101,325 Pa and a

temperature of 51 ℃. The internal and bottom boundaries of the orifice plate were defined as an adiabatic wall. Coupled walls were defined between the adjoining copper block, insulation and fluid. The outside walls of the insulation were also defined as adiabatic walls. Wright *et al.* [42] highlighted the importance of including a hydrostatic pressure gradient to the pressure outlet to account for the added hydrostatic pressure during the evaporation process, as depicted in Figure 39 (b). Finally, a uniform heat flux was applied at the bottom of the copper block, with PEEK surrounding the copper block to act as perfect insulation.

Constant solid material thermal properties were used for the copper block and the PEEK insulation (see Table 2). Table 3 shows the fluid properties of the working fluid HFE-7100. The liquid properties were constant at 51 ℃ and 1 atm, and the vapour properties were constant as a saturated vapour at 61 ℃ and 1 atm. All fluid properties were gained through multiple sources, including [100], [66] and [17].

Table 2: Solid material properties at 25 ℃

Property	Copper [71]	PEEK [71]
Density [kg/m^3]	8 978	1 310
Specific heat [$J/(kg\,K)$]	381	1 340
Thermal conductivity [$W/(m\,K)$]	387.6	0.2498

Table 3: Fluid properties

Fluid	HFE-7100		
Saturation pressure [Pa]	101 325		
Saturation temperature [℃]	61		
Surface tension [N/mm]	11.1027		
	Liquid		Vapour
Temperature [℃]	25	51	61
Density [kg/m^3]	1 481	1 444.34	9.12008
Specific heat [$J/(kg\,K)$]	1 183	1 141.86	938.43
Thermal conductivity [$W/(m\,K)$]	0.069	0.0899557	0.0140958
Viscosity [$kg/(m\,s)$]	5.63e-04	0.00041954	1.1409e-05
Molecular weight [$kg/kmol$]	250.064		
Latent heat [kJ/kg]	111.7		

Table 4: Inlet and outlet conditions of a quarter symmetry domain based on an experiment done by Rau and Garimella [17]

Inlet boundary conditions	
Phase	Liquid
Temperature [℃]	51
Turbulence intensity [%]	5
Outlet boundary conditions	

Backflow phase	Mixture
Backflow turbulence intensity [%]	5
Backflow vapour fraction	From neighbouring cell

Table 4 shows the inlet and outlet conditions of the 3D quarter symmetry domain. Turbulence intensity is left as a Fluent default of 5%. The inlet profile of the jet was assumed to be uniform. Section 4.5.3.1 provides an investigation into including the plenum upstream of the orifice plate to assess the orifice plate pressure drop and test the sensitivity of the uniform flow assumption. Outlet backflow conditions were set to allow for liquid and vapour to recirculate from neighbouring cells.

4.4 Mesh independence study

Figure 39 (b) shows the domain division to allow for a higher-quality mesh. The constant mesh size was enforced in the jet and fin regions, while the mesh grew with a maximum of 20% in the bulk fluid region. The mesh study aimed to decrease the mesh density between the fins with a minimum allowable refinement of five cells between fins. Polyhedral and hexahedral cells were used to compare mesh types at the same mesh density. In addition, automatic mesh adaption was enabled to allow for automatic mesh refinement in possible unstable cells. Possible unstable cells were identified as cells with unrealistic high vapour velocities. For the mesh independence study, all computations were done at a uniform heat flux input of 23.24 W/cm^2 and a fixed time step of 0.0001 seconds. The maximum CFL number was kept under 5 for all cases as Ansys Fluent is able to sustain CFL numbers larger than 1 [101]. It is also important to note that the implicit method used in the current transient simulation is unconditionally stable [72]. All the data handling code of this section is provided in Appendix E: Mesh independence study.

Various factors contributed to the mesh density study, including cell and node density (see Table 5), stagnation region temperature, area-weighted average base wall temperature (see Table 6), dry-out area percentage on the base wall, and nucleation boiling area percentage on the base wall (see Table 7). The stagnation region temperature was calculated through an area-weighted average of 10% of the jet diameter centred on the longitudinal axis of the jet inlet. The dry-out and fully developed nucleation boiling area percentages were defined as the portion of the base surface area between the fins, excluding the fin tops, experiencing an evaporative heat flux contribution above 95% and between 50% and 95% respectively of the total heat flux.

Table 6 shows the simulation error of the stagnation temperature in brackets calculated from

$$Simulation\ error = \left| \frac{T_{experiment} - T_{simuation}}{T_{experiment}} \right| \times 100 \qquad (79)$$

where $T_{experiment}$ is equal to 8.56 ℃.

Table 5: Mesh independence study cell and node density comparison

# Cells between fins	Cell density [$cells/mm^3$]	Node density [$nodes/mm^3$]
	Polyhedral	
8	866.04	4840.13
7	556.93	3107.89

5	210.13	1124.45
	Hexahedral	
8	395.34	417.89
7	246.94	263.23
5	111.54	120.71

Table 6: Mesh independence study stagnation and average flat wall superheat comparison

# Cells between fins	Stagnation region superheat [℃]	Average flat wall superheat [℃]
	Polyhedral	
8	9.86 [9.95 %]	10.9
7	10.02 [11.78 %]	10.5
5	10.30 [14.96 %]	10.7
	Hexahedral	
8	9.82 [9.53 %]	10.55
7	9.85 [9.88 %]	10.58
5	10.02 [11.78 %]	10.72

Table 7: Mesh independence study dry-out and nucleation boiling area contribution

# Cells between fins	Dry-out area [%]	Nucleation boiling area [%]
	Polyhedral	
8	18.38	29.60
7	16.30	31.25
5	14.25	33.46
	Hexahedral	
8	20.13	36.25
7	19.93	36.46
5	15.51	39.21

As expected, a noticeably lower cell and mesh density was gained with hexahedral cells than with polyhedral cells, leading to a significantly lower computational cost if hexahedral cells were used. The stagnation temperature decreased with increased mesh density for both mesh types. The decrease in stagnation temperature could be due to better-resolved turbulent flow in the pin-fin vicinity, increasing mixing. The height of the first cell could also lead to variable wall temperatures. y^+ gave a reasonable estimate of the needed first boundary layer height, but due to the complexity of the flow and mesh in the pin-fin vicinity, y^+ was no longer a helpful tool. Figure 40 depicts the difference between the polyhedral and hexahedral meshes at an average of eight cells between fins.

(a)   (b)
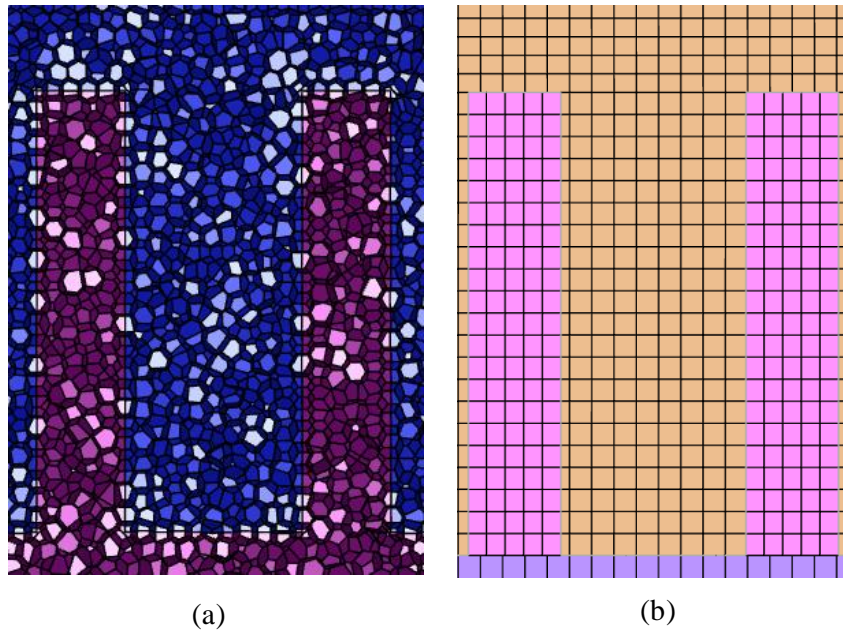
Figure 40: Mesh type between fins using eight cells: (a) polyhedral mesh and (b) hexahedral mesh

Figure 41 compares the predicted stagnation temperatures between polyhedral and hexahedral mesh types at the selected cell densities tabulated in Table 6. A mesh refinement led to both types converging into the same stagnation temperature. Both hexahedral and polyhedral fine meshes produced accurate results with an error of 9.53% to 9.95% when considering the upper limit of the experimental stagnation superheat uncertainty. Thus, the following investigation only considered the fine mesh cases of 8 cells between the fins as 10 cells between the fins is to computational expensive for the small gain in accuracy.
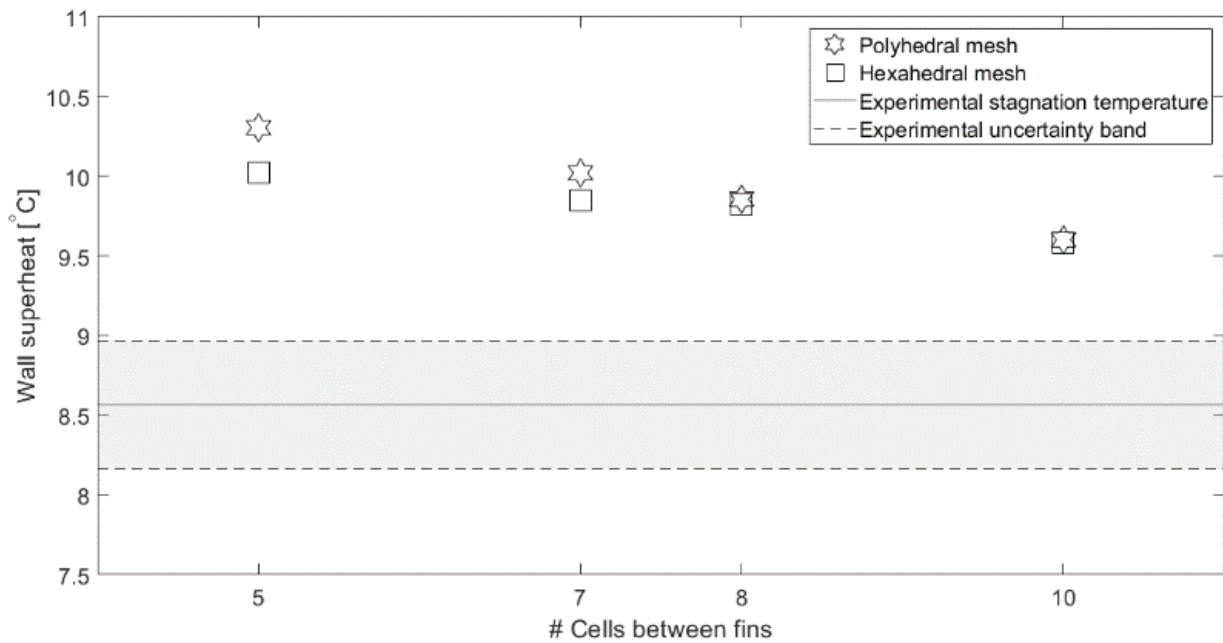
Figure 41: Mesh independence study: stagnation wall superheat comparison

Plots of both the dry-out area contribution and fully developed nucleate boiling area contribution led to cyclic behaviour over time (see Figure 43 and Figure 44). The cyclic behaviour was due to the formation and coalescence of vapour columns at the outer regions of the domain, followed by the ability of the liquid to rewet the surface. Rau and Garimella visualised the cyclic process in their experiment, illustrated in Figure 42, for their porous-coated pin-fin surface [17].

Dry-out between fins

Liquid starting to rewet surface

Large vapour bubbles departing and replaced by liquid
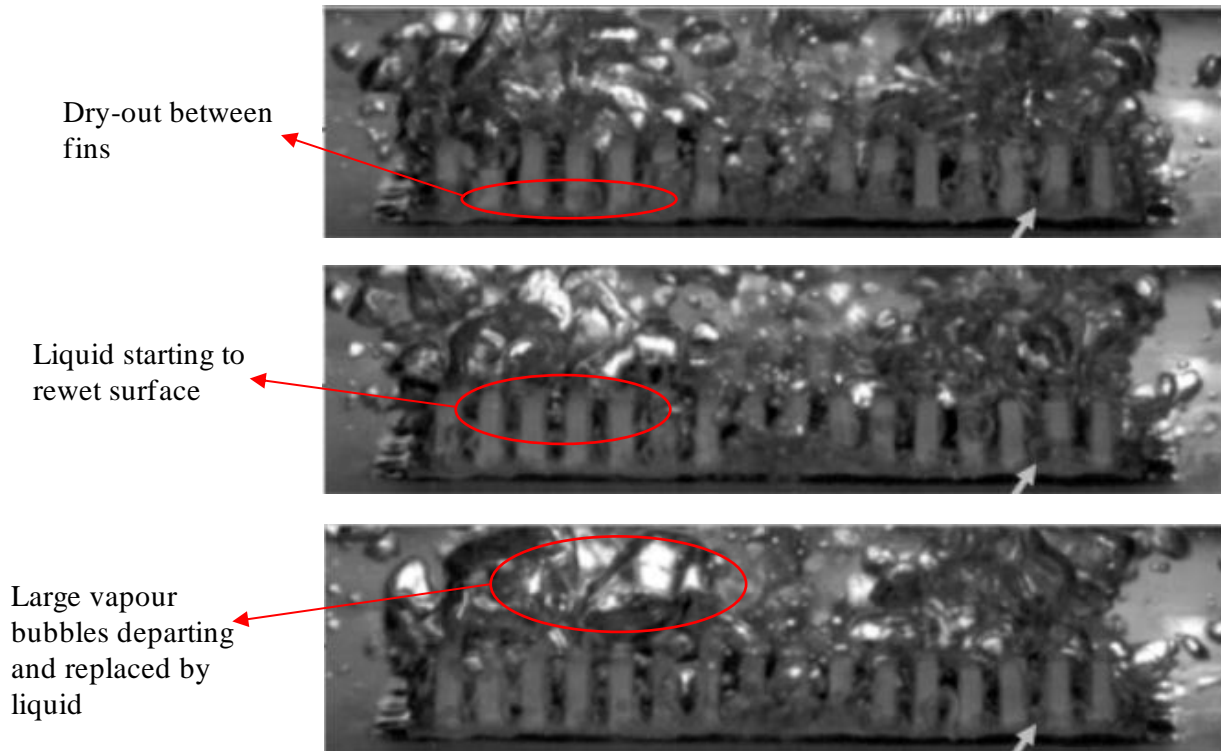
Figure 42: Bubble formation and coalescence and surface rewetting, adapted from [17]

Figure 43 and Figure 44 show the evaporation and nucleate boiling regions of the CFD models indicating the respective boiling contribution on the base surface at the peak, average, and minimum with the dry-out area contribution (red) and nucleate boiling contribution (purple). The horizontal dashed lines in Figure 43 and Figure 44 represent the respective average values gained from each graph (see Table 7). A coupled behaviour of the dry-out and nucleate boiling area contributions was found because the decrease in the dry-out area contribution increased the nucleation boiling area contribution and contrariwise. The difference between the polyhedral and hexahedral results was negligible in the dry-out area contribution. On the other hand, results showed a more significant difference in the nucleate boiling area contribution, where the hexahedral cells predicted a 6.65% higher average nucleate boiling contribution (see Figure 44).

Similar results were gained for both fine polyhedral and fine hexahedral cases. Hexahedral cells are the preferred meshing method due to the reduction in computational costs. However, in this study, all further parametric investigations were done with a polyhedral mesh due to the delayed release of a Fluent with meshing tool that could mesh complex geometries with hexahedral cells.
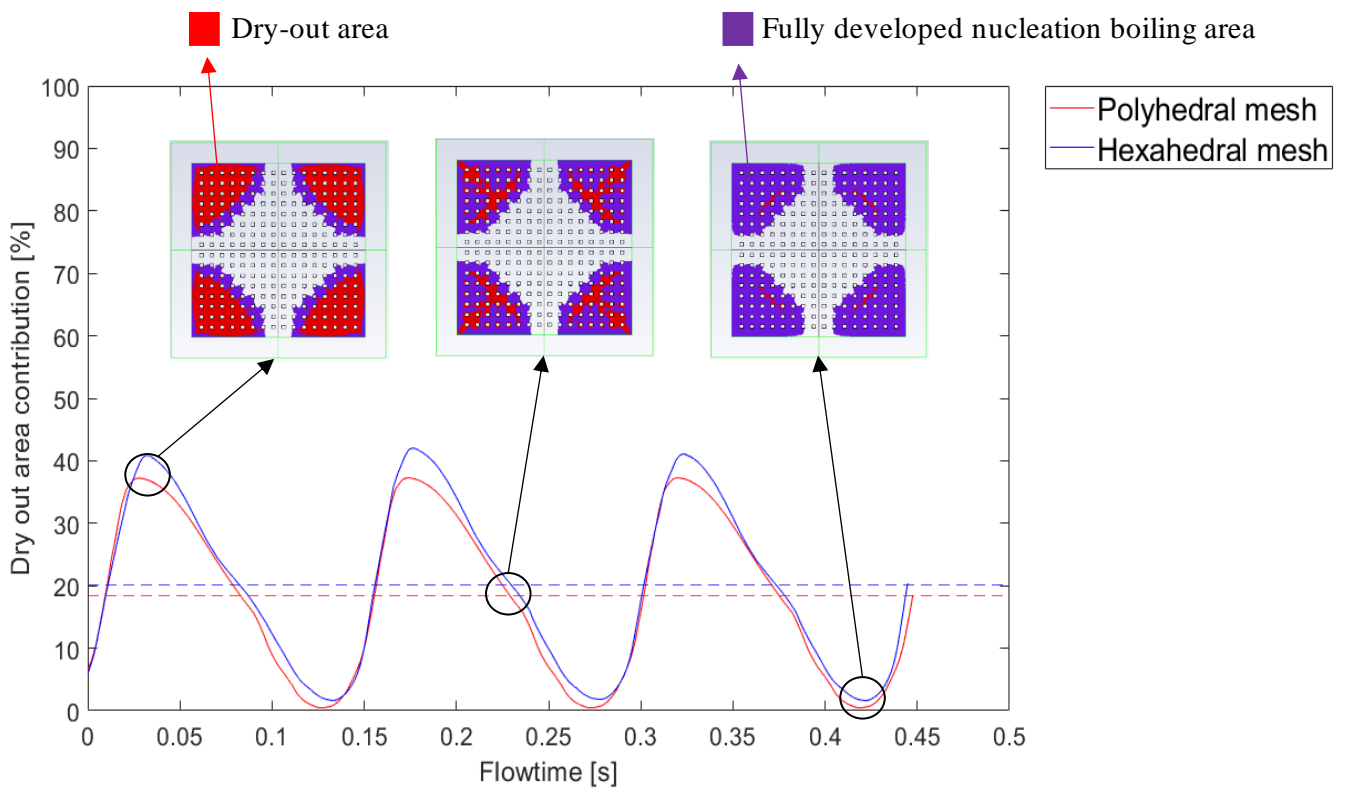
Figure 43: Mesh independence study: dry-out area contribution comparison at eight cells between fins
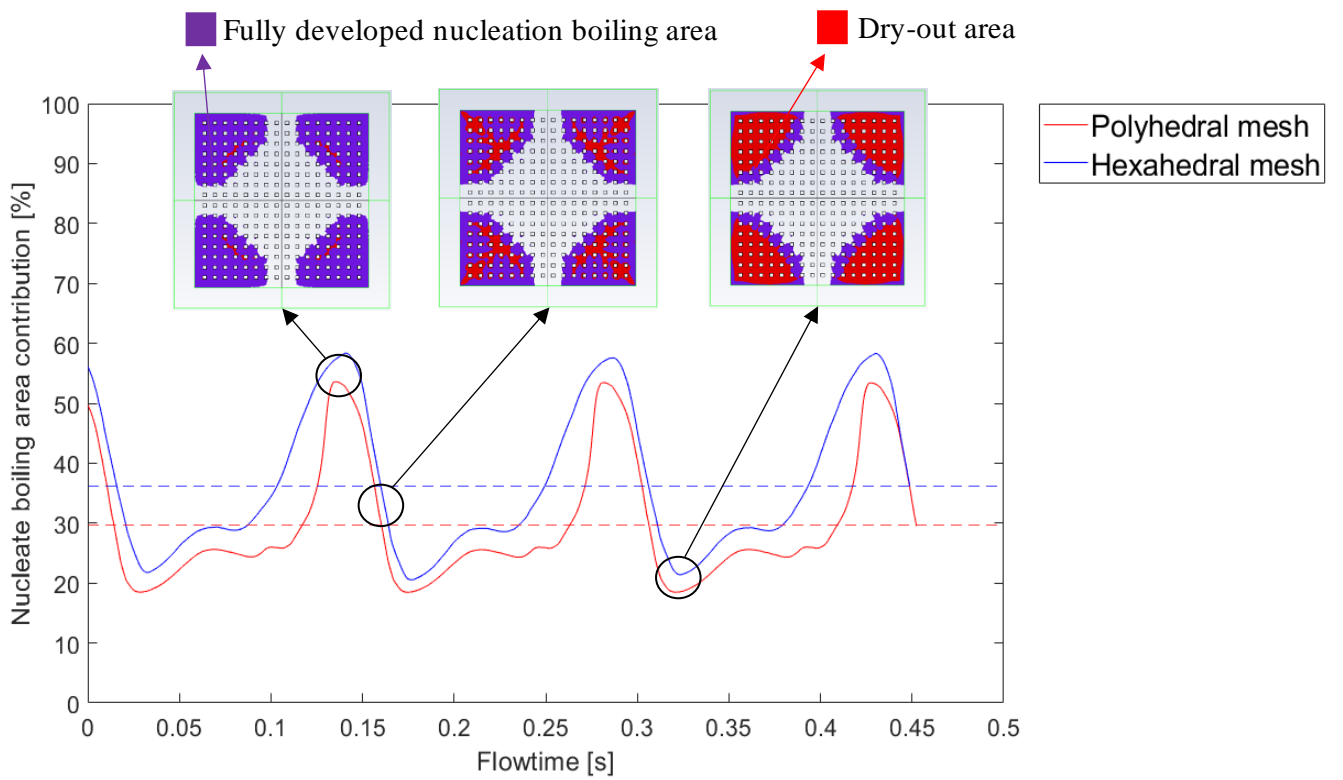
Figure 44: Mesh independence study: nucleate boiling area contribution comparison at eight cells between fins

Figure 45 shows frame by frame the cyclic behaviour of the vapour distribution in the domain depicted in Figure 43 and Figure 44, and Figure 42. The vapour distribution (red) illustrates the vapour fraction in cells above 0.5, and the liquid distribution represents the liquid velocity distribution in the domain above 3 m/s. The initial frame (a) shows the dry-out area before reaching the peak, as shown in Figure 43, with the vapour film distributed over the entire corner of the domain. Frame (b) shows the peak of the dry-out area being reached, whereafter the vapour column started to detach from the surface, shown in Frames (c-d), indicated as the intermediate area contribution in Figure 43 and Figure 44. Frame (e) represents the peak of the fully developed nucleation boiling area contribution, whereas the dry-out area contribution increased, shown in Frame (f) to (i). Finally, the vapour column separated and condensed, shown in Frames (e) to (i), from which frame (a) commences. The cyclic behaviour of the vapour column was linked to the experimental results gained, shown in Figure 42. The Eulerian multiphase model has limitations on vapour bubble tracking. Thus, the vapour is represented as one large vapour column. If a more detailed representation of vapour bubbles is required, the volume of fluid method, which tracks the vapour-free surface, has to be considered.
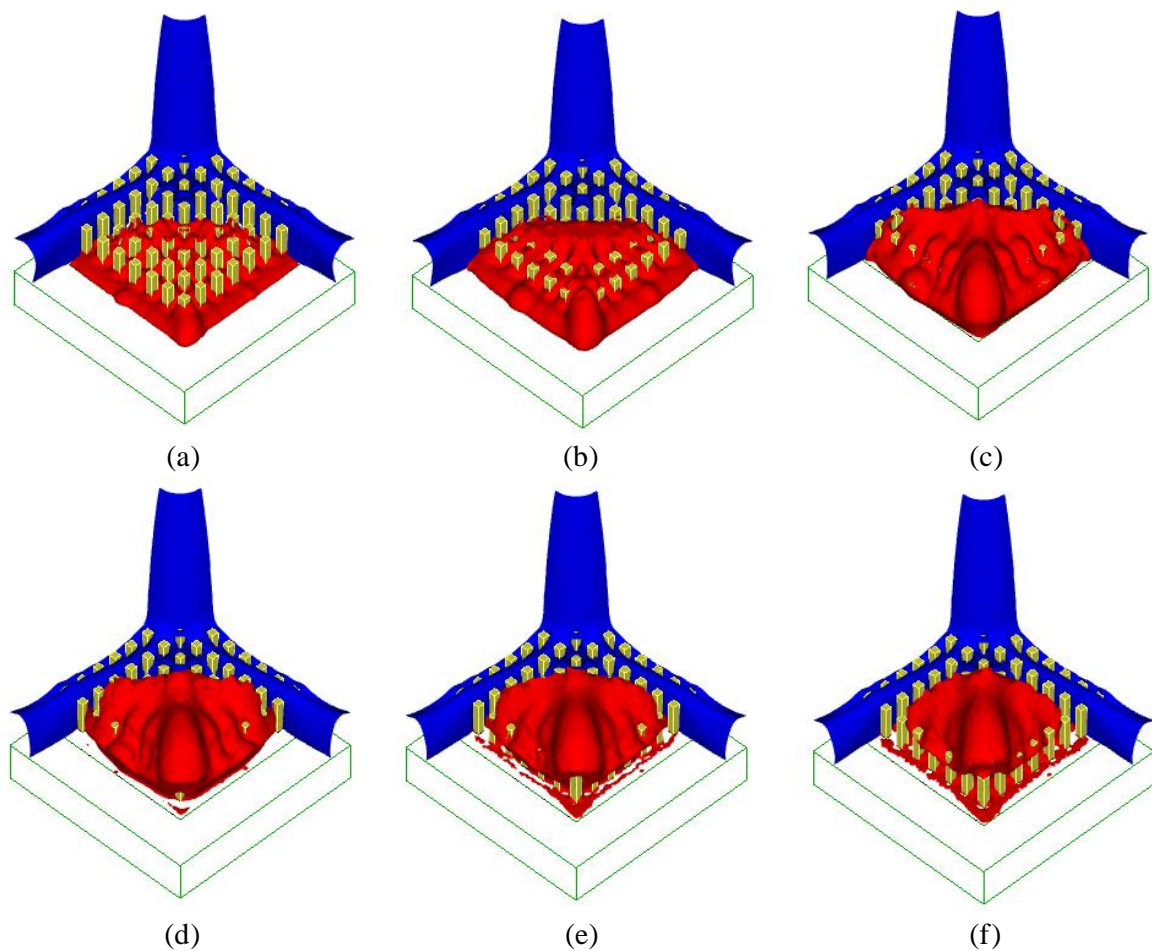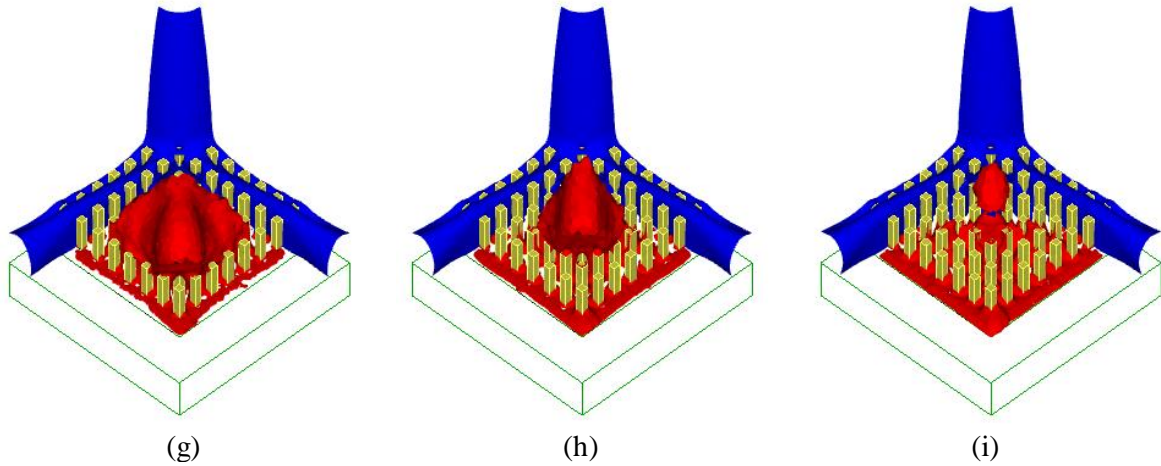
(a)   (b)   (c)

(d)   (e)   (f)

4.5 Results and discussion

4.5.1 Boiling curve

Figure 46 depicts the predicted boiling curve of Rau and Garimella for a confined single jet impinging on a uniform pin-fin layout, plotted with the current numerical results for comparison. Horizontal and vertical uncertainty bars depict the experimental uncertainty of the wall superheat and the heat flux respectively. The simulation error at each point was less than 12% for the four heat fluxes considered, including experimental uncertainty. The heat transfer throughout the boiling curve was underpredicted because each simulated result predicted a higher wall superheat than the experimental results did. Underprediction of heat transfer is preferred because an overprediction of heat transfer will lead to lower simulated wall superheats and may be detrimental to the surface as the actual wall superheat may be higher than the predicted wall superheat. All the data handling code of this section is provided in Appendix E: Boiling curve.

Narumanchi *et al.* [38] reported that errors of up to 30% were acceptable for jet impingement boiling. Wright *et al.* [42] reported slightly smaller errors of up to 21% for a multi-jet array with an overprediction of the onset of nucleate boiling departure. The overprediction was attributed to the fact that the standard RPI boiling model was only applicable to the fully developed nucleate-boiling regime and that the Cole bubble departure frequency model was not applicable to highly subcooled boiling (9 °C in that study).

The RNG k-ϵ model showed substantial improvements over the standard k-ϵ models used by previous researchers for jet boiling, shown by Wright *et al. [42],* where the RNG theory provided an analytically derived differential formula for effective viscosity that accounted for low Reynolds number effects [71]. Therefore, the slight deviation from experimental results could be attributed to the ability of the RNG k-ϵ model to capture the complex multiphase flow patterns throughout the domain. The small deviation could also be attributed to the ability of the non-equilibrium near-wall treatment in conjunction with a fine mesh to resolve the constant production and dissipation of turbulence between the fins subject to severe pressure gradients.

The use of constant liquid properties also affected the predicted wall superheat. Due to the high degree of subcooling, the author believes that using non-constant properties would have increased the simulation error because liquid properties at a temperature higher than 51 ℃ would decrease the heat transfer ability of the liquid.

Figure 46 represents the stagnation wall temperature (also measured in the experiment) and does not include the detrimental effects of local dry-out throughout the domain, as discussed in Section 4.4. Although the stagnation region followed the linear top portion of the boiling curve, the maximum wall temperature started to dive off, representing the critical heat flux in the dry-out regions.
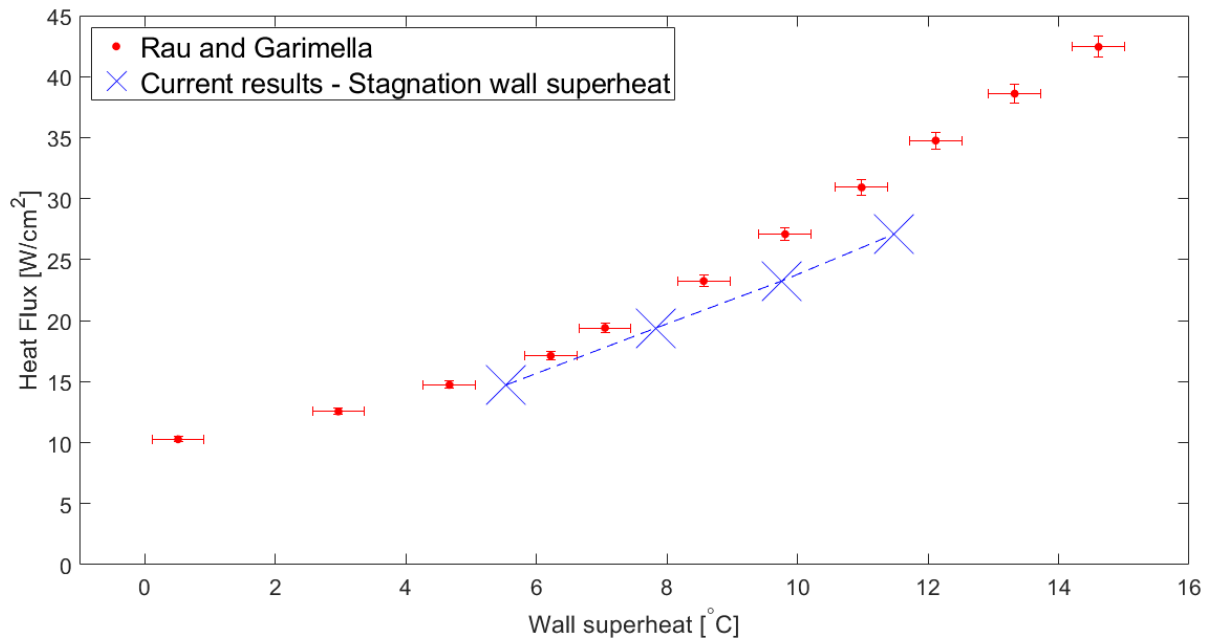
Figure 46: Boiling curve validation of a single jet numerical model of Rau and Garimella [17] on a uniform pin-fin layout using stagnation wall superheat

The current numerical model was limited with convergence instabilities occurring if the maximum vapour contribution or maximum evaporation heat flux contribution in any cell in the domain increased over 99.9%. Therefore, the maximum possible heat flux at which the current numerical model had stability was $27\ W/cm^2$ and this point was used as the highest validating point on the boiling curve.

4.5.2 Validation with flow time

Figure 47 depicts the total heat rate extracted by the fluid compared with the total heat rate applied to the solid (left axis) and the total heat flux applied to the solid (right axis). The liquid velocity distribution was allowed to develop fully throughout the domain and reach a steady state before the initial heat flux was applied to the solid. As shown by the dashed red line in Figure 47, each heat flux was allowed to reach steady state initially through a ten-second time window, whereas, afterwards, the window was reduced as a steady state was reached in a shorter time window. The first heat flux did not reach a steady state and was not used in comparing the results. Therefore, the initial heat flux required a larger time window to reach a steady state. As the second heat flux reached a steady state, the following heat flux was applied because the total heat rate at the first and second heat flux plateaued without any noise. As the heat flux increased, the initial gradient of the total heat rate into the liquid increased along with the numerical noise. The boiling model was already active at an input heat flux of $14.7\ W/cm^2$. However, a steady state was reached without significant oscillations in the total heat rate into the fluid. Oscillations in the total heat rate into the fluid arose at higher heat fluxes. Oscillations could be attributed to the drastic production and dissipation of turbulence in the near-wall regions, affecting the heat transfer ability of the fluid. All the data handling code of this section is provided in Appendix E: Validation with flow time.
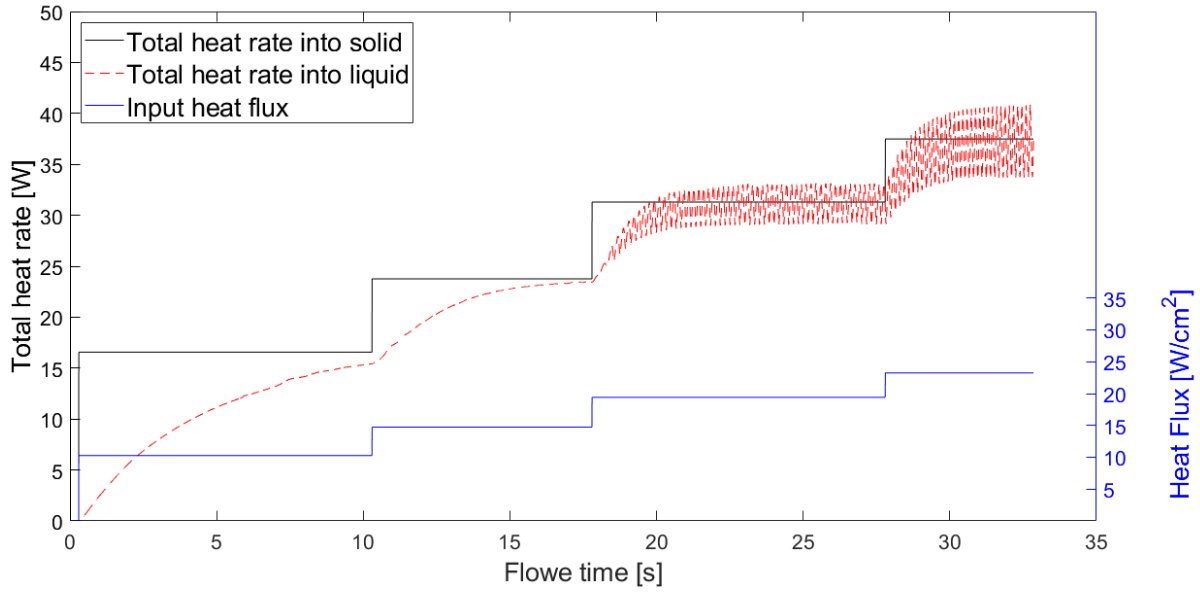
Figure 47: Total heat rate into the solid compared with the total heat rate into the fluid over time

Figure 48 depicts the stagnation, average and maximum wall superheat on the flat surface between the fins. The results show a similar trend to the total heat output graph, with an initial sharp increase in temperature followed by a steady increase towards a steady state. A slight jump in the wall superheat is shown at the point where the boiling model activated with a maximum wall superheat of approximately 1 °C. Slight numerical noise resulted in higher heat fluxes but is insignificant compared with those shown in Figure 47.

Figure 49 and Figure 50 show the evaporation area contributions on the base wall between the fins over time. The surface only reached local dry-out at a heat flux of 19.4 W/cm^2, whereas the fully developed nucleate boiling contribution was activated at a heat flux of 14.4 W/cm^2 and resulted in a noisy contribution reaching a steady state. The cyclic behaviour discussed in Section 4.4 initiated at a heat flux of 19.4 W/cm^2. The cyclic pattern of the dry-out area contribution (see Figure 49) remained constant over time, while the amplitude increased and the local minimum increased above zero at the highest heat flux. The cyclic pattern of the fully developed nucleation boiling area contribution (see Figure 50) changed over time, with a small second local minimum forming at a heat flux of 19.4 W/cm^2, becoming more prominent at 23.24 W/cm^2 and dissipating at 27 W/cm^2. The zoomed snippet also shows why the nucleation boiling area contribution average did not shift between a heat flux of 19.4 W/cm^2 and 23.24 W/cm^2: the cyclic plot had two local minimums and only one local maximum, even though the local maximum was higher at 23.24 W/cm^2 than at 19.4 W/cm^2.
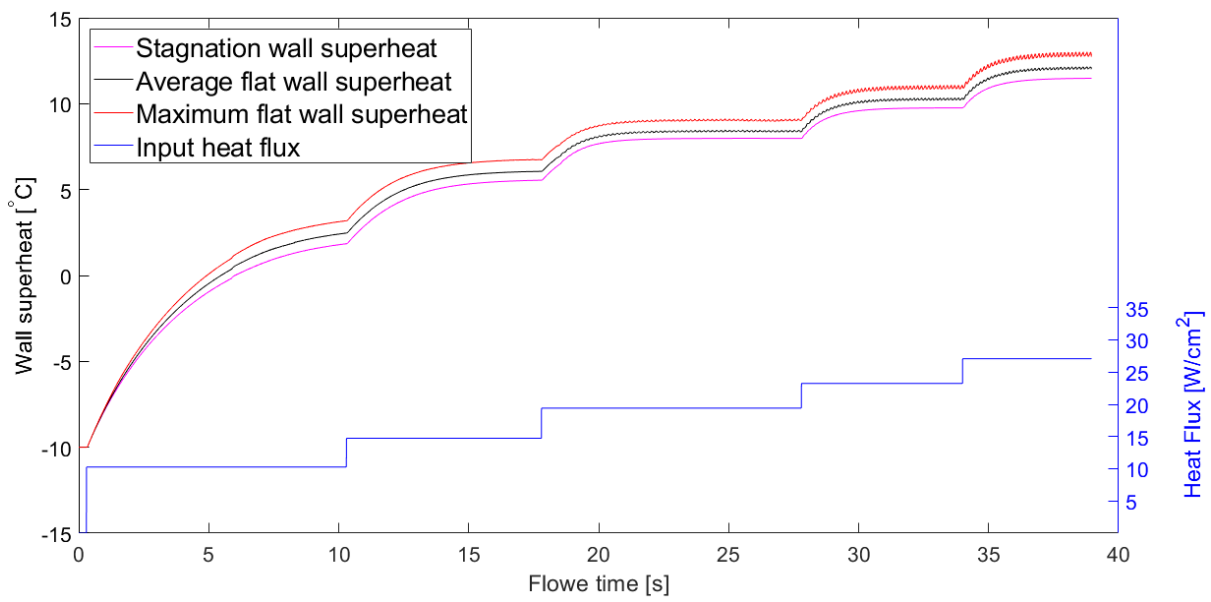
Figure 48: Stagnation, average and maximum wall superheat over time
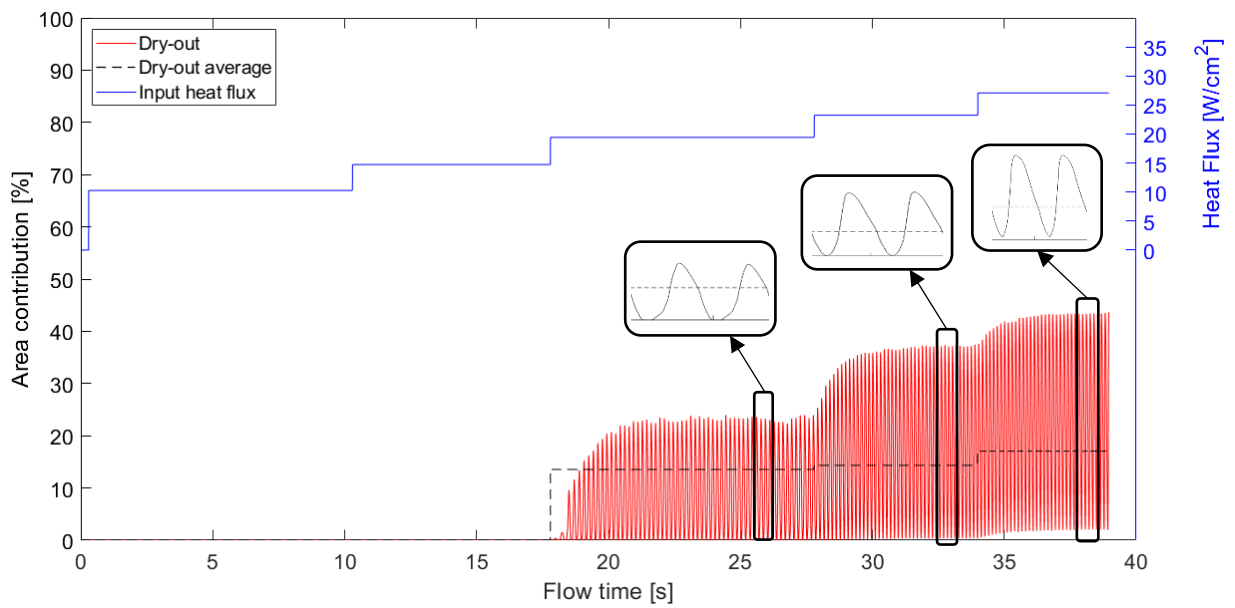
Figure 49: Dry-out area contributions over time
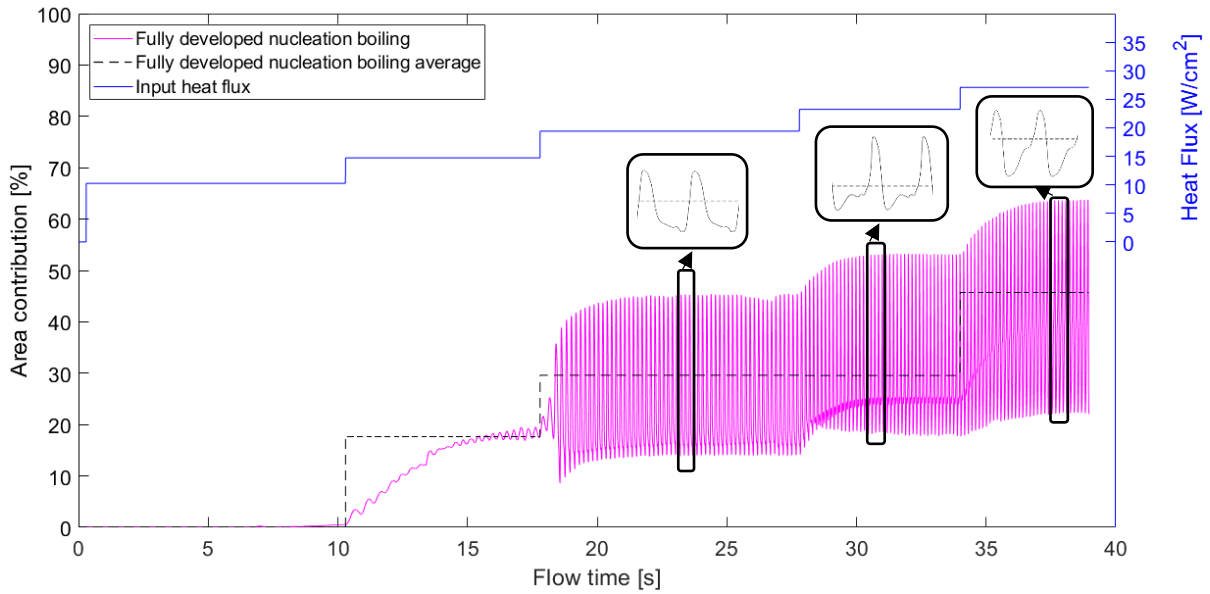
Figure 50: Fully developed nucleation boiling area contributions over time

Figure 51 depicts the change in the cell density in the pin-fin vicinity over time as a result of the automatic mesh refinement. The cell density slightly increased after the ONB, but as the input heat flux increased, a sharp increase was found in the cell density. The automatic mesh adaption tool aimed to refine all the poor quality cells between the pin-fins created by the automatic meshing tool. Figure 51 indicates that all bad cells were refined to finer, higher-quality cells, and the cell density remained constant throughout the subsequent heat fluxes. The mesh adaption tool only changed the cell density from 867 $cells/mm^3$ to 877 $cells/mm^3$, with the conclusion that the automatic mesh adaption tool did not have a significant impact on the total cell count in the domain.
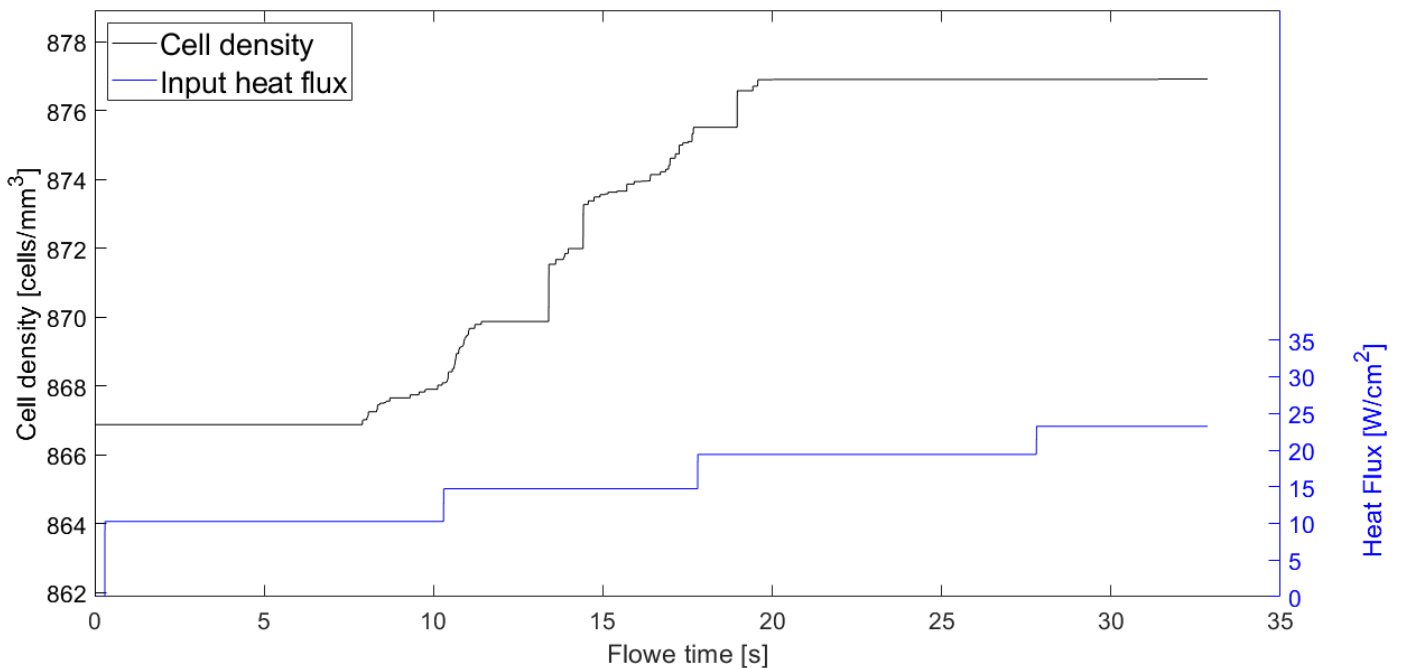
Figure 51: Cell density over time due to automatic mesh refinement

4.5.3 Properties variation with heat flux

4.5.3.1 Pressure drop

Figure 52 depicts the pressure drop across the domain. Rau and Garimella [17] found that the pressure drop remained constant throughout the boiling curve for a specific flow rate. The current study measured the pressure drop as the difference between the area-weighted average pressure at the inlet and the outlet of the computational domain. The results from the current study differed by 30% from the pressure drop Rau and Garimella reported when not considering the orifice plate. Therefore, a further investigation consisting of a larger computational domain, which included the plenum upstream of the orifice plate, and imitating the locations of the pressure probes in the experiment (shown in Figure 37), yielded a much more accurate pressure drop with an error of less than 1% for both the single-phase and 23.2 W/cm^2 conditions (labelled as Extended domain in Figure 52). The volumetric flow rate of the liquid (1 800 ml/min) was kept constant between the two studies. All the data handling code of this section is provided in Appendix E: Pressure drop study.
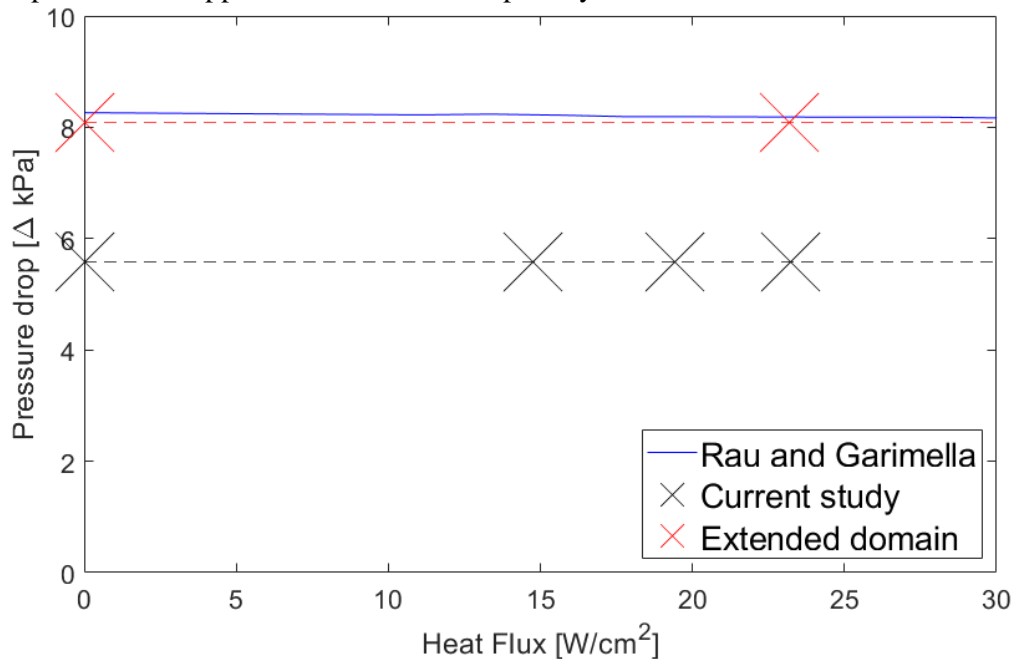
Figure 52: Pressure drop vs input heat flux

Figure 53 (a) depicts the single-phase velocity contours of the extended domain and the current study. The maximum velocity shown in Figure 53 (a) was higher than in Figure 53 (b), impinging on the surface at a higher velocity and resulting in a higher velocity in the flow-boiling regions. The change in the maximum velocity in the extended domain resulted from the bulk liquid forcing the liquid through the hole in the orifice plate, creating a separation region near the circumference of the hole.

The previous results considered a uniform velocity inlet. Figure 54 depicts the pressure contours between the two cases (with and without plenum). The extended domain resulted in a higher jet and stagnation pressure due to the upstream pressure of the extended domain. Less than 1% difference in stagnation wall superheat was obtained by the two studies at a heat flux of 23.24 W/cm^2, implying that while the addition of the extended domain did not make a significant impact on the wall superheat, it did capture the experimental pressure drop accurately.
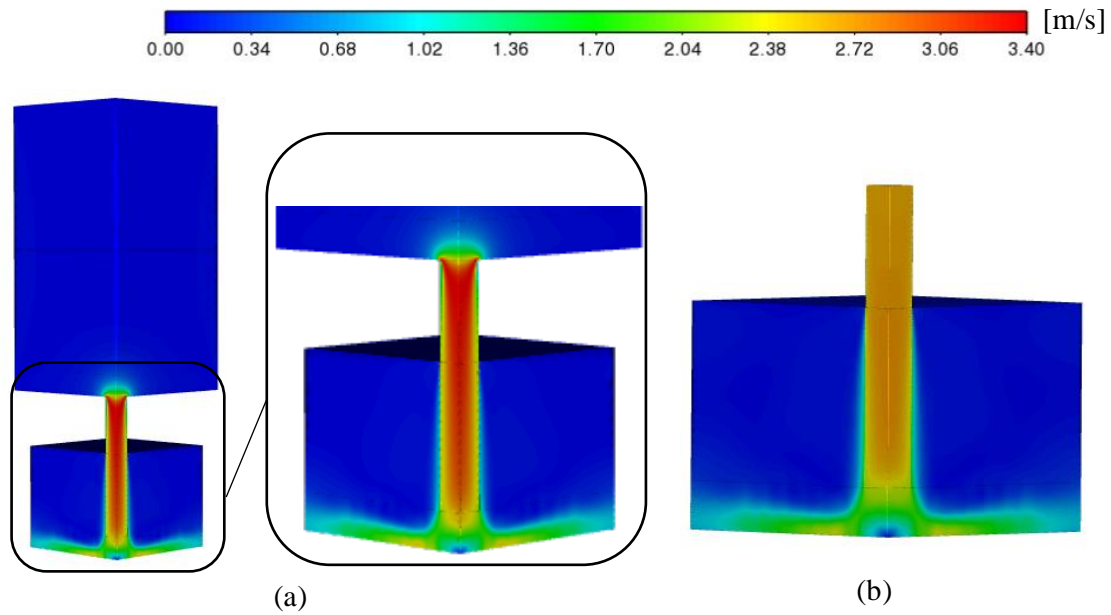
Figure 53: Velocity contours of (a) extended domain and (b) current study
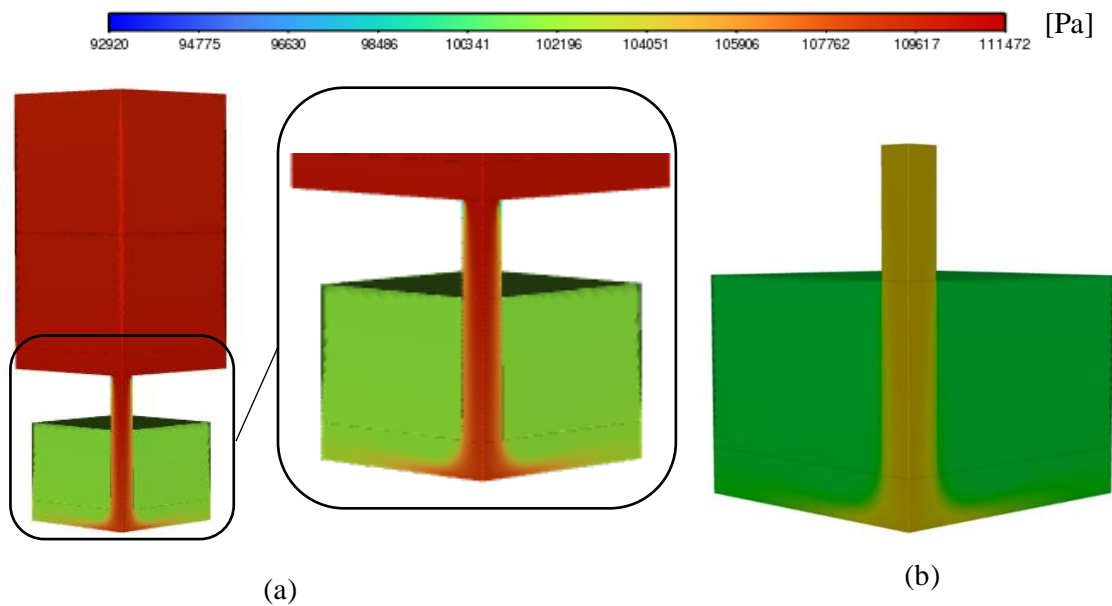
Figure 54: Pressure contours of (a) extended domain and (b) current study

4.5.3.2 Turbulent kinetic energy

Figure 55 depicts the volume-averaged turbulent kinetic energy in the pin-fin vicinity throughout the boiling curve. The turbulent kinetic energy increased with an increase in the area contribution of the fully developed nucleation boiling (see Figure 50). This increase was due to the increased turbulent interaction between the liquid and the vapour as boiling increased over the surface.

66
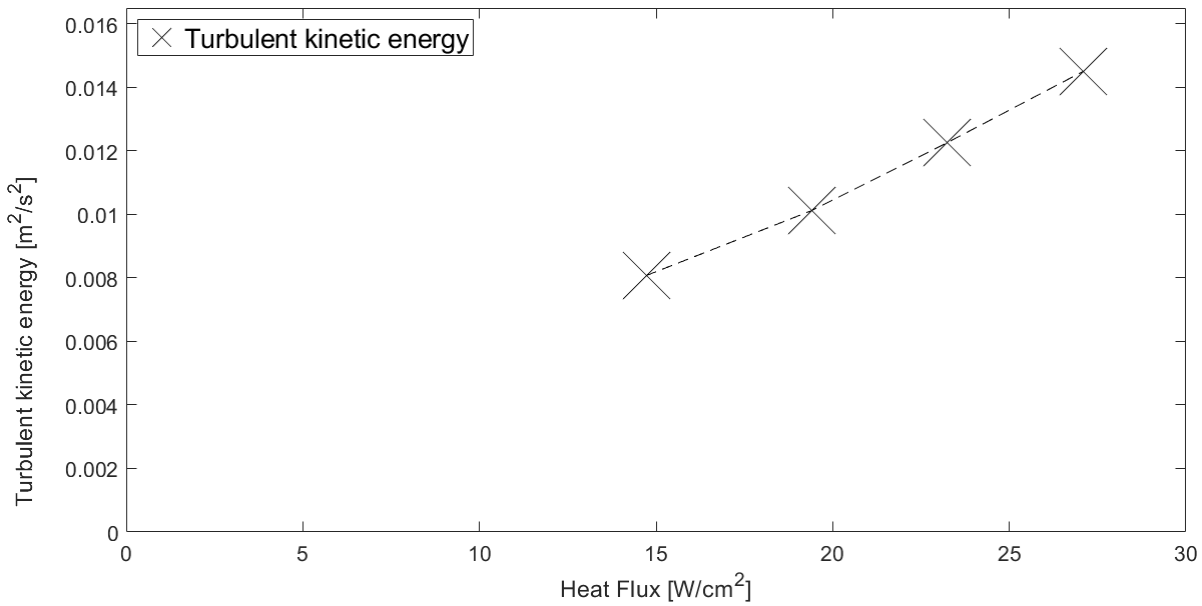
Figure 55: Change in turbulent kinetic energy

4.5.4 Contour plots

This section includes contour plots of the validation case at $23.24 \ W/cm^2$ of solid and liquid temperature, liquid velocity and mixture turbulence to further explain the previous integrated results.

4.5.4.1 Liquid velocity distribution

Figure 56 (a) depicts the liquid velocity adjacent to the base wall. Figure 56 corresponds to Figure 4 (b) in Section 1.1. The maximum liquid velocity was 3.8% higher than the jet inlet velocity, caused by the high-pressure difference between the pressurised stagnation region and the outlet boundary. Stagnant liquid is found in the core of the stagnation region because the jet created a pressure dome between the first four pin-fins, as shown in Figure 56 (b).

| (a) | (b) |
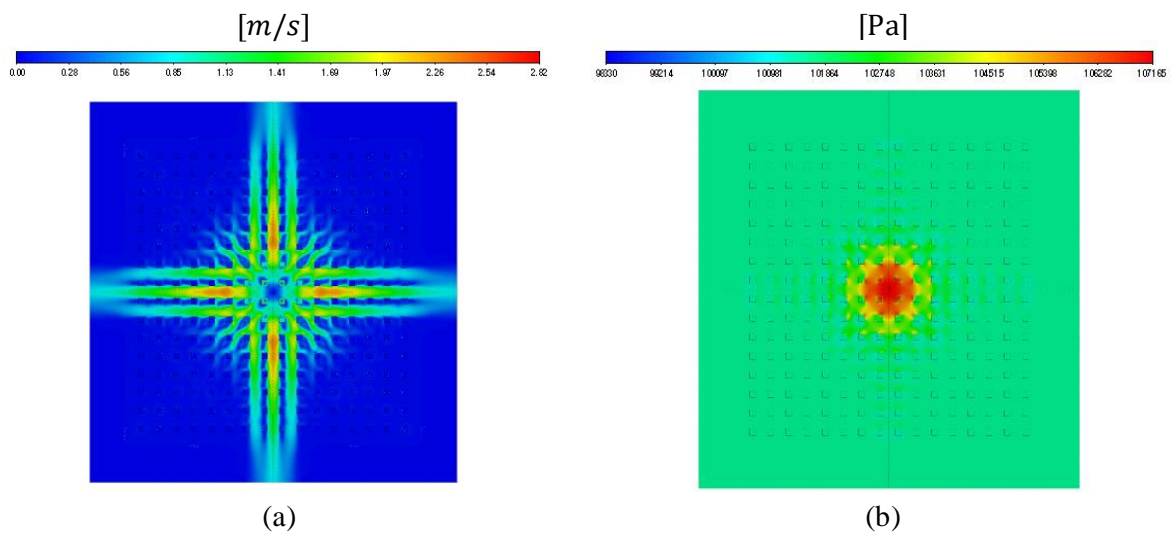
Figure 56: (a) Liquid velocity and (b) pressure distribution adjacent to the base wall

4.5.4.2 Solid temperature

Figure 57 plots the temperature contours through the copper block and PEEK insulation. Figure 57 (a) illustrates the domain name configuration through a 45° and symmetry plane. A significant temperature jump resulted from the minimum temperature in the insulation and the maximum temperature in the copper block due to the thermal conductivity of the copper block being three orders of magnitude larger than the thermal conductivity of the PEEK insulation. Therefore, the high rate at which heat passed through the copper formed a more uniform temperature distribution than for the PEEK insulation. However, the low thermal conductivity of the insulation could also cause the temperature gradient to develop significantly slower than for the copper block. Thus, a much longer run-time would be required for the temperature gradient to reach a steady state. In addition, the top part of the insulation was equal to the jet inlet temperature, which was also a set liquid outlet boundary condition. Therefore, the reversed flow entering the domain from the outlet could cause the top part of the insulation to remain at 51 ℃.

A cool cross was formed over the pin-fins, shown in Figure 58 (a) with a 6.3 ℃ temperature difference between the coolest and warmest parts of the base wall. The vapour column formed at the edges of the domain increased the temperature of the pin-fins inside the vapour column. Figure 58 (b) shows the thermal gradient in the pin-fins, with the highest temperature at the base of the fins and the coolest at the top, indicating that heat going into the bottom of each pin was not purely conducted to the top of each fin but dissipated into the fluid along the way. The base temperature distribution followed the same trends as for the pin-fins, where the coolest temperature was located at the jet stagnation region and hot zones were formed at the outer edges.

(a)   (b)
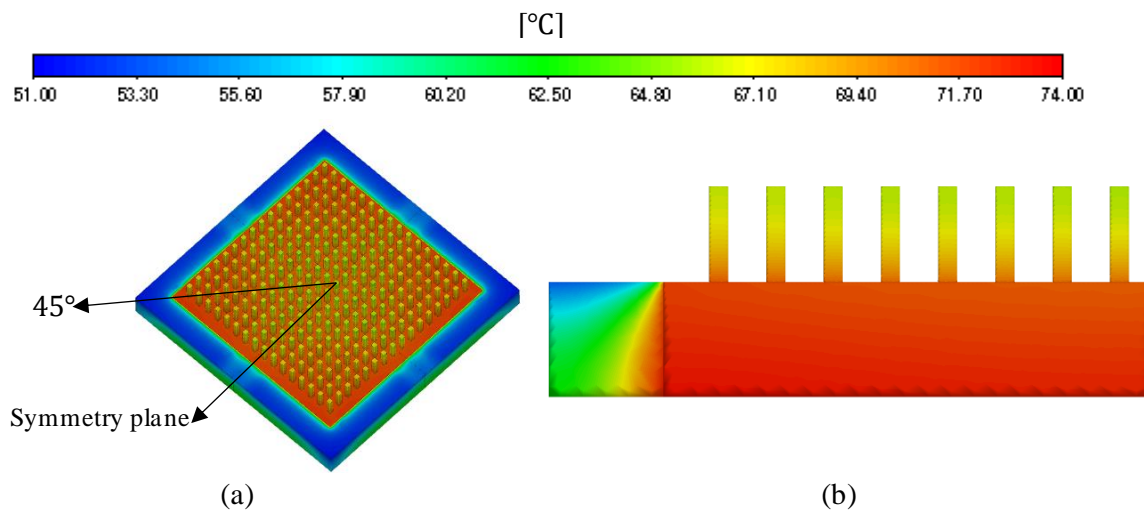
Figure 57: Copper block and PEEK insulation temperature contours at 23.24 W/cm^2: (a) 3D isometric view and (b) symmetry plane side view
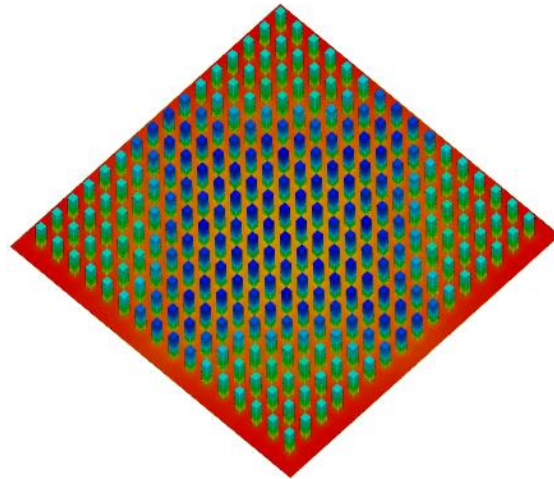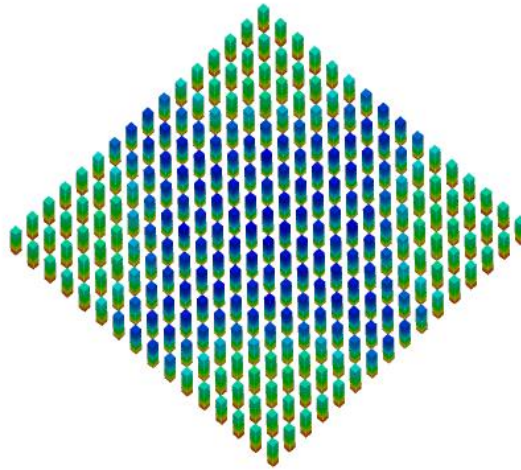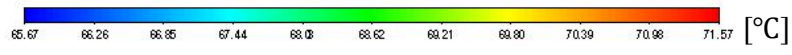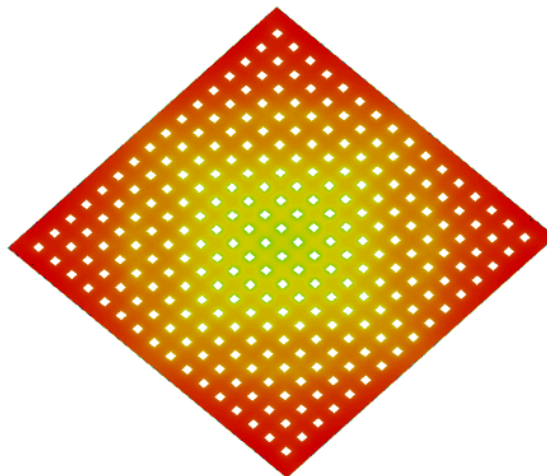
Figure 58: Full domain wall temperature [°C] of (a) base and pin-fins, (b) isolated pin-fins and (c) isolated base

4.5.4.3 Heat flux contributions

Figure 59 shows the heat flux contributions across the base surface for the convective heat flux (a), quenching heat flux (b) and evaporative heat flux (c). The convective heat flux was a maximum at the liquid acceleration regions just after the stagnation regions. These regions were also the regions with the highest liquid velocity. The quenching contribution plot correlated to the flow-boiling areas where the liquid could rewet the surface. The jet stagnation region was dominated by quenching as the impinging liquid continuously removed vapour formed under the jet. Finally, the highest evaporation contribution areas corresponded to the pool-boiling areas where quenching was minimal because the liquid could not actively rewet the surface.

The cool temperature distributions throughout the solid, shown in Section 4.5.4.2, corresponded to the high quenching heat flux regions in Figure 59 (b). Conversely, the hot pockets in the outer regions shown in Figure 58 (c) related to the high evaporative heat flux regions.

(a)

(b)
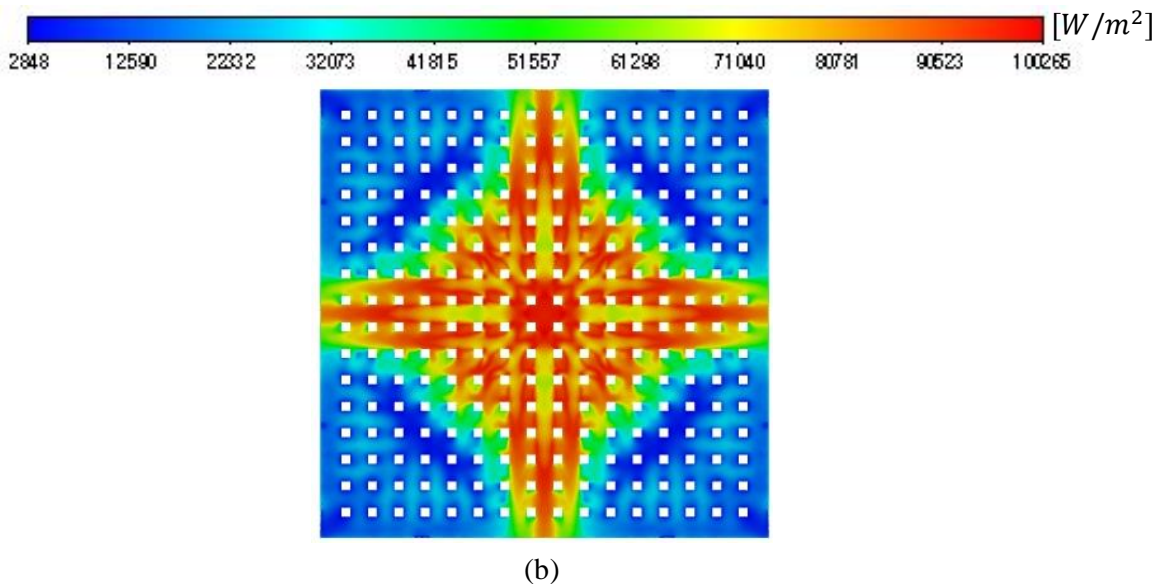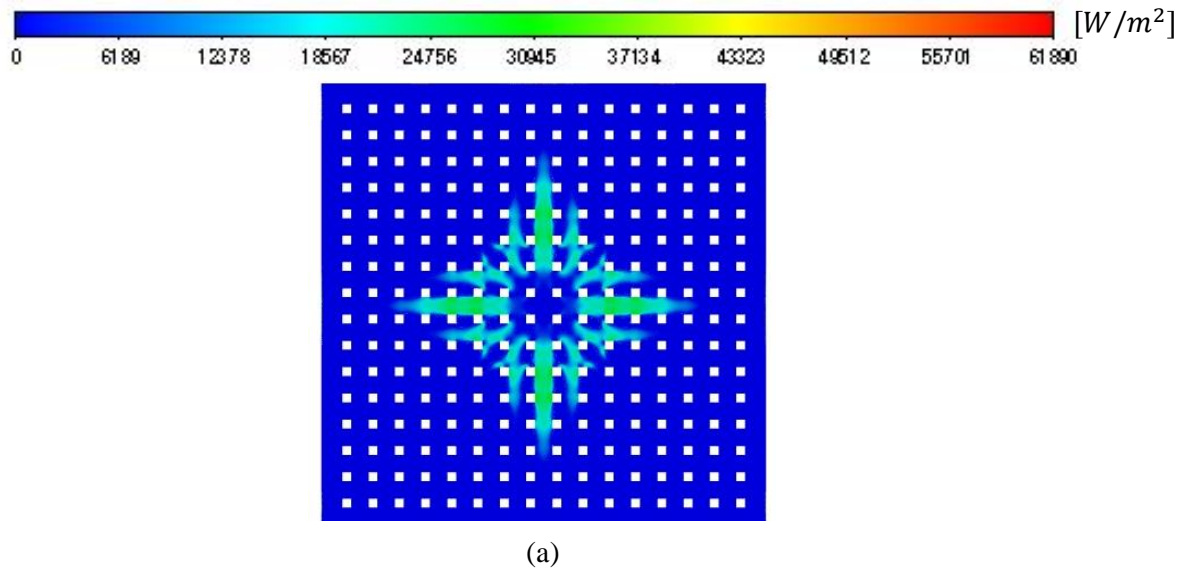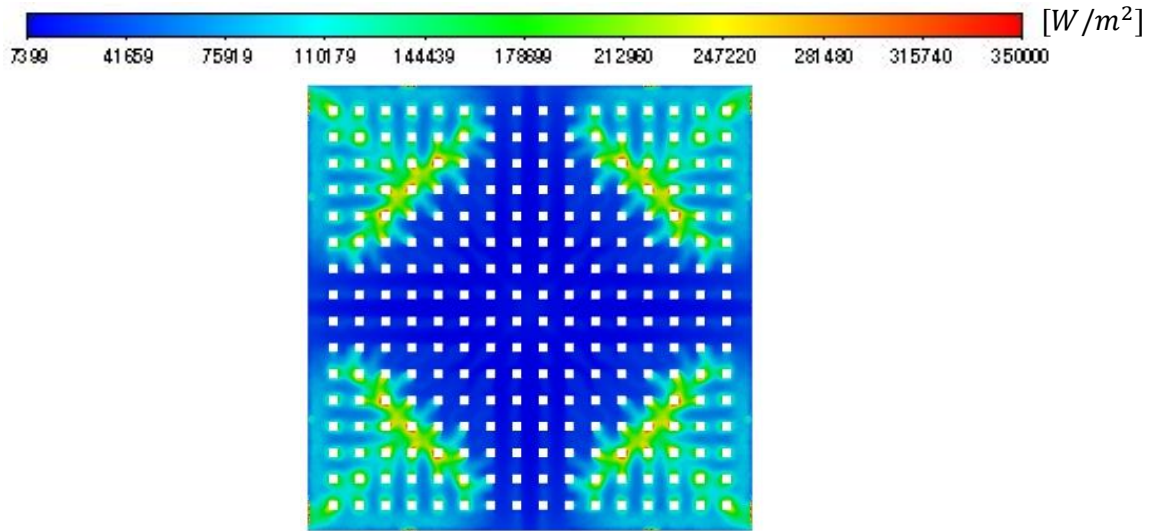
(c)

Figure 59: Heat flux $[W/cm^2]$ contribution plots at 23.2 W/cm^2 of (a) convective heat flux, (b) quenching heat flux and (c) evaporative heat flux

Figure 60 depicts the total heat flux at 23.2 W/cm^2, showing the total heat flux as a snippet in time, where the maximum total heat flux corresponded to the evaporative heat flux because the evaporative heat flux dominated at 23.2 W/cm^2.
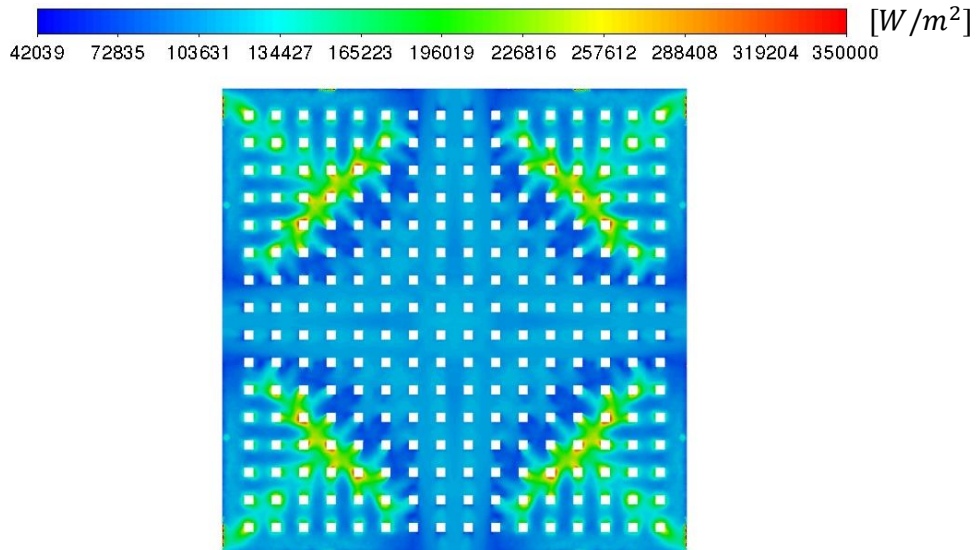
Figure 60: Total heat flux contribution plot at 23.2 W/cm^2

4.5.4.4 Cyclic behaviour

4.5.4.4.1 Liquid temperature

The cyclic behaviour of the liquid temperature distribution at a 45° angle shown in Figure 61 (a-f) followed the same trend as for the vapour formation illustrated in Figure 45. The warmest liquid was located inside the vapour column because the column consisted of both vapour and liquid phases. The liquid temperature reached saturation as the dry-out region formed, shown in Figure 59 (b-c). However,

as the vapour column detached from the surface, the vapour column condensed, and the liquid temperature decreased. A distinct temperature difference was found between the jet region and the adjacent bulk liquid temperature. The liquid temperature in the jet core remained at approximately 51 ℃. In contrast, the adjacent bulk liquid temperature was between 54 ℃ and 57 ℃, influenced by the warm liquid created and convected upwards by the vapour column, and recirculated between the jet and vapour column. Figure 61 also includes the timestamps relative to the initial plot with a frequency of 7.7 Hz.
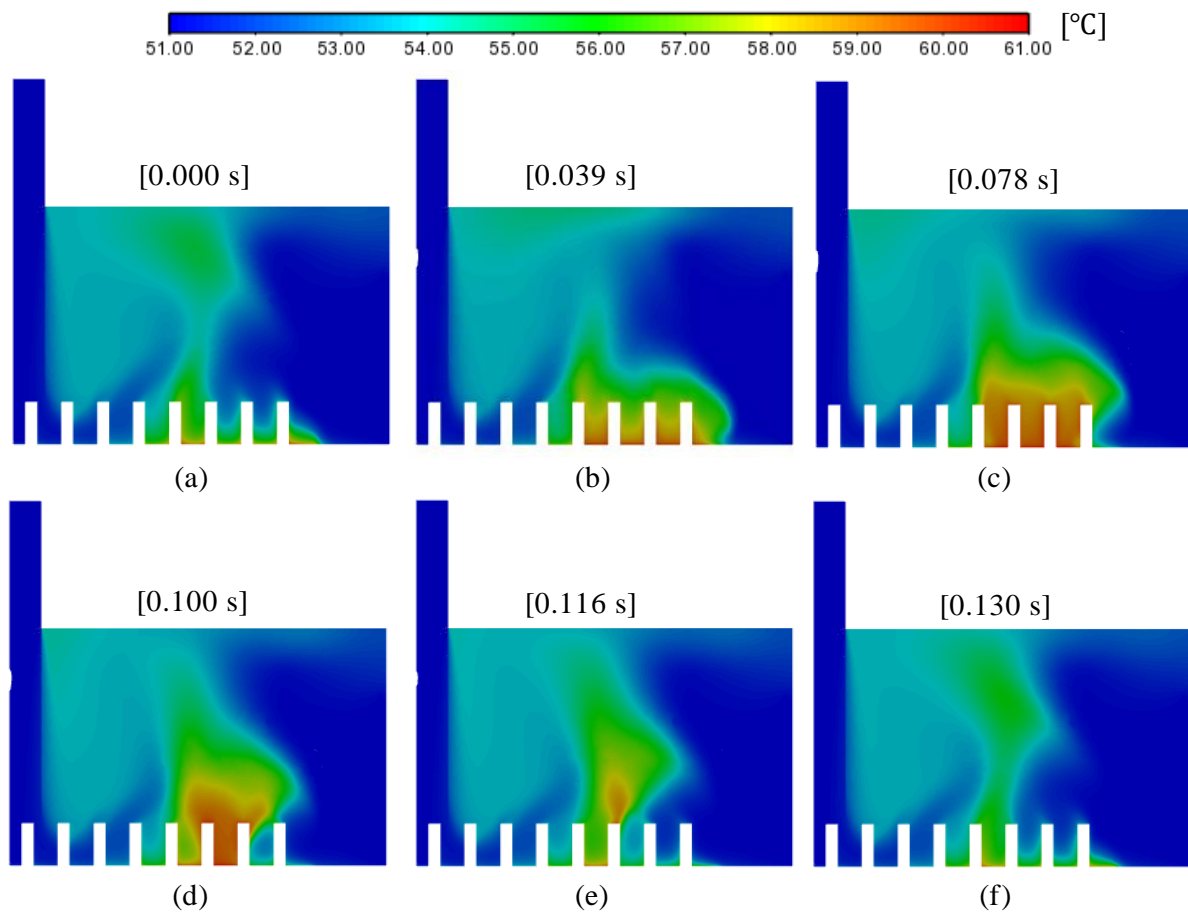
Figure 61:45° 2D liquid temperature cyclic behaviour

4.5.4.5 Vapour fraction and turbulent kinetic energy

Figure 62 (a-f) depicts the detailed vapour fraction and turbulent kinetic energy corresponding to the 3D vapour column plot in Figure 45 and the 2D 45° plane turbulent kinetic energy distribution, which is scaled from 0 to 1. A maximum vapour fraction was located inside the core of the vapour column, dissipating to the outer regions of the vapour column. The rear ends of the outer pin-fins acted as the origin of the large vapour column, coalescing with vapour formed at the front end of the outer pin-fins to create the large vapour column. Figure 62 also included the timestamps relative to the initial plot with a frequency of 7.7 Hz, corresponding to the frequency of the liquid temperature plots in Figure 61.

A maximum turbulent kinetic energy was located just outside the stagnation region as the liquid entered the staggered facing pin-fins. The local maximum in turbulent kinetic energy followed the vapour column as the vapour column grew and condensed. The local maximum of the vapour fraction did not correspond to the local maximum of the turbulent kinetic energy because the turbulent energy of vapour was much lower than that of the liquid.
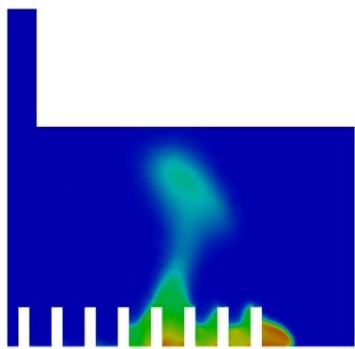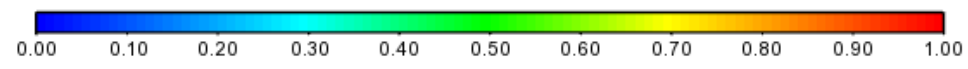
[0.000 s]
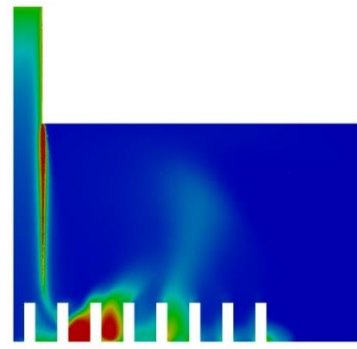
(a)
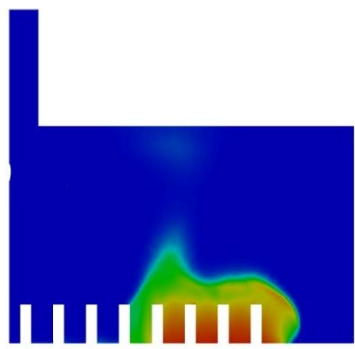
[0.034 s]

(b)

[0.089 s]

(c)

[0.114 s]

(d)

[0.120 s]

(e)

[0.130 s]

(f)
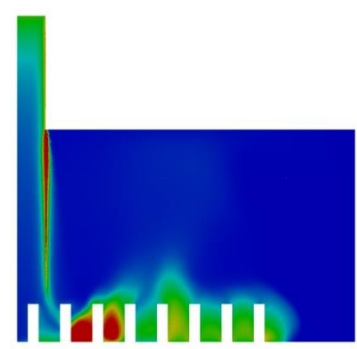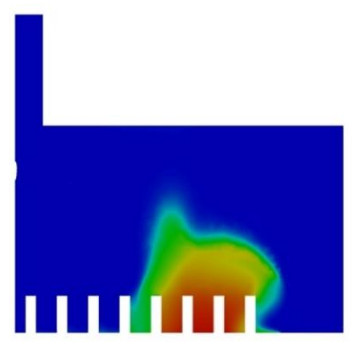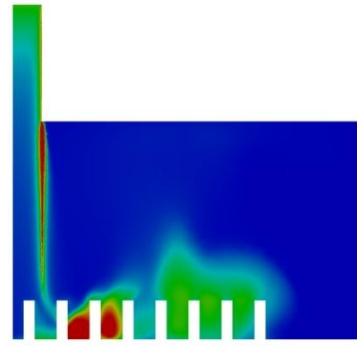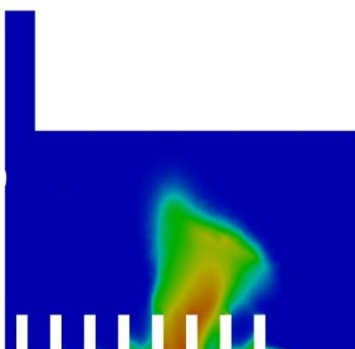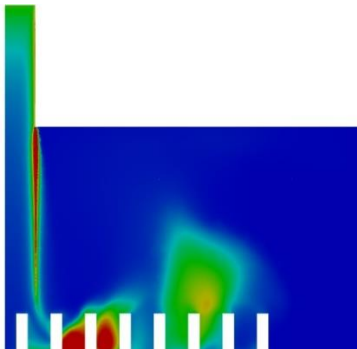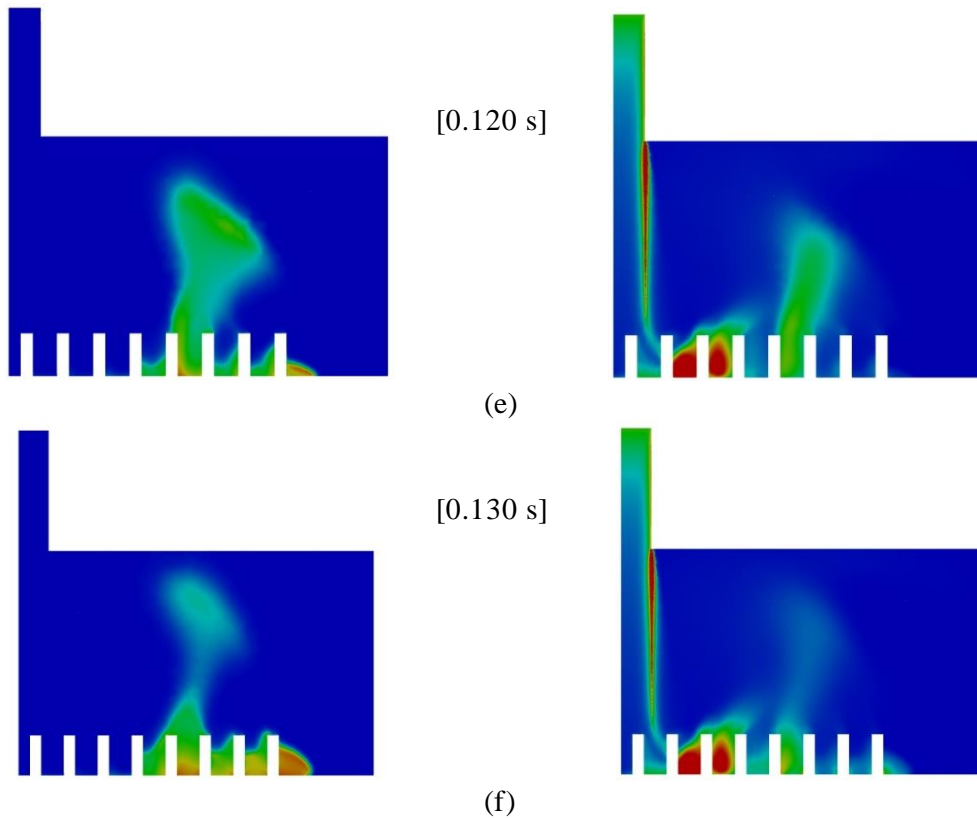
Figure 62: 45 degree 2D vapour fraction (left) and turbulent kinetic energy (right) cyclic behaviour

4.6 Experimental validation conclusion

The numerical validation of boiling jet impingement heat transfer on a pin-fin surface resulted in an error of 5.1% to 12.3% compared with that of the boiling curve published by Rau and Garimella [17], including the reported experimental uncertainties. The numerical results deviated from the experimental results at higher heat fluxes as the numerical boiling curve had a constant gradient. A mesh-independent study showed that a higher mesh density in the pin-fin vicinity reduced the simulation error, with hexahedral and polyhedral cells predicting identical stagnation wall temperatures with eight cells between opposing pin-fins. Hexahedral cells are the preferred cell type as they decrease computational costs while keeping the same accuracy level. However, the current study only considered polyhedral cells due to software limitations. The fully developed nucleation boiling and dry-out area contributions resulted in cyclic behaviour over time due to the formation and dissipation of vapour in the outer regions of the domain.

An extended domain simulating the pressure drop over the orifice plate resulted in an accurate prediction of the pressure drop, mimicking the locations of the experimental pressure probes; however, resulting in the same stagnation wall superheat prediction. In addition, turbulent kinetic energy increased with heat flux due to the increased turbulent interaction between the liquid and the vapour as boiling increased over the surface and interacted with the pin-fins. The temperature distribution on the top wall formed a cross through the domain, agreeing with the liquid velocity distribution. The liquid temperature at the outer edges of the domain created hot pockets around the vapour columns generated in the wakes of the pin-fins as the liquid transitioned to a vapour.

5 Parametric Study

This section presents the effect of the inlet Reynolds number, pin-fin height, spacing and distribution on the heat transfer coefficient, pressure drop, and evaporation boiling area contributions. All results in this chapter were time-averaged after each simulation reached a quasi-steady state at an input heat flux of 23.24 W/cm^2. The parametric analysis presented in this chapter considered the validation case in Section 4 as the base case and this case was used as a reference point. All the data handling code of this section is included in Appendix E: Data handling code.

5.1 Inlet Reynolds number

The inlet jet Reynolds number was lowered to 25 000 and raised to 45 000 as the base case had an inlet Reynolds number of 35 000. The inlet Reynolds numbers 25 000, 35 000 and 45 000 corresponded to inlet velocities of 1.94 m/s, 2.72 m/s, and 3.49 m/s respectively. Figure 63 compares the wall superheat at the stagnation region among the three Reynolds numbers. An apparent decrease in the stagnation wall superheat was obtained with an increased jet Reynolds number. This result was expected and was also found by Esmailpour *et al.* [40] and Wright *et al.* [42]. The increase in jet velocity led to a higher stagnation pressure because the jet was stagnated perpendicular to the wall, increasing the hydrostatic pressure force exerted on evaporating bubbles in the stagnation regions, as discussed in Section 2.3.4.2. An increase in stagnation pressure also led to a higher pressure drop between the stagnation region and outlet boundaries, increasing the liquid acceleration towards the outlet and ultimately increasing heat transfer in the flow-boiling regions, pointing to the classic trade-off between heat transfer and pressure drop. All the data handling code of this section is presented in Appendix E: Parametric study: Inlet Reynolds number.
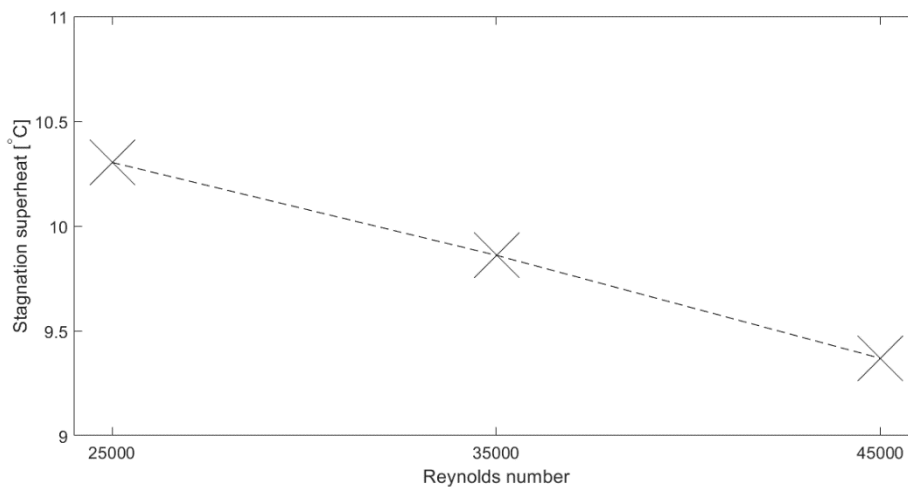
Figure 63: Parametric study: inlet Reynolds number stagnation superheat

Figure 64 depicts the pressure drop between the jet inlet and outlet boundary over the range of Reynolds numbers. An increase in Reynolds number led to an approximate quadratic increase; with a doubling in jet inlet Reynolds number, the pressure drop quadrupled. Figure 64 indicates that the pressure drop was driven by the dynamic pressure between the jet inlet and the stagnation region. The liquid velocity distribution shown in Figure 65 corresponded to the pressure contour plots shown in Figure 64. A higher stagnation pressure resulted in a higher liquid velocity towards the outlet boundary, accelerating through the pin-fin channels with the lowest resistance. The ability of the liquid to reach the "dry-out" regions was not linked to the stagnation pressure because the high-velocity regions stayed constant, with the only change being the velocity magnitude in the high-velocity regions.
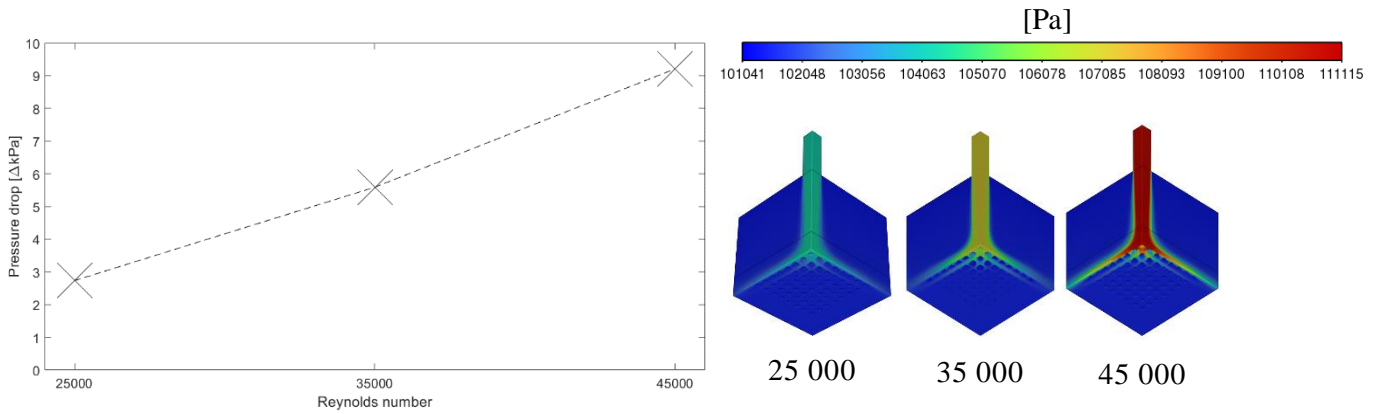
Figure 64: Parametric study: inlet Reynolds number pressure drop [Pa]
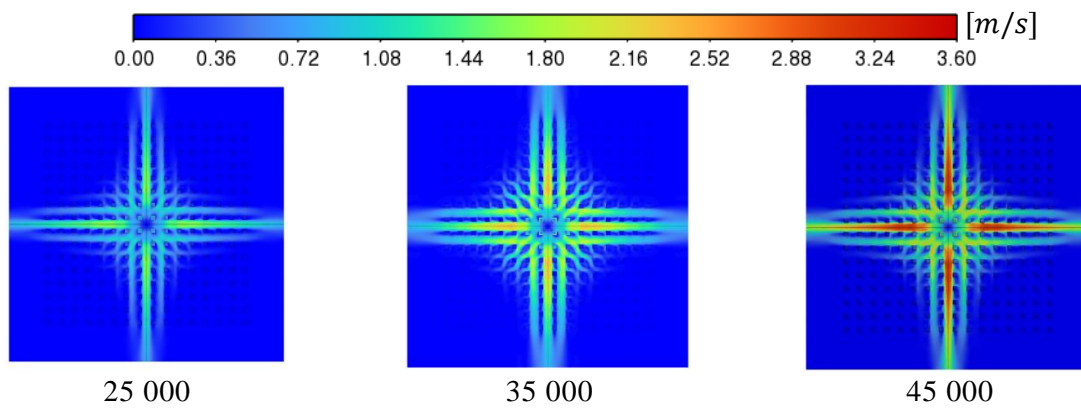
Figure 65: Parametric study: inlet Reynolds number liquid velocity distribution [m/s]

Figure 66 depicts the change in the volume average turbulent kinetic energy in the pin-fin region. The volume average turbulent kinetic energy remained approximately constant between the Reynolds numbers of 25 000 and 35 000. However, the volume of average turbulent kinetic energy was doubled at the high Reynolds number of 45 000. The increase in turbulent kinetic energy at the high Reynolds number resulted from the increased pressure difference between the stagnation region and the outlet boundary, increasing turbulence generated from the pin-fins as the fluid was forced towards the outlet boundary.
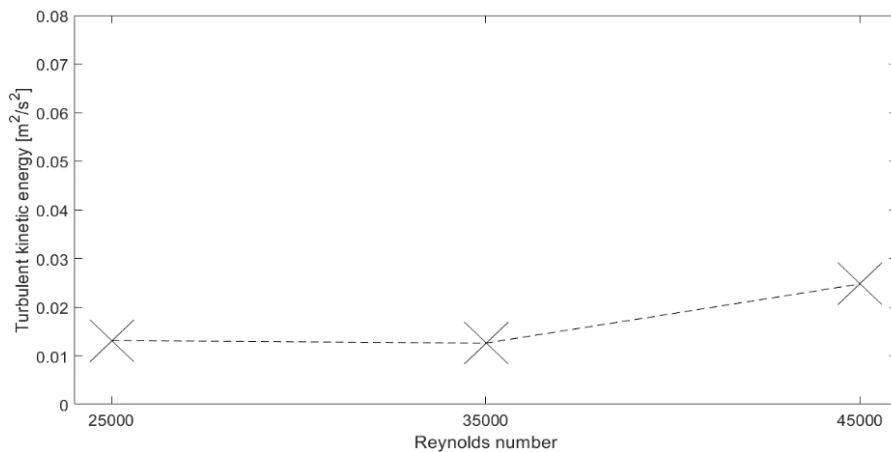
Figure 66: Parametric study: inlet Reynolds number turbulent kinetic energy $[m^2/s^2]$

Figure 67 shows the area contribution on the base wall between the fins of each boiling regime. An increase in the Reynolds number led to a slight decrease in the dry-out area contribution, reaching a plateau as the Reynolds number increased. Therefore, the Reynolds number had a limited influence on the dry-out region. Other parameters, such as fin height and pitch, had to be investigated to reduce the dry-out area contribution. The fully developed nucleate boiling regime contribution reached a minimum at a Reynolds number of 35 000, with the developing nucleate boiling regime reaching a peak. The influence of the fully developed and developing nucleate boiling area contributions was a complex phenomenon. The low liquid velocity in the flow-boiling region at a Reynolds number of 25 000 struggled to effectively remove formed bubbles from the heated surface, thus leading to a higher fully developed nucleate boiling region and a lower developing nucleate boiling region. An increase in Reynolds number increased the liquid velocity in the flow-boiling regions, increasing the ability of the liquid to actively remove vapour from the heated surface effectively, thus increasing the developing nucleate boiling area contribution, and consequently, decreasing the fully developed nucleate boiling area contribution. The slight increase in the fully developed nucleate boiling area contribution at the Reynolds number of 45 000 was due to the ability of the liquid to more effectively flow into the surrounding pin-fins adjacent to the main pathway, slightly extending the high-velocity regions.

In conclusion, the increase in Reynolds number led to a lower stagnation wall superheat, but the ability to reduce the dry-out area contribution was limited. Therefore, further investigation was required into the influence of pin-fin height and spacing on the dry-out area contribution.
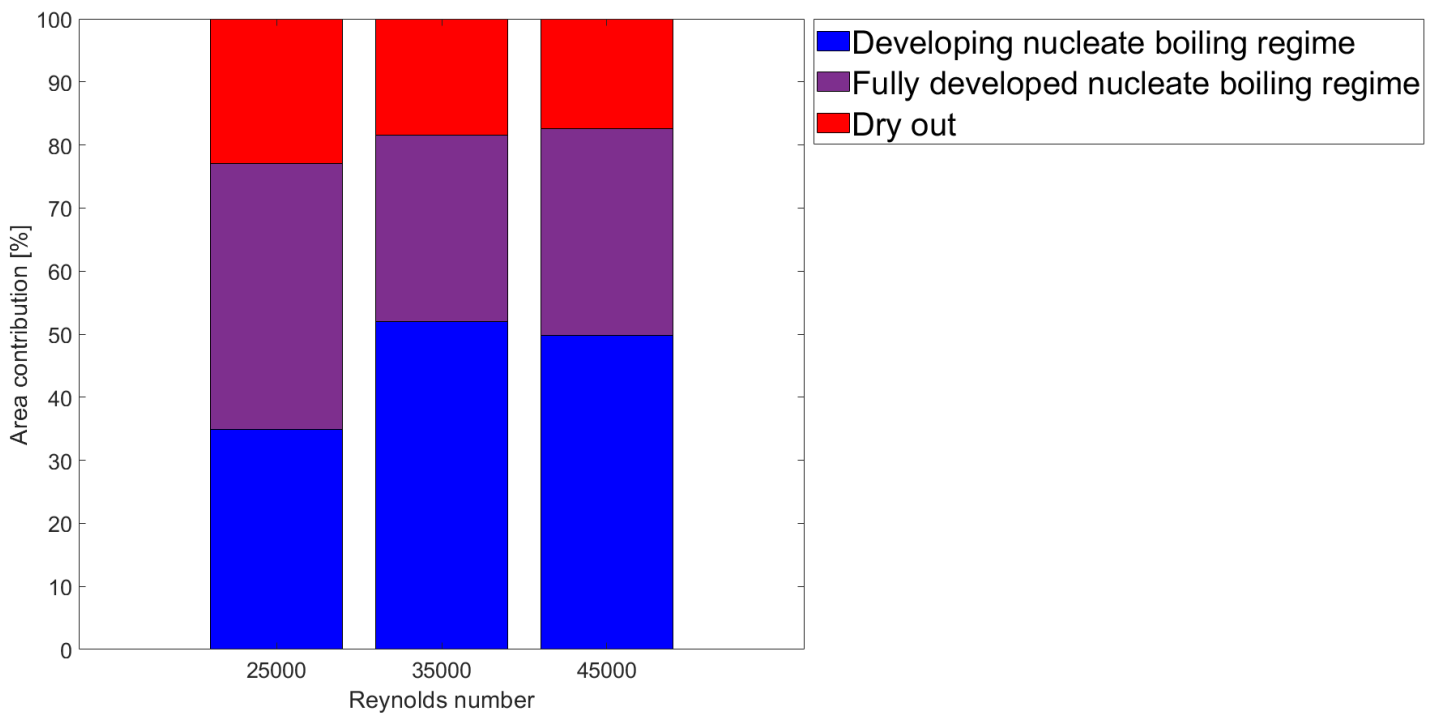
Figure 67: Parametric study: inlet Reynolds number boiling-type area contribution

5.2 Fin height and spacing

This section presents the effect of pin-fin height and spacing on the stagnation and average wall superheat of the base surface between the pin-fins. The investigation also included the effect on pressure drop, volume-averaged turbulent kinetic energy between the fins, nucleate boiling area contribution, and dry-out area contribution. Rau and Garimella [17] highlighted the importance of fin spacing when designing a pin-finned surface. Figure 68 depicts the validation case's dry-out (red) and fully developed nucleate boiling (purple) area contributions at a maximum dry-out contribution. This investigation aimed to decrease the dry-out area contribution shown in Figure 68 by increasing the fin spacing to allow for better liquid flow between the channels of the pin-fins and decreasing the pin-fin height to reduce flow obstruction caused by the fins, allowing the liquid to access the dry-out area more effectively. All the data handling code of this section is presented in Appendix E: Parametric study: Pin-fin height, spacing and distribution.
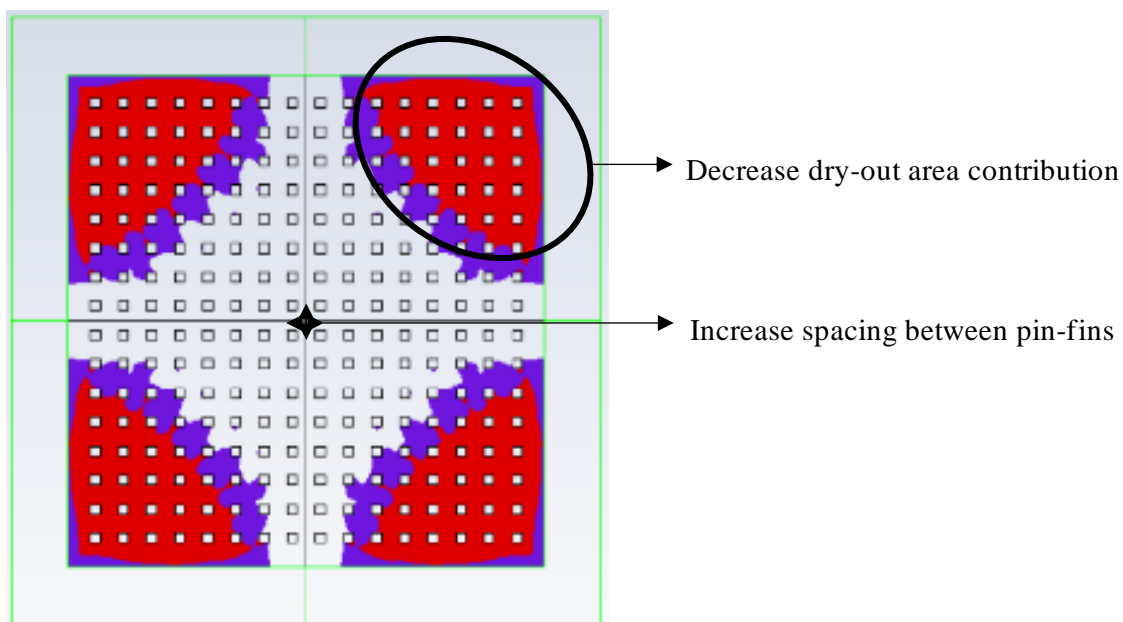
Figure 68: Peak dry-out contribution on base case

All cases in this study were done at the same inlet jet velocity of 2.716 m/s and heat flux of 23.24 W/cm^2. The number of pin-fins in the domain was also kept constant at 256. The surface augmentation factor was constant throughout each spacing at a selected pin-fin height to decrease the effect of surface augmentation on heat transfer. Table 8 provides the augmentation factor for each fin height and spacing combination. The surface augmentation factor was approximately halved between the highest and lowest fin height. The decrease in the augmentation factor could influence the heat transfer ability of the surface because the total area in which heat transfer occurred decreased.

Table 8: Parametric study: fin height and spacing augmentation factor

Fin height [mm]	Fin spacing [mm]		
	1.000	1.075	1.150
2.500	2.98	2.98	2.98
1.250	1.99	1.99	1.99
0.625	1.5	1.5	1.5
0.312	1.25	1.25	1.25

Figure 69 depicts the influence of fin height and spacing on the stagnation wall superheat. An apparent increase in stagnation wall superheat resulted from a decrease in fin height, with the blue to dark yellow colour scheme indicating the intenseness of the gradient. As stated above, the decrease in the surface augmentation factor would harm heat transfer as the surface area of which heat could be transferred from the solid to the fluid decreased, thus increasing the wall superheat. In addition, the increase in fin spacing led to a slight increase in stagnation wall superheat. The widening of flow channels would allow liquid to flow "easier" from the stagnation region to the outlet, thus decreasing the turbulence around the stagnation region and ultimately decreasing heat transfer. A $7.28\,°C$ difference was obtained between the lowest stagnation wall superheat at fin height of $2.5\,mm$ and fin spacing of $1\,mm$ and the highest stagnation wall superheat at fin height of $0.312\,mm$ and fin spacing of $1.15\,mm$.
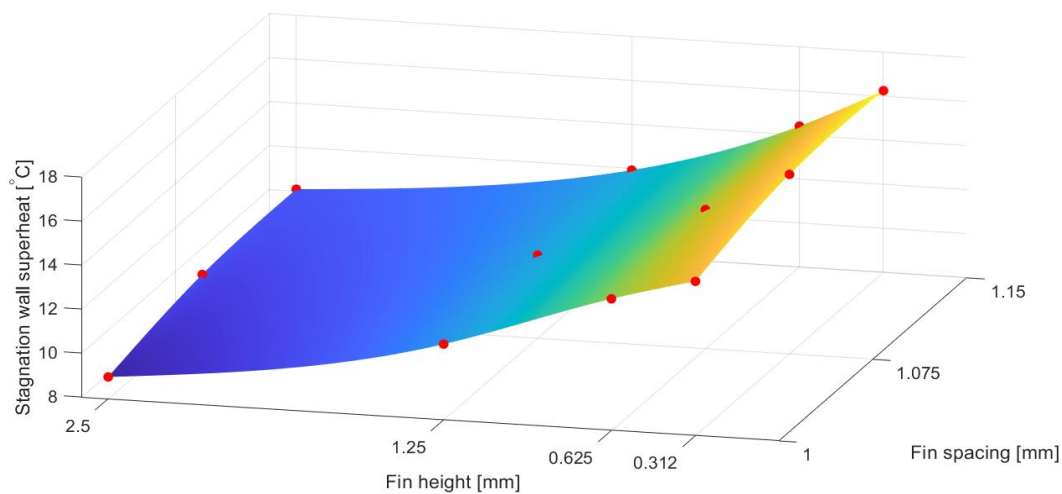
Figure 69: Parametric study: fin height and spacing stagnation wall superheat

A similar trend resulted from the average wall superheat of the flat surface between the pin-fins (see Figure 70), with an increase in the average wall superheat resulting from a decrease in fin height. Again, this increase in wall superheat was due to a decrease in surface area. A small peak in average wall superheat was formed at a fin spacing of $1.075\,mm$ across all fin heights.
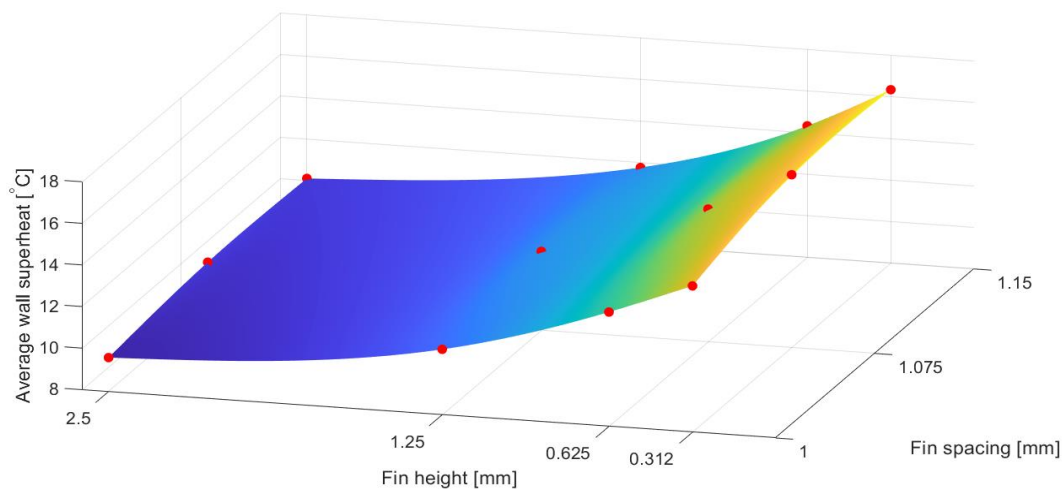
Figure 70: Parametric study: fin height and spacing average wall superheat of the base surface between the pin-fins

Figure 71 depicts the pressure drop between the jet inlet and outlet. The pressure drop across all fin height and spacings remained approximately constant with a slight increase as a low fin spacing and

medium fin height combination. The results of Section 0 indicated that the pressure drop across the domain was mainly driven by the dynamic pressure difference of the jet and not the flow obstruction caused by the pin-fins. However, the pin-fin height and spacing would have a larger influence on the pressure drop if the jet-to-target spacing was reduced.
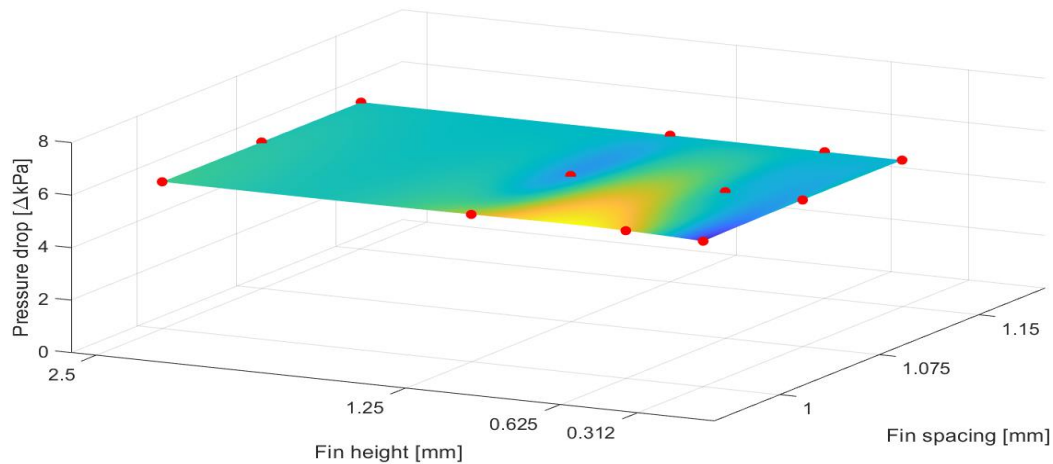
Figure 71: Parametric study: fin height and spacing pressure drop [kPa]

Figure 72 depicts the volume-averaged turbulent kinetic energy in the pin-fin region for each fin height and spacing combination. The average turbulent kinetic energy increased with a decrease in fin height. This increase in turbulent kinetic energy was due to the elimination of stagnation regions in the pin-fin vicinity. As a result, the flow was able to move across the domain from the stagnation region, increasing the overall turbulence in the domain. A local minimum was formed at a fin spacing of 1.075 mm. Figure 70 shows that a local maximum in average wall superheat resulted in a fin spacing of 1.075 mm. Therefore, the average wall superheat increased at a fin spacing of 1.075 mm due to the reduction in turbulent kinetic energy at a fin spacing of 1.075 mm.
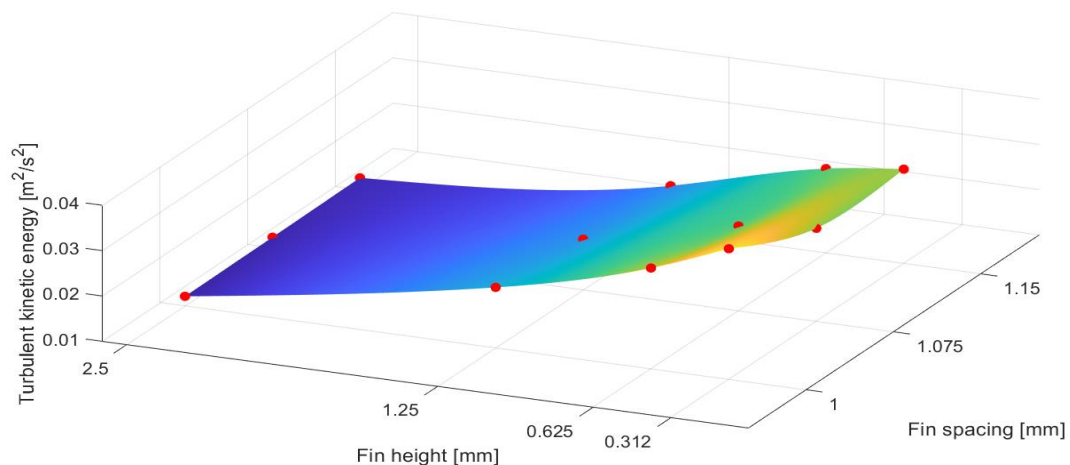
Figure 72: Parametric study: fin height and spacing volume-averaged turbulent kinetic energy in the pin-fin region

Figure 73 depicts the time-averaged dry-out area contribution of the base wall between the fins. Dry-out was eliminated at a fin height of $0.312\,mm$ and reached a peak at a fin height of $1.25\,mm$ at spacings of $1.075\,mm$ and $1.150\,mm$. The illumination of dry-out was linked to the volume-averaged turbulent kinetic energy, shown in Figure 72, because the highest turbulent kinetic energy eliminated dry-out. Turbulence enhanced the ability of the liquid to remove vapour from the heated surface, avoiding any damage to the heated surface. The dry-out area contribution at a fin height of $2.5\,mm$ reduced from 16.7% to 7.4% when the fin spacing was increased while forming a small peak at a fin spacing of 1.075 mm. A similar trend resulted from all other fin heights. A peak dry-out contribution was formed at a pin-fin height of 1.25 mm. The peak was formed from the trade of increasing the surface augmentation to increase heat transfer, thus the decrease at the highest pin-fin height, and the increase of turbulence and high-velocity regions resulted in the decrease at lower pin-fin heights.
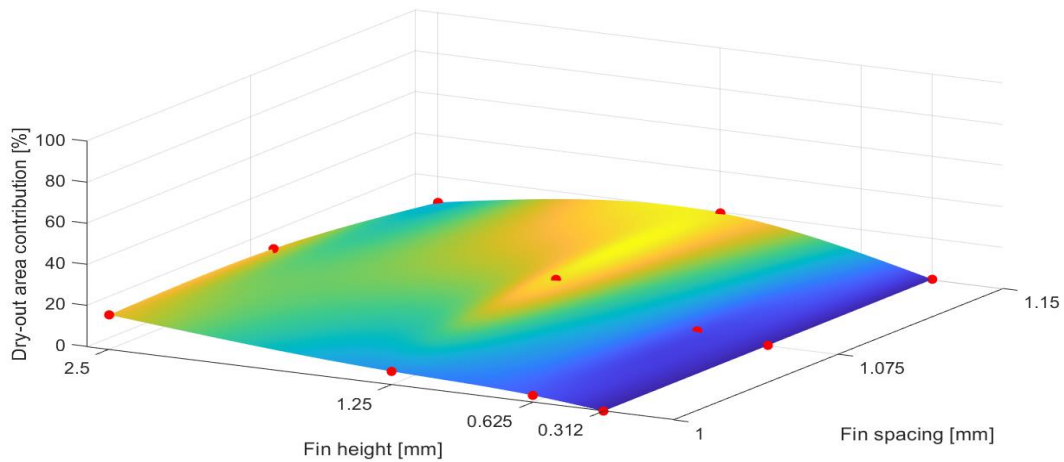
Figure 73: Parametric study: fin height and spacing dry-out area contribution

Figure 74 depicts the averaged fully developed nucleation boiling area contribution of the flat wall between the fins. An opposite trend to the dry-out area contribution resulted. A decrease in the dry-out area contribution led to the compromised areas entering the fully developed nucleate boiling regime, thus increasing the area contribution.
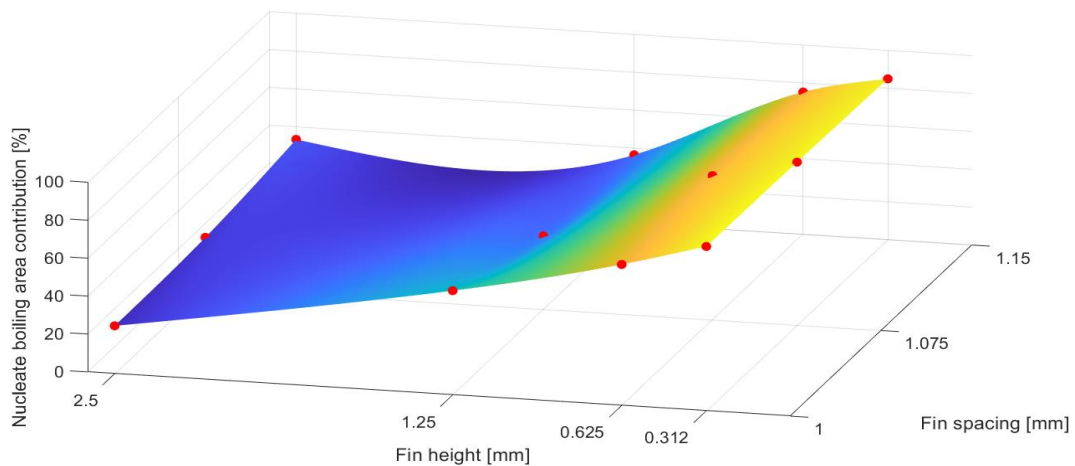
Figure 74: Parametric study: fin height and spacing fully developed nucleate boiling area contribution

Although pin-fin height reduction eliminated the dry-out area contribution, the heat transfer deteriorated due to the reduction in surface augmentation. Therefore, further study was needed to investigate the

effect of pin-fin distribution to keep the heat transfer quality but attempt to reduce the dry-out area contribution.

Figure 75 depicts the heat flux contours of a pin-fin height and spacing of 1.25 mm and 1 mm respectively. The decrease in pin-fin height increased the quenching heat flux contribution throughout the base surface, which was linked to an increase in the high-velocity liquid regions shown in Figure 78. The evaporative heat flux region slightly decreased compared with that of a pin-fin height of 2.5, and the total heat flux plot still corresponded to the evaporative heat flux as the evaporative heat flux was the dominant heat flux component in the outer regions. The convective heat flux was excluded from Figure 75 because the contribution was negligible.
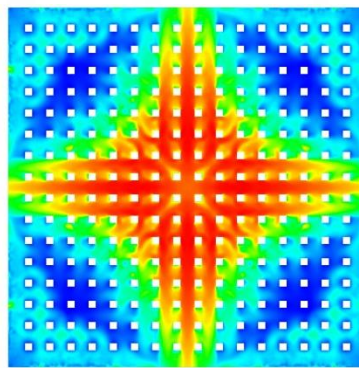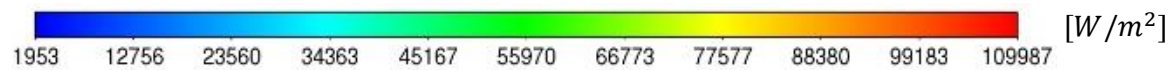
(a)
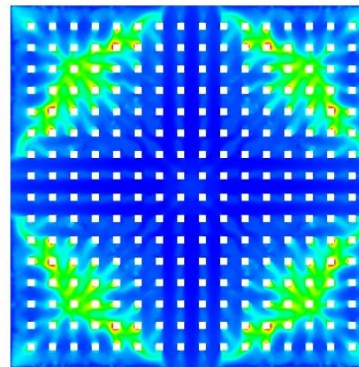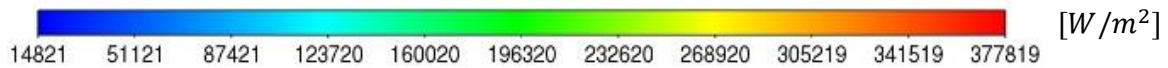
(b)
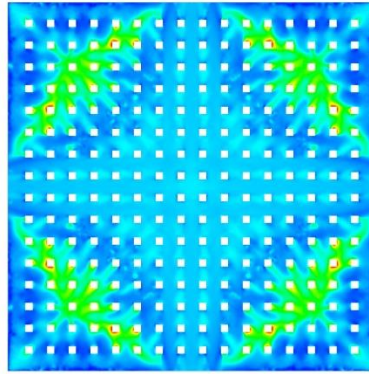
(c)

Figure 75: Contour plots of (a) the quenching heat flux, (b) evaporative heat flux and (c) the total heat flux at a pin-fin height and spacing of 1.25 mm and 1 mm respectively, while kept at a constant heat flux of $23.2\ W/m^2$

Figure 76 depicts the heat flux contours of a pin-fin height and spacing of 0.312 mm and 1 mm respectively. The further decrease in pin-fin height slightly changed the quenching heat flux contour as the liquid was no longer forced through the pin-fin channels, thus decreasing the quenching ability in those channels. The evaporative heat flux decreased in the outer region of the domain as the dry-out area contribution was eliminated at a pin-fin height of 0.312 mm. The maximum evaporative heat flux also decreased as the dry-out regions caused a spike in the local maximum evaporative regions at higher pin-fins. The total heat flux corresponded well to the high-velocity liquid regions shown in Figure 79, with vapour only forming at the outer edges of the domain. The convective heat flux was excluded from Figure 76 because the contribution was negligible.

$[W/m^2]$

| 10553 | 21066 | 31580 | 42093 | 52606 | 63120 | 73633 | 84146 | 94660 | 105173 | 115686 |

(a)

83
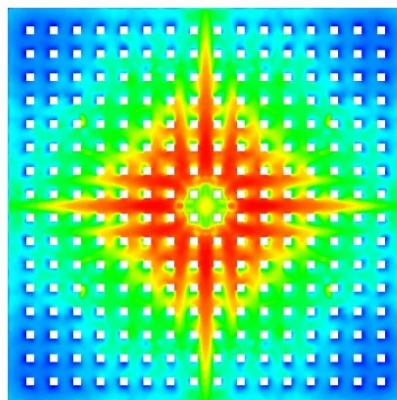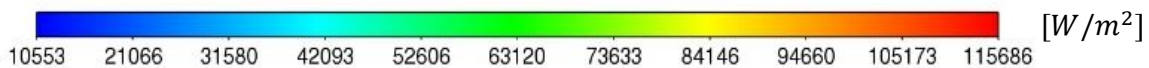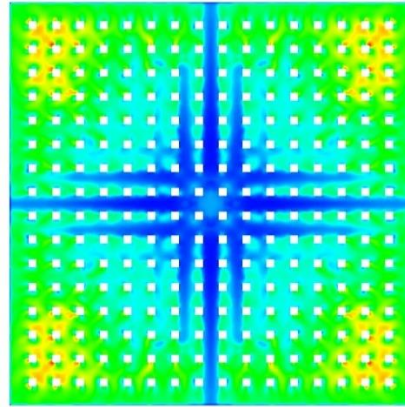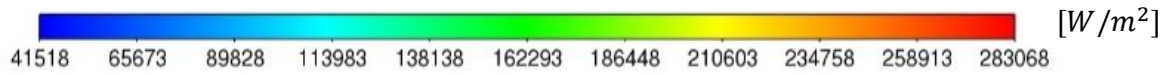
(b)
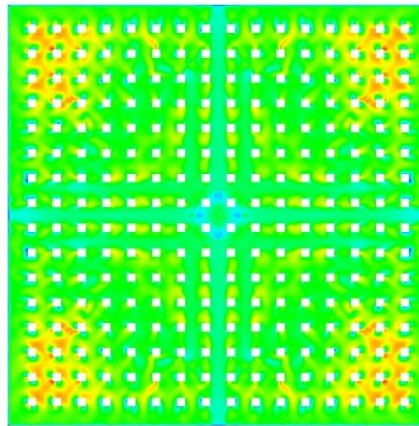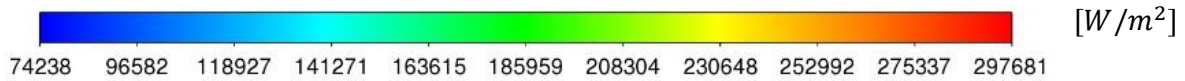
(c)

Figure 76: Contour plots of (a) the quenching heat flux, (b) evaporative heat flux and (c) the total heat flux at a pin-fin height and spacing of 0.312 mm and 1 mm respectively, while kept at a constant heat flux of 23.2 W/m^2

Figure 77 presents the cyclic behaviour of the vapour column at the highest pin-fin height and largest spacing. The evaporation and condensation cycle behaved in a similar fashion to that shown in Figure 45. However, there was a noticeable difference at the base of the pin-fins as each pin-fin base acted as nucleation sites, which are clearly shown in (e-f). The increase in spacing between the fins delayed the coalescence of the vapour evaporating from the nucleation sites, whereas the period in which vapour coalesced between the pin-fins decreased with a decrease in pin-fin spacing.

Figure 77 also shows that the high-velocity liquid regions remained constant between the narrow pin-fin and increased pin-fin spacing. However, if the pin-fin height decreased, as shown in Figure 78, the high-velocity liquid regions started to engulf the vapour column, forming a wave as the evaporating vapour pushed the liquid from the outer edge of the domain. Figure 79 shows that the high-velocity liquid regions was able to cover the low pin-fins, keeping the vapour column underneath the high-velocity liquid regions. The liquid flow over the pin-fins restricted the cyclic behaviour of the vapour column and the vapour column remained constant.
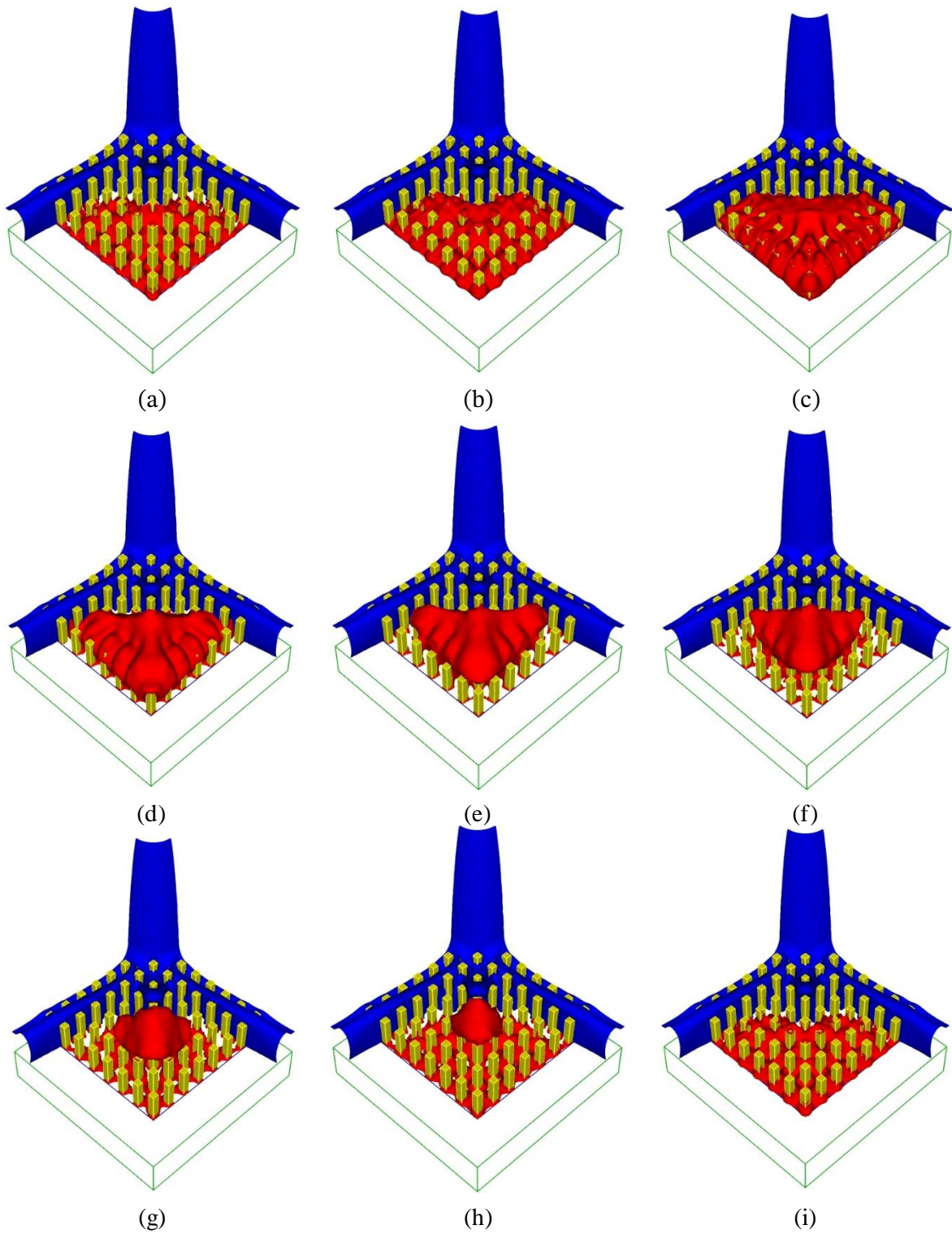
Figure 77: Parametric study: cyclic behaviour of a vapour column at a pin-fin height of 2.5 mm and spacing of 1.15 mm (liquid velocity above 0.3 m/s (blue) and cell vapour fraction above 0.5 (red) between frames (a) to (i)). Time series has intervals of 15 ms.
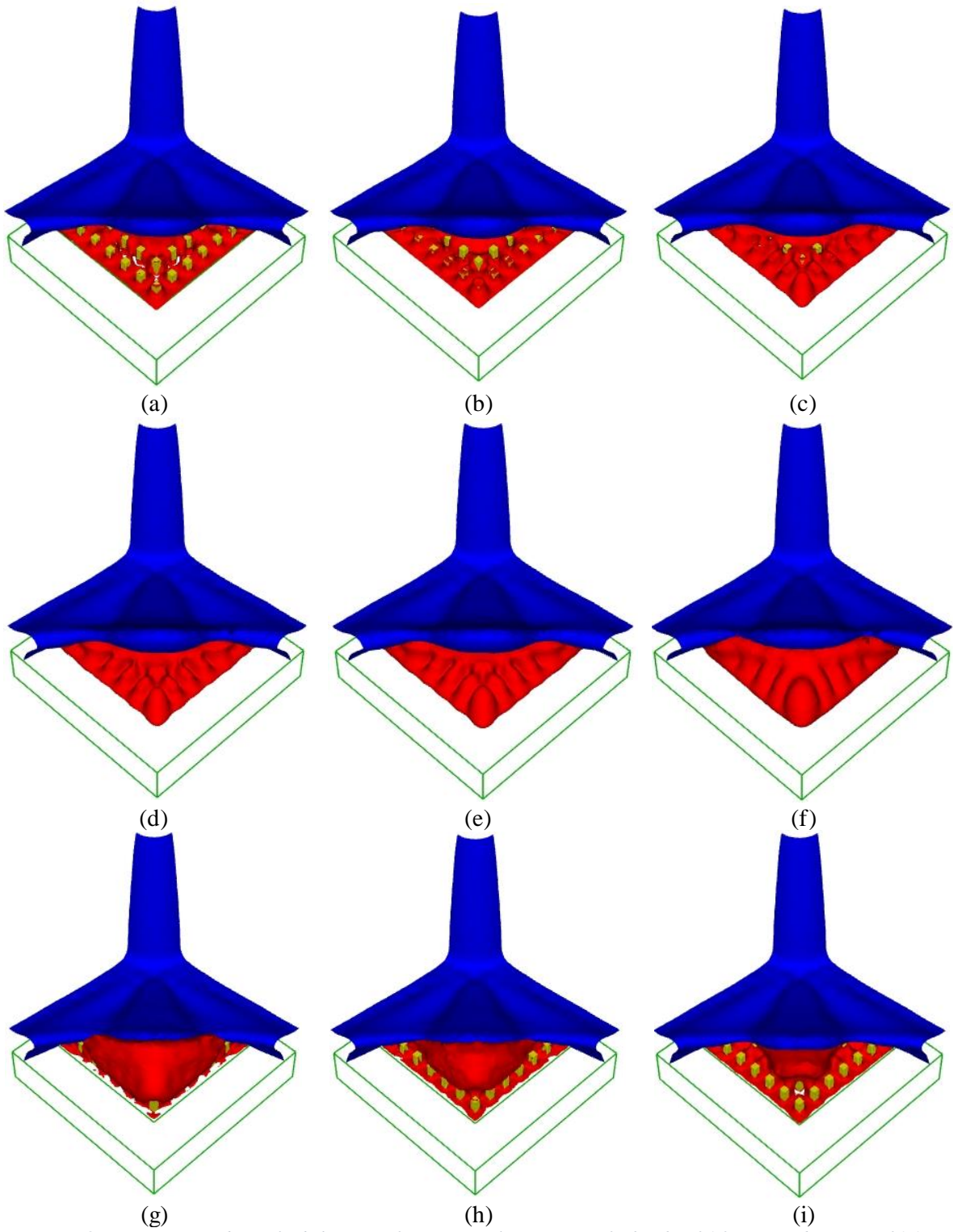
Figure 78: Parametric study: cyclic behaviour of a vapour column at a pin-fin height of 1.25 mm and spacing of 1.15 mm (liquid velocity above 0.3 m/s (blue) and cell vapour fraction above 0.5 (red) between frames (a) to (i)). Time series has intervals of 2 ms.
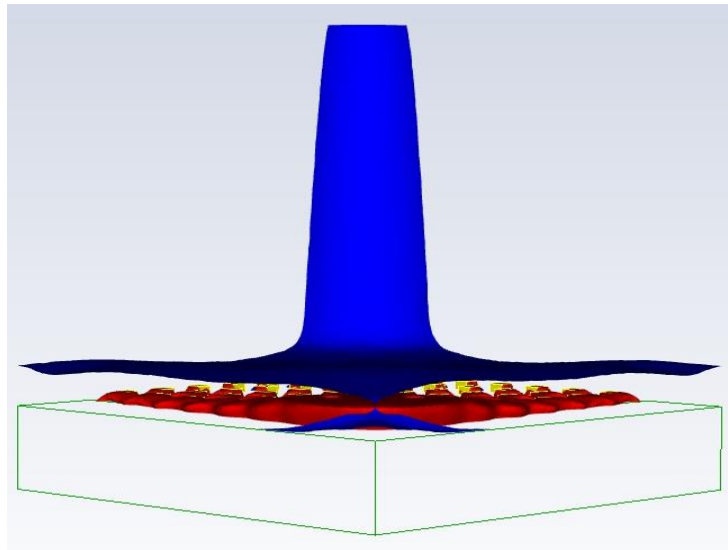
Figure 79: Parametric study: vapour column formation at a pin-fin height of 0.312 mm and spacing of 1.075 mm (liquid velocity above 0.3 m/s (blue) and cell vapour fraction above 0.5 (red))

5.3 Fin distribution

This section investigates the effect of pin-fin distribution on heat transfer and dry-out area contribution. Section 5.2 concluded that the highest pin-fins produced the highest heat transfer rate but only slightly eliminated the dry-out area contribution with an increase in pin-fin spacing. Figure 80 provides the dimensions and distribution of the current study with a pin-fin height of 2.5 mm, while all other domain dimensions remained constant. The star layout would potentially allow the liquid to reach the outer edges of the domain, decreasing the possibility of dry-out. The surface augmentation factor decreased slightly from 2.98 to 2.92 to allow for a symmetric star arrangement. The star arrangement was inspired by Jenkins *et al. [37]* and consisted of a flat surface at the jet stagnation region to allow the jet to spread towards the outer boundaries. The first ring of pin-fins was placed at a diameter of 7.66 mm, and the following pin-fins were placed at a radial pitch of 1.35 mm. The minimum distance between the pin-fins in the first ring was 0.9 mm, from which the spacing increased. An additional ray was created when the spacing between rows exceeded 2.3 mm to increase the surface augmentation at the outer edges. The current study had the same liquid inlet velocity of 2.716 m/s and a constant input heat flux of $23.24 \, W/cm^2$ as for the base case. All the data handling code of this section is provided in Appendix E: Parametric study: Pin-fin height, spacing and distribution.
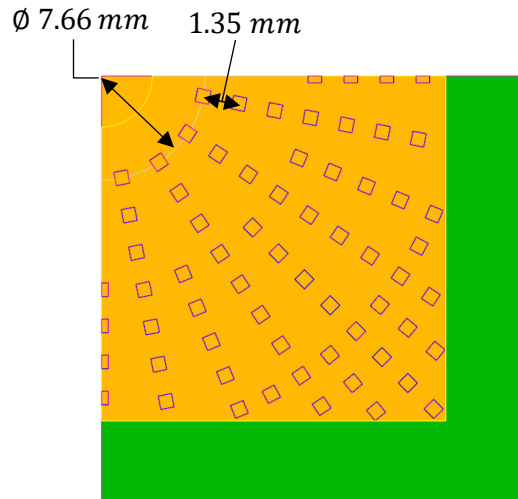
Figure 80: Parametric study: fin distribution layout

Figure 81 shows the single-phase liquid velocity distribution between the in-line arrangement (a) and the star arrangement (b). A clear increase in high-velocity zones was obtained in the star arrangement compared with the in-line arrangement. Even though the pin-fin arrangement changed at the stagnation region, the maximum liquid velocity at which the liquid accelerated after the stagnation region to the outlet boundary remained constant. As a result, the pressure drop across the domain for the two cases remained constant, highlighting the results from Section 0, namely that the pressure drop was mainly driven by the velocity inlet stagnation and not the flow obstructions in the pin-fin regions.

Figure 82 depicts the boiling curve comparison for the average base wall superheat between the in-line pin-fins and star pin-fin arrangements. The star arrangement led to a slight decrease in the average base wall superheat at an input heat flux of $23.24 \, W/cm^2$ even though the star arrangement had a slightly lower surface augmentation factor. The average dry-out area contribution at the base of the pin-fins decreased from 17% to less than 1%, eliminating the dry-out area contribution. The CHF of the star arrangement increased by a large amount, with the highest numerical result having a dry-out area contribution of 40%, located at the densely packed outer pin-fin region.
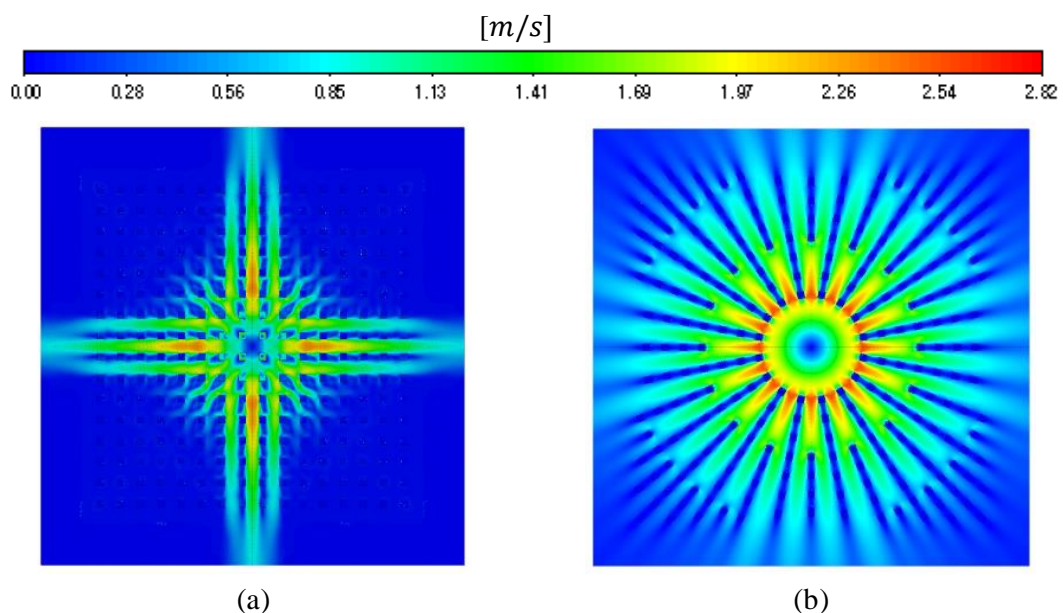
Figure 81: Parametric study: fin distribution liquid velocity of (a) in-line arrangement and (b) star arrangement [m/s]

88
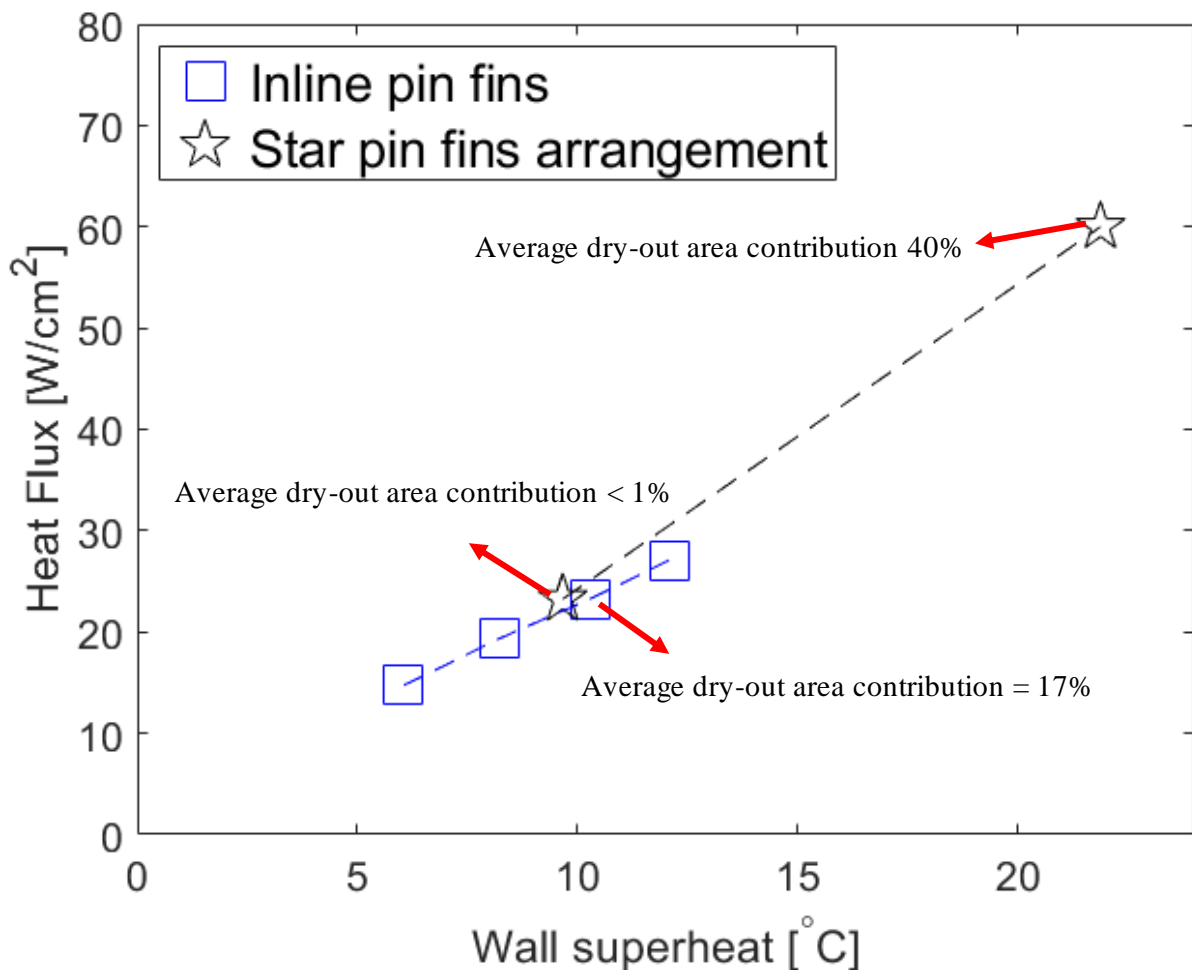
Figure 82: Parametric study: average base wall temperature boiling curve comparison between in-line pin-fins and star pin-fin arrangement

Figure 83 depicts the heat flux contribution plot, including the subdivisions of (a) convective heat flux, (b) quenching heat flux, (c) evaporative heat flux and (d) the total heat flux. The convective heat flux contribution increased with the star arrangement compared with the in-line pin-fin arrangement, with a maximum contribution from outside the stagnation region as the liquid accelerated to the outer edges of the domain. The quenching heat flux was the dominant heat flux throughout the domain of the liquid's ability to actively remove vapour from the heated surface due to decreased flow obstructions. Finally, the maximum evaporative heat flux was located at the outer edges of the domain as the density of the pin-fins increased. Therefore, the total heat flux corresponded to the quenching heat flux and would only correspond to the evaporative heat flux at a higher input heat flux.
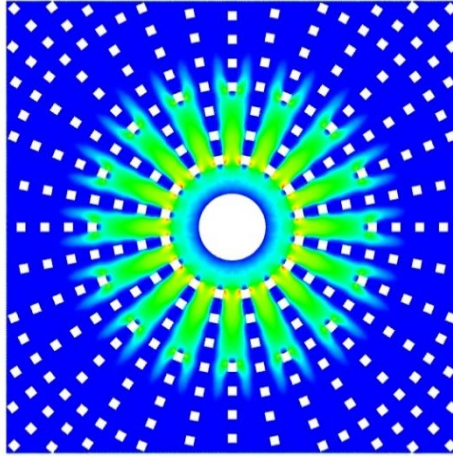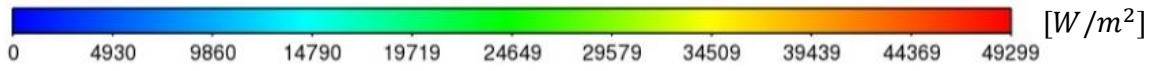
(a)
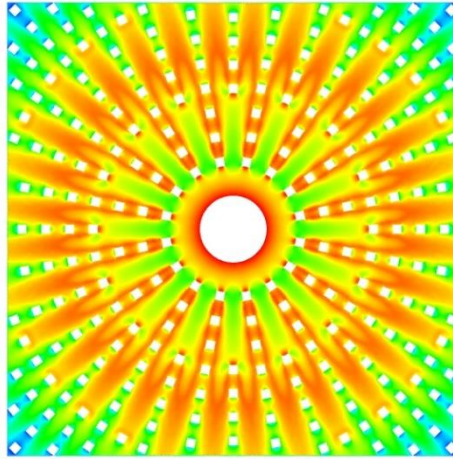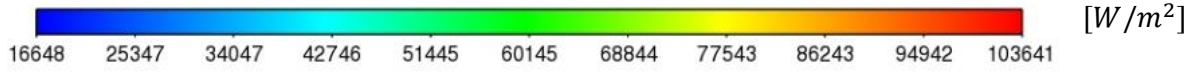
(b)
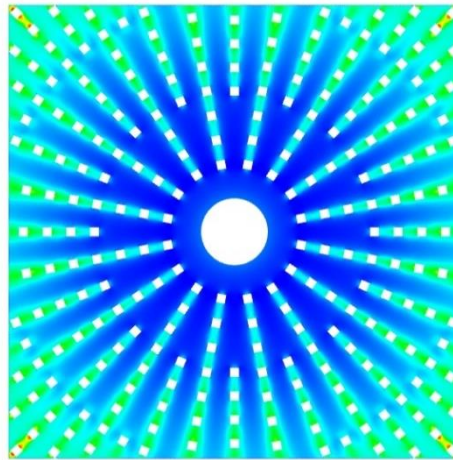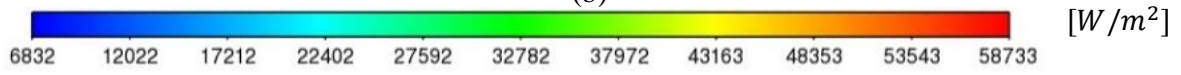
(c)
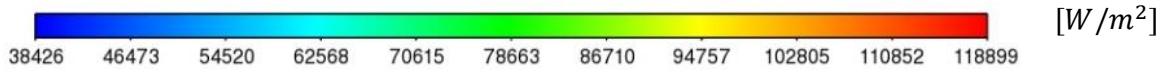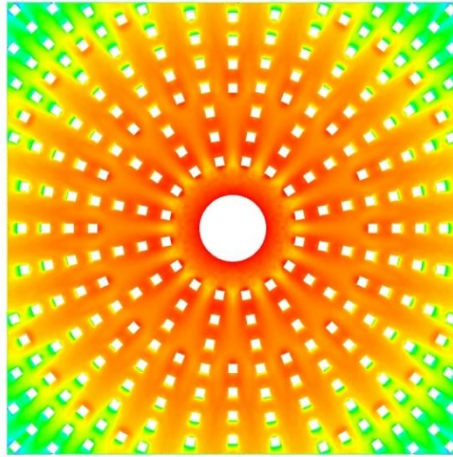
(d)

Figure 83: Contour plots of (a) the liquid convective heat flux, (b) quenching heat flux, (c) evaporative heat flux and (d) the total heat flux at a star pin-fin distribution while kept at a constant heat flux of 23.2 W/m^2

Figure 84: Parametric study: High liquid velocity and maximum vapour column distribution of the star pin-fin arrangement at the highest heat flux of $60\ W/cm^2$ shows the high liquid velocity and maximum vapour column distribution of the star pin-fin arrangement at the highest heat flux of $60\ W/cm^2$. The high-velocity liquid regions were obstructed by the evaporation vapour column and not by the pin-fins.Figure 84: Parametric study: High liquid velocity and maximum vapour column distribution of the star pin-fin arrangement at the highest heat flux of $60\ W/cm^2$ shows that the liquid formed a wave over the vapour column. The vapour column pushed through the high-velocity liquid region as the heat flux intensified.
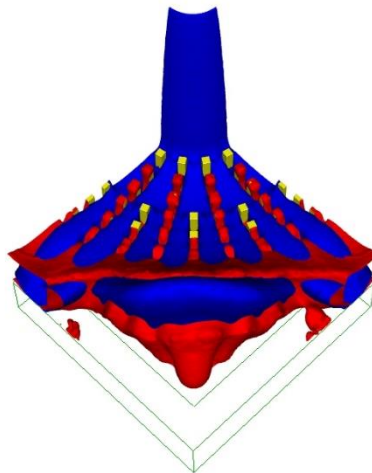
Figure 84: Parametric study: High liquid velocity and maximum vapour column distribution of the star pin-fin arrangement at the highest heat flux of $60\ W/cm^2$. (liquid velocity above 0.3 m/s (blue) and cell vapour fraction above 0.5 (red))

5.4 Parametric study conclusion

This section showed promising results regarding the enhancement of surface heat transfer and elimination of dry-out areas. The increase in jet inlet velocity increased the heat transfer at the stagnation region but had a limited capability to eliminate dry-out regions at the outer edge of the domain. The increase in pin-fin spacing and decrease in pin-fin height decreased flow obstruction and allowed the high-velocity liquid regions to spread over the domain. However, heat transfer was mainly linked to surface augmentation. Therefore, a pin-fin distribution study showed promising results to eliminate dry-out and increase heat transfer through keeping the surface augmentation factor as high as possible.

6 Conclusion and Future Work

6.1 Conclusions

This dissertation presented research on the numerical validation and optimisation of boiling jet impingement heat transfer on pin-fin surfaces. The inclusion of structured surfaces in boiling jet impingement resulted in highly complex flow patterns, creating different boiling regimes throughout the domain, including impingement boiling at the jet stagnation region, flow boiling in the pin-fin-formed channels perpendicular to the stagnation region and pool boiling in the outer regions of the domain due to the flow obstruction caused by the pin-fins. Various turbulence, interphase transfer and near-wall treatment models were investigated to determine the influence on flow patterns and heat transfer.

Chapter 4 validated the numerical model against the experimental results of Rau and Garimella [17], focusing on a single jet impinging on a surface populated with an array of in-line pin-fins. Corresponding to the experiments, a dielectric fluid HFE-7100 was used as the working fluid due to its low boiling point, high dielectric strength and high surface wettability. The key findings of this section were as follows:

1. The stagnation wall superheat was predicted within 9.95% of the experimental results at low heat fluxes, increasing to an error of 12.3% at higher heat fluxes. The inclusion of a y^+ insensitive near-wall treatment model increased numerical stability and accuracy due to the complex flow patterns between the pin-fins.
2. An increase in mesh density in the pin-fin vicinity increased the accuracy of the numerical model with hexahedral and polyhedral cells predicting identical stagnation wall temperatures with eight cells between opposing pin-fins. Hexahedral cells were the preferred cell type as they decreased computational costs while keeping the same accuracy level.
3. The fully developed nucleation boiling and dry-out area contributions resulted in cyclic behaviour over time due to the formation and dissipation of vapour in the outer regions of the domain.
4. An extended domain simulating the pressure drop over the orifice plate resulted in an accurate prediction of the pressure drop, mimicking the locations of the experimental pressure probes. However, the extended domain resulted in the same stagnation wall superheat prediction.
5. Turbulent kinetic energy increased with heat flux due to an increased turbulent interaction between the liquid and the vapour as boiling increased over the surface.
6. The temperature distribution on the top wall formed a cross through the domain, agreeing with the liquid velocity distribution. The liquid temperature at the outer edges of the domain created hot pockets around the vapour columns as the liquid transitioned to a vapour.

Chapter 5 presented a parametric study demonstrating the influence of the inlet jet Reynolds number, pin-fin height, spacing and distribution on heat transfer and evaporation area contributions. The key findings of this chapter were as follows:

1. Inlet jet Reynolds number
   a. The increase in jet velocity led to a higher stagnation pressure, increasing the hydrostatic pressure force exerted on evaporating bubbles in the stagnation regions, ultimately increasing heat transfer at the stagnation region.
   b. The increase in stagnation pressure also led to a higher pressure drop between the stagnation region and outlet boundaries, increasing the liquid acceleration towards the outlet and ultimately increasing heat transfer in the flow-boiling regions.

c. The distribution of liquid velocity across the domain was not affected by inlet jet velocity but by flow obstruction caused by the distribution and dimensions on the pin-fins, limiting the ability to reduce dry-out areas.

2. Pin-fin height and spacing
    a. The decrease in pin-fin height and increase in pin-fin spacing reduced flow obstruction and allowed liquid to reach the outer edges of the domain, reducing the dry-out area contributions.
    b. The decrease in the surface augmentation factor was detrimental to heat transfer as the surface area decreased of which heat could be transferred from the solid to the fluid.
    c. The pressure drop across all ranges of pin-fin height and spacing combinations remained approximately constant. Therefore, the pressure drop across the domain was mainly driven by the dynamic pressure difference and not the flow obstruction caused by the pin-fins.
    d. Turbulent kinetic energy increased with a decrease in pin-fin height due to eliminating stagnation regions in the pin-fin vicinity. As a result, the flow could move across the domain from the stagnation region, increasing the overall turbulence in the domain.

3. Pin-fin distribution
    a. Increasing high-velocity regions through decreasing flow obstruction eliminated the possibility of dry-out.
    b. Heat transfer remained constant with different pin-fin configurations at the same surface augmentation factor. Therefore, heat transfer was mainly linked to surface augmentation.

The surface augmentation factor and liquid velocity distribution are the most essential parameters to keep in mind throughout the design process. These parameters will increase heat transfer and decrease the possibility of dry-out regions.

6.2 Future work

This research study illustrated that surface enhancements in the form of pin-fins showed promising results in enhancing heat transfer in boiling jet impingement. Furthermore, heat transfer was successfully predicted with the RPI boiling model, resulting in a conservative model that underpredicted heat transfer at the stagnation region when compared with the experimental results. Therefore, if dry-out zones were eliminated, enhanced surfaces in boiling jet impingement could result in a higher heat transfer coefficient and effectively cool down modern-day high heat flux electronic components.

However, the following aspects need to be considered because boiling jet impingement on pin-fin surfaces has not yet been fully understood:

- Including structured surfaces increased turbulence near the heated wall. However, the effect of the wake created by each structure and the interference of adjacent pin-fin wakes on local heat transfer and dry-out needs to be better understood.
- Increasing the surface augmentation factor increased the average heat transfer between the solid and the liquid. However, densely packed pin-fins obstructed flow to reach the whole domain, leading to local dry-out and possible surface damage. Therefore, the microchip surface design process should allow the impinging liquid to reach the whole domain.
- To the best of the author's knowledge, boiling jet impingement on pin-fin surface experiments done up to date have only considered the stagnation temperature when plotting the boiling curve. The CFD model correlated well with the experimental results at the stagnation temperature. However, no experimental data were available to compare the CFD

results with the wall temperature across the whole surface; similarly, for the vapour formation in the outer regions of the domain.

- The single jet created dry-out regions. Thus, a further investigation needs to consider implementing a multi-jet array to cool down the dry-out areas. Different spent fluid removal techniques also need to be investigated in parallel with a multi-jet array to remove vapour forming between the jets actively.

Before pin-finned surfaces can be implemented in boiling jet impingement, the following challenges have to be met:

- The current study showed that the hydrostatic pressure drop between the jet inlet and stagnation region dominated the pressure drop at a jet-to-target spacing of 4 H/D, thus the surface could be altered to optimise heat transfer without significantly increasing the pressure drop at 4 H/D. However, the influence of surface argumentation on the pressure drop would increase if the jet-to-target spacing decreased.

- The use of a dielectric fluid in the current study allowed the fluid to be in direct contact with the electronic component. However, the influence of different dielectric fluids on heat transfer needs further investigation to find a link between the fluid properties and turbulence produced throughout the domain. The role of saturation temperature, latent heat and heat capacity needs to be explored to find their relationship with respect to an ideal surface temperature range.

- Other surface enhancement techniques in the form of turbulators should be investigated to further increase the turbulent production in the domain. A "sweet spot" must be found between the surface augmentation factor and turbulence production.

References

1.   S.M. Ghiaasiaan, *Two-phase flow, boiling and condensation*. 2008, New York: Cambridge University Press.
2.   F.M. White and H. Xue, *Fluid Mechanics*. 9th ed. 2021, New York, NY: McGraw Hill LLC.
3.   A.B. Ahmed and M.S. Hamed, Bubble dynamics under an impinging jet. *12th International Conference on Heat Transfer, Fluid Mechanics and Thermodynamics*, 2016.
4.   N. Zuckerman and N. Lior, Jet impingement heat transfer: physics, correlations, and numerical modeling. *Advances in Heat Transfer*, 2006. **39**: p. 565-631.
5.   C. Agrawal, Surface quenching by jet impingement, A review. *Steel Research International*, 2019. **90**(1800285).
6.   H. Fayyaz and A. Shah, Steady viscous flow inside deep, shallow and skewed cavities by an implicit Navier-Stokes solver. *International Journal of Advanced and Applied Sciences*, 2018. **5**(1): p. 170-176.
7.   Z. Zhang, X. Wang, and Y. Yan, A review of the state-of-the-art in electronic cooling. *e-Prime - Advances in Electrical Engineering, Electronics and Energy Conversion and Management*, 2021. **1**.
8.   S.V.J. Narumanchi, V. Hassani, and D. Bharathan, *Modeling single-phase and boiling liquid jet impingement cooling in power electronics*. 2005, National Renewable Energy Laboratory: Colorado.
9.   K. Esmailpour, A. Azizi, and S.M. Hosseinalipour, Numerical study of jet impingement subcooled boiling on superheated surfaces. *Scientia Iranica*, 2019. **26**(B): p. 2369-2381.
10.   H.H. Cho, K.M. Kim, and J. Song, *Applications of impingement jet cooling systems*, in *Cooling systems: Energy, engineering and applications*. 2011, Nova Science Publishers: New York.
11.   V.S. Devahdhanush and I. Mudawar, Review of critical heat Flux (CHF) in jet impingement boiling. *International Journal of Heat and Mass Transfer*, 2021. **169**.
12.   Y.-h. Qiu and Z.-h. Liu, Critical heat flux in saturated and subcooled boiling for R-113 jet impingement on the stagnation zone. *Applied Thermal Engineering*, 2005. **25**: p. 2367-2378.
13.   H.C. Unal, Maximum bubble diameter, maximum bubble-growth time and bubble-growth rate during the subcooled nucleate flow boiling of water up to 17.7 mn/m2. *International Journal of Heat and Mass Transfer*, 1975. **19**: p. 643-649.
14.   H. Bian, C. Kurwitz, Z. Sun, K. Cheng, and K. Chen, Enhanced nucleate boiling on 3D-printed micro-porous structured surface. *Applied Thermal Engineering*, 2018. **141**: p. 422-434.
15.   J. Du, C. Zhao, and H. Bo, Investigation of bubble departure diameter in horizontal and vertical subcooled flow boiling. *International Journal of Heat and Mass Transfer*, 2018. **127**: p. 796-805.
16.   G. Liang and I. Mudawar, Review of nanoscale boiling enhancement techniques and proposed systematic testing strategy to ensure cooling reliability and repeatability. *Applied Thermal Engineering*, 2021. **184**.
17.   M.J. Rau and S.V. Garimella, Confined jet impingement with boiling on a variety of enhanced surfaces. *American Society of Mechanical Engineers Journal of Heat Transfer*, 2014. **136**.
18.   P. Sikdar, K.P. Sinhamahapatra, and S.M. Dash, *Lattice boltzmann simulations of a lid-driven cavity at different moving lengths of the top lid*, in *National Conference on Fluid Mechanics and Fluid Power (FMFP)*. 2019: PSG College of Technology, Coimbatore, India.
19.   F.L. Cui, F.J. Hong, and P. Cheng, Comparison of normal and distributed jet array impingement boiling of HFE-7000 on smooth and pin-fin surfaces. *International Journal of Heat and Mass Transfer*, 2018. **126**: p. 1287-1298.
20.   W. Wana, D. Deng, Q. Huang, T. Zeng, and Y. Huang, Experimental study and optimization of pin fin shapes in flow boiling of micro pin fin heat sinks. *Applied Thermal Engineering*, 2017. **114**: p. 436-449.

21.   S. Feng, Y. Yan, and C. Lai, Experimental study on flow boiling characteristics of hybrid micro-channels with gradient distribution pillars and bypass. *International Journal of Heat and Mass Transfer*, 2022. **186**.

22.   V.S. Devahdhanush and I. Mudawar, Critical heat flux of confined round single jet and jet array impingement boiling. *International Journal of Heat and Mass Transfer*, 2021. **169**.

23.   M.J. Rau, S.V. Garimella, E.M. Dede, and S.N. Joshi, Boiling heat transfer from an array of round jets with hybrid surface enhancements. *The American Society of Mechanical Engineers Journal of Heat Transfer*, 2015. **137**.

24.   S.A. Zaki, A.Z. Jaafar, h.F. Mohammad, M.S.M. Ali, and A.A. Razak, Investigation of surface roughness impact on mean wind flow using RNG k-ε model. *Jurnal Teknologi (Sciences & Engineering)*, 2016. **78**: p. 21-28.

25.   R.J. McGlen, R. Jachuck, and S. Lin, Integrated thermal management techniques for high power electronic devices. *Applied Thermal Engineering*, 2004. **24**: p. 1143–1156.

26.   Y. Deng, M. Zhang, Y. Jiang, and J. Liu, Two-stage multichannel liquid-metal cooling system for thermal management of high-heat-flux-density chip array. *Energy Conversion and Management*, 2022. **259**.

27.   H. Herwig, High heat flux cooling of electronics: The need for a paradigm shift. *American Society of Mechanical Engineers Journal of Heat Transfer*, 2013. **135**: p. 1-2.

28.   J.R. Black, Electromigration-A brief survey and some recent results. *IEEE Transactions on Electron Devices*, 1969. **16**(4).

29.   K. Nishikawa, Historical devolpment in the research of boiling heat transfer. *The Japan Society of Mechanical Engineers International Journal*, 1987. **30**.

30.   J.G. Leidenfrost, On the fixation of water in diverse fire. *International Journal of Heat Transfer*, 1966. **9**(11): p. 1153-1166.

31.   M. Jakob, Heat transfer in evaporation and condensation. *Mechanical Engineering*, 1936. **58**: p. 643-660.

32.   S.G. Kandlikar, *Similarities and differences between flow boiling in microchannels and pool boiling*, in *2nd Micro and Nano Flows Conference*. 2009.

33.   M.J. Rau and S.V. Garimella, Local two-phase heat transfer from arrays of confined and submerged impinging jets. *International Journal of Heat and Mass Transfer*, 2013. **67**: p. 487-498.

34.   R. Viskanta, Heat transfer to impinging isothermal gas and flame jets. *Experimental Thermal and Fluid Science*, 1993. **6**: p. 111-134.

35.   H. Martin, Heat and mass transfer between impinging gas jets and solid surfaces. *Advances in Heat Transfer*, 1977. **13**: p. 1-60.

36.   S. Ndao, Y. Peles, and M.K. Jensen, Experimental investigation of flow boiling heat transfer of jet impingement on smooth and micro structured surfaces. *International Journal of Heat and Mass Transfer*, 2012. **55**: p. 5093-5101.

37.   R. Jenkins, R. Lupoi, R. Kempers, and A.J. Robinson, Heat transfer performance of boiling jet array impingement on micro-grooved surfaces. *Experimental Thermal and Fluid Science*, 2017. **80**: p. 293-304.

38.   S. Narumanchi, A. Troshko, D. Bharathan, and V. Hassani, Numerical simulations of nucleate boiling in impinging jets: Applications in power electronics cooling. *International Journal of Heat and Mass Transfer*, 2008. **51**: p. 1-12.

39.   S. Abishek, R. Narayanaswamy, and V. Narayanan, Effect of heater size and Reynolds number on the partitioning of surface heat flux in subcooled jet impingement boiling. *International Journal of Heat and Mass Transfer*, 2013. **59**: p. 247-261.

40.   K. Esmailpour, A. Azizi, and S.M. Hosseinalipour, Numerical study of jet impingement subcooled boiling on superheated surfaces. *Scientia Iranica*, 2019. **26**: p. 2369-2381.

41.   L. Qiu, S. Dubey, F.H. Choo, and F. Duan, Effect of conjugation on jet impingement boiling heat transfer. *International Journal of Heat and Mass Transfer*, 2015. **91**: p. 584-593.

42.   D. Wright, K.J. Craig, P. Valluri, and J.P. Meyer, Computational investigation of single and multi-jet array impingement boiling. *Applied Thermal Engineering*, 2023. **218**.

43. L. Hussain, M.M. Khan, M. Masud, F. Ahmed, Z. Rehman, Ł. Amanowicz, and K. Rajski, Heat transfer augmentation through different jet impingement techniques: A state-of-the-art review. *Energies*, 2021. **14**(20).

44. M. Molana and S. Banooni, Investigation of heat transfer processes involved liquid impingement jets: A review. *Brazilian Journal of Chemical Engineering*, 2013. **30**: p. 413-435.

45. K.S. Choo and S.J. Kim, Comparison of thermal characteristics of confined and unconfined impinging jets. *International Journal of Heat and Mass Transfer*, 2010. **53**: p. 3366–3371.

46. K. Jambunathan, E. Lai, M.A. Moss, and B.L. Button, A review of heat transfer data for single circular jet impingement. *International Journal of Heat and Fluid Flow*, 1993. **13**: p. 106-115.

47. H. Reichardt, Gesetzmiissigkeiten der freien Turbulenz. *VDI Forschungsheft*, 1942. **414**.

48. S. Nawani and M. Subhash, A review on multiple liquid jet impingement onto flat plate. *Materials Today: Proceedings*, 2021. **46**: p. 11190-11197.

49. K. Abe and K. Suga, Large eddy simulation of passive scalar in complex turbulence with flow impingement and flow separation. *Heat Transfer—Asian Research*, 2001. **30**: p. 402-418.

50. Y.A. Cengel and A.J. Ghajar, *Heat and mass transfer: Fundamentals and applications*. Vol. 6. 2020, New York, NY: McGraw-Hill Education.

51. J.H. Lienhard, *Heat transfer by impingement of circular free-surface liquid jets*, in *7th ISHMT-ASME Heat and Mass Transfer Conferences*. 2006: IIT Guwahati, India.

52. L.S. Tong and Y.S. Tang, *Boiling heat transfer and two-phase flow*. Series in Chemical and Mechanical Engineering, ed. G.F. Hewitt and C.L. Tien. Vol. Second Edition. 2010, New York: CRC Press.

53. S. Nuklyama, The maximum and minimum values of the heat q transmitted from metal to boiling water under atmospheric pressure. *International Journal of Heat and Mass Transfer*, 1934. **9**: p. 1419-1433.

54. S. Jun, J. Kim, S.M. You, and H.Y. Kim, Effect of subcooling on pool boiling of water from sintered copper microporous coating at different orientations. *Science and Technology of Nuclear Installations*, 2018. **2018**: p. 9.

55. Y.Y. Jiang, H. Osada, M. Inagaki, and N. Horinouchi, Dynamic modeling on bubble growth, detachment and heat transfer for hybrid-scheme computations of nucleate boiling. *International Journal of Heat and Mass Transfer*, 2013. **56**: p. 640-652.

56. Y. Koizumi, M. Shoji, M. Monde, Y. Takata, and N. Nagai, *Boiling research and advances*. 2017, Amsterdam: Elsevier.

57. S. Fan and F. Duan, Correlations for heat transfer characteristics of the onset of nucleate boiling in submerged jet impingement. *International Journal of Thermal Sciences*, 2021. **170**(107071).

58. R. Cardenas and V. Narayanan, Submerged jet impingement boiling of water under subatmospheric conditions. *American Society of Mechanical Engineers Journal of Heat Transfer*, 2012. **134**.

59. Y. Katto and M. Kunihiro, Study of the mechanism of burn-out in boiling systems of high burn-out heat flux. *The Japan Society of Mechanical Engineers International Journal*, 1973. **16**: p. 1357-1366.

60. R. Cardenas and V. Narayanan, Heat transfer characteristics of submerged jet impingement boiling of saturated FC-72. *International Journal of Heat and Mass Transfer*, 2012. **55**: p. 4217-4231.

61. Y. Katto and M. Shimizu, Upper limit of CHF in the saturated forced convection boiling on a heated disk with a small impinging jet. *American Society of Mechanical Engineers Journal of Heat Transfer*, 1979. **101**: p. 265-269.

62. Monde, Masanori, Kusuda, Hisao, Uehara, and Haruo, Burnout heat flux in saturated forced convection boiling with two or more impinging jets. *Heat Transfer - Japanese Research*, 1980. **9**: p. 18-31.

63. R.K. Skema and A.A. Slanciauskas, Critical heat fluxes at jet cooled flat surfaces. *Heat Transfer in Electronic and Microelectronic Equipment* 1990: p. 621-626.

64. V.V. Sychev, V.V. Sychev, A.I. Ruban, and G.L. Korolev, *Asymptotic theory of separated flows*. 1998: Cambridge University Press.

65. M.J. Esteve, P. Reulet, and P. Millan, Flow field characterisation within a rectangular cavity.

66.   I. Pranoto, M.A. Rahman, and J. Waluyo, The role of pin fin array configurations and bubble characteristics on the pool boiling heat transfer enhancement. *Fluids*, 2022. **7**.

67.   K.N. Rainey and S.M. You, Pool boiling heat transfer from plain and microporous, square pin-finned surfaces in saturated FC-72. *American Society of Mechanical Engineers Journal of Heat Transfer*, 2000. **122**: p. 509-516.

68.   F.P. Incropera, D.P. Dewitt, T.L. Bergman, and A.S. Lavine, *Fundamentals of Heat and Mass Transfer*. Vol. 6. 2007: John Wiley & Sons, Inc.

69.   D.C. Wadsworth and I. Mudawar, Enhancement of single-phase heat transfer and critical heat flux from an ultra-high-flux simulated microelectronic heat source to a rectangular impinging jet of dielectric liquid. *American Society of Mechanical Engineers Journal of Heat Transfer*, 1992. **114**: p. 764-768.

70.   M. Ariz, N. Huda, and A. Husain, Thermal performance analysis of jet impingement with effusion scheme. *Procedia Engineering*, 2015. **127**: p. 110-117.

71.   ANSYS, *Ansys Fluent Theory Guide*. 2022.

72.   H.K. Versteeg and W. Malalasekera, *An introduction to computational fluid dynamics*. Second Edition ed. 2007, Glasgow: Pearson Education Limited.

73.   E. Guerrero, F. Muñoz, and N. Ratkovich, Comparison between eulerian and vof models for two-phase flow assessment in vertical pipes. *Journal of Oil, Gas and Alternative Energy Sources*, 2017. **7**(1): p. 73-84.

74.   M. Shademan, *CFD simulation of impinging jet flows and boiling heat transfer*, in *Department of Mechanical, Automotive & Materials Engineering*. 2015, University of Windsor: Windsor, Ontario, Canada.

75.   S.E. Kim and D. Choudhury, A near-wall treatment using wall functions sensitized to pressure gradient. *The American Society of Mechanical Engineers*, 1995. **2017**.

76.   A. Tomiyama, Struggle with computational bubble dynamics. *Multiphase Science and Technology*, 1998. **10**: p. 369-405.

77.   S.P. Antal, R.T. Lahey, and J.E. Flaherty, Analysis of phase distribution in fully developed laminar bubbly two-phase flow. *International Journal of Multiphase Flow*, 1991. **17**: p. 635-652.

78.   M. Lopez de Bertodano, R.T. Lahey, and O.C. Jones, Turbulent bubbly two-phase flow data in a triangular duct. *Nuclear Engineering and Design*, 1994. **146**: p. 43-52.

79.   A.A. Troshko and Y.A. Hassan, A two-equation turbulence model of turbulent bubbly flows. *International Journal of Multiphase Flow*, 2001. **27**: p. 1965-2000.

80.   S.M.A.N.R. Abadi, A. Ahmadpour, and J.P. Meyer, Numerical simulation of pool boiling on smooth, vertically aligned tandem tubes. *International Journal of Thermal Sciences*, 2018. **132**: p. 628-644.

81.   Z. Xiaobin, X. Wei, C. Jianye, W. Yuchen, and K. Tang, CFD simulations and experimental verification on nucleate pool boiling of liquid nitrogen. *Physics Procedia*, 2015. **67**: p. 569-575.

82.   J. Gu, Q. Wang, Y. Wu, J. Lyu, S. Li, and W. Yao, Modeling of subcooled boiling by extending the RPI wall boiling model to ultra-high pressure conditions. *Applied Thermal Engineering*, 2017. **124**: p. 571–584.

83.   D.M. Godino, S.F. Corzo, and D.E. Ramajo, CFD simulation of conjugated heat transfer with full boiling in OpenFOAM(R). *Applied Thermal Engineering*, 2022. **213**(118627).

84.   D.-w. Yuan, L.-m. Pan, D. Chen, H. Zhang, J.-h. Wei, and Y.-p. Huang, Bubble behavior of high subcooling flow boiling at different system pressure in vertical narrow channel. *Applied Thermal Engineering*, 2011. **31**: p. 3512-3520.

85.   J.Y. Tu and G.H. Yeoh, On numerical modelling of low-pressure subcooled boiling flows. *International Journal of Heat and Mass Transfer*, 2002. **45**: p. 1197–1209.

86.   B. Koncar, I. Kljenak, and B. Mavko, Modelling of local two-phase flow parameters in upward subcooled flow boiling at low pressure. *International Journal of Heat and Mass Transfer*, 2004. **47**: p. 1499–1513.

87.   N. Kurul, *Multidimensional effects in two-phase flow including phase change*. 1990, Rensselaer Polytechnic Institute.

88. H. Anglart. *Modelling of vapour generation at wall in subcooled boiling two-phase flow*. in *First CFDS international user conference*. 1993. Oxford, UK.

89. H. Anglart and O. Nylund, CFD application to prediction of void distribution in two-phase bubbly flows in rod bundles. *Nuclear Engineering and Design*, 1996. **163**: p. 81-98.

90. N. Kurul and M.Z. Podowski. *On the modeling of multidimensional effects in boiling channels*. in *Proceedings of the 27th National Heat Transfer Conference*. 1991. Minneapolis, Minnesota, USA.

91. V.H. Del Valle and D.B.R. Kenning, Subcooled flow boiling at high heat flux. *International Journal of Heat and Mass Transfer*, 1985. **28**: p. 1907-1920.

92. R. Cole, A photographic study of pool boiling in the region of the critical heat flux. *American Institute of Chemical Engineers*, 1960: p. 538.

93. E. Krepper and R. Rzehak, CFD for subcooled flow boiling: Simulation of DEBORA experiments. *Nuclear Engineering and Design*, 2011. **241**: p. 3851–3866.

94. M. Lemmert and L.M. Chawla, Influence of flow velocity on surface boiling heat transfer coefficient in heat transfer in boiling. *Academic Press and Hemisphere*, 1977.

95. N.W. Snyder and T.T. Robin, Mass-transfer model in subcooled nucleate boiling. *ASME Journal of Heat and Mass Transfer*, 1969. **91**: p. 404-411.

96. M.G. Cooper and A.J.P. Lloyd. *Transient local heatflux in nucleate boiling*. in *Proceedings of Third International Heat Transfer Conference,*. 1966. Chicago, Illinois.

97. M.G. Cooper, The microlayer and bubble growth in nucleate pool boiling,. *International Journal of Heat and Mass Transfer*, 1969. **12**: p. 915-934.

98. K. Torikai, M. Hori, M. Akiyama, T. Kobori, and H. Adachi, *Boiling heat transfer and burnout mechanism in boiling-water cooled reactor.*, in *Third United Nations International Conference on the Peaceful Uses of Atomic Energy*. 1964.

99. A.H. Abdelmessih, F.C. Hooper, and S. Nangia, Flow effects on bubble growth and collapse in surface boiling,. *International Journal of Heat and Mass Transfer*, 1972. **15**: p. 115-125.

100. M.H. Rausch, L. Kretschmer, S. Will, A. Leipertz, and A.P. Fröba, Density, Surface Tension, and Kinematic Viscosity of Hydrofluoroethers HFE-7000, HFE-7100, HFE-7200, HFE-7300, and HFE-7500. *Journal of Chemical & Engineering Data*, 2015. **60**: p. 3759-3765.

101. ANSYS, *Ansys Fluent User's guide*. 2022.

Appendix A: Numerical model validation of jet impingement boiling on flat surfaces

This section tests the numerical model against experimental and previous numerical work on jet impingement boiling on flat surfaces. The current numerical model is validated against the experimental work of Devahdhanush and Mudawar [22] and the numerical work of Wright *et al.* [42], included in Figure A-2. Devahdhanush and Mudawar [22] experimentally investigated a confined multi-jet array impinging on a square flat surface with the working fluid as R134a. A detailed description of the experimental setup is given by Devahdhanush and Mudawar [22] and Wright *et al.* [42]. Tabel A-1 includes a summary of the domain conditions [42].

Table A-1: Devahdhanush and Mudarwar [22] domain conditions

Parameter	Value
Nozzle diameter [mm]	2.06
Number of nozzles	9
Jet to target spacing	2.29
Jet inlet velocity [m/s]	4.01
Mass flowrate [kg/s]	0.1476
Saturation pressure [Pa]	771278
Saturation temperature [˚C]	29.14
Inlet temperature [˚C]	20.14

Wright *et al.* [42] outlined the domain parameters, included in Figure A-1. The numerical domain includes a copper block with fibreglass insulation.
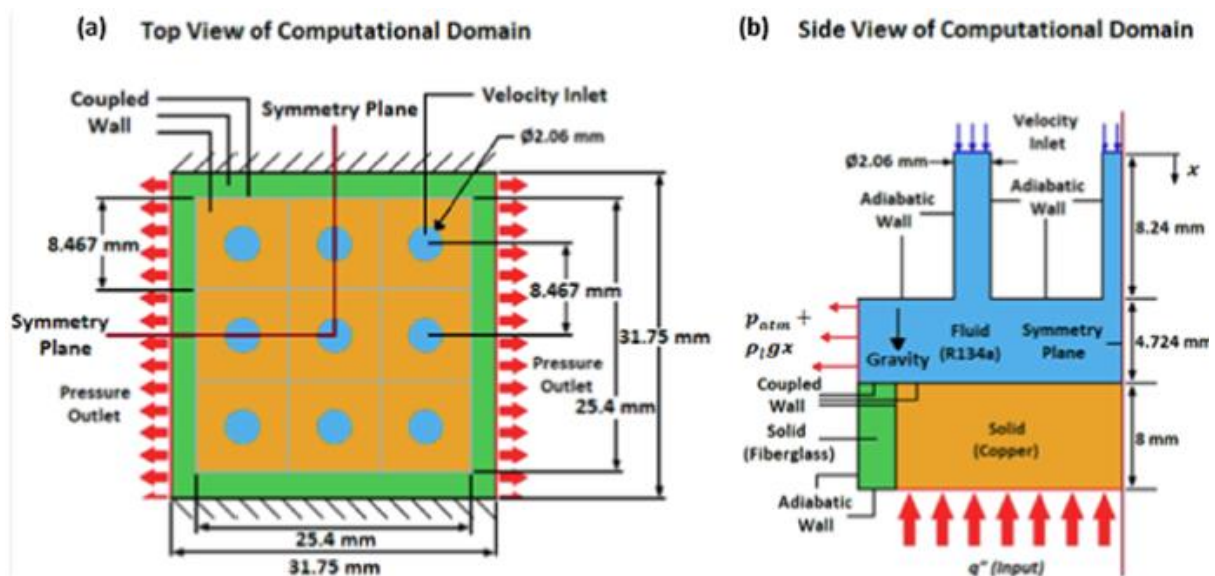
Figure A-1: 3D domain parameters of Devahdhanush and Mudarwar [21], outlined by Wright *et al.* [41] of (a) top view and (b) side view on the symmetry plane

Table A-2 includes the fluid properties of R134a at saturation pressure.

Table A-2: Devahdhanush and Mudarwar [22] fluid properties, outlined by Wright *et al.* [42].

Fluid		R134a
Surface tension (N/m)		0.0075
	Liquid	Vapour
Temperature [˚C]	20.14	29.14
Density [kg/m^3]	1 224.82	36.60
Specific heat [J/kg·K]	1405.9	1059.44
Dynamic viscosity [$N \cdot s/m^2$]	2.0701E-04	1.1869E-05
Thermal conductivity [W/m·K]	0.0832	0.0142
Specific enthalpy [J/kg]	227 665	414 399

The current model produced similar results to Wright *et al.* [42] in the fully developed nucleation boiling regime, slightly outperforming Wright *et al.* [42] at lower heat fluxes and capturing the slope of the boiling curve. As with Wright *et al.* [42], the current model struggled to accurately capture the departure from nucleation boiling as the slope of the current result's curve remains unchanged and the results can not be trusted beyond this point.

The validation of the current model on a flat surface proves the robustness of the current model and can be used to predict the boiling curve of jet impingement on both pin-fin and flat surfaces. Although the current model produces similar results to Wright *et al.* [42], it is recommended to use the numerical model of Wright *et al.* [42] on flat surfaces, as a coarser mesh can be used which will save computational costs.
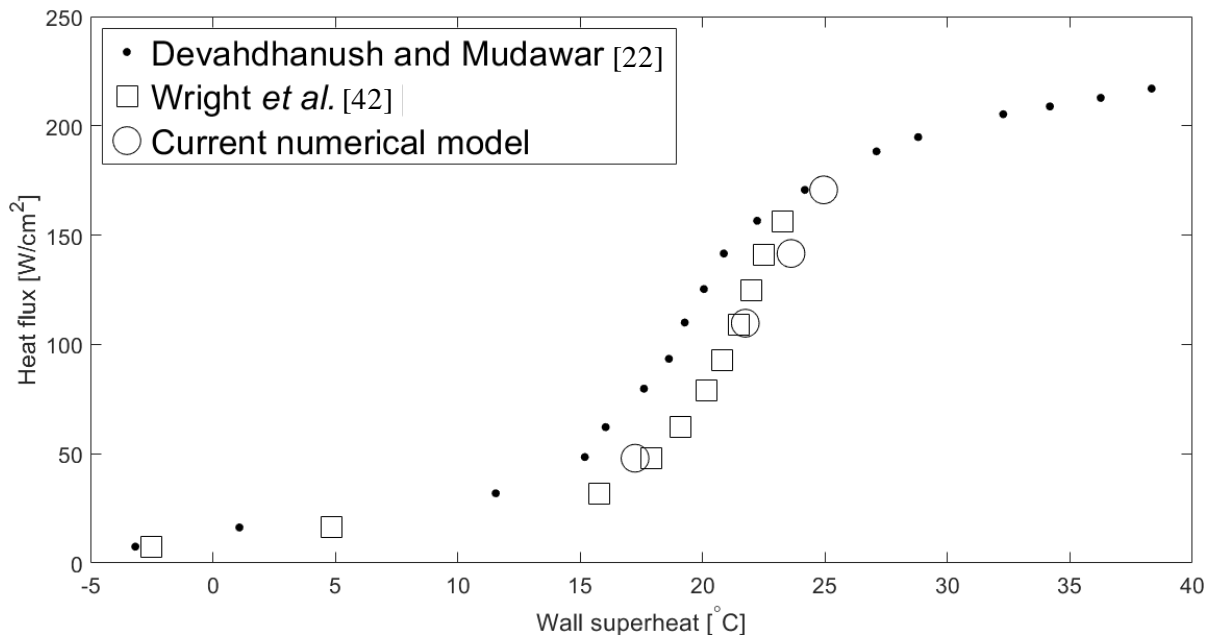
Figure A-2: Numerical validation of boiling jet impingement on a flat surface

Appendix B: Vapour formation comparison based on the selected domain

This section compares the current computational domain used in this study with an extended domain to analyse the differences, if any, in flow patterns and vapour formation through changing the selected control volume. Figure B-1 compares the chosen compare volumes with the experimental setup. The control volume is extended (Figure B-1, red) to investigate the effect of the change in outlet position and the inclusion of a side wall on the fluid flow, bubble formation, growth and departure.
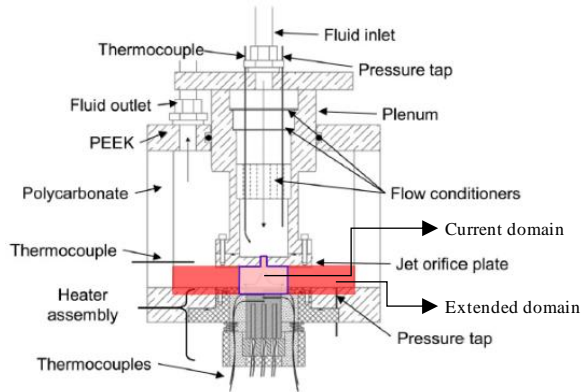
Figure B-1: Selected control volumes on experimental setup with the current study in highlighted in purple and the extended domain highlighted in red.

Figure B-2 compares the current study's (a) top view and (b) symmetry plane side view with the extended domain's (c) top view and (d) symmetry plane side view.

(a)

(b)

(c)

(d)
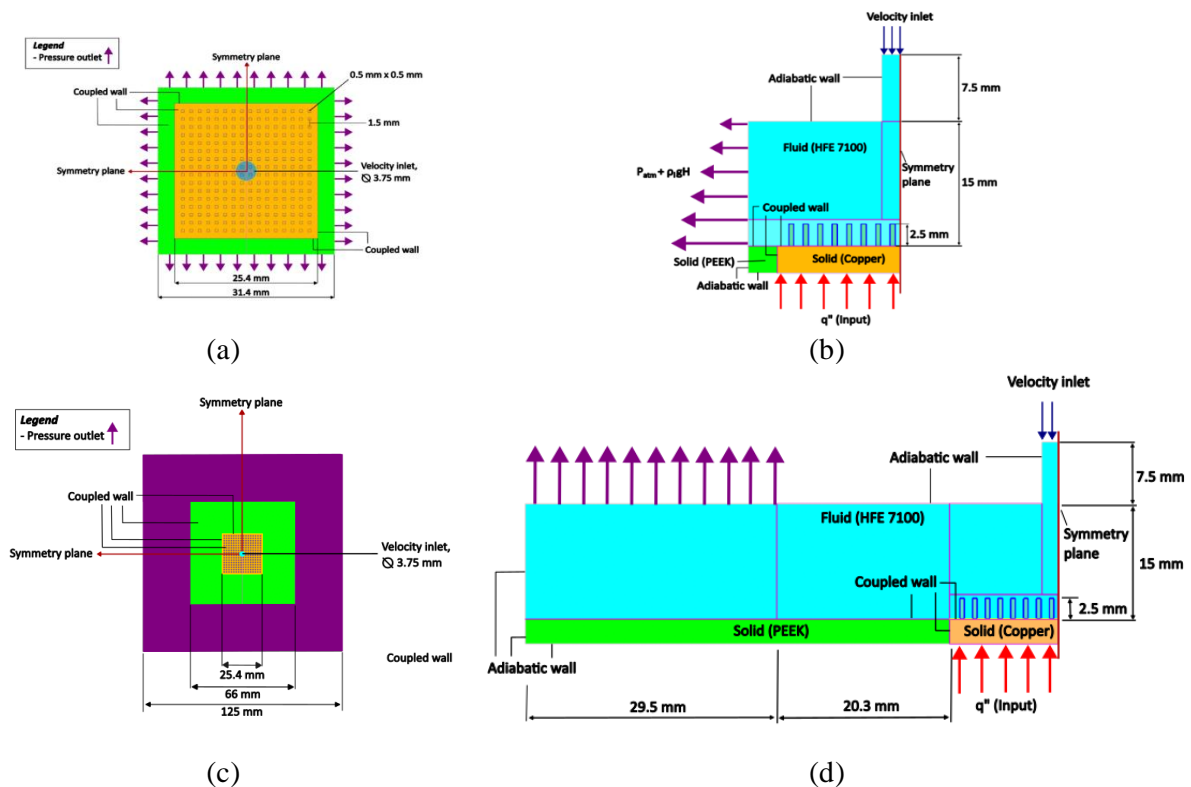
Figure B-2: Computational domain comparison of the current study's (a) top view and (b) symmetry plane side view, and the extended domain's (c) top view and (d) symmetry plane side view, including the effects of conjugation.

Figure B-3 compares the single-phase liquid velocity of the current domain and the extended domain. Both domains resulted in equivalent liquid velocity profiles, with high liquid-velocity regions in the jet and between the pin fins. The liquid pressure also resulted in equivalent pressure profiles (see Figure B-4). The liquid velocity flow paths (see Figure B-5) are also equivalent as the flow spreads from the jet stagnation region towards the outer edges of the copper block.

(a)

(b)
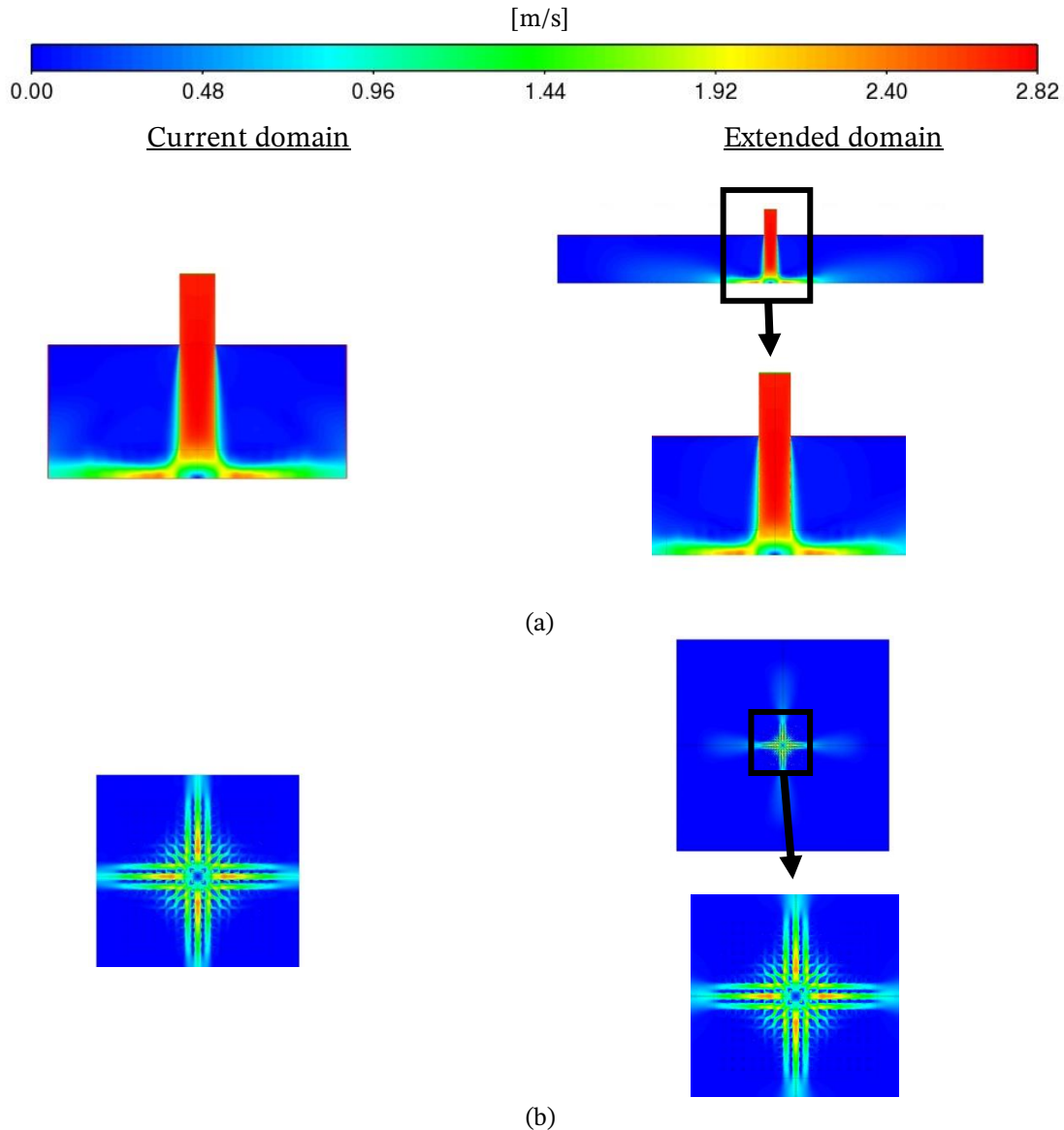
Figure B-3: Liquid velocity comparison of the current domain (left) and the extended domain (right) of (a) side view and (b) top view of the base wall.

A heat flux of $23.4\ W/cm^2$ is applied to the bottom of the copper block to compare the stagnation wall temperature and vapour formation in the domain. The comparison in stagnation wall superheat resulted in a negligible difference of 1 %. It is important to note that Ansys Fluent's Eulerian multiphase model does not resolve the interface between the phases [71]. Thus, the vapour formation represents a column of vapour bubbles. A negligible difference in vapour formation is found between the two domains over a single cycle, as shown in Figure B-6.

This extended study concludes that the assumed flow conditions and control volume of the current study is adequate to accurately validate the experimental study of Rau and Garimella [17].
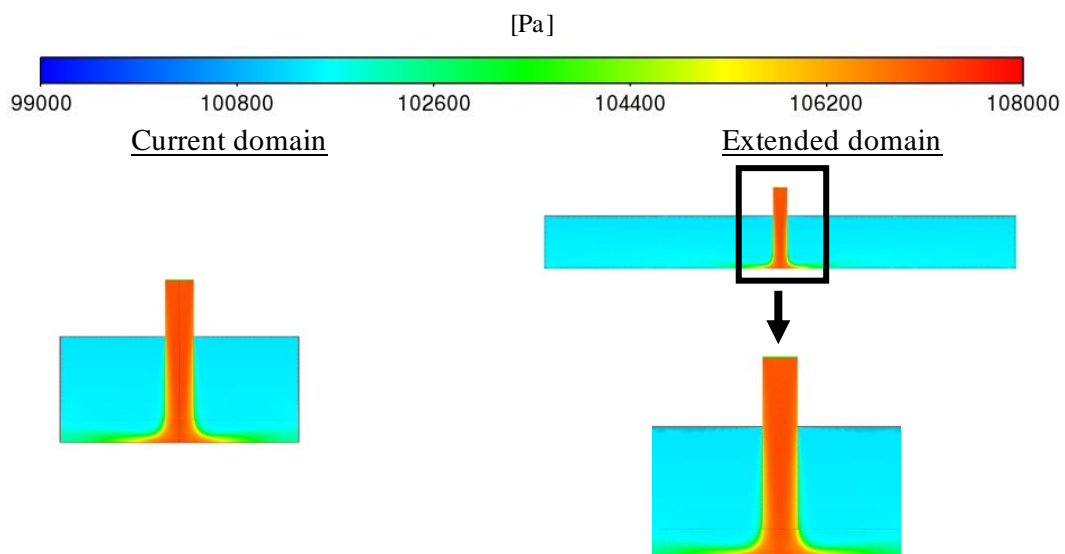
Figure B-4: Liquid pressure comparison of the current domain (left) and the extended domain (right).
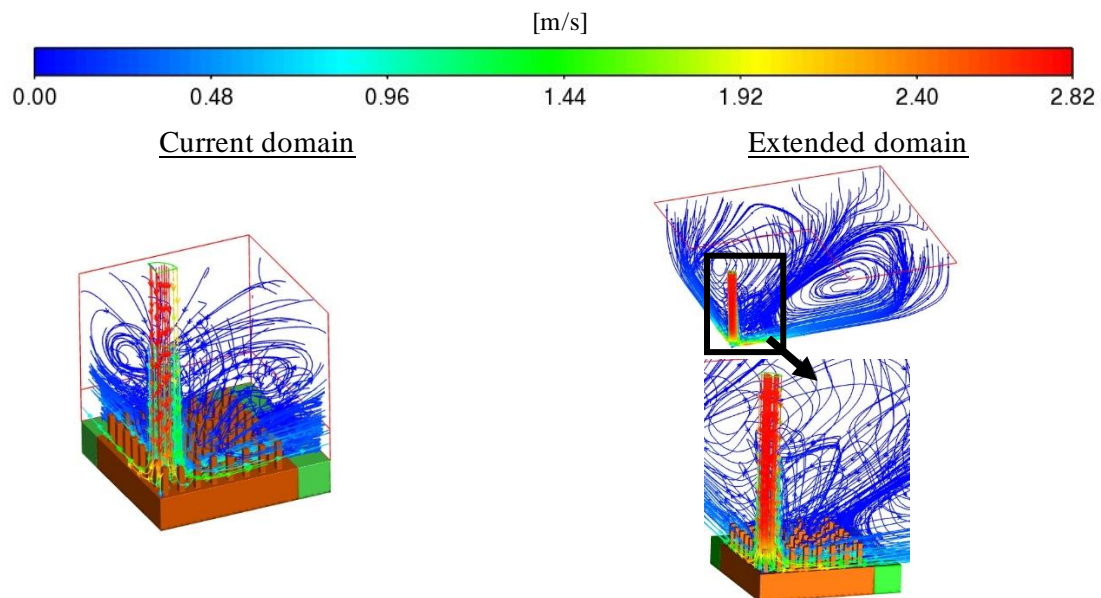
Figure B-5: Liquid velocity comparison of the current domain (left) and the extended domain (right).

(a)

E

(b)

(c)

(d)

(e)

(f)

(g)

F

(h)

(i)
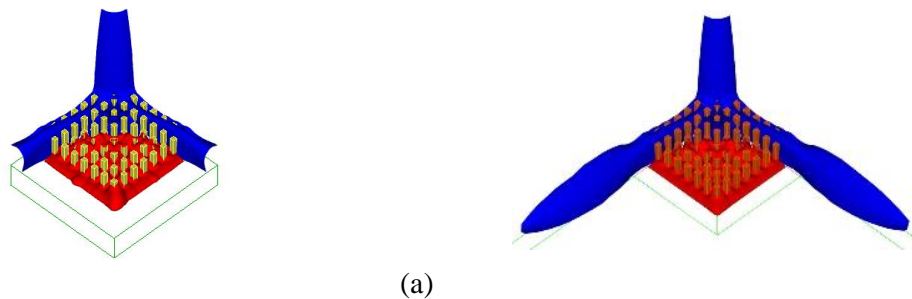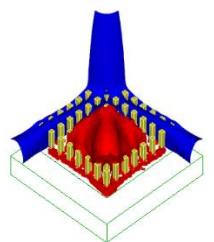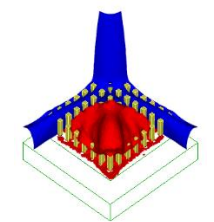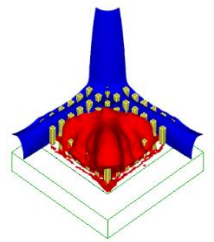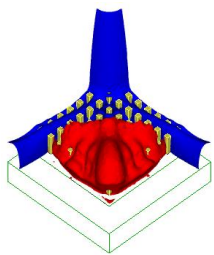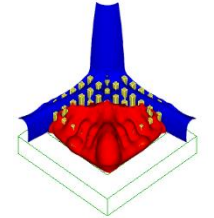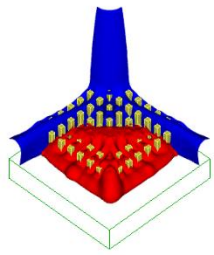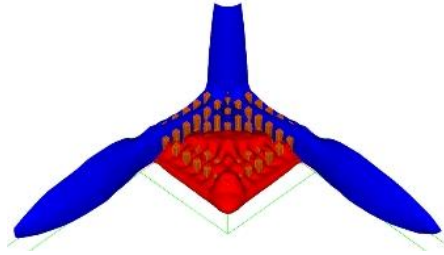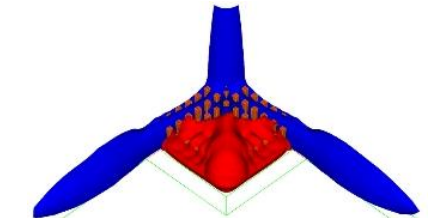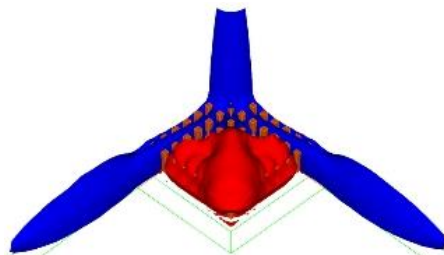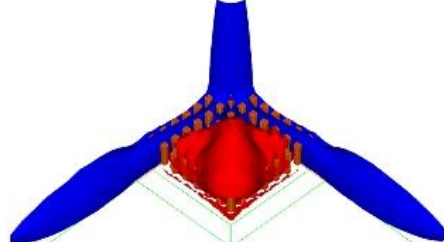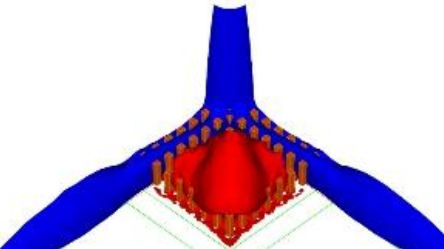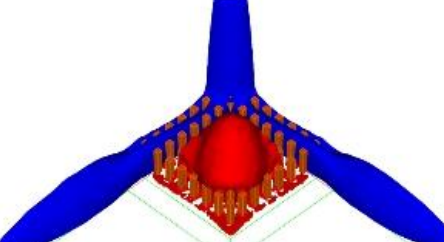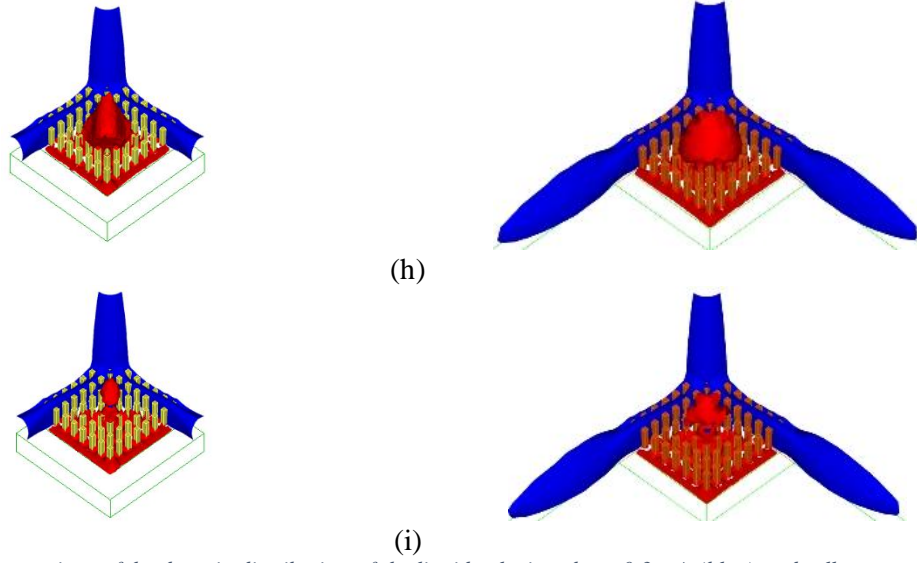
Figure B-6: Comparison of the domain distribution of the liquid velocity above 0.3 m/s (blue) and cell vapour fraction above 0.5 (red) between frames (a) to (i) of the current domain (left) and the extended domain (right), time series separated by intervals of 15 ms.

Appendix C: Numerical Procedure

This section provides the additional detailed implementation of the solution method outlined in Section 3.6 in Ansys Fluent v222. Including Text User Interface (TUI) commands and relaxation factors.

The poor mesh numerics option is enabled in Ansys Fluent through the use of the following TUI command:

```
solve/set/poor-mesh-numerics/enable? yes 1
```

where the first 'yes' enables the poor mesh numerics and the corrected solution order is set to 1. The poor mesh numerics is set to be based on cell and gradient quality through

```
solve/set/poor-mesh-numerics/cell-quality-based? Yes

solve/set/poor-mesh-numerics/gradient-quality-based? yes 0.2

solve/set/poor-mesh-numerics/solution-and-quality-based? yes 0.2 5
```

The body forces are ensured to be solved solved implicitly through

```
solve/set/numerics yes yes yes 0.75
```

where the first 'yes' enables the implicit solver, the second 'yes' to solve the rotating frame problems using absolute velocities (Fluent default) and the third 'yes' limits high-order terms for the PRESTO! pressure scheme which is followed with a blending factor of 0.75 between the 1st to higher-order terms. The blending factor can range from 0 to 1. It is important to note that the virtual mass implicit solver is not enabled by default and has to be enabled in the Eulerian multiphase model.

A energy numerical noise filter is enabled to limited the fluctuations in heat transfer caused by the variations in the mixture properties during phase change as the fluid density and thermal properties are dependant on the phase compositions and fluid temperature.

```
solve/set/advanced/energy-numerical-noise-filter yes
```

The liquid volume fraction effects are used to modify the heat transfer coefficient through

```
solve/set/multiphase-numerics/boiling-parameters/liquid-vof-factor
yes
```

The number of smoothing sweeps for the vapour node-based smoothing is increased to enhance stability and achieved through

```
solve/set/surface-tension yes 4 0.75 yes
```

where the first 'yes' enables node based smoothing, 4 the number of smoothing which can be chosen to be any number between 1 and 5, 0.75 the smoothing relaxation factor and the last 'yes' enables the use of the volume of fluid gradients at the nodes for curvature calculations. Table C-1 includes the suggested under-relaxation factors for the present study.

Table C-1: Suggested under-relaxation factors

Parameter	Suggested Under-Relaxation Factor
Pressure	0.6
Density	0.5
Body Forces	0.8
Momentum	0.2

Vaporization Mass	0.8
Volume Fraction	0.3
Turbulent Kinetic Energy	0.3
Turbulent Dissipation Rate	0.3
Turbulent Viscosity	0.5
Energy	0.3

It is recommended that most of the multigrid solution controls are left on default with the exception of a few changes. The pressure and energy cycle type is changed to F-cycle and the pressure termination is dropped two orders of magnitude to 0.001 whilst using the BCGSTAB stabilization method. All pre-sweeps settings are set to 1 and post-sweeps to 3. Aggressive coarsening is enabled if the coarsen level is higher than 4.

Appendix D: Ansys SpaceClaim Script

This section provides the Phyton script that automates the geometry creation for the parametric studies. The script implemented the API version of V22. This code automatically built the geometry in Ansys Spaceclaim v222.

```python
# Python Script, API Version = V22

#Copper block
Copper_block_side_length = 12700
Copper_block_thickness = 3000

#Fins
Fin_pitch = 1000
fin_width = 500
Fin_height = 2500
fin_side_spacing = Fin_pitch/2

#Domain
Inlet_diameter = 3750
Inlet_length = 7500
Fluid_domain_height = 15000

# Sketch Heated Surface
plane = Plane.PlaneZX
result = ViewHelper.SetSketchPlane(plane)
point1 = Point2D.Create(UM(0),UM(0))
point2 = Point2D.Create(UM(Copper_block_side_length),UM(0))
point3 = Point2D.Create(UM(Copper_block_side_length),UM(Copper_block_side_length))
result = SketchRectangle.Create(point1, point2, point3)

# Solidify Heated Surface
mode = InteractionMode.Solid
result = ViewHelper.SetViewMode(mode, None)
# EndBlock

# Extrude Copper Block
selection = FaceSelection.Create(GetRootPart().Bodies[0].Faces[0])
options = ExtrudeFaceOptions()
options.KeepMirror = True
options.KeepLayoutSurfaces = False
options.KeepCompositeFaceRelationships = True
options.PullSymmetric = False
options.OffsetMode = OffsetMode.IgnoreRelationships
options.Copy = False
options.ForceDoAsExtrude = False
options.ExtrudeType = ExtrudeType.Cut
result = ExtrudeFaces.Execute(selection, UM(-Copper_block_thickness), options)
# EndBlock

# Set Sketch Plane
sectionPlane = Plane.PlaneZX
result = ViewHelper.SetSketchPlane(sectionPlane, None)
# EndBlock

# Set New Sketch
result = SketchHelper.StartConstraintSketching()
# EndBlock

# Sketch first fin
start = Point2D.Create(UM(fin_side_spacing),UM(fin_side_spacing))
end = Point2D.Create(UM(fin_side_spacing),UM(fin_side_spacing + fin_width))
result = SketchLine.Create(start,end)
start = Point2D.Create(UM(fin_side_spacing),UM(fin_side_spacing + fin_width))
end = Point2D.Create(UM(fin_side_spacing + fin_width),UM(fin_side_spacing + fin_width))
result = SketchLine.Create(start,end)
start =  Point2D.Create(UM(fin_side_spacing + fin_width),UM(fin_side_spacing + fin_width))
end = Point2D.Create(UM(fin_side_spacing + fin_width),UM(fin_side_spacing))
result = SketchLine.Create(start,end)
start = Point2D.Create(UM(fin_side_spacing + fin_width),UM(fin_side_spacing))
end = Point2D.Create(UM(fin_side_spacing),UM(fin_side_spacing))
result = SketchLine.Create(start,end)
```

```
# Solidify Sketch
mode = InteractionMode.Solid
result = ViewHelper.SetViewMode(mode, None)
# EndBlock

# Extrude first fin
selection = FaceSelection.Create(GetRootPart().Bodies[0].Faces[6])
options = ExtrudeFaceOptions()
options.KeepMirror = True
options.KeepLayoutSurfaces = False
options.KeepCompositeFaceRelationships = True
options.PullSymmetric = False
options.OffsetMode = OffsetMode.IgnoreRelationships
options.Copy = False
options.ForceDoAsExtrude = False
options.ExtrudeType = ExtrudeType.Add
result = ExtrudeFaces.Execute(selection, UM(Fin_height), options)
# EndBlock

# Create Fin Pattern
selection = FaceSelection.Create([GetRootPart().Bodies[0].Faces[7],
    GetRootPart().Bodies[0].Faces[8],
    GetRootPart().Bodies[0].Faces[6],
    GetRootPart().Bodies[0].Faces[10],
    GetRootPart().Bodies[0].Faces[9]])
data = FillPatternData()
data.LinearDirection = EdgeSelection.Create(GetRootPart().Bodies[0].Edges[11])
data.FillPatternType = FillPatternType.Grid
data.XSpacing = UM(Fin_pitch)
data.YSpacing =  UM(Fin_pitch)
data.Margin = UM(1)
data.RowXOffset =  UM(0)
data.RowYOffset =  UM(0)
data.ColumnXOffset =  UM(0)
data.ColumnYOffset =  UM(0)
result = Pattern.CreateFill(selection, data, None)
# EndBlock

# Extrude Insulation
selection = FaceSelection.Create(GetRootPart().Bodies[0].Faces[1])
options = ExtrudeFaceOptions()
options.KeepMirror = True
options.KeepLayoutSurfaces = False
options.KeepCompositeFaceRelationships = True
options.PullSymmetric = False
options.OffsetMode = OffsetMode.IgnoreRelationships
options.Copy = False
options.ForceDoAsExtrude = False
options.ExtrudeType = ExtrudeType.Add
result = ExtrudeFaces.Execute(selection, UM(3000), options)
# EndBlock
selection = FaceSelection.Create(GetRootPart().Bodies[0].Faces[2])
options = ExtrudeFaceOptions()
options.KeepMirror = True
options.KeepLayoutSurfaces = False
options.KeepCompositeFaceRelationships = True
options.PullSymmetric = False
options.OffsetMode = OffsetMode.IgnoreRelationships
options.Copy = False
options.ForceDoAsExtrude = False
options.ExtrudeType = ExtrudeType.Add
result = ExtrudeFaces.Execute(selection, UM(3000), options)
# EndBlock

# Create fluid section
selection = FaceSelection.Create(GetRootPart().Bodies[0].Faces[5])
result = DatumPlaneCreator.Create(selection, False, None)
# EndBlock

 #set offset to move afterwards
selection = Selection.Create(GetRootPart().DatumPlanes[0])
direction = Move.GetDirection(selection)
options = MoveOptions()
options.CreatePatterns = False
```

```
options.DetachFirst = False
options.MaintainOrientation = False
options.MaintainMirrorRelationships = True
options.MaintainConnectivity = True
options.MaintainOffsetRelationships = True
options.Copy = False
options.SnapAssociatedVertices = True
result = Move.Translate(selection, direction, UM(5000), options)
# EndBlock

# Set Sketch Plane
sectionPlane = Plane.Create(Frame.Create(Point.Create(UM(7850), UM(5000), UM(7850)),
    Direction.DirZ,
    Direction.DirX))
result = ViewHelper.SetSketchPlane(sectionPlane, None)
# EndBlock

# Sketch Fluid bottom
start = Point2D.Create(UM(9000),UM(-9000))
end = Point2D.Create(UM(9000),UM(9000))
result = SketchLine.Create(start,end)
start = Point2D.Create(UM(9000),UM(9000))
end = Point2D.Create(UM(-9000),UM(9000))
result = SketchLine.Create(start,end)
start = Point2D.Create(UM(-9000),UM(9000))
end = Point2D.Create(UM(-9000),UM(-9000))
result = SketchLine.Create(start,end)
start = Point2D.Create(UM(-9000),UM(-9000))
end = Point2D.Create(UM(9000),UM(-9000))
result = SketchLine.Create(start,end)

# Solidify Sketch
mode = InteractionMode.Solid
result = ViewHelper.SetViewMode(mode, None)
# EndBlock

# Extrude fluid
selection = FaceSelection.Create(GetRootPart().Bodies[1].Faces[0])
options = ExtrudeFaceOptions()
options.KeepMirror = True
options.KeepLayoutSurfaces = False
options.KeepCompositeFaceRelationships = True
options.PullSymmetric = False
options.OffsetMode = OffsetMode.IgnoreRelationships
options.Copy = False
options.ForceDoAsExtrude = False
options.ExtrudeType = ExtrudeType.Add
result = ExtrudeFaces.Execute(selection, UM(Fluid_domain_height), options)
# EndBlock

# Set Sketch Plane
sectionPlane = Plane.Create(Frame.Create(Point.Create(UM(7850), UM(20000), UM(7850)),
    Direction.DirZ,
    Direction.DirX))
result = ViewHelper.SetSketchPlane(sectionPlane, None)
# EndBlock

# Set New Sketch
result = SketchHelper.StartConstraintSketching()
# EndBlock

# Sketch Circle
Inlet_radius = Inlet_diameter/2
origin = Point2D.Create(UM(-7850), UM(-7850))
result = SketchCircle.Create(origin, UM(Inlet_radius))
# EndBlock

# Solidify Sketch
mode = InteractionMode.Solid
result = ViewHelper.SetViewMode(mode, None)
# EndBlock

# Extrude Inlet
selection = FaceSelection.Create(GetRootPart().Bodies[1].Faces[5])
options = ExtrudeFaceOptions()
```

```
options.KeepMirror = True
options.KeepLayoutSurfaces = False
options.KeepCompositeFaceRelationships = True
options.PullSymmetric = False
options.OffsetMode = OffsetMode.IgnoreRelationships
options.Copy = False
options.ForceDoAsExtrude = False
options.ExtrudeType = ExtrudeType.Add
result = ExtrudeFaces.Execute(selection, UM(Inlet_length), options)
# EndBlock

# Delete Selection extra circle and bottom fluid plane
selection = FaceSelection.Create(GetRootPart().Bodies[2].Faces[0])
result = Delete.Execute(selection)
selection = Selection.Create(GetRootPart().DatumPlanes[0])
result = Delete.Execute(selection)
# EndBlock

# Rename 'Solid' to 'Fluid'
selection = BodySelection.Create(GetRootPart().Bodies[1])
result = RenameObject.Execute(selection,"Fluid")
# EndBlock

 #Move Fluid over solid body + 1000, Thus -6000
selection = BodySelection.Create(GetRootPart().Bodies[1])
direction = Direction.DirY
options = MoveOptions()
options.CreatePatterns = False
options.DetachFirst = False
options.MaintainOrientation = False
options.MaintainMirrorRelationships = True
options.MaintainConnectivity = True
options.MaintainOffsetRelationships = True
options.Copy = False
options.SnapAssociatedVertices = True
result = Move.Translate(selection, direction, UM(-6000), options)
# EndBlock

# Cut fluid with solid
targets = BodySelection.Create(GetRootPart().Bodies[1])
tools = BodySelection.Create(GetRootPart().Bodies[0])
options = MakeSolidsOptions()
result = Combine.Intersect(targets, tools, options)
# EndBlock

# Delete Extra solid
selection = BodySelection.Create(GetRootPart().Bodies[2])
result = Delete.Execute(selection)
# EndBlock

# Create Planes to cut fluid
selection = FaceSelection.Create(GetRootPart().Bodies[0].Faces[0])
result = DatumPlaneCreator.Create(selection, False, None)
selection = FaceSelection.Create(GetRootPart().Bodies[0].Faces[3])
result = DatumPlaneCreator.Create(selection, False, None)
selection = FaceSelection.Create(GetRootPart().Bodies[0].Faces[2])
result = DatumPlaneCreator.Create(selection, False, None)
selection = FaceSelection.Create(GetRootPart().Bodies[0].Faces[1])
result = DatumPlaneCreator.Create(selection, False, None)
# EndBlock

# Slice Extra sides
selection = BodySelection.Create(GetRootPart().Bodies[1])
datum = Selection.Create(GetRootPart().DatumPlanes[3])
result = SplitBody.ByCutter(selection, datum)
selection = BodySelection.Create(GetRootPart().Bodies[1])
datum = Selection.Create(GetRootPart().DatumPlanes[0])
result = SplitBody.ByCutter(selection, datum)
selection = BodySelection.Create(GetRootPart().Bodies[1])
datum = Selection.Create(GetRootPart().DatumPlanes[1])
result = SplitBody.ByCutter(selection, datum)
selection = BodySelection.Create(GetRootPart().Bodies[1])
datum = Selection.Create(GetRootPart().DatumPlanes[2])
result = SplitBody.ByCutter(selection, datum)
# EndBlock
```

M

```
# Delete Extra sides
selection = BodySelection.Create(GetRootPart().Bodies[3])
result = Delete.Execute(selection)
selection = BodySelection.Create(GetRootPart().Bodies[2])
result = Delete.Execute(selection)
selection = BodySelection.Create(GetRootPart().Bodies[3])
result = Delete.Execute(selection)
selection = BodySelection.Create(GetRootPart().Bodies[2])
result = Delete.Execute(selection)
selection = Selection.Create(GetRootPart().DatumPlanes[3])
result = Delete.Execute(selection)
selection = Selection.Create(GetRootPart().DatumPlanes[2])
result = Delete.Execute(selection)
selection = Selection.Create(GetRootPart().DatumPlanes[0])
result = Delete.Execute(selection)
selection = Selection.Create(GetRootPart().DatumPlanes[0])
result = Delete.Execute(selection)
# EndBlock

# Create Plane for insulation
selection = Face1
result = DatumPlaneCreator.Create(selection, False, Info1)
selection = Face2
result = DatumPlaneCreator.Create(selection, False, Info2)
# EndBlock

# Move plane to cut for insulation
selection = DatumPlane1
direction = Move.GetDirection(selection)
options = MoveOptions()
options.CreatePatterns = False
options.DetachFirst = False
options.MaintainOrientation = False
options.MaintainMirrorRelationships = True
options.MaintainConnectivity = True
options.MaintainOffsetRelationships = True
options.Copy = False
options.SnapAssociatedVertices = True
result = Move.Translate(selection, direction, UM(-3000), options, Info3)
selection = DatumPlane2
direction = Move.GetDirection(selection)
options = MoveOptions()
options.CreatePatterns = False
options.DetachFirst = False
options.MaintainOrientation = False
options.MaintainMirrorRelationships = True
options.MaintainConnectivity = True
options.MaintainOffsetRelationships = True
options.Copy = False
options.SnapAssociatedVertices = True
result = Move.Translate(selection, direction, UM(-3000), options, Info4)
# EndBlock

# Slice Inslution
selection = Body1
datum = DatumPlane1
result = SplitBody.ByCutter(selection, datum, Info5)
selection = Body1
datum = DatumPlane2
result = SplitBody.ByCutter(selection, datum, Info6)
# EndBlock

# Merge two cut insulation bodies
targets = BodySelection.Create(Body2, Body3)
result = Combine.Merge(targets, Info7)
# EndBlock

# Delete planes for insulation
selection = Selection.Create(DatumPlane2, DatumPlane1)
result = Delete.Execute(selection)
# EndBlock

# Rename 'Solid1' to 'Insulation'
selection = Body2
```

```
result = RenameObject.Execute(selection,"Insulation")
# EndBlock

# Cut fluid section for constant mesh size over fins
selection = Body4
visibility = VisibilityType.Hide
inSelectedView = False
faceLevel = False
ViewHelper.SetObjectVisibility(selection, visibility, inSelectedView, faceLevel)
# EndBlock

# Create plane for fluid cut
selection = Face3
result = DatumPlaneCreator.Create(selection, False, Info8)
# EndBlock

# Move plane for fluid cut
selection = DatumPlane3
direction = Move.GetDirection(selection)
options = MoveOptions()
options.CreatePatterns = False
options.DetachFirst = False
options.MaintainOrientation = False
options.MaintainMirrorRelationships = True
options.MaintainConnectivity = True
options.MaintainOffsetRelationships = True
options.Copy = False
options.SnapAssociatedVertices = True
result = Move.Translate(selection, direction, UM(Fin_height+500), options, Info9)
# EndBlock

# Slice Fluid section
selection = Body4
datum = DatumPlane3
result = SplitBody.ByCutter(selection, datum, Info10)
# EndBlock

# Rename 'Fluid' to 'Fluid_fins'
selection = Body4
result = RenameObject.Execute(selection,"Fluid_fins")
# EndBlock

# Rename 'Fluid1' to 'Fluid_bulk'
selection = Body5
result = RenameObject.Execute(selection,"Fluid_bulk")
# EndBlock

# Delete plane which is used to cut fluid
selection = DatumPlane3
result = Delete.Execute(selection)
# EndBlock

# Slice fluid bulk with pipe
selection = Body13
toolFaces = Face27
result = SplitBody.ByCutter(selection, toolFaces, True, Info12)
# EndBlock

# Rename 'Fluid_bulk1' to 'Fluid_bulk'
selection = Body14
result = RenameObject.Execute(selection,"Fluid_bulk")
# EndBlock

# Rename 'Fluid_bulk' to 'Fluid_pipe'
selection = Body13
result = RenameObject.Execute(selection,"Fluid_pipe")
# EndBlock

# Create inlet
primarySelection = Face28
secondarySelection = Selection.Empty()
result = NamedSelection.Create(primarySelection, secondarySelection)
result = NamedSelection.Rename("Group1", "inlet")
# EndBlock
```

O

```
# Create outlet_bulk
primarySelection = FaceSelection.Create(Face28, Face29, Face30)
secondarySelection = Selection.Empty()
result = NamedSelection.Create(primarySelection, secondarySelection)
result = NamedSelection.Rename("Group1", "outlet_bulk")
# EndBlock

# Create outlet_fins
primarySelection = FaceSelection.Create(Face31, Face32)
secondarySelection = Selection.Empty()
result = NamedSelection.Create(primarySelection, secondarySelection)
result = NamedSelection.Rename("Group1", "outlet_fins")
# EndBlock

# Create wall_confinement
primarySelection = Face33
secondarySelection = Selection.Empty()
result = NamedSelection.Create(primarySelection, secondarySelection)
result = NamedSelection.Rename("Group1", "wall_confinement")
# EndBlock

# Create wall_heated
primarySelection = Face34
secondarySelection = Selection.Empty()
result = NamedSelection.Create(primarySelection, secondarySelection)
result = NamedSelection.Rename("Group1", "wall_heated")
# EndBlock

# Create wall_insulation_bottom
primarySelection = Face35
secondarySelection = Selection.Empty()
result = NamedSelection.Create(primarySelection, secondarySelection)
result = NamedSelection.Rename("Group1", "wall_insulation_bottom")
# EndBlock

# Create wall_insulaton_side
primarySelection = FaceSelection.Create(Face36, Face37)
secondarySelection = Selection.Empty()
result = NamedSelection.Create(primarySelection, secondarySelection)
result = NamedSelection.Rename("Group1", "wall_insulaton_side")
# EndBlock

# Create symmetry_z
primarySelection = FaceSelection.Create(Face38, Face39, Face40, Face41, Face42)
secondarySelection = Selection.Empty()
result = NamedSelection.Create(primarySelection, secondarySelection)
result = NamedSelection.Rename("Group1", "symmetry_z")
# EndBlock

# Create symmetry_x
primarySelection = FaceSelection.Create(Face43, Face44, Face45, Face46, Face47)
secondarySelection = Selection.Empty()
result = NamedSelection.Create(primarySelection, secondarySelection)
result = NamedSelection.Rename("Group1", "symmetry_x")
# EndBlock

# Create wall_pipe
primarySelection = Face48
secondarySelection = Selection.Empty()
result = NamedSelection.Create(primarySelection, secondarySelection)
result = NamedSelection.Rename("Group1", "wall_pipe")
# EndBlock

# Create wall_fins_top
primarySelection = PatternMembers2
secondarySelection = Selection.Empty()
result = NamedSelection.Create(primarySelection, secondarySelection)
result = NamedSelection.Rename("Group1", "wall_fins_top")
# EndBlock

# Create wall_fins_side
primarySelection = PatternMembers3
secondarySelection = Selection.Empty()
result = NamedSelection.Create(primarySelection, secondarySelection)
result = NamedSelection.Rename("Group1", "wall_fins_side")
```

```python
# EndBlock

# Create wall_fins_flat
primarySelection = Face49
secondarySelection = Selection.Empty()
result = NamedSelection.Create(primarySelection, secondarySelection)
result = NamedSelection.Rename("Group1", "wall_fins_flat")
# EndBlock

# Create wall_insulation_fluid
primarySelection = Face50
secondarySelection = Selection.Empty()
result = NamedSelection.Create(primarySelection, secondarySelection)
result = NamedSelection.Rename("Group1", "wall_insulation_fluid")
# EndBlock

# Change Object Visibility
selection = Body15
visibility = VisibilityType.Hide
inSelectedView = False
faceLevel = False
ViewHelper.SetObjectVisibility(selection, visibility, inSelectedView, faceLevel)
# EndBlock

# Create wall_solid_insulation
primarySelection = FaceSelection.Create(Face51, Face52)
secondarySelection = Selection.Empty()
result = NamedSelection.Create(primarySelection, secondarySelection)
result = NamedSelection.Rename("Group1", "wall_solid_insulation")
# EndBlock

# Change Object Visibility
selection = Body15
visibility = VisibilityType.Show
inSelectedView = False
faceLevel = False
ViewHelper.SetObjectVisibility(selection, visibility, inSelectedView, faceLevel)
# EndBlock

# Change Object Visibility
selection = Body16
visibility = VisibilityType.Show
inSelectedView = False
faceLevel = False
ViewHelper.SetObjectVisibility(selection, visibility, inSelectedView, faceLevel)
# EndBlock

# Create internal_fluid_fins_bulk
primarySelection = Face53
secondarySelection = Selection.Empty()
result = NamedSelection.Create(primarySelection, secondarySelection)
result = NamedSelection.Rename("Group1", "internal_fluid_fins_bulk")
# EndBlock

# Change Object Visibility
selection = Body13
visibility = VisibilityType.Show
inSelectedView = False
faceLevel = False
ViewHelper.SetObjectVisibility(selection, visibility, inSelectedView, faceLevel)
# EndBlock

# Create internal_fluid_pipe_bulk
primarySelection = FaceSelection.Create(GetRootPart().Bodies[4].Faces[6])
secondarySelection = Selection.Empty()
result = NamedSelection.Create(primarySelection, secondarySelection)
result = NamedSelection.Rename("Group1", "internal_fluid_pipe_bulk")
# EndBlock

# Create fluid_bulk
primarySelection = Body14
secondarySelection = Selection.Empty()
result = NamedSelection.Create(primarySelection, secondarySelection)
result = NamedSelection.Rename("Group1", "fluid_bulk")
# EndBlock
```

Q

```
# Create fluid_pipe
primarySelection = Body13
secondarySelection = Selection.Empty()
result = NamedSelection.Create(primarySelection, secondarySelection)
result = NamedSelection.Rename("Group1", "fluid_pipe")
# EndBlock

# Create fluid_fins
primarySelection = Body16
secondarySelection = Selection.Empty()
result = NamedSelection.Create(primarySelection, secondarySelection)
result = NamedSelection.Rename("Group1", "fluid_fins")
# EndBlock

# Create insulation
primarySelection = Body15
secondarySelection = Selection.Empty()
result = NamedSelection.Create(primarySelection, secondarySelection)
result = NamedSelection.Rename("Group1", "insulation")
# EndBlock

# Create solid
primarySelection = Body17
secondarySelection = Selection.Empty()
result = NamedSelection.Create(primarySelection, secondarySelection)
result = NamedSelection.Rename("Group1", "solid")
# EndBlock

# Create Plane to cut fluid pipe
selection = Face4
result = DatumPlaneCreator.Create(selection, False, Info11)
selection = Body6
datum = DatumPlane4
result = SplitBody.ByCutter(selection, datum, Info14)
selection = DatumPlane4
result = Delete.Execute(selection)
# EndBlock

# Share Topology
options = ShareTopologyOptions()
options.Tolerance = UM(0.2)
options.PreserveInstances = True
result = ShareTopology.FindAndFix(options, Info13)
# EndBlock

# Delete Objects
result = NamedSelection.Delete("wall_pipe")
# EndBlock

# Create wall_pipe
primarySelection = Face5
secondarySelection = Selection.Empty()
result = NamedSelection.Create(primarySelection, secondarySelection)
result = NamedSelection.Rename("Group1", "wall_pipe")
# EndBlock

# Rename 'Fluid_pipe' to 'Fluid_pipe_bottom'
selection = Body7
result = RenameObject.Execute(selection,"Fluid_pipe_bottom")
# EndBlock

# Rename 'Fluid_pipe1' to 'Fluid_pipe_top'
selection = Body8
result = RenameObject.Execute(selection,"Fluid_pipe_top")
# EndBlock

# Delete Objects
result = NamedSelection.Delete("fluid_pipe")
# EndBlock

# Create Named Selection Group
primarySelection = Body8
secondarySelection = Selection.Empty()
result = NamedSelection.Create(primarySelection, secondarySelection)
```

R

```
# EndBlock

# Rename Named Selection
result = NamedSelection.Rename("Group1", "fluid_pipe_top")
# EndBlock

# Create Named Selection Group
primarySelection = Body7
secondarySelection = Selection.Empty()
result = NamedSelection.Create(primarySelection, secondarySelection)
# EndBlock

# Rename Named Selection
result = NamedSelection.Rename("Group1", "fluid_pipe_bottom")
# EndBlock

# Change Object Visibility
selection = Body8
visibility = VisibilityType.Hide
inSelectedView = False
faceLevel = False
ViewHelper.SetObjectVisibility(selection, visibility, inSelectedView, faceLevel)
# EndBlock

# Create Named Selection Group
primarySelection = Face6
secondarySelection = Selection.Empty()
result = NamedSelection.Create(primarySelection, secondarySelection)
# EndBlock

# Rename Named Selection
result = NamedSelection.Rename("Group1", "interior_fluid_pipe_top_bottom")
# EndBlock

# Change Object Visibility
selection = Body8
visibility = VisibilityType.Show
inSelectedView = False
faceLevel = False
ViewHelper.SetObjectVisibility(selection, visibility, inSelectedView, faceLevel)
# EndBlock

# Create Named Selection Group
primarySelection = Selection.CreateByGroups(SelectionType.Primary, "outlet_bulk") - Face7
secondarySelection = Selection.Empty()
result = NamedSelection.Replace("outlet_bulk", primarySelection, secondarySelection)
# EndBlock

# Change Object Visibility
selection = Body9
visibility = VisibilityType.Hide
inSelectedView = False
faceLevel = False
ViewHelper.SetObjectVisibility(selection, visibility, inSelectedView, faceLevel)
# EndBlock

# Change Object Visibility
selection = Body10
visibility = VisibilityType.Hide
inSelectedView = False
faceLevel = False
ViewHelper.SetObjectVisibility(selection, visibility, inSelectedView, faceLevel)
# EndBlock

# Create Named Selection Group
primarySelection = Selection.CreateByGroups(SelectionType.Primary, "internal_fluid_fins_bulk") - Face8
secondarySelection = Selection.Empty()
result = NamedSelection.Replace("internal_fluid_fins_bulk", primarySelection, secondarySelection)
# EndBlock

# Create Named Selection Group
primarySelection = Face8
secondarySelection = Selection.Empty()
```

```
result = NamedSelection.Create(primarySelection, secondarySelection)
# EndBlock

# Rename Named Selection
result = NamedSelection.Rename("Group1", "internal_fluid_fins_pipe")
# EndBlock

# Change Object Visibility
selection = Body10
visibility = VisibilityType.Show
inSelectedView = False
faceLevel = False
ViewHelper.SetObjectVisibility(selection, visibility, inSelectedView, faceLevel)
# EndBlock

# Change Object Visibility
selection = Body9
visibility = VisibilityType.Show
inSelectedView = False
faceLevel = False
ViewHelper.SetObjectVisibility(selection, visibility, inSelectedView, faceLevel)
    # EndBlock
```

Appendix E: Data handling code

This section provides all the data handling code for each section.

Appendix E: Mesh independence study

```
clear all
% load matrices
% load poly
load("p012.mat")
load("p014.mat")
load("p02.mat")
% load hex
load("h012.mat")
load("h014.mat")
load("h02.mat")
% create flowtime
count = 10000;
flowtime = 1:(count+1);
flowtime = flowtime*0.0001;
%poly
data = p012;
tmax_p012 = data(end-count:end,9)-273.15-61;
tavg_p012 = data(end-count:end,10)-273.15-61;
tstag_p012 = data(end-count:end,14)-273.15-61;
data = p014;
tmax_p014 = data(end-count:end,9)-273.15-61;
tavg_p014 = data(end-count:end,10)-273.15-61;
tstag_p014 = data(end-count:end,14)-273.15-61;
data = p02;
tmax_p02 = data(end-count:end-10,9)-273.15-61;
tavg_p02 = data(end-count:end-10,10)-273.15-61;
tstag_p02 = data(end-count:end-10,15)-273.15-61;
%hex
data = h012;
tmax_h012 = data(end-count:end,3)-273.15-61;
tavg_h012 = data(end-count:end,5)-273.15-61;
tstag_h012 = data(end-count:end,13)-273.15-61;
data = h014;
tmax_h014 = data(end-count:end,4)-273.15-61;
tavg_h014 = data(end-count:end,3)-273.15-61;
tstag_h014 = data(end-count:end,6)-273.15-61;
data = h02;
tmax_h02 = data(end-count:end,9)-273.15-61;
tavg_h02 = data(end-count:end,8)-273.15-61;
tstag_h02 = data(end-count:end,11)-273.15-61;
%create mean lists
mesh_size = [8 7 5];
poly_results = [mean(tstag_p012) mean(tstag_p014) mean(tstag_p02)];
hex_results = [mean(tstag_h012) mean(tstag_h014) mean(tstag_h02)];
% plot max temp
figure(1)
plot(flowtime,tmax_p012,'r',flowtime,tmax_p014,'c',flowtime(1:end-
10),tmax_p02,'m',flowtime,tmax_h012,'b',flowtime,tmax_h014,'k',flowtime,tmax_h02,'g')
hold on
yline(mean(tmax_p012),'r')
hold on
yline(mean(tmax_p014),'c')
hold on
yline(mean(tmax_p02),'m')
hold on
yline(mean(tmax_h012),'b')
hold on
yline(mean(tmax_h014),'k')
hold on
yline(mean(tmax_h02),'g')
legend("poly 0.12","poly 0.14","poly 0.2","hex 0.12","hex 0.14","hex
0.2","FontSize",30,"Location","northeastoutside")
title('Maximum flat surface temperature',"FontSize",30)
ylabel("Wall superheat","FontSize",30)
xlabel("flowtime","FontSize",30)
%plot average surface temp
```

```matlab
figure(2)
plot(flowtime,tavg_p012,'r',flowtime,tavg_p014,'c',flowtime(1:end-
10),tavg_p02,'m',flowtime,tavg_h012,'b',flowtime,tavg_h014,'k',flowtime,tavg_h02,'g')
legend("poly 0.12","poly 0.14","poly 0.2","hex 0.12","hex 0.14","hex 0.2")
hold on
yline(mean(tavg_p012),'r')
hold on
yline(mean(tavg_p014),'c')
hold on
yline(mean(tavg_p02),'m')
hold on
yline(mean(tavg_h012),'b')
hold on
yline(mean(tavg_h014),'k')
hold on
yline(mean(tavg_h02),'g')
legend("poly 0.12","poly 0.14","poly 0.2","hex 0.12","hex 0.14","hex
0.2","FontSize",30,"Location","northeastoutside")
title('Average flat surface temperature',"FontSize",30)
ylabel("Wall superheat","FontSize",30)
xlabel("flowtime","FontSize",30)
%plot stag temp
figure(3)
plot(flowtime,tstag_p012,'r',flowtime,tstag_p014,'c',flowtime(1:end-
10),tstag_p02,'m',flowtime,tstag_h012,'b',flowtime,tstag_h014,'k',flowtime,tstag_h02,'g')
legend("poly 0.12","poly 0.14","poly 0.2","hex 0.12","hex 0.14","hex
0.2","FontSize",30,"Location","northeastoutside")
title('Stagnation temperature',"FontSize",30)
ylabel("Wall superheat","FontSize",30)
xlabel("flowtime","FontSize",30)
confidence = [4 5 6 7 8 9];
%plot mesh comparison
xconf = [confidence confidence(end:-1:1)];
y = 8.5633270 + 0*confidence;
yconf = [y-0.4 y(end:-1:1)+0.4];
figure(4)
plot(mesh_size,poly_results,'rx',mesh_size,hex_results,'bx','MarkerSize',50)
hold on
yline(8.5633270,'k')
hold on
yline(8.5633270+0.4,'k--')
hold on
yline(8.5633270-0.4,'k--')
hold on
p = fill(xconf,yconf,'k','FaceAlpha',.1);
p.FaceColor = [128 128 128]/255;
p.EdgeColor = 'none';
legend("Polyhedral mesh","Hexahedral mesh","Experimental stagnation temperature","Experimental
uncertainty band","FontSize",15,"Location","northeast")
%title('Stagnation temperature',"FontSize",30)
ylabel("Wall superheat [^{\circC]","FontSize",20)
xlabel("# Cells between fins","FontSize",20)
ylim([7.5 11])
xlim([4 9])
xticks([5 7 8]);
ax = gca;
ax.FontSize = 16;
set(gcf,'color','w');
%create stagnation temperute table
poly_results = poly_results';
hex_results = hex_results';
uncertaincy_temp = 0.4;
upper_exp_temp = 8.5633270 + uncertaincy_temp;
poly_error = abs((upper_exp_temp - poly_results)/upper_exp_temp)*100;
hex_error = abs((upper_exp_temp - hex_results)/upper_exp_temp)*100;
```

Appendix E: Boiling curve

```matlab
clear all
load("simr_0_58000.mat")
load("simr_58001_178000.mat")
load("simr_178001_246000.mat")
load("simr_246000_300000.mat")
load("simr_300001.mat")
```

```matlab
load('Single_exp_data.mat')
ave_number = 5000;

Re_stag = [10.3 9.86 9.36];
tstag = cat(1,simr058000(:,14), simr58001178000(:,14), simr178001246000(:,14),
simr246000300000(:,14), simr300001(:,14))-273.15-61;
tmax = cat(1,simr058000(:,9), simr58001178000(:,9), simr178001246000(:,9),
simr246000300000(:,9), simr300001(:,9))-273.15-61;
qin = cat(1,simr058000(:,3), simr58001178000(:,3), simr178001246000(:,3), simr246000300000(:,3),
simr300001(:,3));
q_exp = Singleexpdata(1:11,2);
t_exp =Singleexpdata(1:11,1);
q_sim = [14.7341 19.4033 23.2425 27.0817];
pos_end_14_7 = 178003;
pos_end_19_4 = 210004;
pos_end_23_4 = 340000;
pos_end_27 = 389600;
t_sim = [mean(tstag(pos_end_14_7-ave_number:pos_end_14_7)) mean(tstag(pos_end_19_4-
ave_number:pos_end_19_4)) mean(tstag(pos_end_23_4-ave_number:pos_end_23_4))
mean(tstag(pos_end_27-ave_number:pos_end_27))];
tmax_sim = [mean(tmax(pos_end_14_7-ave_number:pos_end_14_7)) mean(tmax(pos_end_19_4-
ave_number:pos_end_19_4)) mean(tmax(pos_end_23_4-ave_number:pos_end_23_4)) mean(tmax(pos_end_27-
ave_number:pos_end_27))];
%Get stag nation means
%get indecies
get_err_length = length(t_exp);
t_exp_error = [0.4 0.4 0.4 0.4 0.4 0.4 0.4 0.4 0.4 0.4 0.4];
q_exp_error = q_exp*0.02;
%plot wall temperatures
figure(2)
plot(t_exp,q_exp,'r.','MarkerSize',20)
hold on
%plot(t_sim,q_sim,'bx',tmax_sim,q_sim,'kx','MarkerSize',40)
plot(t_sim,q_sim,'bx','MarkerSize',40)
hold on
errorbar(t_exp,q_exp,t_exp_error,'r.','horizontal')
hold on
errorbar(t_exp,q_exp,q_exp_error,'r.','vertical')
hold on
plot(t_sim,q_sim,'b--')%,tmax_sim,q_sim,'k--')
ylim([0 45])
xlim([-1 16])
ylabel("Heat Flux [W/cm^2]","FontSize",60)
xlabel("Wall superheat [^{\circ}C]","FontSize",60)
%legend("Rau and Garimella","Current results - Stagnation wall superheat","Current results -
Maximum wall superheat","FontSize",20,"Location","northwest")
legend("Rau and Garimella","Current results - Stagnation wall
superheat","FontSize",20,"Location","northwest")
ax = gca;
ax.FontSize = 16;
set(gcf,'color','w');
Texp_list = [t_exp(3,1)+0.4 t_exp(5,1)+0.4 t_exp(6,1)+0.4 t_exp(7,1)+0.4];

for i = 1:length(Texp_list)

    Error_list(i) = ((Texp_list(1,i)-t_sim(1,i))/Texp_list(1,i))*100*(-1);
end
%Include Re results
figure(3)
plot(t_exp,q_exp,'r.','MarkerSize',20)
hold on
%plot(t_sim,q_sim,'bx',tmax_sim,q_sim,'kx','MarkerSize',40)
plot(t_sim,q_sim,'b*','MarkerSize',60)
hold on
plot(Re_stag(1),23.24,'k*','MarkerSize',60)
hold on
plot(Re_stag(3),23.24,'k*','MarkerSize',60)
hold on
errorbar(t_exp,q_exp,t_exp_error,'r.','horizontal')
hold on
errorbar(t_exp,q_exp,q_exp_error,'r.','vertical')
hold on
plot(t_sim,q_sim,'b--')%,tmax_sim,q_sim,'k--')
ylim([22.5 24.5])
xlim([8 11])
```

W

```
ylabel("Heat Flux [W/cm^2]","FontSize",60)
xlabel("Wall superheat [^{\circ}[96]C]","FontSize",60)
%legend("Rau and Garimella","Current results - Stagnation wall superheat","Current results -
Maximum wall superheat","FontSize",20,"Location","northwest")
legend("Rau and Garimella","Current results - Stagnation wall
superheat","FontSize",20,"Location","northwest")
ax = gca;
ax.FontSize = 16;
set(gcf,'color','w');
%plot wall temperatures
figure(4)
plot(t_sim,q_sim,'bx','MarkerSize',40)
hold on
plot(t_sim,q_sim,'b--')%,tmax_sim,q_sim,'k--')
ylim([0 45])
xlim([-1 16])
ylabel("Heat Flux [W/cm^2]","FontSize",60)
xlabel("Wall superheat [^{\circ}C]","FontSize",60)
%legend("Rau and Garimella","Current results - Stagnation wall superheat","Current results -
Maximum wall superheat","FontSize",20,"Location","northwest")
legend("Inline pin fins","FontSize",20,"Location","northwest")
ax = gca;
ax.FontSize = 16;
set(gcf,'color','w');
```

Appendix E: Validation with flow time

```
clear all
%check for convegence
%read in data file
load("simr_0_58000.mat")
load("simr_58001_178000.mat")
load("simr_178001_246000.mat")
load("simr_246000_300000.mat")
load("simr_300001.mat")
%define variable location
flowtime_n = 2;
qin_n = 3;
qout_w_n = 4;
qin_w_n = 5;
tmax_n = 9;
tavg_n = 10;
dry_a_n = 12;
nucleate_a_n = 13;
tstag_n = 14;
cells_fins_n = 15;
pin_n = 16;
pout_n = 17;
k_n = 25;
%Stitch data
flat_a = (12700*12700 - 8*8*500*500)/((1E+6)^2);
last_point = simr300001(end,1);
time_step_size = 0.0001;
flowtime_overall = (0:last_point+3)*time_step;flowtime_overall = flowtime_overall';
tmax = cat(1,simr058000(:,tmax_n), simr58001178000(:,tmax_n), simr178001246000(:,tmax_n),
simr246000300000(:,tmax_n), simr300001(:,tmax_n))-273.15-61;
tavg = cat(1,simr058000(:,tavg_n), simr58001178000(:,tavg_n), simr178001246000(:,tavg_n),
simr246000300000(:,tavg_n), simr300001(:,tavg_n))-273.15-61;
tstag = cat(1,simr058000(:,tstag_n), simr58001178000(:,tstag_n), simr178001246000(:,tstag_n),
simr246000300000(:,tstag_n), simr300001(:,tstag_n))-273.15-61;
qin_w = cat(1,simr058000(:,qin_w_n), simr58001178000(:,qin_w_n), simr178001246000(:,qin_w_n),
simr246000300000(:,qin_w_n), simr300001(:,qin_w_n));
qin = cat(1,simr058000(:,qin_n), simr58001178000(:,qin_n), simr178001246000(:,qin_n),
simr246000300000(:,qin_n), simr300001(:,qin_n))./10000;
qout_w = cat(1,simr058000(:,qout_w_n), simr58001178000(:,qout_w_n),
simr178001246000(:,qout_w_n), simr246000300000(:,qout_w_n), simr300001(:,qout_w_n));
pin = qout_w = cat(1,simr058000(:,pin_n), simr58001178000(:,pin_n), simr178001246000(:,pin_n),
simr246000300000(:,pin_n), simr300001(:,pin_n));
pout_avg = cat(1,simr058000(:,pout_n), simr58001178000(:,pout_n), simr178001246000(:,pout_n),
simr246000300000(:,pout_n), simr300001(:,pout_n));
dry_a = cat(1,simr058000(:,dry_a_n), simr58001178000(:,dry_a_n), simr178001246000(:,dry_a_n),
simr246000300000(:,dry_a_n), simr300001(:,dry_a_n));
```

```matlab
nucleate_a = cat(1,simr058000(:,nucleate_a_n), simr58001178000(:,nucleate_a_n),
simr178001246000(:,nucleate_a_n), simr246000300000(:,nucleate_a_n), simr300001(:,nucleate_a_n));
dry_a = (dry_a./flat_a)*100;
nucleate_a = (nucleate_a./flat_a)*100;
k_vol = cat(1,simr058000(:,k_n), simr58001178000(:,k_n), simr178001246000(:,k_n),
simr246000300000(:,k_n), simr300001(:,k_n));
%plot wall temperatures
figure(1)
yyaxis left
ax = gca;
ax.YColor = 'k';
plot(flowtime_overall,tstag,'m-',flowtime_overall,tavg,'k-',flowtime_overall,tmax,'r-')
ylabel("Wall superheat [^{\circ}C]","FontSize",20)
xlabel("Flowe time [s]","FontSize",20)
yyaxis right
plot(flowtime_overall,qin,'b')
label_h = ylabel("Heat Flux [W/cm^2]","FontSize",20,'Color','k');
ylim([-0 80])
yticks([5 10 15 20 25 30 35])
xlim([0 40])
legend("Stagnation wall superheat","Average flat wall superheat","Maximum flat wall
superheat","Input heat flux","FontSize",20,"Location","northwest")
label_h.Position(1) = 42; % change horizontal position of ylabel
label_h.Position(2) = 20; % change vertical position of ylabel
set(gca, 'YColor','b')
ax = gca;
ax.FontSize = 16;
set(gcf,'color','w');
%plot heat rates
figure(2)
ax = gca;
ax.FontSize = 16;
set(gcf,'color','w');
xlabel("Flowe time [s]","FontSize",20)
yyaxis left
ax.YColor = 'k';
plot(flowtime_overall,qin_w,'k',flowtime_overall,qout_w,'r')
ylabel("Total heat rate [W]","FontSize",20,'Color','k')
ylim([0 60])
yyaxis right
ax.YColor = 'k';
plot(flowtime_overall,qin,'b')
label_h = ylabel("Heat Flux [W/cm^2]","FontSize",20,'Color','k');
ylim([-0 80])
yticks([5 10 15 20 25 30 35])
legend("Total heat rate into solid","Total heat rate into liquid","Input heat
flux","FontSize",20,"Location","northwest")
label_h.Position(1) = 42; % change horizontal position of ylabel
label_h.Position(2) = 20; % change vertical position of ylabel
set(gca, 'YColor','b')
% create mean arrays for evap area
ave_number = 1000;
pos_end_10 = 103000;
pos_end_14_7 = 178003;
pos_end_19_4 = 278004;
pos_end_23_4 = 340000;
pos_end_27 = 389600;
pos_end_30_9 = length(dry_a);
dry_a_mean = [0 mean(dry_a(pos_end_14_7-ave_number:pos_end_14_7)) mean(dry_a(pos_end_19_4-
ave_number:pos_end_19_4)) mean(dry_a(pos_end_23_4-ave_number:pos_end_23_4))
mean(dry_a(pos_end_27-ave_number:pos_end_27)) mean(dry_a(pos_end_30_9-
ave_number:pos_end_30_9))];
nucleate_a_mean = [0 mean(nucleate_a(pos_end_14_7-ave_number:pos_end_14_7))
mean(nucleate_a(pos_end_19_4-ave_number:pos_end_19_4)) mean(nucleate_a(pos_end_23_4-
ave_number:pos_end_23_4)) mean(nucleate_a(pos_end_27-ave_number:pos_end_27))
mean(nucleate_a(pos_end_30_9-ave_number:pos_end_30_9))];
%dry
dry_a_mean_array = zeros(pos_end_30_9,1);
dry_a_mean_array(1:pos_end_10,1) = dry_a_mean(1);
dry_a_mean_array(pos_end_10+1:pos_end_14_7,1) = dry_a_mean(2);
dry_a_mean_array(pos_end_14_7+1:pos_end_19_4,1) = dry_a_mean(3);
dry_a_mean_array(pos_end_19_4+1:pos_end_23_4,1) = dry_a_mean(4);
dry_a_mean_array(pos_end_23_4+1:pos_end_27,1) = dry_a_mean(5);
dry_a_mean_array(pos_end_27+1:pos_end_30_9,1) = dry_a_mean(6);
%nucleate
```

Y

```matlab
nucleate_a_mean_array = zeros(pos_end_30_9,1);
nucleate_a_mean_array(1:pos_end_10,1) = dry_a_mean(1);
nucleate_a_mean_array(pos_end_10+1:pos_end_14_7,1) = nucleate_a_mean(2);
nucleate_a_mean_array(pos_end_14_7+1:pos_end_19_4,1) = nucleate_a_mean(3);
nucleate_a_mean_array(pos_end_19_4+1:pos_end_23_4,1) = nucleate_a_mean(4);
nucleate_a_mean_array(pos_end_23_4+1:pos_end_27,1) = nucleate_a_mean(5);
nucleate_a_mean_array(pos_end_27+1:pos_end_30_9,1) = nucleate_a_mean(6);
%plot dry and nucleate area
figure(3)
yyaxis left
ax = gca;
ax.YColor = 'k';
plot(flowtime_overall,dry_a,'r-')
hold on
plot(flowtime_overall,dry_a_mean_array,'--k','LineWidth',1)
ylabel("Area contribution [%]","FontSize",20)
xlabel("Flow time [s]","FontSize",20)
ax = gca;
ylim([0 100])
ax.FontSize = 16;
set(gcf,'color','w');
yyaxis right
plot(flowtime_overall,qin,'b')
label_h = ylabel("Heat Flux [W/cm^2]","FontSize",20,'Color','k');
ylim([-50 40])
yticks([0 5 10 15 20 25 30 35])
legend("Dry-out","Dry-out average","Input heat flux","FontSize",14,"Location","northwest")
label_h.Position(1) = 42; % change horizontal position of ylabel
label_h.Position(2) = 20; % change vertical position of ylabel
set(gca, 'YColor','b')
ax = gca;
ax.FontSize = 16;
set(gcf,'color','w');
figure(4)
yyaxis left
ax = gca;
ax.YColor = 'k';
plot(flowtime_overall,nucleate_a,'m-')
hold on
plot(flowtime_overall,nucleate_a_mean_array,'k--','LineWidth',1)
ylabel("Area contribution [%]","FontSize",20)
xlabel("Flow time [s]","FontSize",20)
ax = gca;
ylim([0 100])
ax.FontSize = 16;
set(gcf,'color','w');
yyaxis right
plot(flowtime_overall,qin,'b')
label_h = ylabel("Heat Flux [W/cm^2]","FontSize",20,'Color','k');
ylim([-50 40])
yticks([0 5 10 15 20 25 30 35])
legend("Fully developed nucleation boiling","Fully developed nucleation boiling average","Input
heat flux","FontSize",14,"Location","northwest")
label_h.Position(1) = 42; % change horizontal position of ylabel
label_h.Position(2) = 20; % change vertical position of ylabel
set(gca, 'YColor','b')
ax = gca;
ax.FontSize = 16;
set(gcf,'color','w');
%plot pdef
pdef = pin - pout_avg;
figure(1)
yyaxis left
ax = gca;
ax.YColor = 'k';
plot(flowtime_overall,pdef,'k-')
ylabel("Pressure drop [\Delta kPa]","FontSize",20)
xlabel("Flowe time [s]","FontSize",20)
yyaxis right
plot(flowtime_overall,qin,'b')
label_h = ylabel("Heat Flux [W/cm^2]","FontSize",20,'Color','k');
ylim([0 80])
yticks([0 5 10 15 20 25 30 35])
legend("Pressure drop","Input heat flux","FontSize",20,"Location","northeastoutside")
label_h.Position(1) = 37; % change horizontal position of ylabel
```

Z

```
label_h.Position(2) = 20; % change vertical position of ylabel
set(gca, 'YColor','b')
ax = gca;
ax.FontSize = 16;
set(gcf,'color','w');
%plot cell change
fins_volume = 0.0000006994699*(1000^3);
fins_cell_density = fins_cells/fins_volume;
figure(5)
yyaxis left
ax = gca;
ax.YColor = 'k';
plot(flowtime_overall,fins_cell_density,'k-')
ylabel("Cell density [cells/mm^3]","FontSize",20)
xlabel("Flowe time [s]","FontSize",20)
ax = gca;
ax.FontSize = 16;
set(gcf,'color','w');
ylim([min(fins_cell_density)-5 max(fins_cell_density)+2])
yyaxis right
plot(flowtime_overall,qin,'b')
label_h = ylabel("Heat Flux [W/cm^2]","FontSize",20,'Color','k');
ylim([0 80])
yticks([0 5 10 15 20 25 30 35])
legend("Cell density","Input heat flux","FontSize",20,"Location","northwest")
label_h.Position(1) = 37; % change horizontal position of ylabel
label_h.Position(2) = 20; % change vertical position of ylabel
set(gca, 'YColor','b')
ax = gca;
ax.FontSize = 16;
set(gcf,'color','w');
```

Appendix E: Pressure drop study

```
clear all
load("simr_90001.mat")
load('pressure_vs_q.mat')
qin_list = [0 14.7341 19.4033 23.2425];
pdef_list = [5571 5581 5576 5589]./1000;
p_extend = mean(simr90001(:,28))/1000;
p_exp = pressurevsq(:,2);
q_exp = pressurevsq(:,1);
Cd = mean(pdef_list)/p_extend;
figure(1)
plot(q_exp,p_exp,'b-',qin_list,pdef_list,'kx','MarkerSize',50)
hold on
plot(0,p_extend,'rx','MarkerSize',50)
hold on
plot(23.2,p_extend,'rx','MarkerSize',50)
hold on
yline(mean(pdef_list),'k--')
hold on
yline(p_extend,'r--')
label_h = ylabel("Pressure drop [\Delta kPa]","FontSize",20);
xlabel("Heat Flux [W/cm^2]","FontSize",20)
legend("Rau and Garimella","Current study","Extended
domain","FontSize",20,"Location","southeast")
xlim([0 30])
ylim([0 10])
ax = gca;
ax.YAxis.Exponent = 0;
ax.FontSize = 16;
set(gcf,'color','w');
%label_h.Position(1) = -2.5; % change horizontal position of ylabel
%label_h.Position(2) = 0.006; % change vertical position of ylabel
```

Appendix E: Parametric study: Inlet Reynolds number

```
clear all
load("Re25000.mat")
load("Re45000.mat")
Re_number = [25000 35000 45000];
```

```matlab
dry35_mean = 18.452047;
nucleate35_mean = 29.57888;
results_mat = zeros(3,4);
Pin = [104275.89 107133.65 110752.83];
Pout = [101544.14 101544.39 101543.73];
Pdef = (Pin - Pout)/1000;
kmass = [0.012063971 0.011588599 0.0270015];
kvol = [0.013097345 0.012587001 0.024748321];
Tmax = [72.535669 72.066064 72.19259]-61;
data = Re25000;
flat_area = (145290000)/(1000*1000*1000*1000);
flowtime = data(end-20000:end,2);
tstag25 = data(end-20000:end,6)-273.15-61;
qin25 = data(end-20000:end,8);
qout25 = data(end-20000:end,9);
dry25 = (data(end-20000:end,14)/flat_area)*100;
dry25_mean = mean(dry25);
nucleate25 = (data(end-20000:end,15)/flat_area)*100;
nucleate25_mean = mean(nucleate25);
data = Re45000;
flat_area = (145290000)/(1000*1000*1000*1000);
flowtime = data(end-20000:end,2);
tstag45 = data(end-20000:end,6)-273.15-61;
qin45 = data(end-20000:end,8);
qout45 = data(end-20000:end,9)*(-1);
dry45 = (data(end-20000:end,14)/flat_area)*100;
dry45_mean = mean(dry45);
nucleate45 = (data(end-20000:end,15)/flat_area)*100;
nucleate45_mean = mean(nucleate45);
dry_results = [dry25_mean dry35_mean dry45_mean];
nucleate_results = [nucleate25_mean nucleate35_mean nucleate45_mean];
stag_results = [mean(tstag25(end-5000:end)) 9.86 mean(tstag45(end-5000:end))];
%{
figure(1)
plot(flowtime,tstag25,flowtime,tstag45)
legend("25 000","45 000","FontSize",30,"Location","northeastoutside")
figure(2)
plot(flowtime,qin25,flowtime,qout25)
ylabel("[W]","FontSize",30)
xlabel("flowtime [s]","FontSize",30)
legend("qin","qout","FontSize",30,"Location","northeastoutside")
title("heat rate","FontSize",30)
figure(3)
plot(flowtime,dry45,flowtime,nucleate45)
ylabel("Contribution [%]","FontSize",30)
xlabel("flowtime [s]","FontSize",30)
legend("Dry area contribution","Nucluate area
contribution","FontSize",30,"Location","northeastoutside")
title("Evaporation contribution convergence","FontSize",30)
%}
figure(1)
plot(Re_number,dry_results,Re_number,nucleate_results)
legend("Dry-out area contribution","Nucleate boiling area
contribution","FontSize",20,"Location","northeastoutside")
ylabel("Area contribution [%]","FontSize",30)
xlabel("Reynolds number","FontSize",30)
xticks([25000 35000 45000]);
ylim([0 100])
xlim([24000 46000])
ax = gca;
ax.XAxis.Exponent = 0;
ax.FontSize = 16;
set(gcf,'color','w');
vap_rest = 100 - dry_results - nucleate_results;
bar_chart = [vap_rest(1),nucleate_results(1),dry_results(1)
    vap_rest(2),nucleate_results(2),dry_results(2)
    vap_rest(3),nucleate_results(3),dry_results(3)];
figure(1)
b = bar(bar_chart,'stacked');
b(3).FaceColor = [1 0 0];
b(2).FaceColor = [0.4940 0.1840 0.5560];
b(1).FaceColor = [0 0 1];
xlabel("Reynolds number",'Fontsize',40)
set(gca, 'XTickLabel', {'25000' '35000' '45000'})
ylim([0 100])
```

BB

```
legend("Developing nucleate boiling regime","Fully developed nucleate boiling regime","Dry
out",'Fontsize',30,'Location','northeastoutside')
ylabel("Area contribution [%]","FontSize",40)
%title("Boiling regime affected area","FontSize",40)
ax = gca;
ax.XAxis.FontSize = 22;
ax.YAxis.FontSize = 22;
set(gcf,'color','w');
results_mat(1,3) = Pdef(1);
results_mat(2,3) = Pdef(2);
results_mat(3,3) = Pdef(3);
figure(2)
plot(Re_number,Pdef,'kx',"MarkerSize",60)
hold on
plot(Re_number,Pdef,'k--')
ylabel("Pressure drop [\DeltakPa]","FontSize",30)
xlabel("Reynolds number","FontSize",30)
xticks([25000 35000 45000]);
ylim([0 10])
xlim([24000 46000])
ax = gca;
ax.XAxis.Exponent = 0;
ax.FontSize = 16;
set(gcf,'color','w');
results_mat(1,1) = stag_results(1);
results_mat(2,1) = stag_results(2);
results_mat(3,1) = stag_results(3);
results_mat(1,2) = Tmax(1);
results_mat(2,2) = Tmax(2);
results_mat(3,2) = Tmax(3);
figure(3)
plot(Re_number,stag_results,'kx',Re_number,Tmax,'rx',"MarkerSize",60)
hold on
plot(Re_number,stag_results,'k--',Re_number,Tmax,'r--')
ylabel("Wall superheat [^{\circ}C]","FontSize",20)
xlabel("Reynolds number","FontSize",20)
legend("Stagnation superheat","Maximum superheat",'Fontsize',30,'Location','northeastoutside')
xticks([25000 35000 45000]);
yticks([9 9.5 10 10.5 11 11.5 12]);
ylim([9 12])
xlim([24000 46000])
ax = gca;
ax.XAxis.Exponent = 0;
ax.FontSize = 16;
set(gcf,'color','w');
results_mat(1,4) = kvol(1);
results_mat(2,4) = kvol(2);
results_mat(3,4) = kvol(3);
figure(4)
plot(Re_number,kvol,'kx',"MarkerSize",60)
hold on
plot(Re_number,kvol,'k--')
ylabel("Turbulent kinetic energy [m^2/s^2]","FontSize",30)
xlabel("Reynolds number","FontSize",30)
xticks([25000 35000 45000]);
ylim([0 0.08])
xlim([24000 46000])
ax = gca;
ax.XAxis.Exponent = 0;
ax.FontSize = 16;
set(gcf,'color','w');
```

Appendix E: Parametric study: Pin-fin height, spacing and distribution

```
clear all
load("h2500s1150.mat")
load("h2500s1075.mat")
load("h1250s1075.mat")
load("h1250s1150.mat")
load("h625s1150.mat")
```

```matlab
load("h625s1075.mat")
load("h312s1150.mat")
load("h312s1075.mat")
count = 1000;
spacing_points_real = ([1 1.075 1.15]);
spacing_points_real_mat(1:4,1) = spacing_points_real(1);
spacing_points_real_mat(1:4,2) = spacing_points_real(2);
spacing_points_real_mat(1:4,3) = spacing_points_real(3);
height_points_real = ([2.5 1.25 0.625 0.312]);
height_points_real_mat(1,1:3) = height_points_real(1);
height_points_real_mat(2,1:3) = height_points_real(2);
height_points_real_mat(3,1:3) = height_points_real(3);
height_points_real_mat(4,1:3) = height_points_real(4);
spacing_points = 1:0.001:1.15;
height_points = 0.312:0.001:2.5;
height_points = flip(height_points);
tstag_mat = zeros(length(height_points),length(spacing_points));
tavg_mat = zeros(length(height_points),length(spacing_points));
%find coordinates
for i = 1:length(height_points)
    if height_points(i) == 0.312
        x_0_312 = i;
    elseif height_points(i) == 0.625
        x_0_625 = i;
    elseif height_points(i) == 1.25
        x_1_25 = i;
    elseif height_points(i) == 2.5
        x_2_5 = i;
    end
end
for i = 1:length(spacing_points)
    if spacing_points(i) == 1
        y_1 = i;
    elseif spacing_points(i) == 1.075
        y_1_075 = i;
    elseif spacing_points(i) == 1.15
        y_1_15 = i;
    end
end
data = h2500s1150;
tavg_h2500s1150 = data(:,3)-273.15-61;
tmax_h2500s1150 = data(:,4)-273.15-61;
tstag_h2500s1150 = data(:,6)-273.15-61;
tstag_mat(x_2_5,y_1_15) = mean(tstag_h2500s1150(end-count:end,1));
tstag_mat_real(1,3) = mean(tstag_h2500s1150(end-count:end,1));
tavg_mat(x_2_5,y_1_15) = mean(tavg_h2500s1150(end-count:end,1));
tavg_mat_real(1,3) = mean(tavg_h2500s1150(end-count:end,1));
data = h2500s1075;
tavg_h2500s1075 = data(:,3)-273.15-61;
tmax_h2500s1075 = data(:,4)-273.15-61;
tstag_h2500s1075 = data(:,6)-273.15-61;
tstag_mat(x_2_5,y_1_075) = mean(tstag_h2500s1075(end-count:end,1));
tstag_mat_real(1,2) = mean(tstag_h2500s1075(end-count:end,1));
tavg_mat(x_2_5,y_1_075) = mean(tavg_h2500s1075(end-count:end,1));
tavg_mat_real(1,2) = mean(tavg_h2500s1075(end-count:end,1));
data = h1250s1075;
tavg_h1250s1075 = data(:,3)-273.15-61;
tmax_h1250s1075 = data(:,4)-273.15-61;
tstag_h1250s1075 = data(:,6)-273.15-61;
tstag_mat(x_1_25,y_1_075) = mean(tstag_h1250s1075(end-count:end,1));
tstag_mat_real(2,2) = mean(tstag_h1250s1075(end-count:end,1));
tavg_mat(x_1_25,y_1_075) = mean(tavg_h1250s1075(end-count:end,1));
tavg_mat_real(2,2) = mean(tavg_h1250s1075(end-count:end,1));
data = h1250s1150;
tavg_h1250s1150 = data(:,3)-273.15-61;
tmax_h1250s1150 = data(:,4)-273.15-61;
tstag_h1250s1150 = data(:,6)-273.15-61;
tstag_mat(x_1_25,y_1_15) = mean(tstag_h1250s1150(end-count:end,1));
tstag_mat_real(2,3) = mean(tstag_h1250s1150(end-count:end,1));
tavg_mat(x_1_25,y_1_15) = mean(tavg_h1250s1150(end-count:end,1));
tavg_mat_real(2,3) = mean(tavg_h1250s1150(end-count:end,1));
data = h625s1150;
tavg_h625s1150 = data(:,3)-273.15-61;
tmax_h625s1150 = data(:,4)-273.15-61;
tstag_h625s1150 = data(:,6)-273.15-61;
```

DD

```matlab
tstag_mat(x_0_625,y_1_15) = mean(tstag_h625s1150(end-count:end,1));
tstag_mat_real(3,3) = mean(tstag_h625s1150(end-count:end,1));
tavg_mat(x_0_625,y_1_15) = mean(tavg_h625s1150(end-count:end,1));
tavg_mat_real(3,3) = mean(tavg_h625s1150(end-count:end,1));
data = h625s1075;
tavg_h625s1075 = data(:,3)-273.15-61;
tmax_h625s1075 = data(:,4)-273.15-61;
tstag_h625s1075 = data(:,6)-273.15-61;
tstag_mat(x_0_625,y_1_075) = mean(tstag_h625s1075(end-count:end,1));
tstag_mat_real(3,2) = mean(tstag_h625s1075(end-count:end,1));
tavg_mat(x_0_625,y_1_075) = mean(tavg_h625s1075(end-count:end,1));
tavg_mat_real(3,2) = mean(tavg_h625s1075(end-count:end,1));
data = h312s1150;
tavg_h312s1150 = data(:,3)-273.15-61;
tmax_h312s1150 = data(:,4)-273.15-61;
tstag_h312s1150 = data(:,6)-273.15-61;
tstag_mat(x_0_312,y_1_15) = mean(tstag_h312s1150(end-count:end-50,1));
tstag_mat_real(4,3) = mean(tstag_h312s1150(end-count:end-50,1));
tavg_mat(x_0_312,y_1_15) = mean(tavg_h312s1150(end-count:end-50,1));
tavg_mat_real(4,3) = mean(tavg_h312s1150(end-count:end-50,1));
data = h312s1075;
tavg_h312s1075 = data(:,3)-273.15-61;
tmax_h312s1075 = data(:,4)-273.15-61;
tstag_h312s1075 = data(:,6)-273.15-61;
tstag_mat(x_0_312,y_1_075) = mean(tstag_h312s1075(end-count:end,1));
tstag_mat_real(4,2) = mean(tstag_h312s1075(end-count:end,1));
tavg_mat(x_0_312,y_1_075) = mean(tavg_h312s1075(end-count:end,1));
tavg_mat_real(4,2) = mean(tavg_h312s1075(end-count:end,1));
tmax_h2500s1000 = 10.5812;
tmax_h1250s1000 = 12.128;
tmax_h625s1000 = 14.397;
tmax_h312s1000 = 15.0362;
tstag_h2500s1000 = 8.988;
tstag_mat(x_2_5,y_1) = tstag_h2500s1000;
tstag_mat_real(1,1) = tstag_h2500s1000;
tstag_h1250s1000 = 11.4388;
tstag_mat(x_1_25,y_1) = tstag_h1250s1000;
tstag_mat_real(2,1) = tstag_h1250s1000;
tstag_h625s1000 = 13.9788;
tstag_mat(x_0_625,y_1) = tstag_h625s1000;
tstag_mat_real(3,1) = tstag_h625s1000;
tstag_h312s1000 = 15.01361;
tstag_mat(x_0_312,y_1) = tstag_h312s1000;
tstag_mat_real(4,1) = tstag_h312s1000;
tavg_h2500s1000 = 9.6325;
tavg_mat(x_2_5,y_1) = tavg_h2500s1000;
tavg_mat_real(1,1) = tavg_h2500s1000;
tavg_h1250s1000 = 11.146;
tavg_mat(x_1_25,y_1) = tavg_h1250s1000;
tavg_mat_real(2,1) = tavg_h1250s1000;
tavg_h625s1000 = 13.498;
tavg_mat(x_0_625,y_1) = tavg_h625s1000;
tavg_mat_real(3,1) = tavg_h625s1000;
tavg_h312s1000 = 15.0362;
tavg_mat(x_0_312,y_1) = tavg_h312s1000;
tavg_mat_real(4,1) = tavg_h312s1000;
%tstag plot
tstag_mat(tstag_mat==0) = NaN;
Fstag = inpaint_nans(tstag_mat,3);
figure(1)
surf(spacing_points,height_points,Fstag,'edgecolor', 'none')
hold on
plot3(spacing_points_real_mat,height_points_real_mat,tstag_mat_real,'r.','MarkerSize',30)
xlabel("Fin spacing [mm]","FontSize",30)
ylabel("Fin height [mm]","FontSize",30)
zlabel("Stagnation wall superheat [^{\circ}C]","FontSize",30)
xticks([1.000 1.075 1.150])
yticks([0.312 0.625 1.250 2.500])
ylim([0 2.600])
ax = gca;
ax.XAxis.Exponent = 0;
ax.FontSize = 16;
set(gcf,'color','w');
%tavg plot
tavg_mat(tavg_mat==0) = NaN;
```

```matlab
F = inpaint_nans(tavg_mat,3) ;
figure(2)
surf(spacing_points,height_points,F,'edgecolor', 'none')
hold on
plot3(spacing_points_real_mat,height_points_real_mat,tavg_mat_real,'r.','MarkerSize',30)
xlabel("Fin spacing [mm]","FontSize",50)
ylabel("Fin height [mm]","FontSize",50)
zlabel("Average wall superheat [^{\circ}C]","FontSize",30)
xticks([1.000 1.075 1.150])
yticks([0.312 0.625 1.250 2.500])
ylim([0 2.600])
ax = gca;
ax.XAxis.Exponent = 0;
ax.FontSize = 16;
set(gcf,'color','w');
%create evap mat
dry_mat_real = zeros(4,3);
nucleate_mat_real = zeros(4,3);
data = h2500s1150;
dry_h2500s1150 = (data(:,13)./flat_a)*100;
dry_mat_real(1,3) = mean(dry_h2500s1150(end-count:end,1));
dry_mat(x_2_5,y_1_15) = mean(dry_h2500s1150(end-count:end,1));
nucleate_h2500s1150 = (data(:,14)./flat_a)*100;
nucleate_mat_real(1,3) = mean(nucleate_h2500s1150(end-count:end,1));
nucleate_mat(x_2_5,y_1_15) = mean(nucleate_h2500s1150(end-count:end,1));
data = h2500s1075;
dry_h2500s1075 = (data(:,13)./flat_a)*100;
dry_mat_real(1,2) = mean(dry_h2500s1075(end-count:end,1));
dry_mat(x_2_5,y_1_075) = mean(dry_h2500s1075(end-count:end,1));
nucleate_h2500s1075 = (data(:,14)./flat_a)*100;
nucleate_mat_real(1,2) = mean(nucleate_h2500s1075(end-count:end,1));
nucleate_mat(x_2_5,y_1_075) = mean(nucleate_h2500s1075(end-count:end,1));
data = h1250s1150;
dry_h1250s1150 = (data(:,13)./flat_a)*100;
dry_mat_real(2,3) = mean(dry_h1250s1150(end-count:end,1));
dry_mat(x_1_25,y_1_15) = mean(dry_h1250s1150(end-count:end,1));
nucleate_h1250s1150 = (data(:,14)./flat_a)*100;
nucleate_mat_real(2,3) = mean(nucleate_h1250s1150(end-count:end,1));
nucleate_mat(x_1_25,y_1_15) = mean(nucleate_h1250s1150(end-count:end,1));
data = h1250s1075;
dry_h1250s1075 = (data(:,13)./flat_a)*100;
dry_mat_real(2,2) = mean(dry_h1250s1075(end-count:end,1));
dry_mat(x_1_25,y_1_075) = mean(dry_h1250s1075(end-count:end,1));
nucleate_h1250s1075 = (data(:,14)./flat_a)*100;
nucleate_mat_real(2,2) = mean(nucleate_h1250s1075(end-count:end,1));
nucleate_mat(x_1_25,y_1_075) = mean(nucleate_h1250s1075(end-count:end,1));
data = h625s1150;
dry_h625s1150 = (data(:,13)./flat_a)*100;
dry_mat_real(3,3) = mean(dry_h625s1150(end-count:end,1));
dry_mat_(x_0_625,y_1_15) = mean(dry_h625s1150(end-count:end,1));
nucleate_h625s1150 = (data(:,14)./flat_a)*100;
nucleate_mat_real(3,3) = mean(nucleate_h625s1150(end-count:end,1));
nucleate_mat(x_0_625,y_1_15) = mean(nucleate_h625s1150(end-count:end,1));
data = h625s1075;
dry_h625s1075 = (data(:,13)./flat_a)*100;
dry_mat_real(3,2) = mean(dry_h625s1075(end-count:end,1));
dry_mat(x_0_625,y_1_075) = mean(dry_h625s1075(end-count:end,1));
nucleate_h625s1075 = (data(:,14)./flat_a)*100;
nucleate_mat_real(3,2) = mean(nucleate_h625s1075(end-count:end,1));
nucleate_mat(x_0_625,y_1_075) = mean(nucleate_h625s1075(end-count:end,1));
data = h312s1150;
dry_h312s1150 = (data(:,13)./flat_a)*100;
dry_mat_real(4,3) = mean(dry_h312s1150(end-count:end,1));
dry_mat(x_0_312,y_1_15) = mean(dry_h312s1150(end-count:end,1));
nucleate_h312s1150 = (data(:,14)./flat_a)*100;
nucleate_mat_real(4,3) = mean(nucleate_h312s1150(end-count:end,1));
nucleate_mat(x_0_312,y_1_15) = mean(nucleate_h312s1150(end-count:end,1));
data = h312s1075;
dry_h312s1075 = (data(:,13)./flat_a)*100;
dry_mat_real(4,2) = mean(dry_h312s1075(end-count:end,1));
dry_mat(x_0_312,y_1_075) = mean(dry_h312s1075(end-count:end,1));
nucleate_h312s1075 = (data(:,14)./flat_a)*100;
nucleate_mat_real(4,2) = mean(nucleate_h312s1075(end-count:end,1));
nucleate_mat(x_0_312,y_1_075) = mean(nucleate_h312s1075(end-count:end,1));
dry_mat_real(1,1) = 16.72;
```

FF

```matlab
dry_mat(x_2_5,y_1) = 16.72;
dry_mat_real(2,1) = 6.42;
dry_mat(x_1_25,y_1) = 6.42;
dry_mat_real(3,1) = 3.35;
dry_mat(x_0_625,y_1) = 3.35;
dry_mat_real(4,1) = 0.01;
dry_mat(x_0_312,y_1) = 0.01;
dry_mat_real(4,2) = 0.01;
dry_mat(x_0_312,y_1_075) = 0.01;
nucleate_mat_real(1,1) = 25.22;
nucleate_mat_real(2,1) = 54.94;
nucleate_mat_real(3,1) = 74.35;
nucleate_mat_real(4,1) = 86.64;
nucleate_mat(x_2_5,y_1) = 25.22;
nucleate_mat(x_1_25,y_1) = 54.94;
nucleate_mat(x_0_625,y_1) = 74.35;
nucleate_mat(x_0_312,y_1) = 86.64;
%dry plot
dry_mat(dry_mat==0) = NaN;
Fdry = inpaint_nans(dry_mat,3);
figure(3)
surf(spacing_points,height_points,Fdry,'edgecolor', 'none')
hold on
plot3(spacing_points_real_mat,height_points_real_mat,dry_mat_real,'r.','MarkerSize',30)
xlabel("Fin spacing [mm]","FontSize",30)
ylabel("Fin height [mm]","FontSize",30)
zlabel("Dry-out area contribution [%]","FontSize",30)
xticks([1.000 1.075 1.150])
yticks([0.312 0.625 1.250 2.500])
zlim([0 100])
ylim([0 2.600])
ax = gca;
ax.XAxis.Exponent = 0;
ax.FontSize = 16;
set(gcf,'color','w');
%nucleate plot
nucleate_mat(nucleate_mat==0) = NaN;
Fnuc = inpaint_nans(nucleate_mat,3);
figure(4)
surf(spacing_points,height_points,Fnuc,'edgecolor', 'none')
hold on
plot3(spacing_points_real_mat,height_points_real_mat,nucleate_mat_real,'r.','MarkerSize',30)
xlabel("Fin spacing [mm]","FontSize",30)
ylabel("Fin height [mm]","FontSize",30)
zlabel("Nucleate boiling area contribution [%]","FontSize",1)
xticks([1.000 1.075 1.150])
yticks([0.312 0.625 1.250 2.500])
zticks([0 20 40 60 80 100])
zlim([0 100])
ylim([0 2.600])
ax = gca;
ax.XAxis.Exponent = 0;
ax.FontSize = 16;
set(gcf,'color','w');
load("Pdef.mat")
load("kvol.mat")
load('Pdef_full.mat')
load("kvol_full.mat")
kvol_mat(x_2_5,y_1) = kvolfull(1,1);
kvol_mat(x_2_5,y_1_075) = kvolfull(1,2);
kvol_mat(x_2_5,y_1_15) = kvolfull(1,3);
kvol_mat(x_1_25,y_1) = kvolfull(2,1);
kvol_mat(x_1_25,y_1_075) = kvolfull(2,2);
kvol_mat(x_1_25,y_1_15) = kvolfull(2,3);
kvol_mat(x_0_625,y_1) = kvolfull(3,1);
kvol_mat(x_0_625,y_1_075) = kvolfull(3,2);
kvol_mat(x_0_625,y_1_15) = kvolfull(3,3);
kvol_mat(x_0_312,y_1) = kvolfull(4,1);
kvol_mat(x_0_312,y_1_075) = kvolfull(4,2);
kvol_mat(x_0_312,y_1_15) = kvolfull(4,3);
%kvol
kvol_mat(kvol_mat==0) = NaN;
F = inpaint_nans(kvol_mat,3);
figure(1)
surf(spacing_points,height_points,F,'edgecolor', 'none')
```

```matlab
hold on
plot3(spacing_points_real_mat,height_points_real_mat,kvolfull,'r.','MarkerSize',30)
xlabel("Fin spacing [mm]","FontSize",30)
ylabel("Fin height [mm]","FontSize",30)
zlabel("Turbulent kinetic energy [m^2/s^2]","FontSize",30)
xticks([1.000 1.075 1.150])
yticks([0.312 0.625 1.250 2.500])
%zlim([0 0.04])
ylim([0 2.600])
xlim([0.950 1.200])
ax = gca;
ax.XAxis.Exponent = 0;
ax.FontSize = 16;
set(gcf,'color','w');
p_mat(x_2_5,y_1) = Pdeffull(1,1);
p_mat(x_2_5,y_1_075) = Pdeffull(1,2);
p_mat(x_2_5,y_1_15) = Pdeffull(1,3);
p_mat(x_1_25,y_1) = Pdeffull(2,1);
p_mat(x_1_25,y_1_075) = Pdeffull(2,2);
p_mat(x_1_25,y_1_15) = Pdeffull(2,3);
p_mat(x_0_625,y_1) = Pdeffull(3,1);
p_mat(x_0_625,y_1_075) = Pdeffull(3,2);
p_mat(x_0_625,y_1_15) = Pdeffull(3,3);
p_mat(x_0_312,y_1) = Pdeffull(4,1);
p_mat(x_0_312,y_1_075) = Pdeffull(4,2);
p_mat(x_0_312,y_1_15) = Pdeffull(4,3);
%Pdef
Pdeffull = Pdeffull/1000;
p_mat = p_mat/1000;
p_mat(p_mat==0) = NaN;
F = inpaint_nans(p_mat,3);
figure(1)
surf(spacing_points,height_points,F,'edgecolor', 'none')
hold on
plot3(spacing_points_real_mat,height_points_real_mat,Pdeffull,'r.','MarkerSize',30)
xlabel("Fin spacing [mm]","FontSize",30)
ylabel("Fin height [mm]","FontSize",30)
zlabel("Pressure drop [\DeltakPa]","FontSize",30)
xticks([1.000 1.075 1.150])
yticks([0.312 0.625 1.250 2.500])
zlim([0 8])
ylim([0 2.600])
xlim([0.950 1.200])
ax = gca;
ax.XAxis.Exponent = 0;
ax.FontSize = 16;
set(gcf,'color','w');

figure(4)
plot(t_sim,q_sim,'bsquare','MarkerSize',20)
hold on
plot(star_t,star_q,'kpentagram','MarkerSize',20)
hold on
plot(t_sim,q_sim,'b--')
hold on
plot(star_t,star_q,'k--')%,tmax_sim,q_sim,'k--')
ylim([0 80])
xlim([0 24])
ylabel("Heat Flux [W/cm^2]","FontSize",60)
xlabel("Wall superheat [^{\circ}C]","FontSize",60)
%legend("Rau and Garimella","Current results - Stagnation wall superheat","Current results -
Maximum wall superheat","FontSize",20,"Location","northwest")
legend("Inline pin fins","Star pin fins arrangement","FontSize",20,"Location","northwest")
ax = gca;
ax.FontSize = 16;
set(gcf,'color','w');
```

HH